DOE-ER-0313/72
ORNL/SPR-2023/2704
Distribution
Categories
UC-423, -424

FUSION MATERIALS
SEMIANNUAL PROGRESS REPORT
FOR THE PERIOD ENDING

June 30, 2022

Prepared for
DOE Office of Fusion Energy Sciences
(AT 60 20 10 0)

DATE PUBLISHED: January 2023

Prepared by
OAK RIDGE NATIONAL LABORATORY
Oak Ridge, Tennessee 37831
Managed by
UT-Battelle, LLC
For the
U.S. DEPARTMENT OF ENERGY

FOREWORD

This is the seventy-second in a series of semiannual technical progress reports on fusion materials science activity supported by the Fusion Energy Sciences Program of the U.S. Department of Energy. It covers the period ending June 30, 2022. This report focuses on research addressing the effects on materials properties and performance of exposure to the neutronic, thermal and chemical environments anticipated in the chambers of fusion experiments and energy systems. This research is a major element of the national effort to establish the materials knowledge base for an economically and environmentally attractive fusion energy source. Research activities on issues related to the interaction of materials with plasmas are reported separately.

The results reported are the products of a national effort involving a number of national laboratories and universities. A large fraction of this work, particularly in relation to fission reactor irradiations, is carried out collaboratively with partners in Japan, Russia, and the European Union. The purpose of this series of reports is to provide a working technical record for the use of program participants, and to provide a means of communicating the efforts of fusion materials scientists to the broader fusion community, both nationally and worldwide.

This report has been compiled by Stephanie Melton, Oak Ridge National Laboratory. Her efforts, and the efforts of the many persons who made technical contributions, are gratefully acknowledged.

Daniel Clark
Research Division
Office of Fusion Energy Sciences

TABLE OF CONTENTS

1 FERRITIC/MARTENSITIC STEEL DEVELOPMENT

2 ODS AND NANOCOMPOSITED ALLOY DEVELOPMENT

3 CERAMIC COMPOSITE STRUCTURAL MATERIAL DEVELOPMENT

TABLE OF CONTENTS

4 **PLASMA-FACING AND HIGH HEAT FLUX MATERIALS AND COMPONENT TESTING**

TABLE OF CONTENTS

5.0 ADVANCED MANUFACTURING

No contributions this reporting period.

6.0 EFFECTS OF IRRADIATION

7.0 PLASMA MATERIAL INTERACTIONS

No contributions this reporting period.

8.0 CORROSION AND COMPATIBILITY IN FUSION SYSTEMS

9.0 MODELING AND COMPUTATIONAL STUDIES

TABLE OF CONTENTS

10 **IRRADIATION AND TESTING ANALYSIS, METHODS, EXPERIMENTS, AND SCHEDULES**

1. FERRITIC/MARTENSITIC STEEL DEVELOPMENT

1.1 SPECIMEN SIZE AND GEOMETRY EFFECTS ON THE MASTER CURVE FRACTURE TOUGHNESS MEASUREMENT OF EUROFER97 AND F82H STEELS

—X. Chen, M. A. Sokolov, Y. Katoh (Oak Ridge National Laboratory), M. Serrano, R. Hernández (CIEMAT), S. Gonzalez De Vicente (IAEA)

OBJECTIVE

Under the International Atomic Energy Agency (IAEA) Coordinated Research Projects (CRP) framework, this work aims for evaluating specimen size and geometry effects on Master Curve fracture toughness measurement of fusion structural materials. The ultimate goal is to establish a Mater Curve testing and analysis guideline based on interlaboratory round-robin results and best practices.

PROGRESS AND STATUS

Under the auspices of IAEA, a Coordinated Research Project (CRP) entitled “Towards the Standardization of Small Specimen Test Techniques for Fusion Applications” started in 2017. The overall objective of the project is to provide a set of guidelines for small specimen test techniques (SSTT) based on commonly agreed best practices on main test techniques including tensile, creep, low cycle fatigue, fracture toughness, and fatigue crack growth rate. This would act as the first step toward a full standardization of SSTT. Fusion structural materials, i.e., reduced activation ferritic/martensitic (RAFM) steels such as EUROFER97 and F82H, were used for testing. In addition, the project would generate additional mechanical property data of RAFM steels tested by SSTT.

For the fracture toughness task of the CRP, three testing methods including Master Curve, local approach, and ductile approach were evaluated. This study focused on the Master Curve method based on the American Society for Testing and Materials [ASTM] International standard E1921-21a “Standard Test Method for Determination of Reference Temperature, T_0, for Ferritic Steels in the Transition Range” [1] and commonly agreed best practice from researchers at Oak Ridge National Laboratory (ORNL), the Center for Energy, Environmental and Technological Research (CIEMAT), and United Kingdom Atomic Energy Authority (UKAEA) [2].

Detailed descriptions of the test materials, testing matrix, specimen types and geometries, experimental setup, and preliminary results have been reported in one of the previous Fusion Semiannual reports [3]. One major issue encountered by then was the misalignment of the fatigue precrack frame which resulted in the skewed fatigue precrack front and unrealistically low Master Curve reference temperature, T_0, measured from 0.5T compact tension (0.5T CT) and 4mm mini-compact tension (4mm miniCT) specimens for EUROFER97 and F82H. Since then, we have made significant improvements to the 10-kip fatigue precrack frame, as shown in Figure 1. For instance, we minimized the number of components utilized, replaced regular washers with fatigue-grade washers, machined new specimen grips, and applied spiral washers with preload to remove the load train slack and misalignment. With the improved fatigue precrack frame, we significantly increase our chance of creating straight fatigue precrack fronts for 0.5T CT and 4mm miniCT specimens as illustrated in Figure 2.

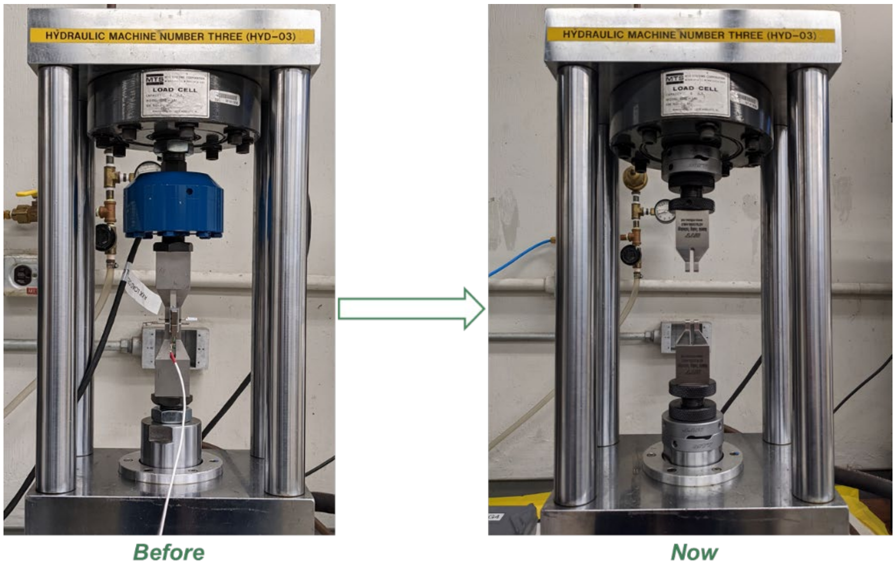

Figure 1. Improvement of the 10-kip fatigue precrack frame alignment.

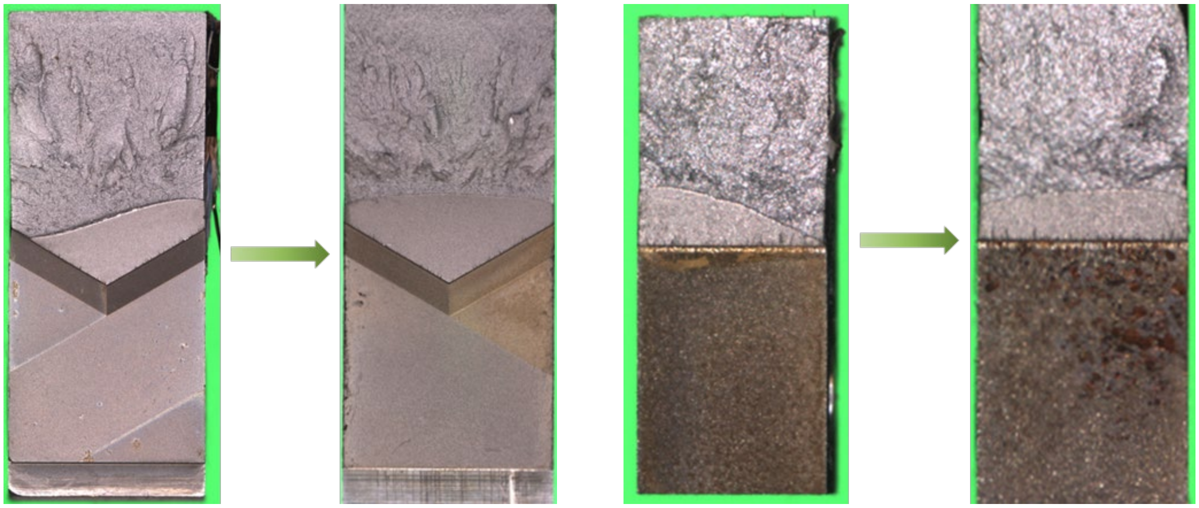
(a) (b)

Figure 2. Comparision of fatigue precrack front straightness before and after alignment improvement for (a) 0.5T CT specimens and (b) 4mm miniCT specimens.

Thereafter, we reperformed tests on 0.5T CT and 4mm miniCT specimens for EUROFER97 Batch #3 and F82H-BA12 with the Master Curve results shown in Figure 3 and Figure 4, respectively. Also shown in the same figures are Master Curve results obtained from miniature bend bar specimens which did not have any fatigue precrack issues from the earlier work. Regardless of specimen types tested, results in these two figures show that the ASTM E1921 Master Curve and its tolerance bounds show an excellent representation of transition fracture toughness for EUROFER97 batch 3 and F82H-BA12. Specifically, the Master Curve predicts the median fracture toughness of both materials at the test temperature, and most valid tests are bound by 2% and 98% tolerance bounds. In addition, the derived Master Curve reference temperature, T_0, is within the typical range of T_0 for RAFM steels.

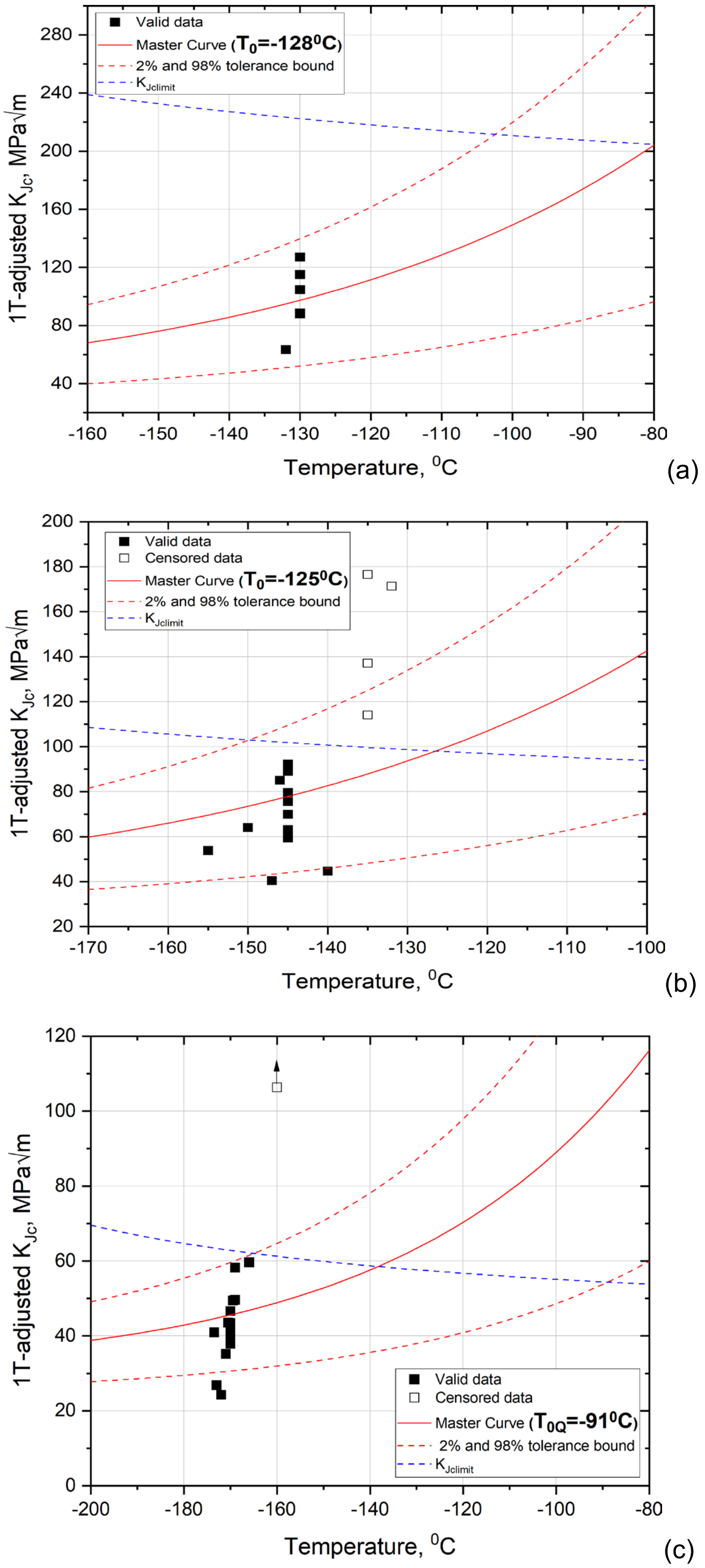

Figure 3. Master Curve results of EUROFER97 batch #3 obtained from (a) 0.5T CT, (b) 4mm miniCT, and (c) miniature bend bar specimens.

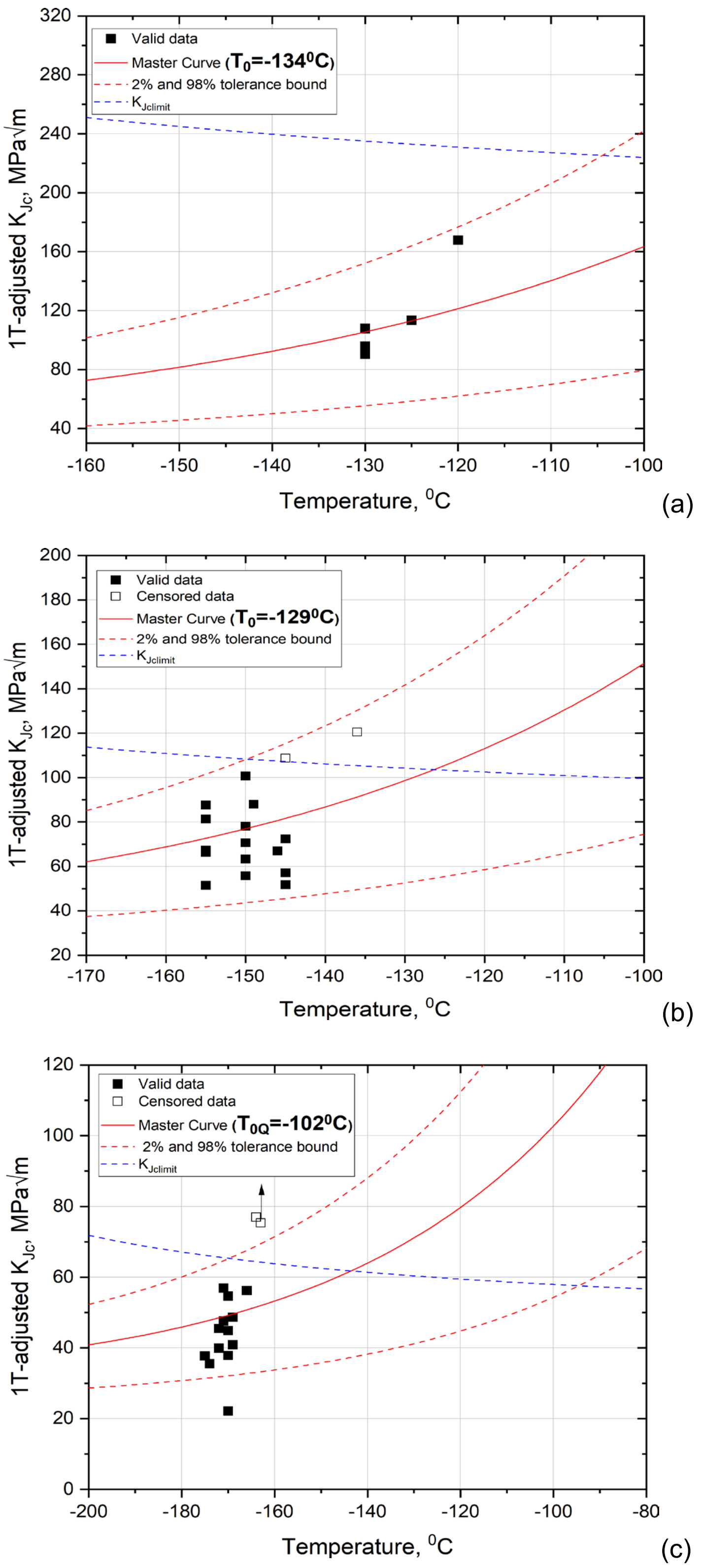

Figure 4. Master Curve results of F82H-BA12 obtained from (a) 0.5T CT, (b) 4mm miniCT, and (c) miniature bend bar specimens.

We also compared our 0.5T CT results with those from CIEMAT in Figure 5. The CIEMAT test data resulted in lower Master Curve reference temperature, T_0, than our data. However, fracture toughness results from both laboratories overlapped each other at the same test temperature and the difference in T_0, which will be further discussed in the later part of this report, is within two standard deviations.

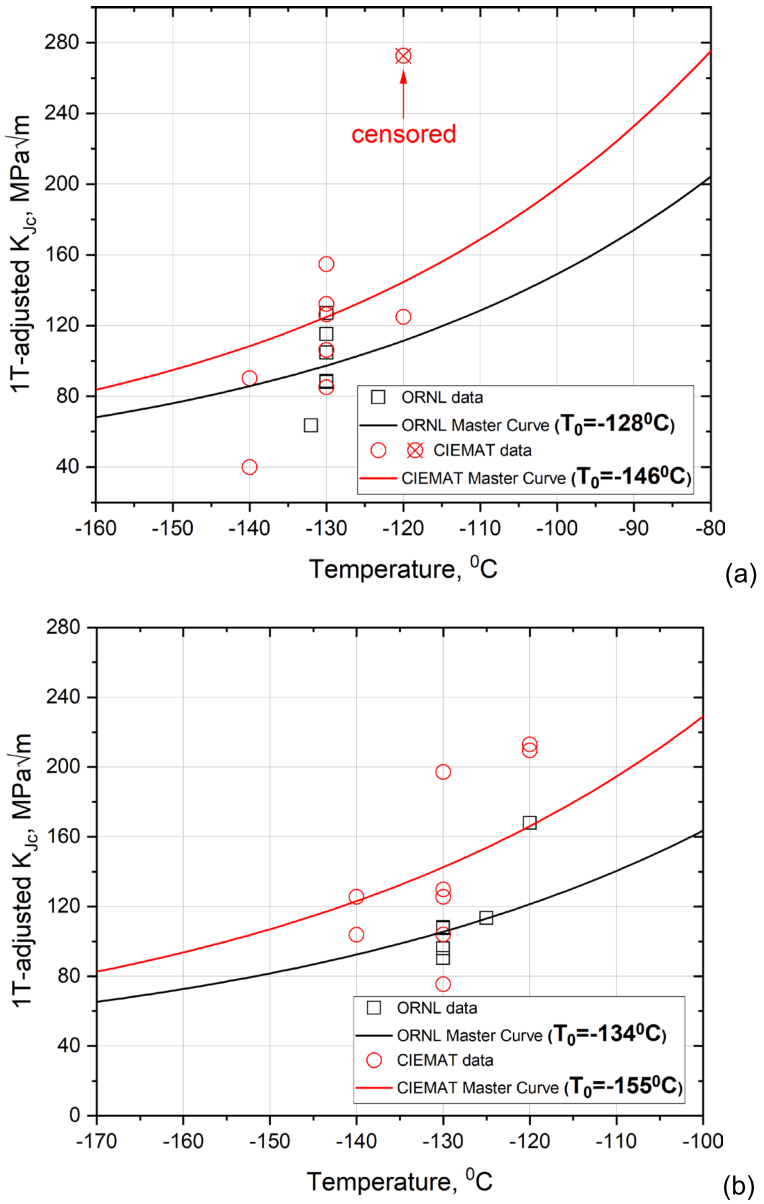

Figure 5. Comparision between ORNL and CIEMAT Master Curve results obtained from 0.5T CT specimens for (a) EUROFER97 batch #3 and (b) F82H-BA12.

Figure 6 compares the Master Curve reference temperature, T_0, obtained from different types of specimens for EUROFER97 batch #3 and F82H-BA12. Using the 0.5T CT results as a baseline, T_0 from 4mm miniCT specimens was within one standard deviation from T_0 obtained from 0.5T CT indicating no size effect of such specimens for T_0 determination. However, T_0 from 1.65 mm bend bar specimens was much higher than that from 0.5T CT demonstrating an apparent size effect. More study is needed to understand the size effect of 1.65 mm bend bar specimens. Figure 6 also shows that the difference between the ORNL 0.5T

CT T_0 and the CIEMAT counterpart was within two standard deviations, meaning statistically insignificant difference between the two. Therefore results from two independent laboratories are comparable to each other. In addition, for the same type of specimens tested, EUROFER97 batch #3 and F82H-BA12 exhibited similar T_0.

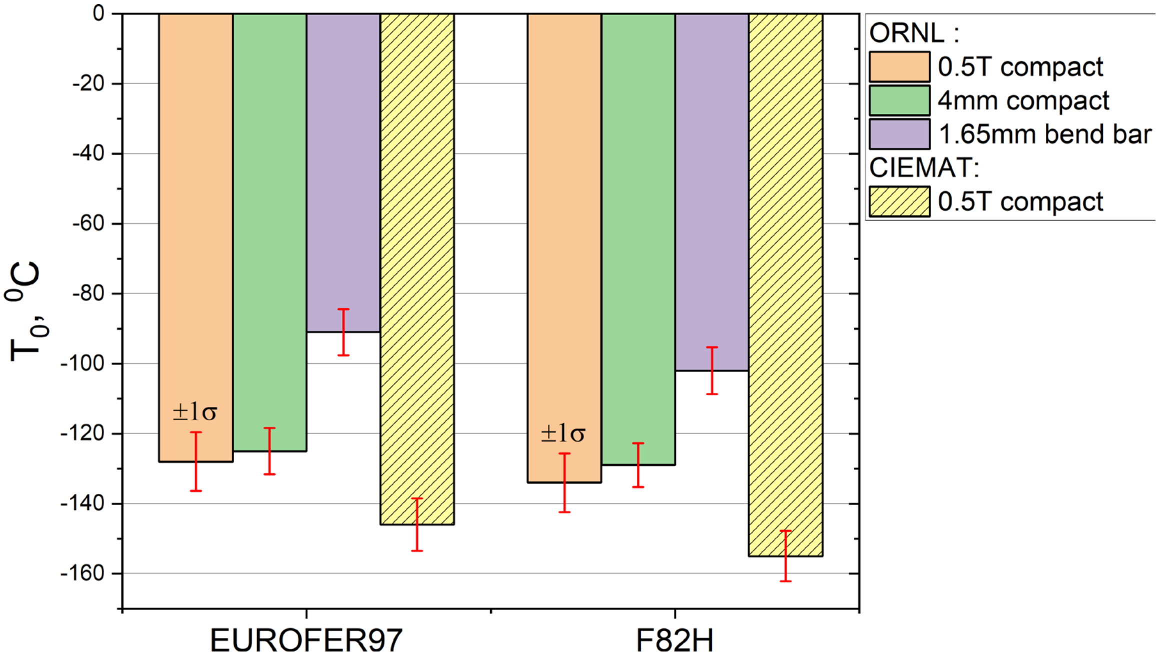

Figure 6. Comparision of the Master Curve reference temperature, T_0, obtained from different types of specimens for EUROFER97 batch #3 and F82H-BA12.

Another field we investigated is the minimum number of uncensored tests for 1.65 mm bend bar specimens needed to derive the Master Curve reference temperature, T_0, in a reliable way. Current ASTM E1921 standard [1] gives recommendations for the minimum number of uncensored tests for larger size specimens where testing can be performed within ±50°C range from T_0. However, due to its small size and low fracture toughness capacity, 1.65 mm bend bar specimens were always tested more than 50°C lower than T_0. Therefore the ASTM E1921 standard is not applicable. In this study, we are proposing a random sampling approach to determine the minimum number of uncensored tests needed for 1.65 mm bend bars. As illustrated in Figure 7, random sampling is a process where a sample with a size smaller than or equal to the whole population is randomly taken from the population. For a certain sample and population size, there are a fixed number of possible combinations of random sampling. For example, if the sample size is 2 and the population size is 4, there are 6 possible combinations of random sampling in total. Assuming all uncensored tests of 1.65 mm bend bar specimens are the whole population, we can pick a sample size and perform random sampling from the population and calculate the range of T_{0Q} for the sample size. Ultimately, our goal is to determine the minimum sample size such that the T_{0Q} range derived from the sample size is within 2 standard deviations from the T_{0Q} derived from the whole population. The calculation was performed for EUROFER97 batch #3 and F82H-BA12 with the range of T_{0Q} shown in Figure 8. For EUROFER97, it took 13 uncensored tests for T_{0Q} to converge within the target range and for F82H-BA12, the number was 11. Therefore, we tentatively determined that the minimum number of uncensored tests is 12 for 1.65 mm bend bar specimens to derive the Master Curve reference temperature, T_{0Q}, in a reliable way.

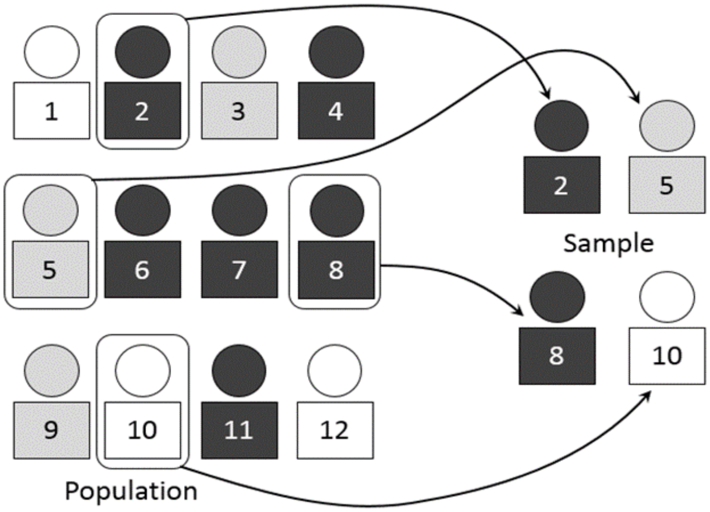

Figure 7. Schematic of a random sampling process (https://commons.wikimedia.org/wiki/File:Simple_random_sampling.PNG, Dan Kernler, CC BY-SA 4.0 <https://creativecommons.org/licenses/by-sa/4.0>, via Wikimedia Commons).

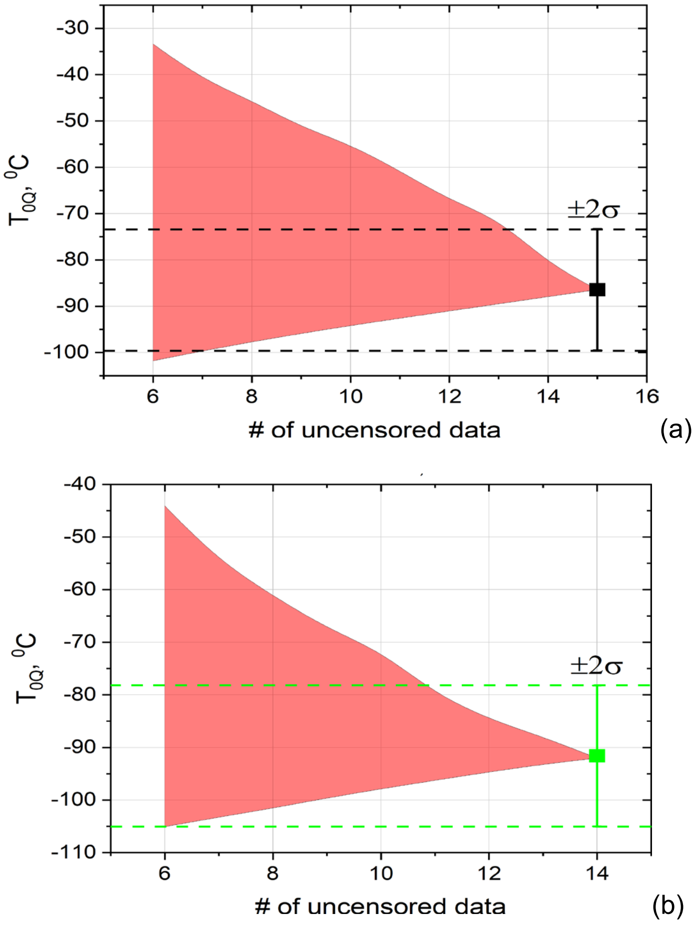

Figure 8. The effect of the number of uncensored data on the possible range of the Master Curve reference temperature T_{0Q} derived from 1.65 mm bend bars for (a) EUROFER97 batch #3 and (b) F82H-BA12.

References

[1] ASTM E1921-21a, Standard Test Method for Determination of Reference Temperature, T_0, for Ferritic Steels in the Transition Range, ASTM International, West Conshohocken, PA, 2021, www.astm.org.

[2] X. Chen et al., "Guidelines for IAEA Small Specimen Test Techniques Master Curve Fracture Toughness Testing", ORNL/LTR-2020/27, July.

[3] X. Chen, J. Reed, E. Manneschmidt, M. Sokolov, "IAEA Sm SPECIMEN TEST TECHNIQUE DEVELOPMENT: MASTER CURVE FRACTURE TOUGHNESS TESTING UPDATE AT ORNL," Fusion Materials Semiannual Report 6/30/2021 DOE/ER-313/70 (2017) 200.

1.2 X-RAY DIFFRACTION STUDY OF LONG-TERM CREEP TESTED G92 FERRITIC/MARTENSITIC STEEL

—D. J. Sprouster, L. L. Snead (Stony Brook University), E. R. Proehl, S. J. Zinkle (University of Tennessee Knoxville)

OBJECTIVE

This work is a direct follow on from our previous FY20 and FY21 synchrotron characterization analysis. In this report, we extend and demonstrate the utility of high-energy x-ray diffraction to identify and capture minor phases in a series of G92 ferritic martensitic alloys subjected to long term creep testing. Additional phases introduced during creep testing include the Laves (FeW_2) phase, that grows in both the gauge and tab region of specimens. Subtle changes in the Body-centered cubic (BCC) host, MX and $M_{23}C_6$ precipitates were also apparent from the quantitative X-Ray Diffraction (XRD) results. Changes in the XRD peak shape position, height, and full-width-at-half-maximum (FWHM), indicate changes in the atomic structure (lattice parameters) and microstructure (dislocation density, coherent grain size, weight fraction of minor phases). These results highlight that synchrotron-based XRD is appreciably sensitive to the creep-induced microstructural transformations and can be employed to quantitatively extract changes in the atomic and microstructural features for both the BCC host and minor precipitate populations.

PROGRESS AND STATUS

Introduction

Strategies to improve the mechanical and creep performance of structural materials for fusion energy applications have led to the realization of engineered microstructures. Quantification of the microstructural evolution with ageing time, temperature, and stress (creep) are key parameters to qualify materials for fusion energy applications. The growth of nm-scale precipitates, and changes in the and BCC host matrix under coupled extremes is needed to optimize material builds and develop microstructural insights that can be compared to thermodynamic modelling. Quantitative XRD methods were employed here to examine the different atomic and microstructural properties of the BCC host and nm-scale precipitates with ageing time.

Experimental Procedure

The XRD measurements were performed at the National Synchrotron Light Source-II (NSLS-II) using the high-energy X-rays available at The Pair Distribution Function (PDF) beamline. All measurements were performed in transmission mode with an amorphous Silicon-based flat panel detector (Perken-Elmer) mounted orthogonal to and centered on the beam path. The sample-to-detector distances and tilts of the detector relative to the beam were refined using a LaB_6 powder standard (National Institute of Standards and Technology [NIST] standard reference material 660c). The wavelength of the incident X-rays was 0.1665 Å (74.46 keV). The sample-to-detector distance was calculated to be 1235.20 mm. 600 individual patterns with detector exposures of 0.1s were collected for each specimen. All raw two-dimensional patterns were background corrected by subtracting a dark current image, and the air and Kapton scattering background within IgorPro (Wavemetrics). Noticeable artefact regions of the detector (like the beam stop, dead pixels) were masked. The corrected and masked two-dimensional detector images were then radially integrated to obtain one-dimensional powder diffraction patterns.

Phase identification was performed using Match3! (Crystal Impact, Bonn, Germany). The background subtracted XRD patterns were Rietveld refined within the MAUD software package. The peak profiles were modeled by a modified pseudo-Voigt function. The instrument contribution to the broadening of the measured profiles was quantified by fitting the LaB_6 NIST powder standard, with a known coherent grain size and negligible microstrain contribution. The Gaussian and Lorentzian-based broadening parameters were subsequently fixed during the analysis of the alloys under investigation to quantify the microstructure (coherent grain size, phase quantification and lattice parameters). The phase fraction, lattice parameter, and coherent grain size (CGS) components were allowed to vary for the different crystal phases present.

The microstrain (μs) components for the $M_{23}C_6$ and Laves phase were not included in the refinements. Therefore, the refined coherent grain size parameters of are lower limits.

Results

The XRD patterns for the six specimens are shown in Figure 1. The phases identified in the samples include MX (MN and MC), $M_{23}C_6$ and Fe_2Mo Laves phase in the "*10*" and "*11*" specimens (both Gauge and Tab specimens show reflections for this phase). For the G92 specimens, the MX peak locations are like a VN phase. The quantitative phase analyses for all specimens are given in Table 1. The XRD analysis resulted in residual weights parameters (RWPs) less than 5% (indicative that he fits are of high quality). The microstructure, including lattice parameters, coherent grain size and microstrain appear to be sample-dependent. The microstrain parameter is directly attributable to two-dimensional defects (such as dislocations), and the coherent grain size is the amount of defect free material (and is thus usually smaller than the grain size from scanning electron microscope [SEM]). The lattice parameters appear to show subtle variations among the different specimens and is potentially related to the processing/alloy chemistry. Finally, the Fe_2Mo increases from 10 to 11, with subtle increases in the gauge and tab regions. It is noted that the pure Fe_2Mo was not capable to refine the reflections associated with the Laves phase. Instead, a modified Fe_2W Laves phase was instead used to refine the reflections. This indicates that the Laves phases are potentially non-stochiometric (Transmission electron microscopes [TEM]-STEM could aid in confirming).

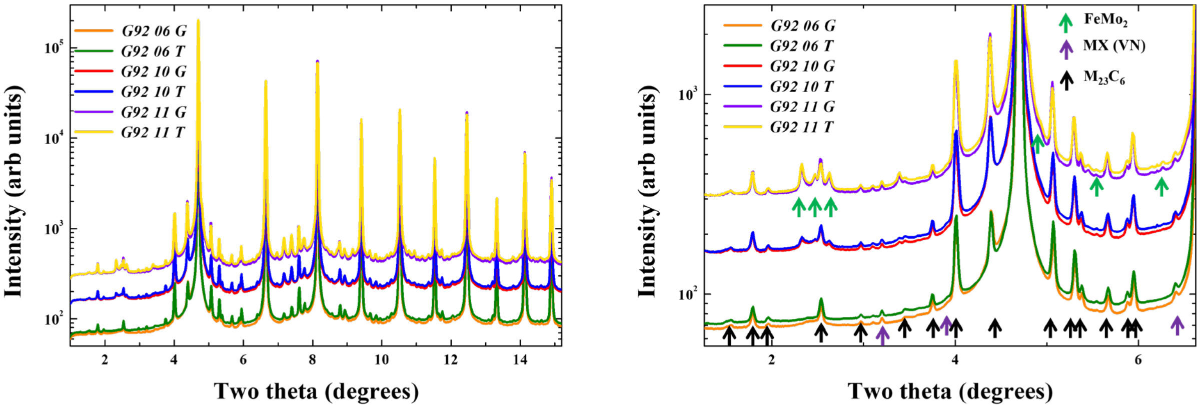

Figure 1. (a) XRD patterns for the six G92 specimens offset vertically by batch. (b) inset showing higher magnification in low angle two-theta region with the multiple phases identified for reference.

Table 1. Results from quantitative XRD analysis. CGS is coherent grain size, us is the XRD-based micro strain.

Sample	**Phase**	**a**	**±**	**c**	**±**	**CGS**	**±**	**μs**	**±**	**Wt.**
	ID	**Å**		**Å**		**nm**		**(1×10^{-3})**		**%**
G92 64-2-06G	Fe	2.8711	0.00003			587.9	53.4	0.74	0.01	97.6 (0.2)
	$M_{23}C_6$	10.6327	0.00104			96.4	17.5			2.3 (0.3)
	Fe_2W									
G92 64-2-06T	Fe	2.87194	0.00003			397.4	10.2	0.84	0.01	97.4 (0.2)
	$M_{23}C_6$	10.64022	0.00044			98.1	10.4			2.5 (0.3)
	Fe_2W									
G92 64-2-10T	Fe	2.87135	0.00004			650	10	0.81	0.01	97.4 (0.2)
	$M_{23}C_6$	10.64328	0.00113			202.0	54.5			2.3 (0.3)
	Fe_2W	4.73615	0.00239	7.73547	0.00673	51.1	11.3			0.3 (0.1)
G92 64-2-10G	Fe	2.87126	0.00002			657.0	19.5	0.46	0.01	98.0 (0.3)
	$M_{23}C_6$	10.64655	0.00074			188.3	19.5			1.8 (0.3)
	Fe_2W	4.73615	0.00239	7.73547	0.00238	52.5	12.8			0.3 (0.1)
G92 64-2-11T	Fe	2.87117	0.00003			663.0	6.5	0.70	0.01	97.3 (0.1)
	$M_{23}C_6$	10.63769	0.00061			94.2	2.6			2.1 (0.5)
	Fe_2W	4.73459	0.00080	7.72436	0.00215	57.3	12.3			1.0 (0.1)
G92 64-2-11G	Fe	2.87148	0.00003			659.2	30.2	0.71	0.01	97.4 (0.2)

Conclusion

The nm-scale creep-induced phases in a series of G92 steels were quantitively captured from the XRD patterns. The minor Fe_2W Laves phase was the best match to experimental data, indicating that the Laves phase precipitates are potentially chemically mixed with other alloying elements. The comparison with TEM and additional mechanical testing (Vickers hardness) is a potential next step to uncover the effects of the creep induced Laves phase precipitates.

Acknowledgements

The work was funded under Grant DE-SC0018332 to the Research Foundation at State University of New York, Stony Brook by the United States Department of Energy (DOE) Office of Fusion Energy Sciences. Use of the 28-ID-1 (Pair Distribution Function [PDF]) beamline at the National Synchrotron Light Source-II, Brookhaven National Laboratory, was supported by the DOE under Contract No. DE-SC0012704.

1.3 DEUTERIUM PERMEATION BEHAVIORS IN FUSION BLANKET STRUCTURAL MATERIALS AND BINARY MODEL ALLOYS—W. Zhong, L. Tan, Y. Katoh (Oak Ridge National Laboratory)

OBJECTIVE

The objective of this work is to investigate deuterium permeation behaviors in castable nanostructured alloys (CNAs), oxide dispersion strengthened (ODS) steel, and binary Fe-9Cr model alloys. The investigated alloys are of distinct microstructure. The CNAs and ODS steels are of small grain size with high number densities of carbide or oxide particles, while the binary model alloy in this work was of large grain size. The effects of these distinct microstructures on deuterium permeation behaviors were investigated in this work.

SUMMARY

Castable nanostructured alloys and oxide dispersion strengthened steels have different intrinsic microstructure in as-fabricated materials. In this work, we selected two representative CNAs of different carbon compositions and one ODS steel. These were a high-C CNA that has $M_{23}C_6$ and TiC precipitates; a low-C CNA that has only TiC precipitates; and 14YWT that has high density of nanoprecipitates. In addition, we also investigated the Fe-Cr binary alloy that has 91%Fe and 9%Cr. Deuterium permeability were investigated for 400°C, 450°C, 500°C, 550°C and 600°C with the deuterium pressure from 50 Torr to 600 Torr, and the results shows similar permeability of these alloys within the investigated temperature.

PROGRESS AND STATUS

To investigate the permeability, one side of the 12.7 mm diameter disc-shape specimen was subjected to high deuterium pressure, where the other side of the specimens was exposed to high vacuum with the mass spectroscopy monitoring the deuterium flux permeating through the specimens. Tests were performed for five different temperatures for each material, and the deuterium flux was measured under four different deuterium pressures at each temperature. As described in Richardson's law [1], permeation flux J is a function of permeability Φ, upstream pressure P_u, downstream pressure P_d and the samples thickness δ, as provided in the formula $J = \Phi(\sqrt{P_u} - \sqrt{P_h})/\delta$. In this study, the downstream pressure is orders of magnitude lower than the upstream pressure, and the permeation flux can be rewritten as $J = \Phi\sqrt{P_u}/\delta$. Therefore, the deuterium flux is a linear function of the square root of the upstream deuterium pressure. Figure 1 shows an example of the measured deuterium flux as a function of square root of deuterium pressure for five temperatures.

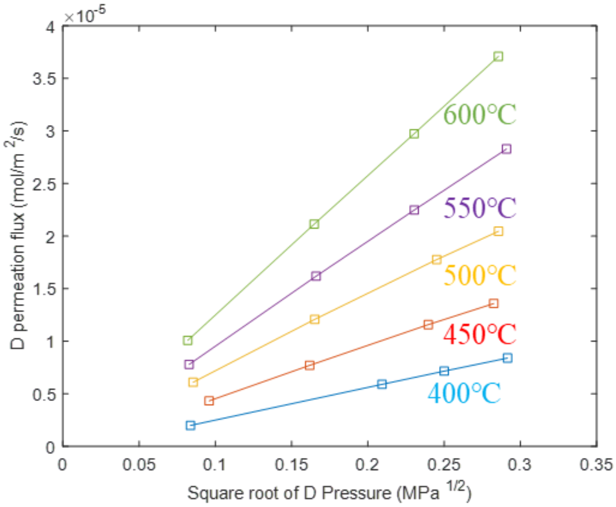

Figure 1. An example of deuterium flux as a function of square root of deuterium pressure at 400°C, 450°C, 500°C, 550°C, and 600°C.

The permeability Φ of each temperature can be determined by its slope in Figure 1. Figure 2 shows the Arrhenius plot of the permeability as function of the reciprocal of temperature for high carbon CNA, low carbon CNA, ODS steels, and binary model alloys. The results were fitted using the equation $\Phi = \Phi_o \exp\left(-\frac{E}{RT}\right)$, where Φ_o is the permeation constant, E is the permeation activation energy, R is the ideal gas constant.

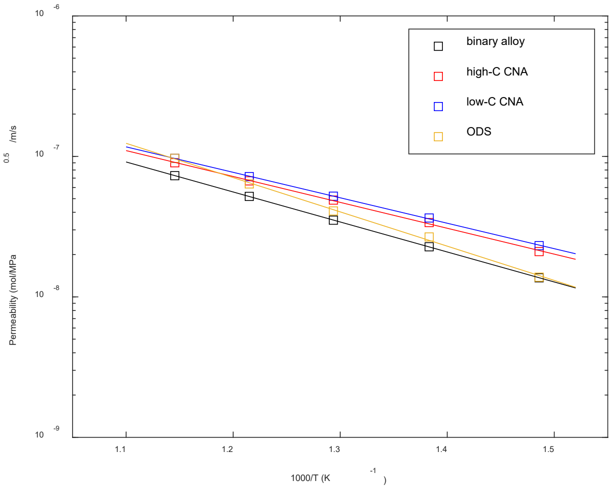

Figure 2. Arrhenius plot of the permeability as function of the reciprocal of temperature for CNAs, ODS steels and binary 9Cr model alloy.

The CNAs alloys have typical tempered martensite structure, with $M_{23}C_6$ and/or MX precipitates distributed at grain boundary and inside the matrix, as shown in Figure 3. The binary model alloy has equiaxed grains shown in Figure 3. The permeabilities of all investigated alloys are within the same order of magnitude in the investigated temperature ranges, with lower permeability in the binary alloy.

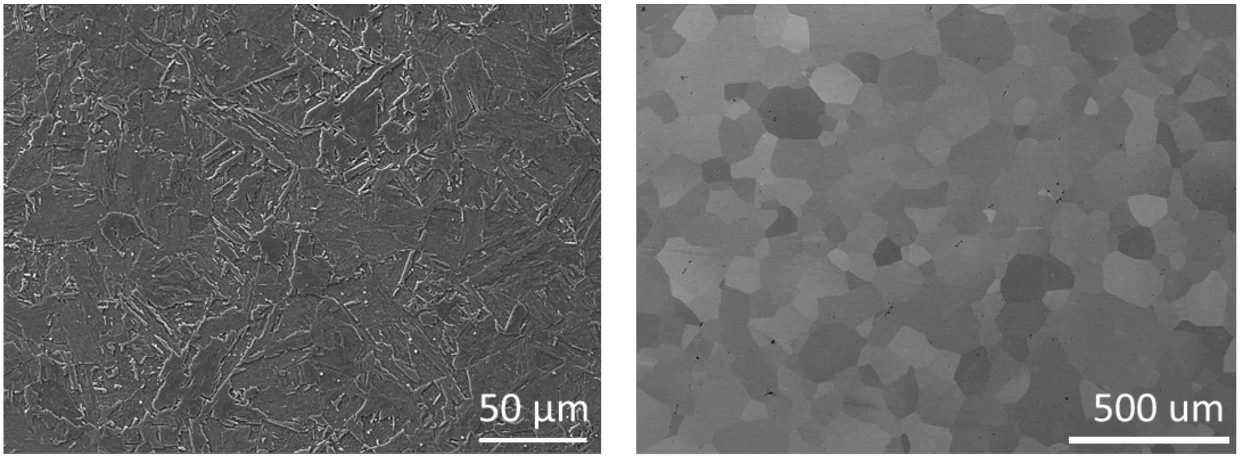

Figure 3. Grain structure of (left) CNAs and (right) binary 9Cr model alloy.

Results

Hydrogen retention and desorption behaviors of representative fusion blanket structural materials and binary alloys are to be investigated to understand the effects from the intrinsic microstructure features in as-fabricated materials.

Reference

[1] K. S. Forcey, I. Iordanova & D. K. Ross (1990) Investigation of structure dependence of diffusivity, solubility, and permeability of hydrogen in hot rolled low carbon steels, Materials Science and Technology, 6:4, 357-363.

1.4 RADIATION RESPONSE OF TANTALUM-ALLOYED CASTABLE NANOSTRUCTURED ALLOYS—W. Zhong, L. Tan, T. S. Byun (Oak Ridge National Laboratory)

OBJECTIVE

Tantalum-alloyed castable nanostructured alloys (CNAs) have been irradiated in High Flux Isotope Reactor (HFIR). The objective of this work is to investigate the neutron irradiation effects on the hardness and the microstructure of tantalum-alloyed CNAs. In this work, the Vickers hardness of four irradiated materials is reported, in comparison to the unirradiated reference. Preliminary microstructure of one of the irradiated samples is presented.

SUMMARY

Ta-alloyed CNAs have been irradiated in HFIR. Vickers hardness of irradiated materials have been tested at room temperature in Low Activation Materials Development and Analysis (LAMDA). Sample that was irradiated at 400°C showed irradiation induced hardening, while samples irradiated at 490°C and above showed irradiation induced softening. Preliminary microstructure characterization was performed to see the grain structure evolution after irradiation.

PROGRESS AND STATUS

The hardness of irradiated tantalum alloyed CNAs was measured using the Vickers indenter at room temperature using the force of 1kgf. The result of hardness as function of damage dose (in the unit of displacement per atoms, dpa) is shown in Figure 1. The irradiation temperature of each sample is labeled next to the symbols. Sample irradiated at 400C shows irradiation induced hardening, while other samples that were irradiated at the temperature above 490C show irradiation induced softening.

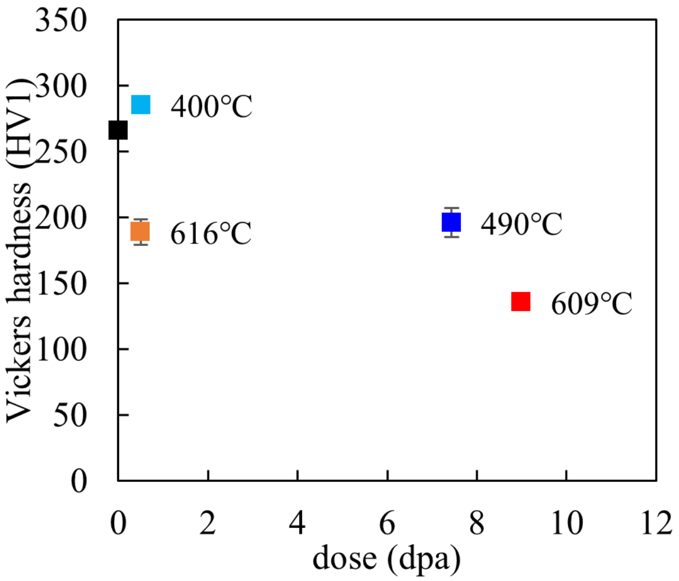

Figure 1. Room temperature Vickers hardness of neutron irradiated and unirradiated Ta-alloyed CNAs.

Preliminary microstructure characterization was performed using the Electron backscattered diffraction (EBSD), with the inverse pole figure-colored maps of the irradiated sample (609°C, 9 dpa) shown in Figure 2. Unlike the tempered martensite grain structure, the grain structure of the as-irradiated sample demonstrates somewhat equiaxed grain structure, with one of the grains in the investigated region having a large grain size over 70 μm, as shown in the Figure 2a. The EBSD was also performed on the gauge section. The IPF result in the gauge section shows large misorientation inside grains, which could be attributed to the dislocation and sub-grain formation from the tensile deformations.

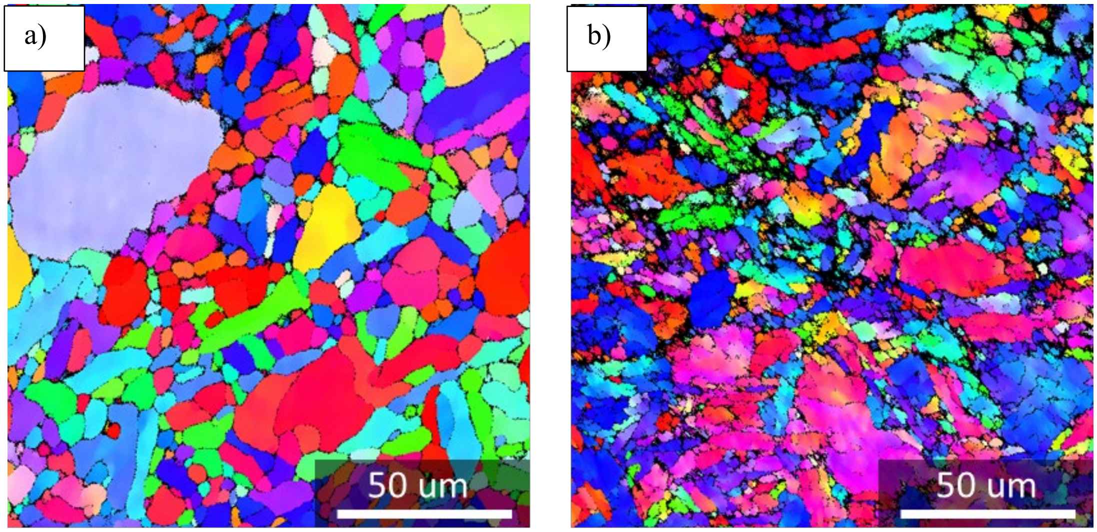

Figure 2. Inverse pole figure of the irradiated sample at 609°C to a damage dose of 9 dpa in the a) tab section, and the b) gauge section.

Results

Detailed microstructure using transmission electron microscopy will be applied to understand the irradiation effects, which will be correlated to the post-irradiation mechanical behaviors.

1.5 PERFORMANCE EVALUATION OF MODIFIED 3Cr-3WVTa BAINITIC STEELS—Y. Yamamoto (Oak Ridge National Laboratory)

OBJECTIVE

This work aims to evaluate the advantages in the mechanical performance of newly proposed, modified 3Cr-3WVTa bainitic steels developed at Oak Ridge National Laboratory (ORNL). The proposed steel was designed to eliminate the need for post-weld heat treatment (PWHT), as well as providing improved mechanical properties of both base metal and weldments compared to those of existing commercial bainitic steels or ferritic martensitic (FM) steels. The target applications are high-temperature structural components in fusion reactors, such as helium cooled vacuum vessels operating up to 450°C and blanket support structures operating up to 550°C.

SUMMARY

Performance evaluation of newly processed, as-normalized "modified 3Cr-3WVTa" steel with refined prior-austenite grains has been initiated in three major aspects: creep, weldment, and isothermal aging. Newly processed steel which applied thermomechanical treatment and normalization at 1000°C resulted in >25-28% of creep strength improvement at 500/550°C compared to that of previously evaluated materials normalized at 1100°C and then tempered at 700°C. A cross sectional characterization of the weld joint with compositionally matched filler metal indicated that the hardness variation across the weldment were relatively small as expected from the alloy design. However, the inter-critical heat affected zone (HAZ) of each weld bead caused lowering the hardness inside the weld metal compared to that of the base metal. Isothermal aging at 500°C has been initiated to evaluate long term thermal stability of newly processed modified 3Cr-3WVTa steel. The hardness, tensile, and short-term creep properties are to be evaluated as a function of aging time.

PROGRESS AND STATUS

A compositionally modified 3Cr-3WVTa bainitic ferritic steel (Mod. 3Cr-3WVTa steel, ID: MLC02T) was proposed to achieve a reduced property inhomogeneity across the weldment in as-welded condition, targeting a PWHT-free bainitic ferritic steel for fusion structural applications. The nominal compositions of the original and modified steels are summarized in Table 1. Initial property evaluation of the modified steel suggested that the as-normalized MLC02T exhibited an improved room-temperature impact toughness compared to that after applying tempering, as opposed to the response in typical low-alloyed bainitic steels. Based on the initial results, the focus of systematic performance evaluation has been shifted to the as-normalized condition. In addition, a refinement of the prior austenite grains (PAG) was also conducted through optimization of thermomechanical treatments as well as normalization temperature, as reported previously, targeting the improved room-temperature mechanical properties including both tensile and toughness. The present report summarizes the progress of property evaluation of MLC02T with the refined PAG in the as-normalized condition.

Table 1. Nominal composition of 3Cr-3WVTa base bainitic steels (balanced Fe)

Name	Alloy composition, wt.%	Remarks
MLC02T	3Cr-3W-0.2V-0.16Si-2.0Mn-0.1Ta-0.05C	Modified (newly proposed)
Original	3Cr-3W-0.2V-0.16Si-0.4Mn-0.1Ta-0.1C	Require PWHT, proposed in 1990's [ref.]

[ref.] R.L. Klueh et al., Int. J. Pressure Vessels and Piping, 84 (2007) 29-36.

A cast ingot of MLC02T produced through vacuum-induction-melting was homogenized at 1200°C, followed by hot-rolling and normalization at 1000°C to prepare an as-normalized plate with ~15 mm thickness and average PAG of ~40 μm. A small piece was sectioned from the plate which applied tempering at 700°C to compare the mechanical performance with and without tempering. Uni-axial tensile creep-rupture tests of the base metal in the as-normalized and normalized-and-tempered conditions were conducted at 500 and

550°C. A part of the as-normalized plate was machined to have a single V groove and then applied a gas tungsten arc weld (GTAW) with a compositionally matched weld filler metal strip. The cross section of the weldments was characterized by optical microscopy, and two-dimensional micro-Vickers hardness map analysis across the weld-HAZ-base metals was conducted in the as-welded condition. In addition, evaluation of long-term thermal stability of the as-normalized microstructure and mechanical properties was initiated through isothermal aging at 500°C targeting for up to 10,000h.

Three creep-rupture tests at 500 and 550°C of the as-normalized MLC02T with refined PAG are currently in progress, as summarized with Larson-Miller Parameter in Figure 1a. The creep rupture strength of the as-normalized materials showed more than 25-28% improvement to date compared to that of previously evaluated MLC02T (normalized at 1100°C + tempered). Direct comparison of the creep rupture curves of the normalized and tempered MLC02T tested at 550°C and 295 MPa (Figure 1b) indicated a clear improvement of creep deformation resistance by applying normalization at 1000°C with nearly double creep rupture life in the tempered material. The test of the as-normalized material is in progress and still in the secondary creep regime after >8,000h testing, expecting significantly longer creep rupture life than the tempered material.

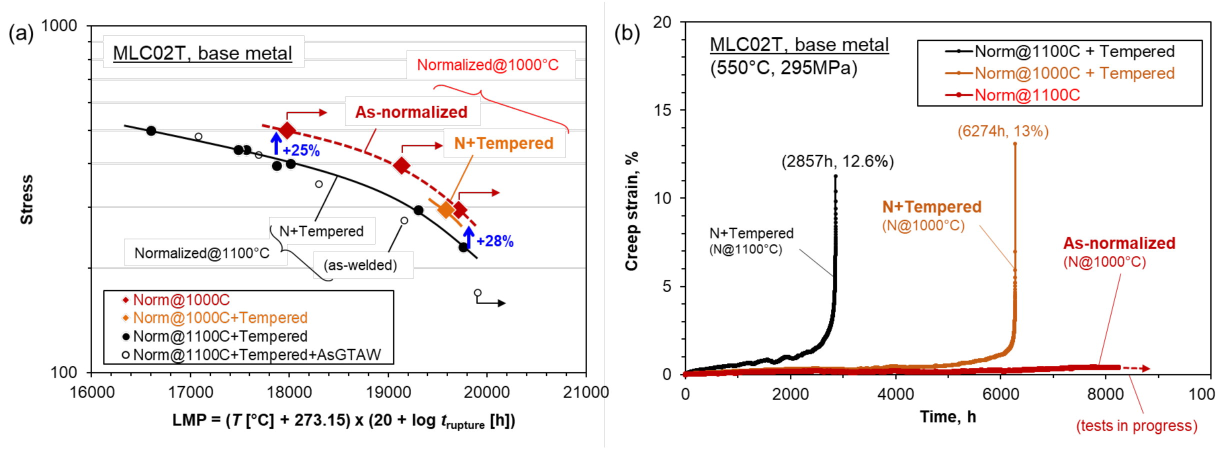

Figure 1. (a) Larson-Miller Parameter (LMP) plot of newly processed modified 3Cr-3WVTa steel base metal with and without tempering, comparing with previously evaluated materials, and (b) creep rupture curves of the modified 3Cr-3WVTa steel before and after re-normalization at 1,000°C, tested at 550°C and 295MPa.

The weld-joint characterization of the as-normalized MLC02T was initiated. The welded plate was prepared by GTAW with a compositionally matched weld filler metal strip produced from the same heat. Figure 2a represents the cross-sectional microstructure of the weldment, showing multiple bead structure in the weld metal, together with the HAZ with 3-5 mm width adjacent to the weld metal. Two-dimensional micro-Vickers hardness map analysis across the weld metal, HAZ, and base metal (Figure 2b) revealed that (1) the hardness inside the weld beads and HAZ, ~310 HV, was almost the same as the base metal (as expected from the alloy design), and (2) the outside edge of HAZ ("inter-critical HAZ") for each weld bead was decorated by a low hardness band (~260 HV). The band formed due to the heat from the overlayed weld beads which raised the temperature of the substrate between Ac1 and Ac3. Although the softening at the inter-critical HAZ is unavoidable in any steels with phase transformation, the hardness gap maintained relatively small due to the hardness control of the base metal through the compositional modification (e.g., the original 3Cr-3WVTa steel weldment exhibited ~360 HV inside the weld beads and HAZ in the as-welded condition). The weld metal consists of multiple, overlapped low hardness bands, leading to the average hardness of the weld metal slightly lower than the base metal, like a tempered condition. Since the tempering is known to negatively impact on the mechanical performance of MLC02T, it is important to experimentally evaluate the mechanical properties of the weld joint. Machining of the test specimens is currently in progress for creep rupture testing across the weld metal and Charpy impact testing of the weld metal in the as-welded condition.

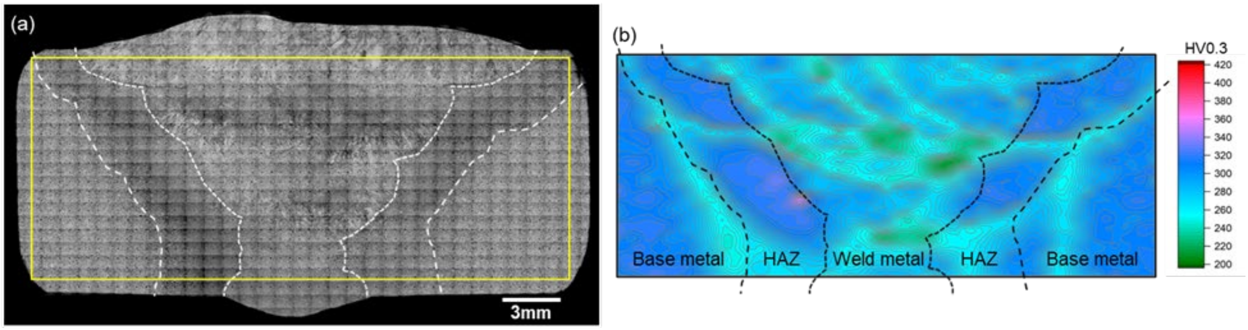

Figure 2. (a) Cross sectional microstructure of As-GTAW MLC02T (as-normalized), and (b) a color contour map (HV0.3) showing micro-Vickers hardness distribution.

Isothermal aging at 500°C in a laboratory air, targeting for up to 10,000 h, was also initiated to evaluate long-term thermal stability in microstructure and mechanical performance of the as-normalized MLC02T plate. The hardness, tensile, and short-term creep properties are to be evaluated as a function of isothermal aging time. To date, aging for 1,000h and 3,000h was completed, and the specimen machining is in progress. The 10,000h aging will be completed in February 2023.

Results

Microstructure characterization of the as-welded, creep ruptured, and isothermally aged MLC02T will be conducted to be correlated with the process or test conditions. Evaluation of the creep rupture performance and Charpy impact toughness of the base metal and cross weld specimens will also be continued/ conducted. A production of compositionally matched metal core wire was completed by an external wire manufacturer in August 2022.

2. ODS AND NANOCOMPOSITED ALLOY DEVELOPMENT

2.1 COLD SPRAY OF GARS ODS STEEL POWDER ON A FERRITIC MARTENSITIC STEEL SUBSTRATE

SUBSTRATE—D. Zhang, X. Ma, K. A. Ross, J. T. Darsell, L. Li, X. Wang, D. J. Edwards, W. Setyawan (Pacific Northwest National Laboratory)

OBJECTIVE

The objective of this work is to explore alternative route of fabricating oxide dispersion strengthened (ODS) steel plate, including the potential of plating such ODS plate onto a substrate of reduced activation ferritic martensitic (RAFM) steel.

SUMMARY

Cold spray was used to deposit ODS steel powder onto ferritic martensitic steel (P92) plate. The feedstock ODS steel powder was provided by collaborators at Ames Laboratory, made with their unique gas atomization reaction synthesis (GARS). The GARS ODS steel powder had the nominal composition of 14YWT (14Cr-0.4Ti-3W-0.35Y-0.1O, wt.%). Meanwhile the largely spherical powder was not ball milled, hence it can be cold sprayed. The P92 steel plate was used as a surrogate for RAFM steel, having nominal composition of 9Cr-2W-Si0.5-Mn0.5-Mo0.4-Ni0.3-V0.2-C0.1, wt.%. The state-of-the-art cold spray system was used with helium carrier gas and robust processing parameters to ensure good deposition quality. We have demonstrated successful cold spray of ODS steel powder onto P92 plate coupons. Microstructure characterization and adherence testing were performed on three coupons with varying powder feedstocks and cold spray conditions. Further progress has been made with the deposition of a larger size plate. This plate will undergo subsequent thermo-mechanical processing and heat treatment to further improve the interface quality and characteristics of dispersed oxide particles.

PROGRESS AND STATUS

Introduction

The conventional fabrication route [1] of ODS steel plate involves production of powder by gas atomization, ball milling, powder vacuum canning, hot isostatic pressing, hot cross rolling, cold rolling, with annealing steps often required in-between rolling steps. This route is time consuming, expensive, hard to scale up, and extremely delicate as cracks can develop and the plate can "bend out of shape" during the laborious rolling process. Based on the realistic consideration that conventional route is not capable of producing tons of ODS steel for fusion energy application, some researchers [1] proposed to "plate" a mm-level thickness of ODS steel onto RAFM steel, with the idea that the ODS steel plating would be a critical top layer to handle expected extreme temperature and radiation dose in a fusion environment. This means that on top of the laborious plate fabrication process, additional bonding step (e.g., diffusion bonding) is required to make ODS steel plating. Therefore, it would be highly desirable to directly deposit an ODS steel layer onto a RAFM steel without the abovementioned laborious steps. Unfortunately, melt based additive methods won't be suitable as dispersed particles tend to agglomerate in molten metal. Cold spray is a solid-state based method that could offer a potential solution. Yet effective cold spray would require the feedstock powder to be largely spherical for aerodynamic purposes. Namely, the flaky ball milled ODS steel powder won't work well with cold spray.

The GARS method produces spherical precursor ODS steel powder with an outer shell of Cr-rich oxide, whereas the nano-oxide forming species, i.e., Y and Ti, are at the powder interior in the form of Fe-intermetallics. Upon heating and consolidation (e.g., hot isostatic pressing [HIP]), oxygen atoms diffuse into the powder interior to react with Y/Ti, forming the Y-Ti-O nano-oxides [2]. Therefore, GARS ODS steel powder offers the geometrical (i.e., spherical) and compositional (i.e., Y/Ti/O species all contained in the powder) requirements for cold spray deposition.

Experimental Procedure

Figure 1(a) shows a cross section overview in scanning electron microscope (SEM) of the GARS ODS steel powder provided by Ames Laboratory. The powder size ranges between 45 µm and 108 µm. Figure 1(b) is medium magnification SEM image of several powder particles, showing the grain substructure inside. Figure 1(c) is high magnification image inside one powder particle, showing bright spots mainly decorating the grain boundaries. Energy dispersive X-ray spectroscopy (EDS) mapping in Figure 1(d) reveals that these bright spots correspond to Y signals, namely these are Fe-Y intermetallic particles.

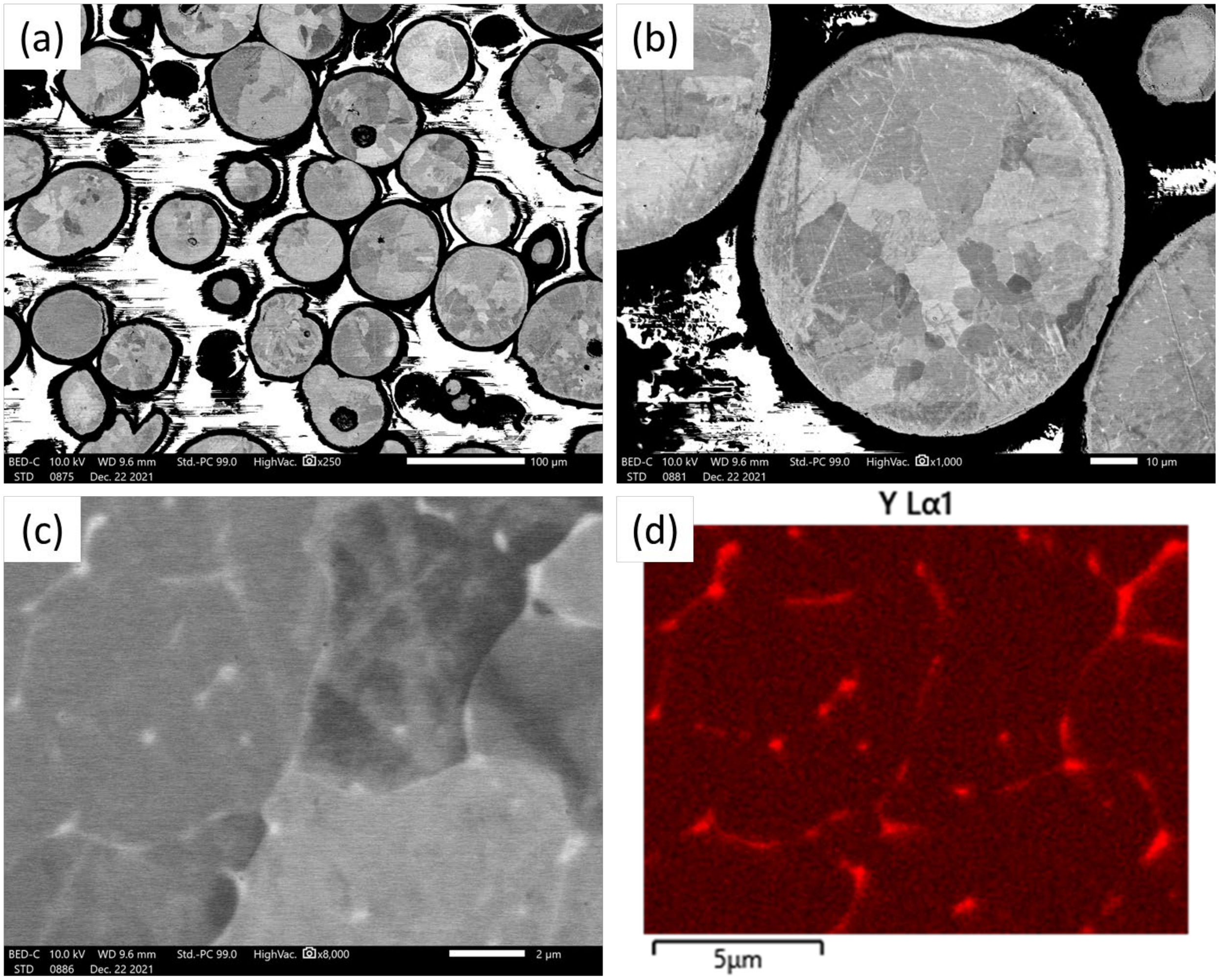

Figure 1. (a) Cross section SEM overview of the GARS ODS steel powder. (b) Grain substructure inside powder particles. (c) Bright spots decorating the grain boundaries. (d) EDS map showing bright spots are Fe-Y intermetallic particles.

The GARS ODS steel powder was sieved to several tighter size ranges, with the 75-90 µm range yielding 555 g powder that was sufficient for cold spray trails. Smaller size ranges yielded insufficient powder for the powder feeder. Therefore, three size ranges, namely 45-53 µm, 53-63 µm, and 63-75 µm were blended back together, yielding 481g powder that met the threshold of the powder feeder. In this way, two size ranges, namely 45-75 µm and 75-90 µm, were cold sprayed to investigate the effectiveness of cold spray in depositing powder with varying sizes. If successful, the two size ranges can also be blended to utilize most of the GARS powder for larger scale cold spray.

Results

For the first-round study, small pieces of P92 plate, i.e., one inch by one inch, were used as substrates. The substrates had as-machined surface which could be beneficial for bonding at the cold spray interface. Based on prior experience with steels and Ni alloys, a set of robust cold spray parameters were chosen to ensure effective deposition and preserve limited GARS powder. For example, helium carrier gas was used at 600 psi, with the gas temperature at 650 °C. It is noted that 650 °C would still be considered "cold" for ODS steel powder since such a temperature wouldn't alter the powder microstructure. For each powder size range (i.e., 45-75 µm and 75-90 µm), two coupons were deposited, with representative coupon images shown in Figure 2 (a) and (b), designated as CS-GARS-1 and CS-GASR-2, respectively. In addition, since there was more 75-90 µm powder to utilize, a third coupon was deposited with slightly lower gas pressure (400 psi, i.e., CS-GARS-3) to test the cold spray quality with reduced gas consumption.

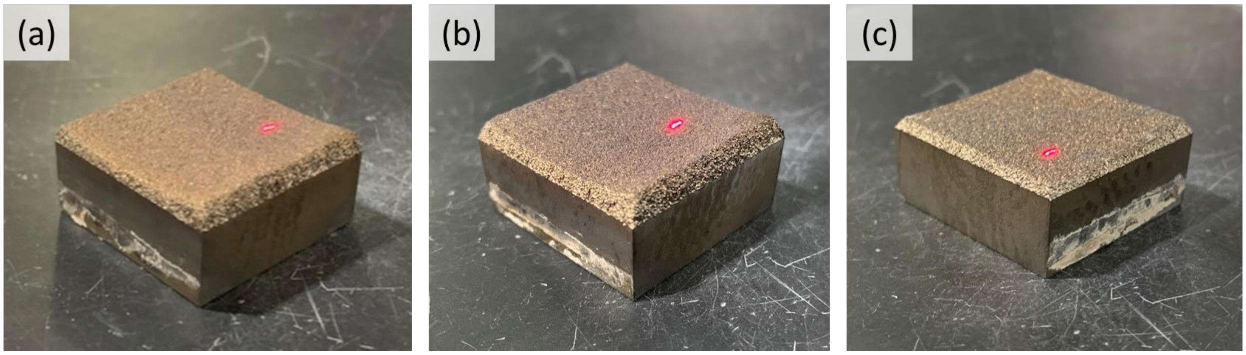

Figure 2. (a) Representative cold spray deposited coupon with 45-75 µm powder, i.e., CS-GARS-1. 8.0g powder was deposited, with average thickness of 1.45 mm. (b) Representative cold spray deposited coupon with 75-90 µm powder, i.e., CS-GARS-2. 8.6g powder was deposited, with average thickness of 1.65 mm. (c) Cold spray deposited coupon with 75-90 µm powder using a lower helium gas pressure (400 psi), i.e., CS-GARS-3. 5.14g powder was deposited, with average thickness of 1.07 mm.

Hardness and microstructure study with SEM, EDS, and electron backscattered diffraction mapping (EBSD) were completed for cross-sections of CS-GARS-1, CS-GARS-2, and CS-GARS-3, as shown in Figures 3, 4, and 5, respectively.

Figure 3(a) is an optical montage overview of CS-GARS-1, with the top-center region underwent microhardness mapping from the ODS steel deposit across the interface with P92 steel. Overall, the "macrostructure" is consistent with other cold spray deposited steels, in that the interface appears to be well bonded, whereas there are still defects/pores through the deposit. The high magnification optical montage of microhardness tested region in Figure 3 (b) and the accompanying hardness map in Figure 3(c) are also consistent. Generally, cold spray induced plastic deformation in the powder lead to increased hardness, especially in regions that are free of defects, such as the red/orange areas with hardness above 260 HV. Meanwhile lower hardness regions (~200 HV) like the blue "holes" in Figure 3(c) are associated with pores in the vicinity. For more detailed microstructure study, (d)-(h) and (i)-(m) are EBSD/SEM/EDS data from the interface area and the interior of the deposit, respectively.

Figure 3 (d) is the image quality (IQ) map of the interface, where the highly deformed profiles of powder particles can be seen in the upper, and the solid P92 substrate material is in the lower. Figure 3(e) is the corresponding orientation map. Note that the "black" areas are mostly associated with the highly deformed areas near the boundaries of the original powder particles (see in (d)), where the severe deformation makes EBSD indexing difficult. However, there is one pore visible in both (d) and (e), and likely another thin crack at the interface. Figure 3(f) is a high-resolution SEM image of the interface, with accompanying elemental maps of Y and O in (g) and (h). Again, one can see that the bonding between GARS ODS powder and P92 substrate is quite well. The dark line outlining the interface is not a gap or crack but is the oxide "shell" from the original GARS powder that has been pressed and "pancaked" onto the P92 substrate. It is interesting to note that even though there is severe deformation occurred to the powder particle, as evidenced by EBSD and the pancaked profile, the oxide shell remains largely continuous, namely it has not been broken down into pieces and dispersed by cold spray impact. In addition, the Y-containing particles can be seen in Figure 3(g). Further study is needed to understand the cold spray impact on these particles.

Figure 3(i) and (j) are EBSD IQ map and orientation map at the interior of CS-GARS-1 deposit. Similar deformed powder particles can be seen. No large pores are present in this location, but smaller defects might exist in between pancaked particle boundaries. Figure 3(k) is SEM image showing several powder particles deformed and "smashed" together. Again, the black lines are not cracks, but from the original oxide shells that has been smashed together, as can be seen in O elemental map in (m). Moreover, much of the oxide shells also contain Y, as show in Y elemental map in (l).

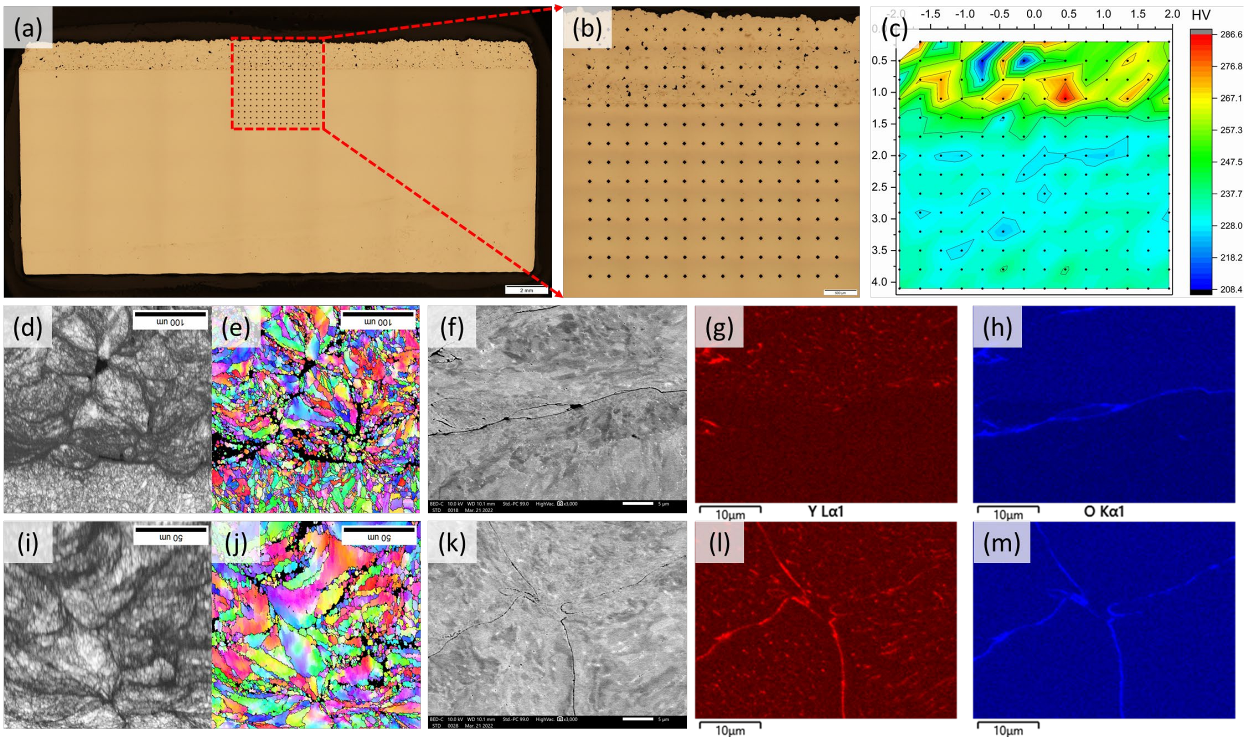

Figure 3. Hardness and microstructure of CS-GARS-1. (a) Optical montage of the cross-section. (b) Higher magnification optical of the microhardness mapped region. (c) Hardness map. (d)-(e) EBSD IQ map and orientation map at the interface. (f)-(h) SEM and elemental maps of Y and O at the interface. (i)-(j) EBSD IQ map and orientation map at the interior of the cold spray deposit. (k)-(m) SEM and elemental maps of Y and O at the interior of the cold spray deposit.

Figure 4 shows the set of optical, hardness, EBSD, SEM, EDS results for CS-GARS-2, which are quite like those for CS-GARS-1. This is understandable since both coupons were deposited with the same cold spray parameters, and the only difference was the powder size (45-75 µm vs. 75-90 µm). Namely the robust cold spray parameters were able to deposit GARS ODS powder across a wide size range. Therefore, blending the two size cuts back together for larger deposit would be feasible.

As for CS-GARS-3 (Figure 5), which was deposited with slightly less aggressive parameters (i.e., lower He gas pressure of 400 psi), it appears that more pores are present in the deposit (Figure 5(b)). Particularly, while pores do exist for all three deposits, CS-GARS-1 and CS-GARS-2 are basically free of pores along the interface, whereas CS-GARS-3's interface is decorated with pores in the vicinity (Figure 5 (b)).

Therefore, only limited microstructure study was done on CS-GARS-3, namely SEM and EDS but without EBSD.

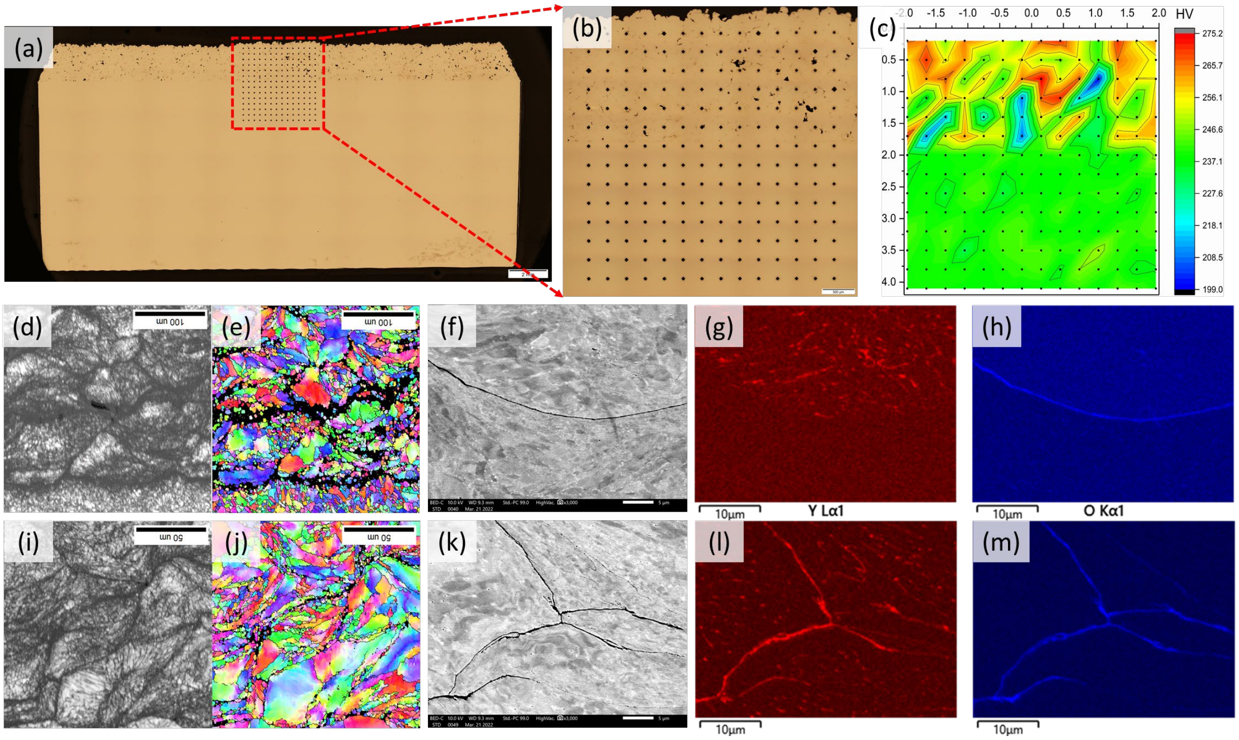

Figure 4. Hardness and microstructure of CS-GARS-2. (a) Optical montage of the cross section. (b) Higher magnification optical of the microhardness mapped region. (c) Hardness map. (d)-(e) EBSD IQ map and orientation map at the interface. (f)-(h) SEM and elemental maps of Y and O at the interface. (i)-(j) EBSD IQ map and orientation map at the interior of the cold spray deposit. (k)-(m) SEM and elemental maps of Y and O at the interior of the cold spray deposit.

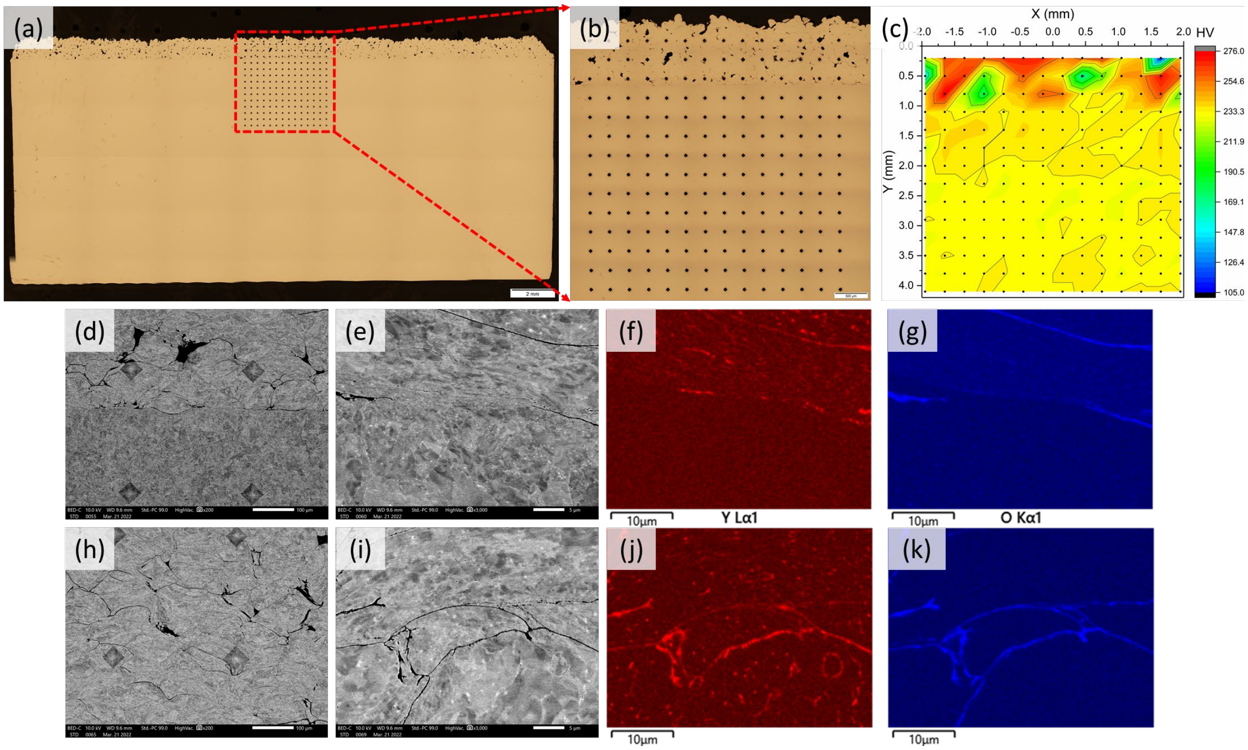

Figure 5. Hardness and microstructure of CS-GARS-3. (a) Optical montage of the cross-section. (b) Higher magnification optical of the microhardness mapped region. (c) Hardness map. (d)-(g) SEM and elemental maps of Y and O at the interface. (h)-(k) SEM and elemental maps of Y and O at the interior of the cold spray deposit.

As mentioned before, a second coupon was made for CS-GARS-1 and CS-GARS-2, respectively, for the purpose of adhesion testing. Bond strength measurements were performed by a Positest AT-A automatic testing machine. The testing machine attaches to the top flat surface of 10 mm diameter cylinder dolly which is epoxied to the coating. Then testing machine pulls on the aluminum dolly at a 150 psi/s rate until separation occurs. Not surprisingly, the adhesion strength of the two are almost the same, namely 58 MPa and 57 MPa. Both coupons generally fractured at the interior of the deposits, indicating strong bonding at the interfaces. Figure 6(a) shows the adhesion tested coupons. Having proved the feasibility of cold spray with two powder size cuts, the two cuts were blended back together (i.e., 45-90 µm), enabling cold spray of a larger area deposit (i.e., plate) on P92 substrate. Figure 6(b) shows the plate with an area of 3” by 3”, and a thickness of ~6 mm.

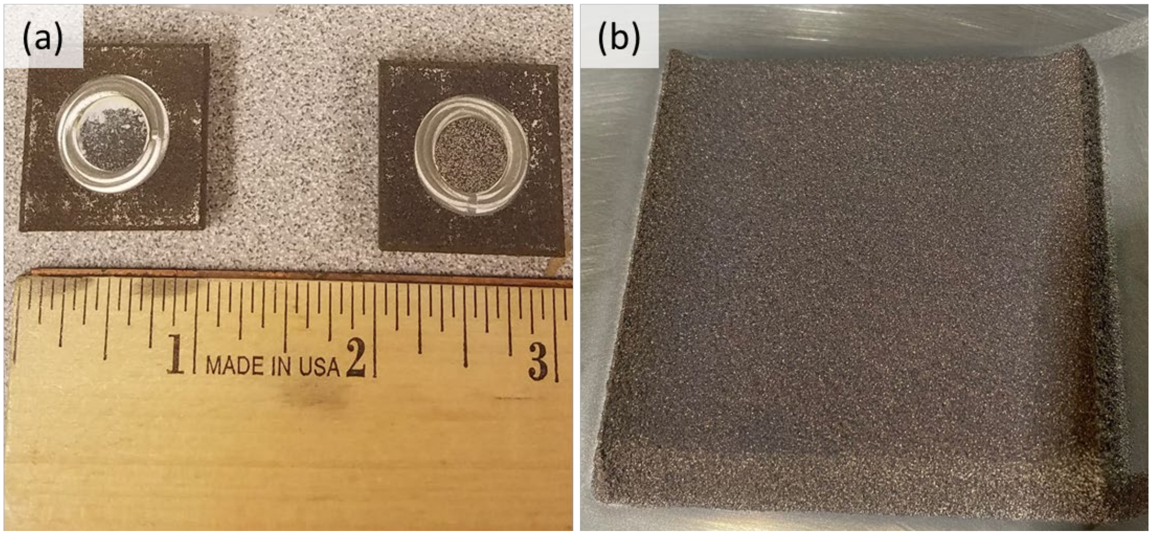

Figure 6. (a) Adhesion tested CS-GARS-1 coupon (left) and CS-GARS-2 coupon (right). (b) Large area (3 by 3”) cold spray deposited plate, with a thickness of ~6 mm.

Future work includes subsequent thermo-mechanical processing of the large plate to further improve the interface quality and characteristics of dispersed oxide particles, Atom Probe Tomography (APT) and transmission electron microscope (TEM) characterization of the microstructures, and mechanical testing.

Acknowledgements

This research is funded by the United States Department of Energy Office of Fusion Energy Sciences under contract DE-AC05-76RL01830. We are grateful to cold spray technical support provided by Chris Smith, Daniel Graff, Gary Neuenschwander, and Eric Loeffler.

References

[1] M. Rieth, M. Dürrschnabel, S. Bonk, G. Pintsuk, G. Aiello, J. Henry, Y. de Carlan, B.E. Ghidersa, H. Neuberger, J. Rey, C. Zeile, N. De Wispelaere, E. Simondon, J. Hoffmann, Impact of materials technology on the breeding blanket design – Recent progress and case studies in materials technology, Fusion Engineering and Design 166 (2021) 112275.

[2] J. Rieken, Gas atomized precursor alloy powder for oxide dispersion strengthened ferritic stainless steel, Ames Laboratory (AMES), Ames, IA (United States), 2011, p. 362.

2.2 SINTERED NANOSTRUCTURED ALLOYS FOR ADVANCED FUSION ENERGY APPLICATIONS

D.J. Sprouster, J. Gentile, B. Cheng, M. Ouyang, W.C. Cunningham, J.R. Trelewicz, L.L. Snead (Stony Brook University), D. Olds, H. Yan, A. Pattammattel (Brookhaven National Laboratory)

SUMMARY

This work incorporates the advanced multimodal x-ray characterization of sintered nanostructured alloys (SNA) developed at Stony Brook University (SBU). Synchrotron-based x-ray powder diffraction (XRD) and coupled X-ray imaging/spectroscopy were employed to quantify the processing-structure properties of SNAs and compared to their castable nanostructured alloys (CNA) counterparts. This work builds upon SBU's efforts to extend the characterization techniques, and to uncover microstructure insight from the moist advanced techniques available at synchrotron facilities.

PROGRESS AND STATUS

Introduction

The first wall tiles and blanket structures of fusion devices must withstand simultaneous exposures to high heat flux, particle bombardment, and intense bulk neutron irradiation environments. Reduced-activation ferritic martensitic (RAFM) steels are critical structural components of first wall tiles and blankets. The extreme operating temperature and radiation environments, however, present challenges for existing RAFM steels. These challenges stem from poor performance of existing RAFM alloys above 550°C, with reduced high temperature creep rupture strengths, and radiation induced embrittlement. A novel class of RAFM steels, with improved performance in extreme environments, are CNAs. The CNAs are engineered with a high density of dispersed nanometre scale MX metal-carbide, metal-nitride, metal-carbonitride (MX) precipitates. These MX precipitates are stable at high temperatures, improve the creep rupture performance, and operate as efficient sinks for radiation induced point defects. In this work, we describe our recent efforts to enhance the fabrication of CNAs, through powder processing and direct current sintering (DCS) methods. Through a combination of electron microscopy (transmission electron microscopy [TEM], scanning electron microscope [SEM], scanning transmission electron microscopy [STEM]), and multimodal x-ray characterization (x-ray diffraction, x-ray absorption spectroscopy, nano xrf imaging), and mechanical testing characterization campaigns, we confirm that DCS yields identical microstructures to the castable method, albeit through a much more rapid fabrication route. Furthermore, our initial success in demonstrating the applicability of DCS to CNA fabrication opens the opportunity to fabricate functionally graded first wall tile structures (i.e., W-CCNZ-CNA), which are essential to the construction, design, and radiation testing of components for International Thermonuclear Experimental Reactor (ITER) and Demonstration (DEMO) reactors.

Experimental Procedure

Materials

A cast CNA7 block containing *8.77Cr 1.46W 0.57Mn 0.08V 0.05Ta 0.13Ti 0.10Si 0.09C* (in weight percent and balance Fe) was gas atomized into powders with approximate sizes of 24.6 um. Next, 20g of this powder was then loaded into a 25mm graphite die and into a direct current sintering system (Sinterland LABOX-3010KF, Japan) placed under vacuum. The sample was placed under static uniaxial compressive pressure of 50MPa, heated at a rate of 100°C/min to 1000°C, and held at temperature for 10 minutes prior to cooling down to room temperature. Following sintering, the compact was loaded into a box furnace, annealed at 1100°C for 2 hours, and quenched in water. A second post sintering heat treatment was applied at 750°C for 2 hours followed by unloading and ambient air cooling. Finally, the compact was sectioned and polished to a mirror finish using standard metallurgical techniques prior to microstructural analysis. Samples for TEM characterization were prepared via focused ion beam (FIB) lift out techniques in a Field Electron and Ion Company (FEI) Helios Nanolab 600 dual beam focused ion beam/scanning electron microscope (FIB/SEM) located at the Center for Functional Nanomaterials (CFN) at Brookhaven National Laboratory (BNL). Cross sectional lamellas were thinned to 300 nm for experiments at the Hard X-Ray Nanoprobe (HXN) Beamline at the National Synchrotron Light Source-II (NSLS-II).

The chemical and electronic structure of the MX and $M_{23}C_6$ precipitates were determined by coupling multimodal x-ray nanoimaging and electron microscopy capabilities. X-ray nanoimaging and nano X-ray Absorption Near Edge structure (XANES) and the Cr K-edge experiments were performed at the HXN Beamline. The specimens examined at HXN were in the form of 5×15×0.3 μm TEM lamella prepared via FIB milling as described above. The incident x-rays had a wavelength of 1.3776 Å at an energy of 9 keV and were focused via a Fresnel zone plate nano focusing optic to a ~40 × 40 nm spot size employing scanning dwell times of 20-100 ms. Two-dimensional x-ray florescence (XRF) spectral maps were processed and visualized in PyXRF [1]. Nanoscale X-ray absorption near-edge spectroscopy or nano-XANES [2, 3] around the Cr K-edge (6539 eV) were performed to quantify the atomic structure of Mn atoms located within the bulk and in Mn-rich particles observable from the XRF maps. A total of 80 individual XRF maps were collected at energies around the Mn K-edge. Spectroscopic analysis was performed on this imaging stack to resolve the local atomic structure of the different Mn environments with 40 nm spatial resolution.

Synchrotron XRD experiments were performed at the Pair Distribution Function (PDF) beamline at the NSLS-II. All measurements were performed in transmission mode with an amorphous silicon based flat panel detector (Perkin-Elmer) mounted orthogonal to the beam path. The sample-to-detector distance and tilts of the detector relative to the beam were refined using a LaB_6 powder National Institute of Standards and Technology (NIST) standard (SRM® 660c). The wavelength of the incident X-rays was 0.1665 Å at an energy of 74 keV. The sample-to-detector distance was calculated to be 1245.91 mm. All raw two-dimensional patterns were background corrected by subtracting a dark current image and noticeable artifact regions of the detector (like the beam stop and dead pixels) masked (methods are described in more detail in References [4, 5]).

Results

The XRD patterns for as-sintered, as-solutionized (at 1100 °C) and as-tempered (at 750 °C) are shown in Figure 1 with phases overlaid for reference. The Body Centred Cubic (BCC) dominates the XRD patterns, with a minor austenite and MX component visible in both as-sintered and as-solutionized. After tempering, the Face Centred Cubic (FCC) phase is removed, and the growth of $M_{23}C_6$ peaks is apparent. The high density of dispersed nanometer scale MX precipitates. The MX and $M_{23}C_6$ phases observed are consistent with the phases observed in CNA counterparts.

Figure 2 shows the STEM and STEM-EDS maps for the tempered spherical nucleic acids (SNA) specimen. Figure 3 shows the corresponding synchrotron-based XRF maps for the as-tempered SNA specimen. The chemical makeup, and size of the precipitates is apparent, with distinct TiC and Cr-W-Mn-C precipitates from both STEM-EDS and XRF imaging. The electronic structure of the Cr atoms, as evidenced by the XANES spectra in Figure 3 (b), show evidence that the Cr atomic environment of the precipitates is subtly different to the Cr atoms within the FCC host.

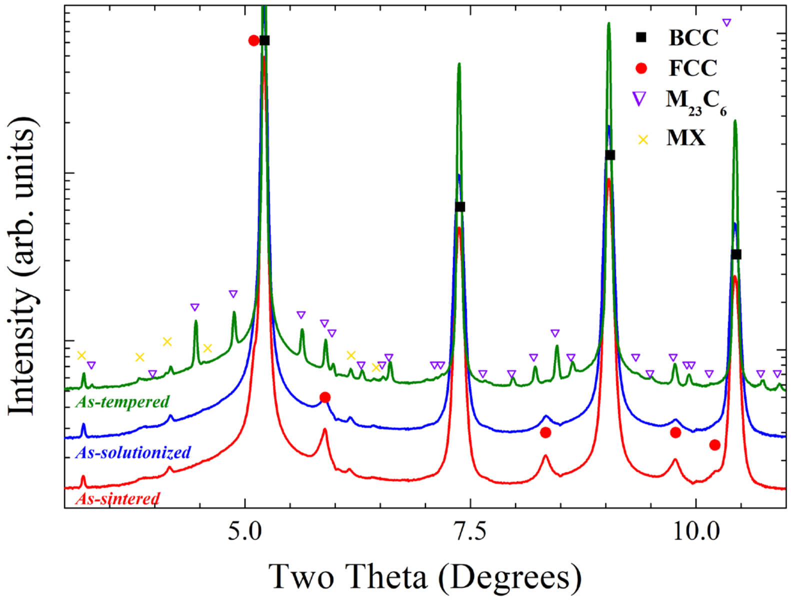

Figure 1. XRD patterns for the SNA specimens. Symbols show the phases identified.

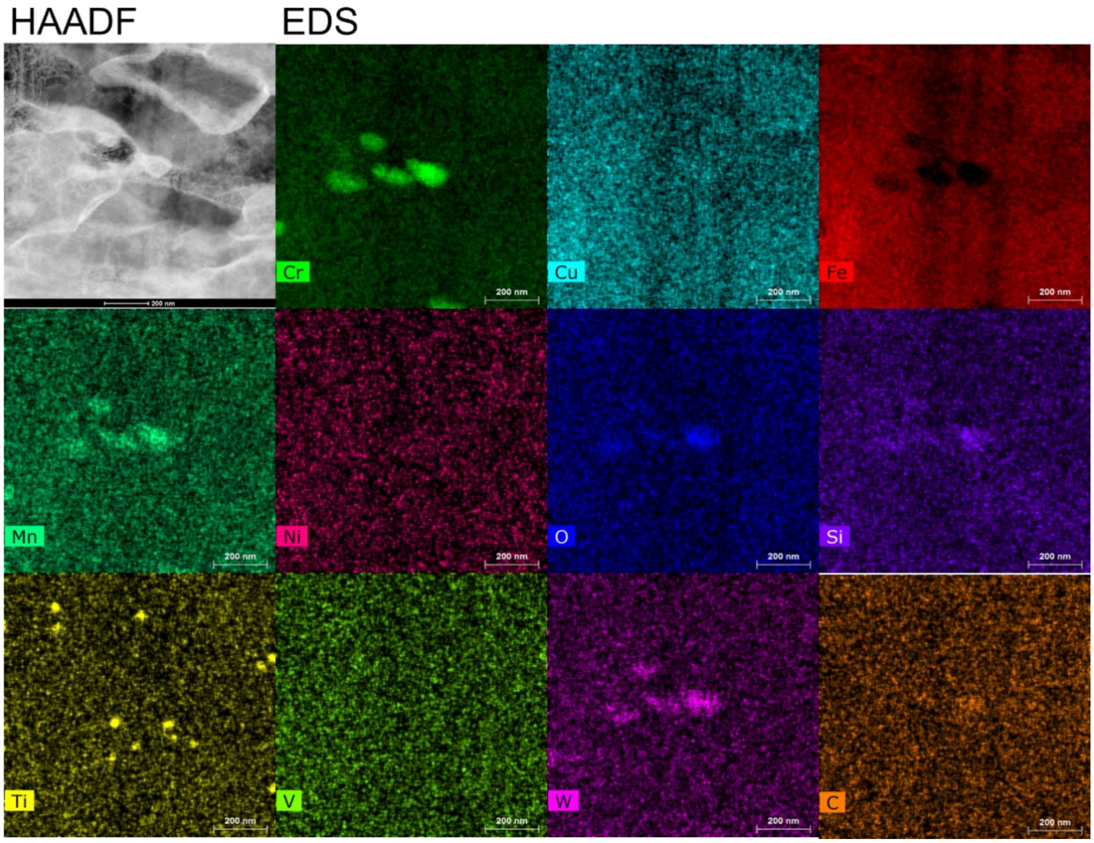

Figure 2. STEM-EDS maps for the tempered SNA specimen.

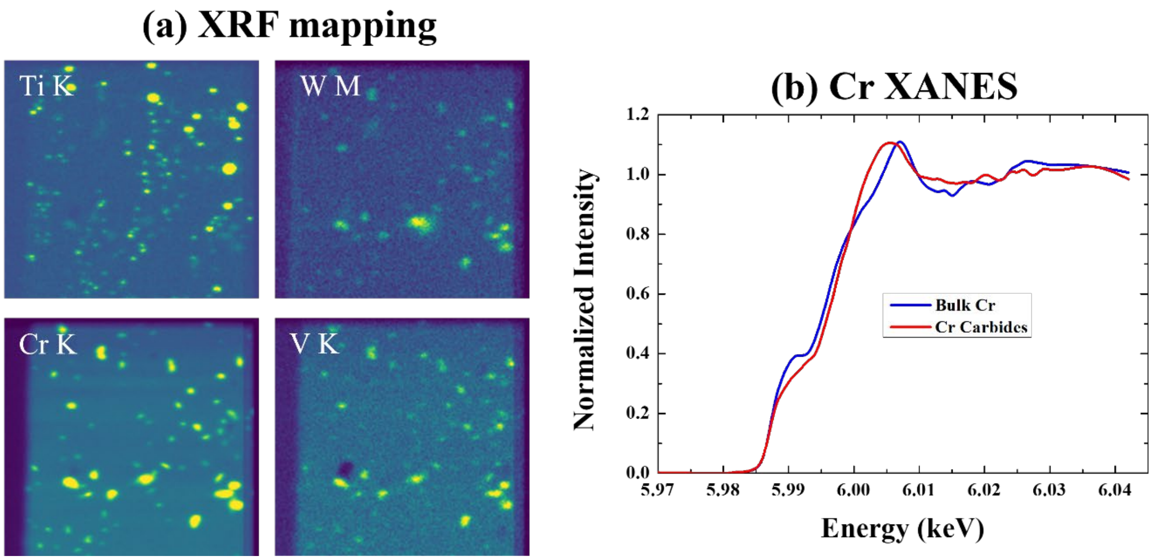

Figure 3. 2D XRF spectral maps highlighting the precipitation of the Ti, W V and Cr alloying elements. (b) Cr K-edge XANES spectra from Cr atoms in the matrix (Blue) and Cr atoms in the carbides (MX and $M_{23}C_6$).

Conclusions

The multimodal microstructural characterizations performed on the sintered nanostructured alloys show that the microstructures and crystal phases are consistent and identical to their castable nanostructured alloys. The next steps will be to quantitatively determine the phase analysis for the sintered alloys and compare to the castable alloys. Additional investigation of the XANES spectra, and STEM EDS results to isolate the signal for the $M_{23}C_6$ and MX precipitates and compare the sizes, fractions, and crystal structures to the theoretically predicted phases from computational thermodynamics. Mechanical properties and thermophysical properties (thermal conductivities) will also be determined and compared to the castable alloys. These promising results highlight distributed control system (DCS) as a viable fabrication route and highlight that these methods have future promise to develop graded structures with SNA material on top of a sintered CCNZ, a significant step in designing realistic structures required for future devices.

Acknowledgements

The work was funded under Grant DE-SC0018332 to the Research Foundation at State University of New York, SBU by the United States Department of Energy (DOE) Office of Fusion Energy Sciences. Use of the 3-ID (HXN) and 28-ID-1 (PDF) beamlines at the NSLS-II, BNL, was supported by the DOE under Contract No. DE-SC0012704.

References

[1] L. Li, H. Yan, W. Xu, D.T. Yu, A. Heroux, W.K. Lee, S.I. Campbell, Y.S. Chu, PyXRF: Python-Based X-ray Fluorescence Analysis Package, in: B. Lai, A. Somogyi (Eds.), X-Ray Nanoimaging: Instruments and Methods Iii2017.

[2] A. Pattammattel, R. Tappero, M. Ge, Y.S. Chu, X. Huang, Y. Gao, H. Yan, High-sensitivity nanoscale chemical imaging with hard x-ray nano-XANES, Science Advances 6(37) (2020) eabb3615.

[3] D.J. Sprouster, W. Streit Cunningham, G.P. Halada, H. Yan, A. Pattammattel, X. Huang, D. Olds, M. Tilton, Y.S. Chu, E. Dooryhee, G.P. Manogharan, J.R. Trelewicz, Dislocation microstructure and its influence on corrosion behavior in laser additively manufactured 316L stainless steel, Additive Manufacturing 47 (2021) 102263.

[4] D.J. Sprouster, J. Sinsheimer, E. Dooryhee, S.K. Ghose, P. Wells, T. Stan, N. Almirall, G.R. Odette, L.E. Ecker, Structural characterization of nanoscale intermetallic precipitates in highly neutron irradiated reactor pressure vessel steels, Scripta Materialia 113 (2016) 18-22.

[5] D.J. Sprouster, R. Weidner, S.K. Ghose, E. Dooryhee, T.J. Novakowski, T. Stan, P. Wells, N. Almirall, G.R. Odette, L.E. Ecker, Infrastructure development for radioactive materials at the NSLS-II, Nucl Instrum Meth A 880 (2018) 40-45.

3. CERAMIC COMPOSITE STRUCTURAL MATERIAL DEVELOPMENT

3.1 FAILURE EVALUATION OF NEUTRON-IRRADIATED SiC/SiC COMPOSITES BY UNDERWATER ACOUSTIC EMISSION—T. Nozawa, H. Tanigawa (National Institutes for Quantum Science and Technology), T. Koyanagi, Y. Katoh (Oak Ridge National Laboratory)

Abstract of a manuscript in Journal of Nuclear Materials 566 (2022) 153787

Understanding the statistical properties of mechanical properties of non-irradiated and neutron irradiated SiC/SiC composites is essential for component design. This study aims to evaluate the detailed damage accumulation behavior of composites focusing on two fracture parameters: proportional limit stress (PLS) and acoustic emission (AE) onset stress. The developmental underwater AE technique, which is benefit in non-contact in-situ failure monitoring method during mechanical testing and in handle of the irradiated material, was first applied to evaluate damage accumulation behavior. Two types of chemical vapor infiltration SiC/SiC composites were used: one reinforced with Hi-Nicalon Type-S SiC fiber and one reinforced with Tyranno-SA3 SiC fiber in the form of satin-woven 2D fabrics with pyrolytic carbon interface. Neutron irradiation in the High Flux Isotope Reactor at Oak Ridge National Laboratory reached a fluence of 30 dpa at a temperature of 620–670 °C. Four-point flexural tests were conducted to evaluate post irradiation strength. Weibull statistics did not suggest marked degradation of composite strength. Detailed failure behavior evaluated by AE demonstrated no irradiation induced change of the AE onset stress (i.e., crack initiation equivalent stress). Failure probability analysis suggests that increasing the reliability of composites (i.e., the Weibull modulus rather than strength itself) is essential to expanding the design margin and benefiting from a probabilistic design approach.

3.2 IRRADIATION-INDUCED CHEMICAL DISORDERING IN CERAMICS: THE CASE OF SiC—T. Koyanagi (Oak Ridge National Laboratory)

Abstract of a manuscript in Journal of Nuclear Materials 565 (2022) 153766

Chemical disordering is one feature of damage that occurs in irradiation environments and is common in ceramic compounds. This study reviews irradiation induced chemical disordering in SiC based materials at elevated temperatures. The results were obtained using advanced analytical tools to characterize atomistic defects and to evaluate the chemistry of defect clusters and homonuclear bond structures. This study demonstrates that chemical disordering is crucial to understanding microstructural stability and establishing a mechanistic modeling of microstructural evolution of irradiated SiC.

3.3 MECHANICAL PROPERTIES OF NEW GRADES OF SiC FIBERS

H. Gietl (Idaho National Laboratory), T. Koyanagi, Y. Katoh (Oak Ridge National Laboratory)

OBJECTIVE

Investigate the potential of the newly developed Tyranno SA4 series SiC fibers for use in refractory material composites for fusion.

SUMMARY

We conducted comparative characterization of the SiC fibers using the single fiber tensile test and the bend stress relaxation (BSR) creep test on Tyranno SA3, SA3', and SA4 SiC fibers before and after annealing at 1500–1800°C for 1–100 h. The new SA4 SiC fiber has a significant advantage in tensile strength compared to the SA3 and SA3' fibers, indicating a great potential for matrix reinforcement. All the fibers possessed similar thermal creep resistance at 1500°C or 1800°C.

PROGRESS AND STATUS

All the examined Tyranno fibers have a highly crystallized structure and near stoichiometric composition. The fibers were received on spools, and all fibers were produced by Ube Corp. in Japan. The diameter of the SA3 fibers is approximately 7.5 μm, whereas the diameter of the SA3' and SA4 fibers is approximately 9 μm.

The BSR experiment was performed with a fixture with three different curvature radii (2, 3, and 6 mm). The fixture was made from nuclear grade graphite to avoid chemical reactions between the fibers and the fixture. The SiC fiber bundles were loaded into the fixture and were then heat treated as described previously. Note that as-fabricated, unheated fiber bundles were straight and did not twist and turn. As the radius changes, the initial bending stress levels systematically change from approximately 300 MPa (6 mm radius) to approximately 1100 MPa (2 mm radius). A fiber bundle within the graphite fixture is shown in Figure 1.

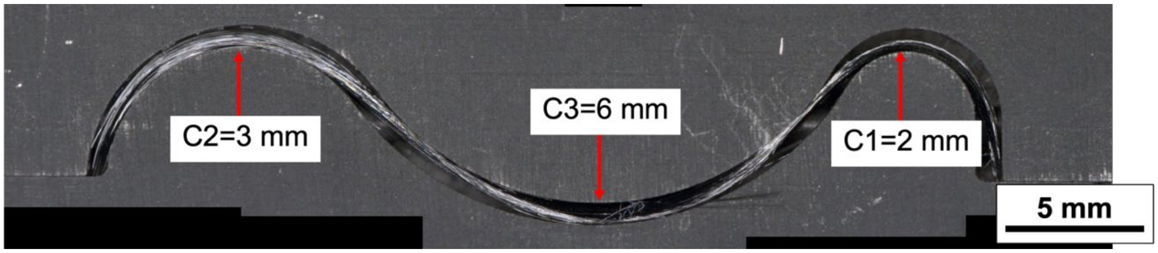

Figure 1. BSR graphite fixture used for the various fibers and temperatures.

Relaxation creep was evaluated using the BSR ratio (m), which is the ratio of final stress (σ_a) to initial stress (σ_0). The BSR ratio can be expressed as

$$m = \frac{\sigma_a}{\sigma_0} = \frac{E_a(\varepsilon_0 - \varepsilon_c)}{E_0 \varepsilon_0} = \frac{E_a}{E_0}\left(1 - \frac{R_0}{R_a}\right), \quad (1)$$

where E is the Young's modulus, ε is the flexural strain, and R is the curvature radius of the specimen. The subscripts a, 0, and c stand for the initial state, final state, and creep, respectively. The BSR ratio varies between 0 for complete relaxation and 1 for no relaxation. The Young's modulus is assumed to be unaffected by the heat treatment.

Creep deformation of the fiber bundles after the heat treatment is visible Figure 2. The resulting curvatures depend on the initial applied stress caused by the curvature radii of the fixture and the annealing temperature. The fiber deformation after 1800°C for 1h (Figure 2b) is larger than after 1500°C for 1h (Figure 2a).

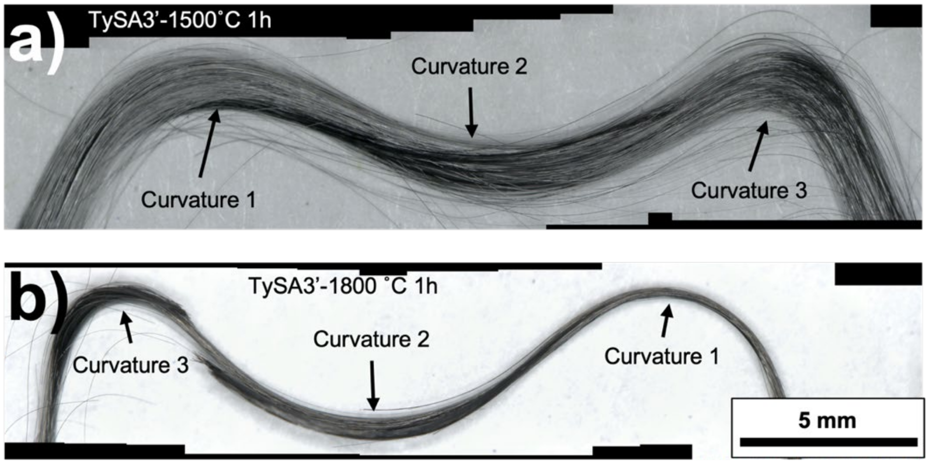

Figure 2. Tyranno SA3' fiber bundles after BSR annealing at a) 1500 °C and b) 1800 °C for 1h.

The BSR ratio is plotted against the initial applied average stress for 1500°C 1h (Figure 3) and 1800°C 1h (Figure 4) annealing.

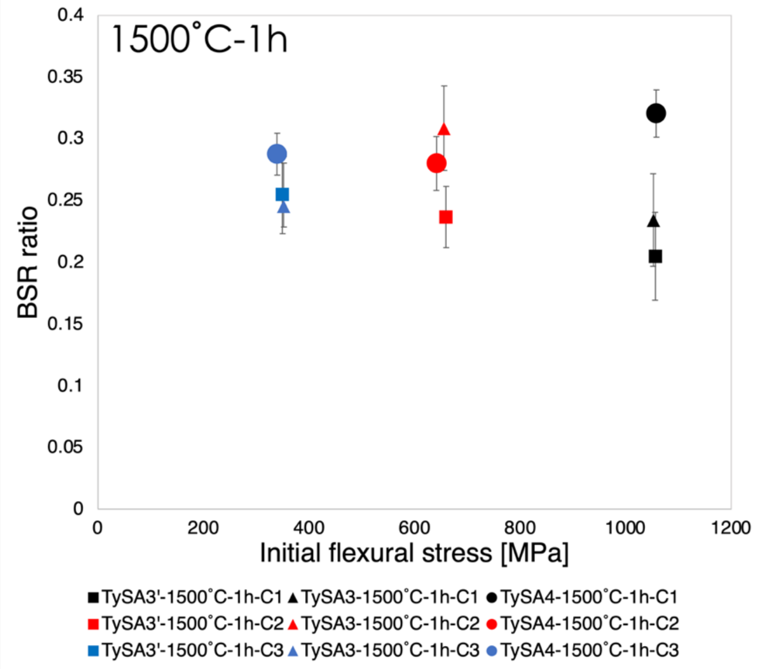

Figure 3. BSR ratio at varying initial flexural stresses for the different curvatures of the holder and different fibers after annealing at 1500 °C for 1h.

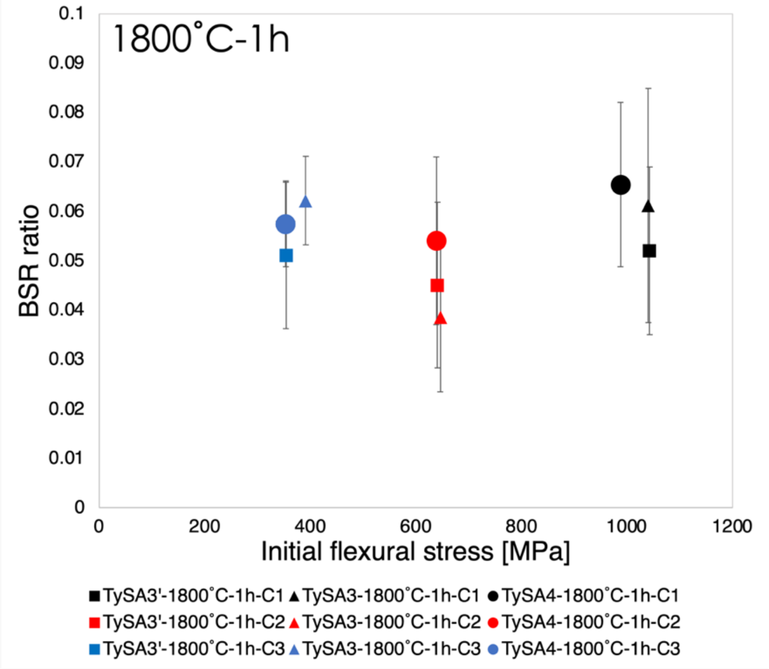

Figure 4. BSR ratio at varying initial flexural stresses for the different curvatures of the holder and different fibers after annealing at 1800 °C for 1h.

Overall, the three SiC fibers experienced similar thermal creep deformation at 1500°C and 1800°C regardless of the magnitude of the initial applied stress. Tensile tests of individual fibers out of the Tyranno SA bundles were performed at room temperature in ambient atmosphere following the ASTM C1557-20 recommended procedures [1]. An Instron universal tensile testing machine (model 3342R3287) with a 5 N load cell and constant displacement of 5 μm/s was used. The individual fibers with a gauge length of 25.4 mm were mounted and aligned on cardboard mounting tabs as illustrated in previous studies and suggested by the ASTM C1557-20 procedure [1,2]. The sides of the cardboard mounting tabs were burned away before the test. The diameter of the tested fiber was measured immediately before each test and used for the stress calculation. The total number of valid tests for each fiber type varied from 35 to 50. Weibull analysis was performed, and the two-parameter Weibull theory was applied to characterize the fracture behavior of brittle SiC fibers [3,4]. The frequency of fiber failure, F_i, was determined with the mean rank method $F_i = n/(N+1)$ at the nth ranked sample with a total of N specimens [2,5]. Weibull strength and the strength distribution analysis (two parameter) were performed. From the tensile test data, the Weibull scale factors σ_0 and modules m were determined. From that, the Weibull average tensile strength (σ_{avg}) was calculated with the equation:

$$\sigma_{avg} = \sigma_0 \Gamma(1 + \frac{1}{m}), \tag{2}$$

where $\Gamma(1 + \frac{1}{m})$ is a gamma function value [3].

In Figure 5, the results from the tensile test and the Weibull plots are shown. As-fabricated SA4 fiber possessed a superior tensile strength of approximately 4 GPa, compared with 2.4 GPa of the SA3 and SA3' fibers. For all three fibers, the degradation of the tensile strength was minimal after annealing at temperatures up to 1800°C for 1h. However, their strength degradation was significant after annealing for 30h. The SA4 fibers showed better strength for annealing up to 10h at 1800°C, but after 30h, the strength was comparable for all fibers. The results of this study suggest that SA4 fiber is a valuable fiber for the reinforcement of a refractory matrix (e.g., SiC and W) because the ultimate strength of the fiber reinforced composites is governed by the fiber’s statistical strength.

The testing conditions and the corresponding Weibull parameters of the fibers are shown in Table 1.

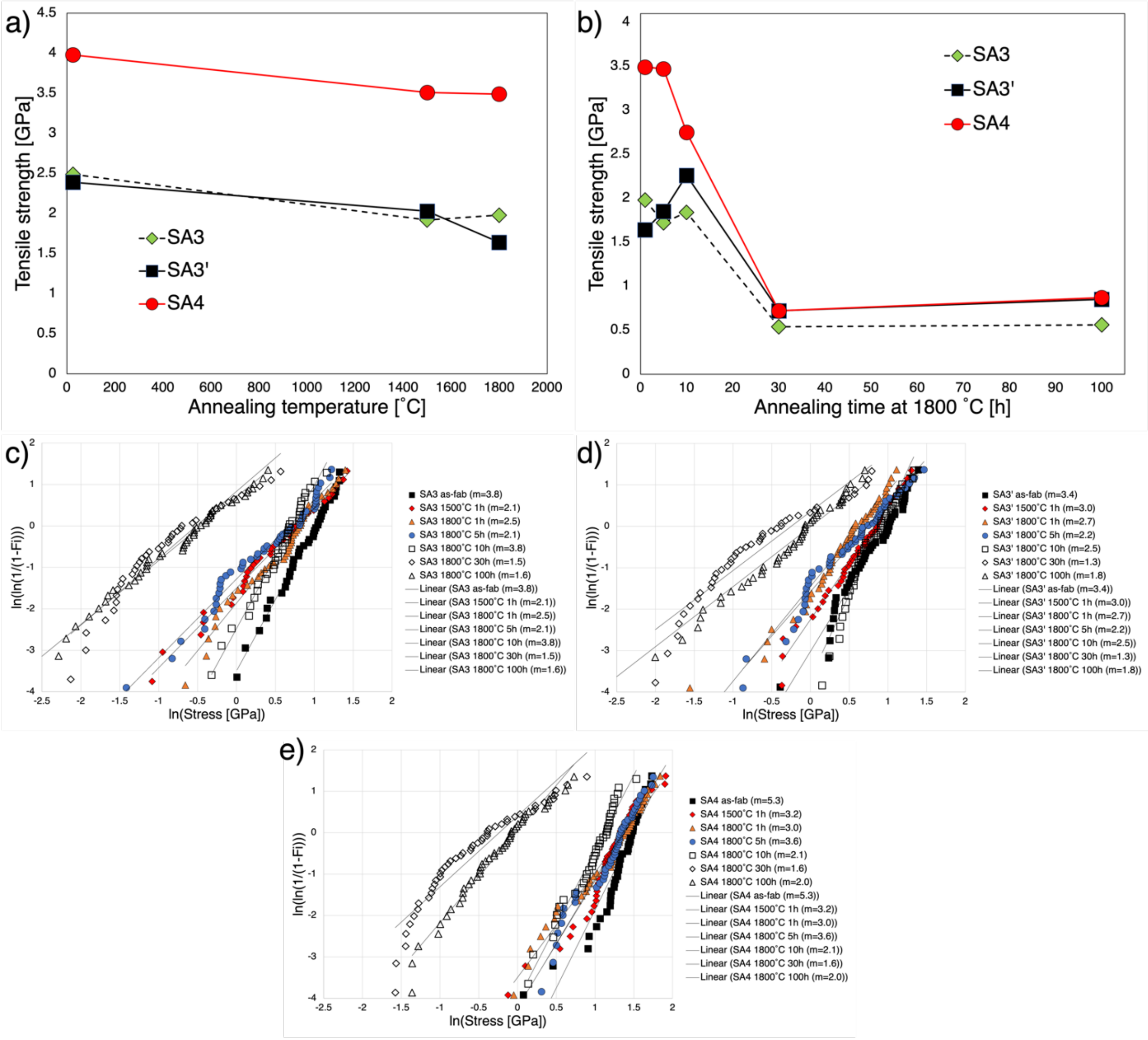

Figure 5. a) Average strength of fibers after annealing for 1h at varying temperatures; b) average strength of fibers after annealing at 1800°C over time; c–e) frequency of fiber failures as function of applied stress and fiber condition for c) SA3, d) SA3', and e) SA4.

Table 1. Testing conditions and Weibull parameters

Fiber	Temperature [°C]	Time [h]	σ_{avg} [GPa]	σ_0 [GPa]	m
SA3	As-fabricated		2.49	2.74	3.8
	1500	1	1.92	2.17	3.0
	1800	1	1.98	2.23	2.7
	1800	5	1.72	1.94	2.2
	1800	10	1.84	2.03	2.5
	1800	30	0.54	0.60	1.3
	1800	100	0.56	0.63	1.8
SA3'	As-fabricated		2.39	2.66	3.4
	1500	1	2.03	2.28	3.0
	1800	1	1.64	1.84	2.7
	1800	5	1.85	2.09	2.2
	1800	10	2.26	2.50	2.5
	1800	30	0.72	0.79	1.3
	1800	100	0.85	0.97	1.8
SA4	As-fabricated		3.98	4.32	5.3
	1500	1	3.51	3.92	3.2
	1800	1	3.49	3.91	3.0
	1800	5	3.47	3.85	3.6
	1800	10	2.75	3.02	2.1
	1800	30	0.72	0.80	1.6
	1800	100	0.87	0.99	2.0

Future Plans

Electron microscopy characterizations of the SiC fibers before and after annealing will be conducted to understand the microstructure mechanical property correlation.

References

[1.] ASTM C1557-20. Standard test method for tensile strength and Young's modulus of fibers.
[2.] Youngblood, G.E., et al., Tensile strength and fracture surface characterization of Hi-Nicalon SiC fibers. Journal of Nuclear Materials, 2001. 289(1-2): p. 1-9.
[3.] Patankar, S., Weibull distribution as applied to ceramic fibres. Journal of Materials Science Letters, 1991. 10(20): p. 1176-1181.
[4.] Weibull, W., A statistical distribution function of wide applicability. Journal of Applied Mechanics, 1951.
[5.] Sha, J.J., et al., Effect of heat treatment on the tensile strength and creep resistance of advanced SiC fibers. Journal of Nuclear Materials, 2004. 329-333: p. 592-596.

3.4 DEVELOPMENT AND RADIATION EFFECTS OF HIGH-HEAT FLUX MATERIALS FOR FUSION ENERGY—D. Bhardwaj, D.J. Sprouster, J. R. Trelewicz, L.L. Snead (Stony Brook University)

PROGRESS AND STATUS

Introduction

Beryllium intermetallic compounds (beryllides) have been of great interest among researchers, due to its ability to be used an advance neutron multiplier in Demonstration Power Plant (DEMO) reactors. They have proven to have:

- Lower chemical reactivity
- Lower swelling against He
- Higher compatibility with structure materials, and
- Reduced tritium retention.

A wide range of literature information is available for different beryllide intermetallic systems (Be-Ti, Be-V, Be-Mo, Be-Zr, etc.) of interest to fusion systems. However, the most studied system for blanket application is Be-Ti.

Experimental Procedure

Phase Diagrams of Fusion-Relevant Beryllides

Beryllides typically stabilize into different crystal phases depending upon the metallic concentration and temperature. As shown in the binary phase diagrams below (Figure 1), most of these phases are line compounds with several potential phases and associated crystal structures. The Ti-based $Be_{12}Ti$ beryllide phase is of high-interest as this phase has the most desirable mechanical and thermomechanical properties, and optimal Be content.

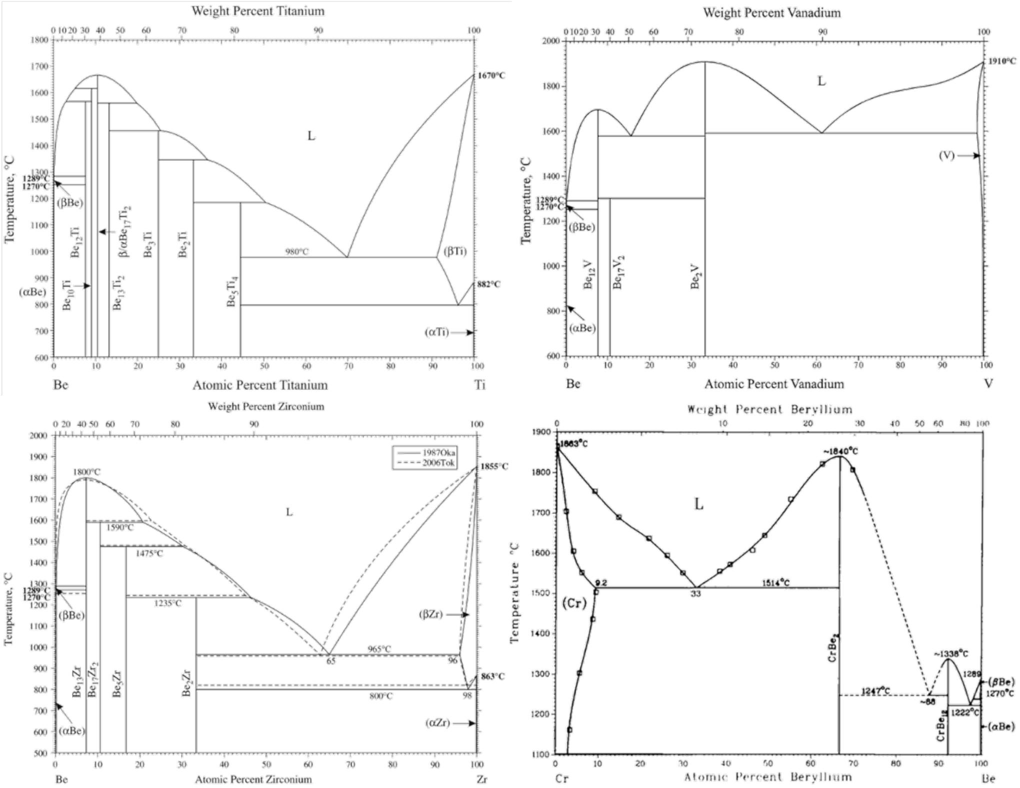

Figure 1. Phase diagrams of (a) Ti, (b) V, (c) Zr (d) Cr beryllides phases.

Processing Of Fusion-Relevant Beryllides

In this task our primary goal is to understand the processing controls necessary to obtain single beryllide structures, along with the impact and possibly the potential of processing complex beryllides for fusion application. Here $Be_{12}Ti$ was synthesized using direct current sintering and optimizing the powder processing of Be and Ti powders. The powder was measured in the stoichiometric ratio (Be, 7.7 at. % Ti) and speed mixed at 800 rpm for 1 minute. Next, 2 gm of the mixed powder was loaded into a 13 mm die and pressed to attain a green body, at an applied pressure of 100 MPa. The pressed green body was subsequently loaded into a 13 mm graphite die and direct current sintered at 1100 °C. In the work performed thus far, we have explored the effect of hold time on optimizing the density, final composition, and microstructure. The sintering parameters are listed in Table 1 below:

Table 1. Sintering Parameters

Vacuum	<10 Pa
Thermometer	K-type
Heating Rate	100 °C /min
Hold Time	20 min, 40 min, 60 min, 80 min
Cooling Rate	Normal cooling
Sintering pressure	6.6 kN/ 50 MPa

After cooling, the pellet was taken out of the graphite die and polished to get rid of the sacrificial graphite and Be_2C layer (formed after reaction between Be and graphite sheet). The pellets are then characterized using X-ray diffraction (XRD) for phase purity. X-ray computed tomography (XCT) measurements were performed to investigate the internal microstructure of compacts both quantitatively and qualitatively.

Internal features observable from XCT include inclusions, porosity, and morphology/spatial features. The XRD patterns were collected in Reflection geometry mode (Bragg-Brentano) utilizing a Bruker D8 Advance diffractometer. A Nickel filter prior to the detector optics was used to filter K_β emission lines. The XRD patterns were recorded with a Two-Theta range of 10-110° with a time/step to be 2s, at a step size of 0.01°. After the data collection the XRD patterns are analyzed in EVA and MATCH3! for phase identification.

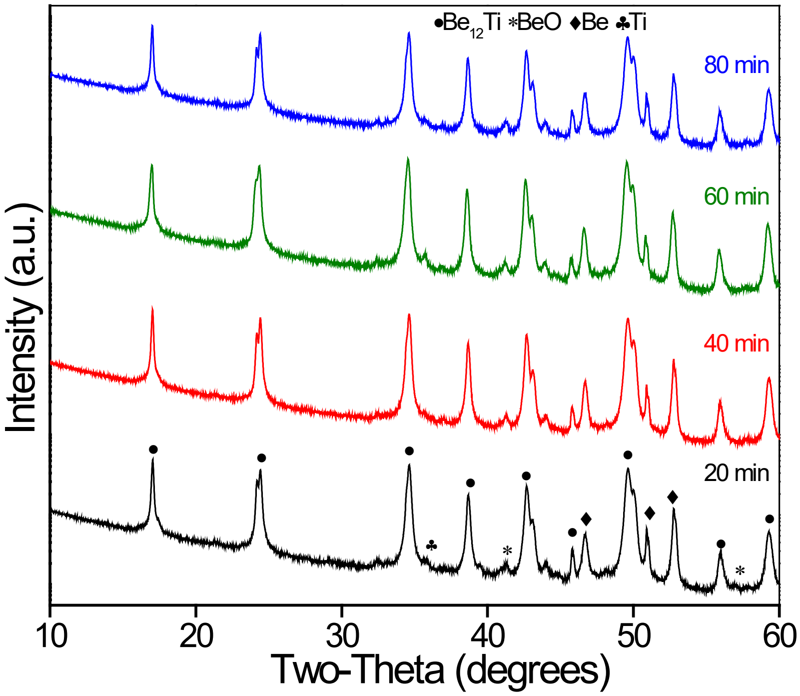

Figure 2. XRD pattern of the Be12Ti synthesized at different hold time using SPS.

Figure 2 shows the XRD patterns of the beryllides synthesized at different hold times. For the pellet synthesized with a hold-time of 20 min, XRD peaks were indexed to four different crystal phases; $Be_{12}Ti$ (space group: I4/mmm); BeO (space group: P63/mc); Be (space group: P63/mc); and Ti (space group: P63/mmc). As the hold time increases from 20 min to 80 min, the Ti peaks disappear due to the complete reaction with Be to form $Be_{12}Ti$. To confirm this, weight fraction and microstructures of the different phases (lattice parameters, coherent particle size) was determined using quantitative XRD analysis (TOPAS, Bruker). Table 2 lists the weight fractions from the XRD analysis.

Table 2. Weight fractions from the XRD analysis

Hold-time	Weight Fraction			
	$Be_{12}Ti$	Be	BeO	Ti
20 min	77.8	20.6	1.6	0.2
40 min	77.1	21.6	1.3	-
60 min	82.0	16.4	1.6	-
80 min	78.3	19.9	1.7	-

The reconstructed XCT cross sections through the different Beryllide compacts are shown in Figure 3 (a)-(d) as a function of sintering hold time. The visible features seen in the XCT images are attributed to presence of different phases seen from the XRD patterns. The light grey, dark grey, white, and black regions are attributed to Be12Ti, Be, Ti and open porosity respectively. The XCT results show additional evidence that the Be and Ti concentration reduce as the hold time increases, thereby confirming the complete reaction and consumption of Ti to form $Be_{12}Ti$. It can also be seen from the change in weight fraction obtained from the XRD data.

Density measurements were performed on all specimens. The density was calculated using the weight fractions of different phases present in the pellets. The density for all the samples was found to be ~99%. Thus, direct current sintering is a successful method that can fabricate high density $Be_{12}Ti$ compacts appropriate for laboratory scale investigations and irradiation testing.

Results

- Morphological and thermophysical properties (thermal conductivity/thermal diffusivity) from Laser Flash Annealing experiments are currently under way.
- Mechanical (Vickers Hardness) testing on the samples, to determine the strength and the role of morphology on the plastic response.
- Here, we have synthesized the hardest beryllide $Be_{12}Ti$. The further processing is to be done for synthesis of Cr, V and Zr beryllide using similar powder methods and DCS.
- The radiation tolerance of these beryllides following neutron irradiation in MITR will be investigated.

Acknowledgements

The work was funded under Grant DE-SC0018332 to the Research Foundation at State University of New York, Stony Brook by the United States Department of Energy Office of Fusion Energy Sciences.

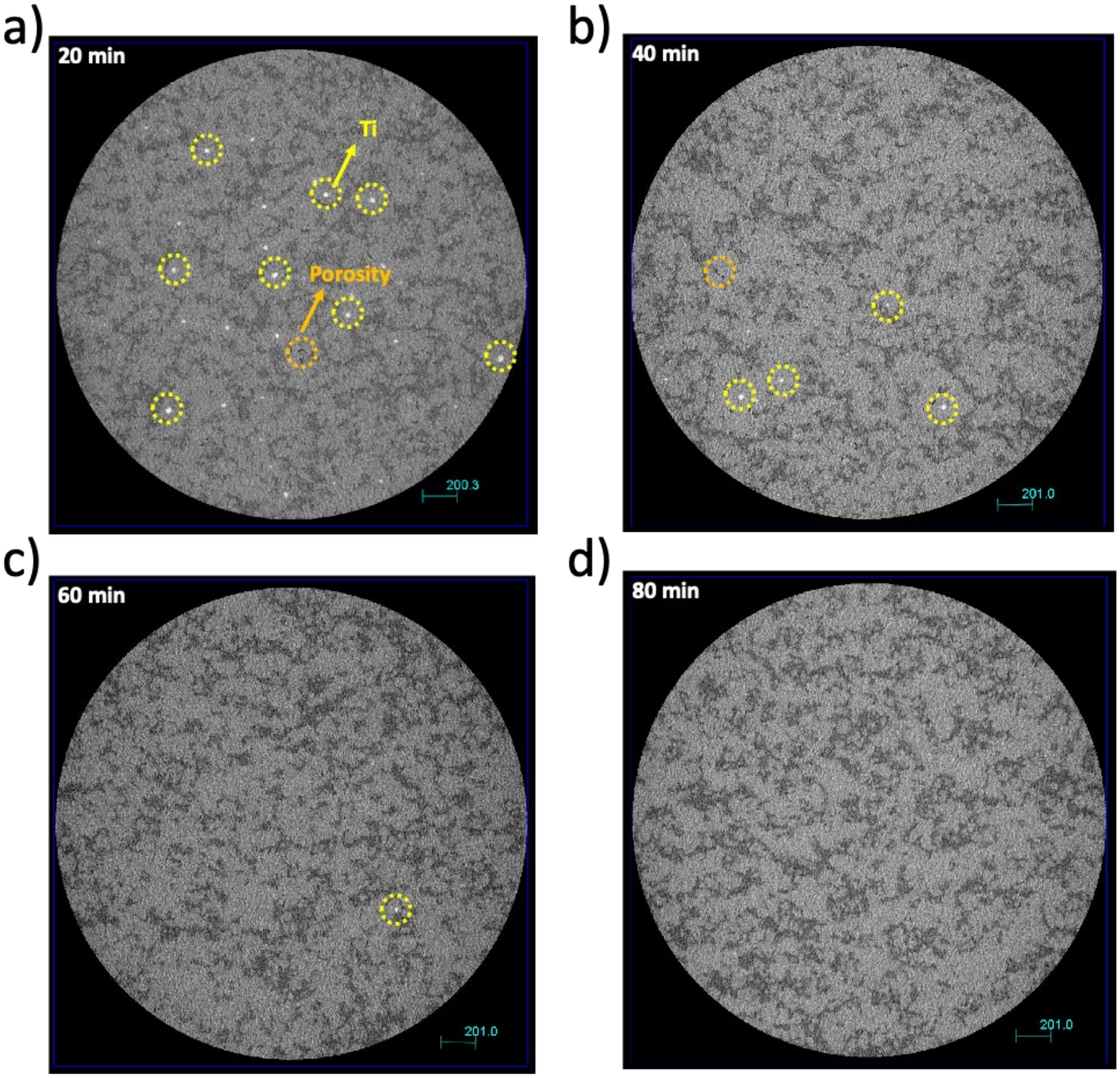

Figure 3. (a)-(d) XCT images of Be12Ti synthesized at different hold time.

3.5 COMBINED XRD AND PDF EXAMINATION OF POWDER AND SOLID Li_2TiO_3—D. J. Sprouster, L. L. Snead (Stony Brook University), P. D. Edmondson (Oak Ridge National Laboratory)

PROGRESS AND STATUS

Introduction

Combined X-ray Powder Diffraction (XRD) and Pair Distribution Function (PDF) measurements were performed on powder and solid Li_2TiO_3 materials, to determine if there were any differences in the local and average structure. The combination of x-ray scattering techniques shows that while the local atomic structures are identical, while the solid material has more pronounced long-range order and lower two-dimensional defects compared to the powder specimen, presumably associated to the processing.

Experimental Procedure

The XRD and PDF experiments were collected at the PDF Beamline at the National Synchrotron Light Source II (NSLS-II). The XRD peak profiles were modeled by a modified pseudo-Voigt function. The instrument contribution to the broadening of the measured profiles was quantified by fitting the LaB_6 National Institute of Standards and Technology (NIST) powder standard, with a known coherent grain size and negligible micro strain contribution. The Gaussian and Lorentzian-based broadening parameters were subsequently fixed during the analysis of the alloys under investigation to quantify the microstructure (coherent grain size and macrostrain components). The lattice parameter, cell angle (β), micro strain and coherent grain size components were allowed to vary for the Li2TiO3 phase (C2/c:b1 space group).

The powder patterns collected with the short PDF detector distance were corrected for PDF-specific corrections (self-absorption, multiple scattering, and Compton scattering) and converted to atomic PDFs, G(r), using PDFgetX3 over a Q-range of 0.8-28 $Å^{-1}$. The PDF structural analysis was carried out using PDFgui over a radial range of 1.0-50 Å. The Ni standard was used to determine the parameters that describe the experimental resolution (Q_{damp} and Q_{broad}) with atomic displacement parameters (ADPs), correlated motion parameter and lattice parameters allowed to vary. The ADP parameters capture diminished x-ray intensity from atom displacements from their mean positions in a crystal structure and can include components from both temperature-dependent atomic vibrations (thermal disorder) and static disorder (such as defects). The scale factor, lattice parameters, correlated motion parameter, and isotropic ADPs (for the Li, Ti, and O atoms) were allowed to refine during the PDF analysis.

The XRD patterns for the powder and solid specimens are shown in Figure 1. The XRD patterns for both specimens are consistent for a single Monoclinic phase, and no additional minor phases are observable. It is noted that the XRD peak heights and locations are different from the powder to the solid specimen, likely due to the powder containing some defects (point defects and extended two-dimensional defects). The quantitative XRD refinement results are given in Table 1. The quantitative refinements of the measured XRD patterns are given in Figure 1 as solid lines. The microstructure clearly changes from Powder to Solid, with a larger coherent grain size and lower micro strain parameters. The micro strain parameter is directly attributable to two-dimensional defects (such as dislocations).

The total scattering patterns are shown in Figure 2 (a) along with the PDF (up to 20Å), in Figure 2 (b). The similarity of the total scattering and PDFs is apparent between the powder and solid, and only subtle differences in the PDFs and short-range order are observable. This is indicative that the atomic scale defects, and intermediate range orders in both specimens are similar. Figure 2 shows the preliminary PDF refinements, for both specimens. While there are some small features at low-radial distance, the overwhelming correlation peaks are modelled with a simple model crystallographic model. The ADP (a measure of the disorder within the specimens), from the analysis are given in Table 2. The larger parameters in the powder sample, compared to the solid specimen, is consistent with the XRD results and a slightly higher overall defect concentration. The larger ADP for the O correlations in the solid material may be a result of the processing.

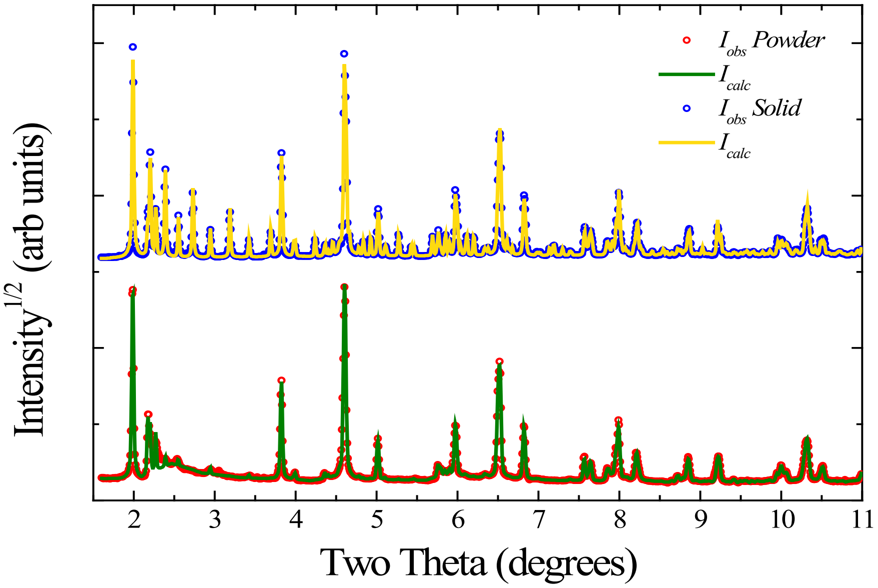

Figure 1. XRD patterns for powder and solid specimens. Solid lines are the Reitveld refinements.

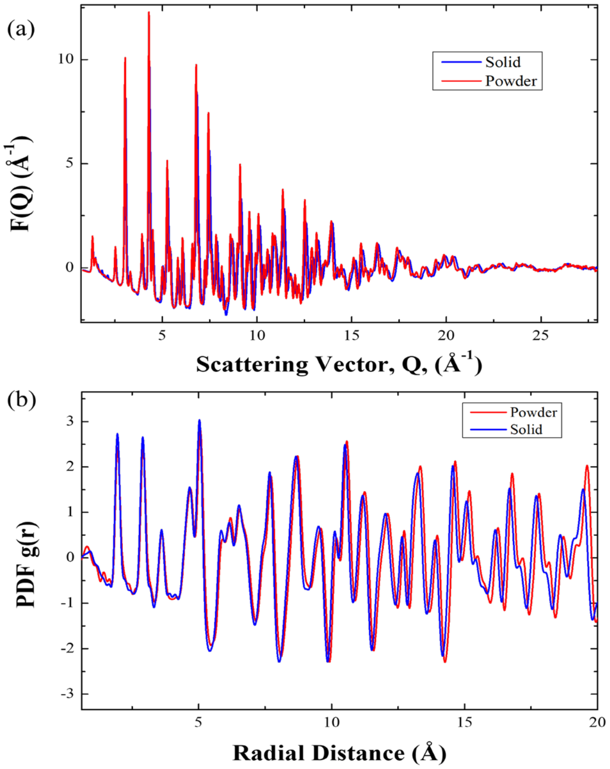

Figure 2. (a) Total scattering diffraction patterns and (b) pair distribution functions for Powder and Solid Li_2TiO_3 specimens.

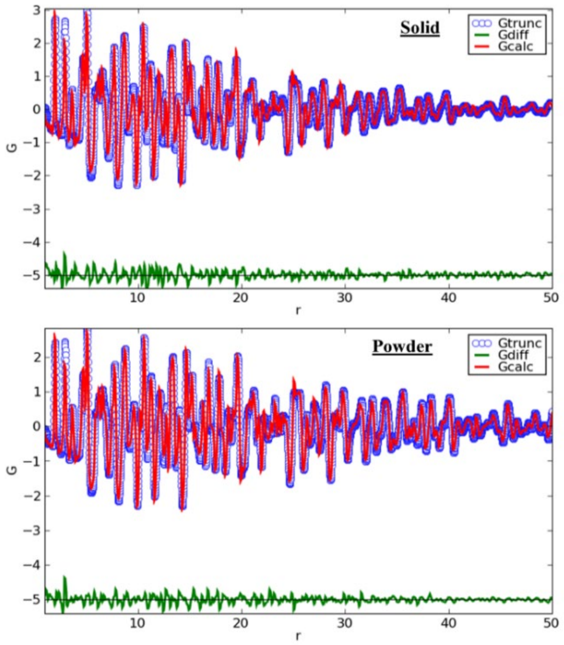

Figure 3. PDFs for powder and solid specimens. Solid lines are the PDF refinements to the experimental data. Green lines are residual.

Table 1. Quantitative XRD results for powder and solid specimens

specimen	a (Å)	b (Å)	c (Å)	β, cell angle (degrees)	Coherent grain size (nm)	Micro strain (arb units)
powder	5.0655 (±0.0003)	8.7774 (±0.0006)	9.7572 (±0.0005)	100.16 (0.008)	356 (±25)	11.2 (±0.4)
solid	5.0589 (±0.0001)	8.7797 (±0.0003)	9.7437 (±0.0003)	100.211 (±0.002)	515 (±5.0)	0.3 (± 0.2)

Table 1. Quantitative results for powder and solid specimens from the PDF analysis. ADP is the atomic displacement parameter.

specimen	ADP -Li	ADP - Ti	ADP - O
powder	14.2(±4.3)	4.8 (±0.4)	9.5 (±1.1)
solid	11.2 (±4.6)	4.7 (±0.51)	12.5 (±1.6)

Results

- Improve the PDF refinements by incorporating an anisotropic atomic displacement parameter.
- Perform small box refinements to quantify if there are any subtle differences in the medium range order because of the initial microstructural defects.
- Compare the XRD and PDF results to thermal conductivity and modelling results.
- Compare results to existing data for similar materials.

Acknowledgements

The work was funded under Grant DE-SC0018332 to the Research Foundation at State University of New York, Stony Brook by the United States Department of Energy (DOE) Office of Fusion Energy Sciences. Use of the 28-ID-1 (PDF) beamline at the NSLS-II, Brookhaven National Laboratory, was supported by the DOE under Contract No. DE-SC0012704.

3.6 FABRICATION OF CERAMIC AND METAL MATRIX ENHANCED SHIELD THROUGH DIRECT CURRENT SINTERING: EFFECT OF LABORATORY ENVIRONMENT ON PRE-SINTERED COMPACT MICROSTRUCTURE

B. Cheng, D. J. Sprouster, J. R. Trelewicz, L. L. Snead (Stony Brook University)

PROGRESS AND STATUS

Introduction

Pre-sintered ceramic composite shielding compacts may suffer from moisture pick up and hydride decomposition in the laboratory environment which could compromise or complicate article processing or ultimately the quality of sintered articles. The goal of this report is to assess the moisture absorptance and hydride stability of pre-sintered compacts, providing direct insight into processing of the shield materials. Successful completion of this task is met by achieving the following criteria:

1. Hydrogen loss < 10% for temperatures consistent with pre-sintering processing.
2. No significant change in metal hydride crystal structure due to compact aging as determined through x-ray diffraction (XRD).
3. No significant oxygen pick up as determined through the absence of new oxide phase formation.

In this report, we performed long term aging of pre-sintered compacts in air and within a vacuum desiccator to evaluate the laboratory environment's effect on moisture absorption and hydride stability. Our results show that only aging in the air after one week led to an obvious weight increase due to moisture absorption while aging in vacuum did not result in any up-take of moisture. The XRD results indicate that the major phases in the pre-sintered compacts were stable, and no new oxide phases emerged. Only a minor amount of hafnium oxide (HfO_2) phase increased after aging in air for one month, while the metal hydride remained stable in both air and vacuum aged compacts. Finally, neither long term air nor vacuum aging altered the ability to sinter cold pressed compacts suggesting the process is relatively robust with respect to laboratory oxygen pick up. Our results met all the metrics for success: Hydrogen loss <10%, no significant changes in metal hydride microstructure, and minor oxygen pick up. To better preserve the original microstructure of MgO-HfH_2 pre-sintered compact, storage in a vacuum desiccator is recommended.

Results

The study of the laboratory environment's effects on the microstructure of pre-sintered compact was investigated with XRD measurements of feedstock powders to characterize the pre-existing phases. Figure 1 (a) and (b) show XRD patterns for feedstock MgO powders. In addition to the MgO phase, a minor $Mg(OH)_2$ phase is observable and represents the major impurity phase in both micron and nano MgO feedstock powders used in the sintering. The $Mg(OH)_2$ is a common impurity in many MgO feedstock powders and can be easily removed by baking MgO in an atmosphere furnace at 500°C for one hour, as we show in Figure 1 (a) and (b). However, there is still a minor amount that remains in nano MgO powder, presumably due to the large surface area intrinsic to nano powders. Increasing the baking time to two hours eliminated $Mg(OH)_2$. Figure 1 (c) shows the XRD pattern of the HfH_2 powder used in the MgO-HfH_2 composite shielding materials. The main phase is $HfH_{1.983}$ with a minor amount of HfO_2 phase.

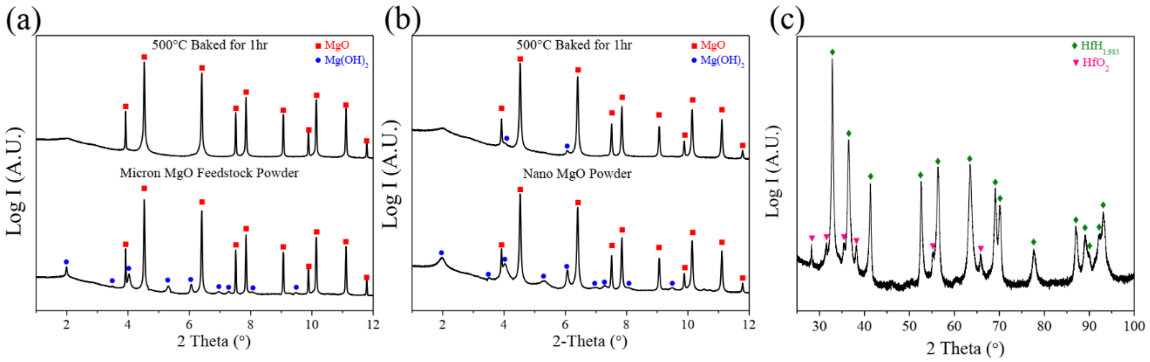

Figure 1. XRD patterns of (a) Micron MgO (b) Nano MgO (c)HfH_2 feedstock powders.

After characterizing the feedstock powders, 25Vol% HfH_2 powder was mixed with MgO powder (Micro to Nano = 4:1) and 1wt%LiF additive. The mixed powders were then cold pressed at 100MPa. The XRD pattern of a representative greenbody is shown in Figure 2 (a). An optical image of a crack free cold pressed green body is displayed in Figure 2 (b). Four crystal phases are quantifiable from the XRD pattern in Figure 2 (a): MgO, $HfH_{1.983}$, HfO_2, and LiF. No $Mg(OH)_2$ phase is observable in the green body. For the aging study, two separate green bodies were prepared from the same starting powder mixture. The first compact was placed in laboratory air; the second compact was placed in a vacuum desiccator with silicon dioxide desiccant, as shown in Figure 2 (c). The two green bodies were aged for one day, one week, one month, and three months to study the hydride decomposition, oxidation, and moisture absorption. Weight and XRD measurements of aged green bodies were taken after each aged period to assess the microstructure stability.

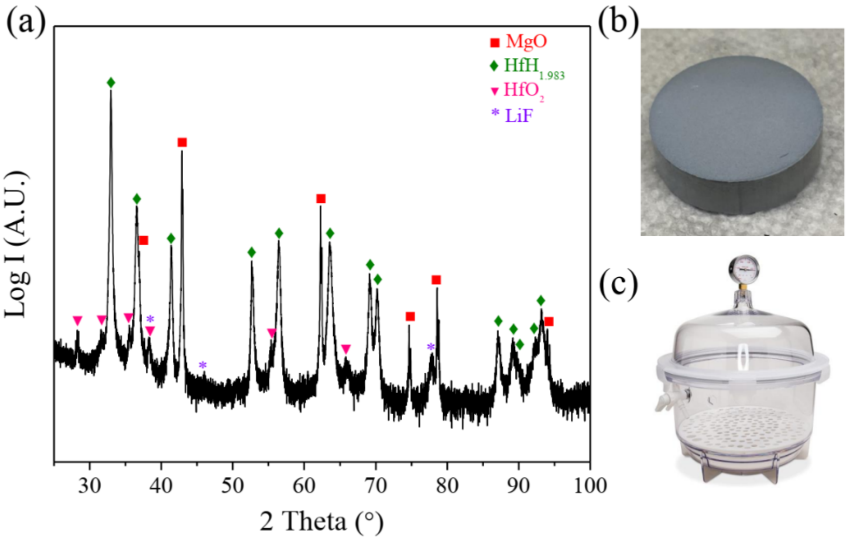

Figure 2. (a) The XRD pattern and (b) optical image of MgO-25%VolHfH_2 green body (c) The desiccator for the vacuum aging.

Figure 3 (a) and (b) show the measured weight and weight changes, respectively, as a function of aging time in air and vacuum. The weight of the vacuum aged green body remained constant. The weight of the air aged green body increased with aging time, most notably after one week. A total weight increase of 2% was observed after three months of air aging. The absorption of moisture at room temperature might account for the weight increase during aging in air. Placing green bodies in a vacuum desiccator can effectively suppress moisture absorption.

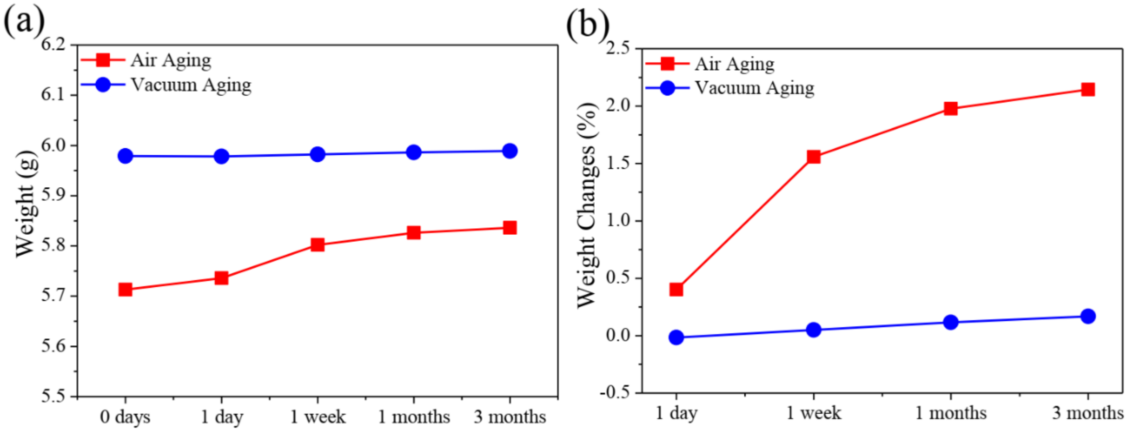

Figure 3. The (a) weight and (b) weight changes of MgO-25%VolHfH_2 Green bodies as a function of aging time in air and vacuum.

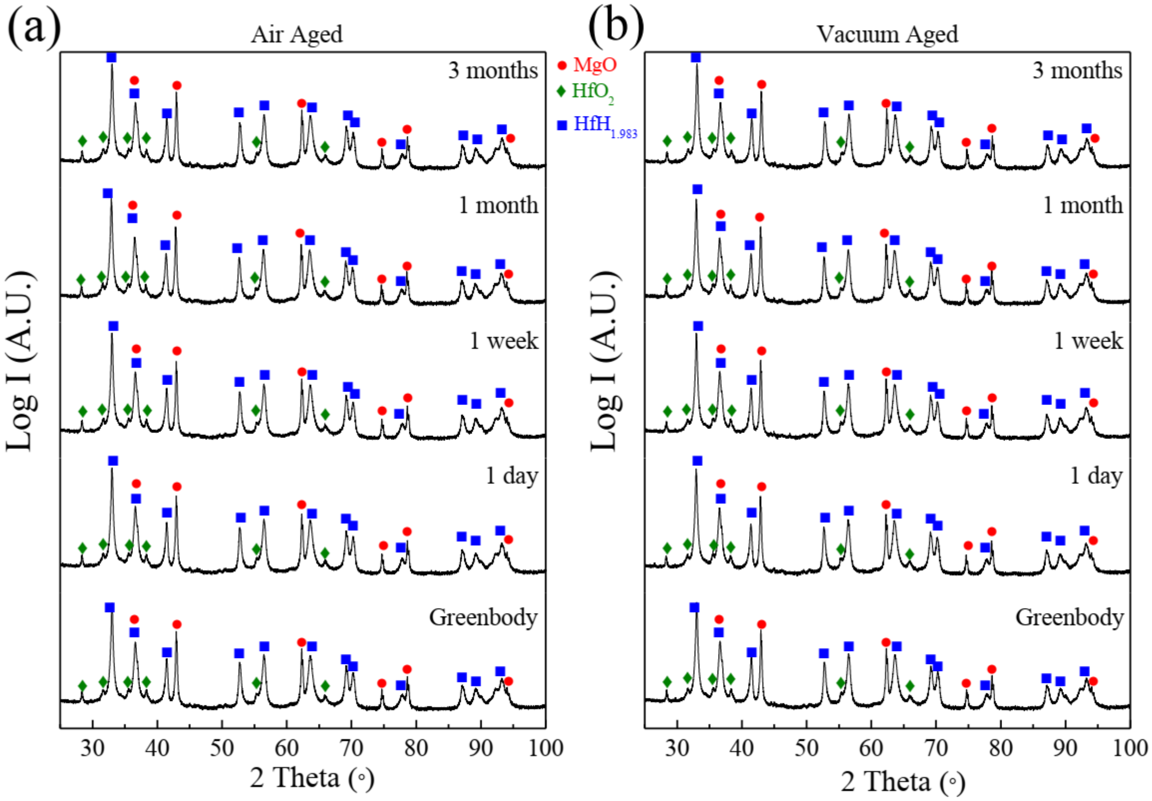

Figure 4. The XRD patterns of (a) air and (b) vacuum aged green bodies with different aging times.

The phase stability of the green bodies is another important aspect of aging that can be characterized by XRD, to determine (if any) the effects of laboratory environment on the hydride decomposition and oxidation. The XRD was used to quantify the phase stability as a function of time for air and vacuum aged green body, as shown in Figure 4 (a) and (b), respectively. Four main phases are identified in all patterns: MgO, $HfH_{1.983}$, HfO_2 and LiF. Due to the minor fraction, the LiF phase is not labeled in Figure 4 or clarity. Qualitatively, no major changes are observable in both air and vacuum aged green bodies, even after aging for three months. To capture the minor changes in phase fraction, Rietveld refinements on each XRD pattern we performed, and the quantitative phase fraction results (weight %) are shown in Figure 5 (a). Both air and vacuum aged green bodies $HfH_{1.983}$ weight percentage is constant with ageing time as shown in Figure 5 (b). The HfO_2 phase in air and vacuum aged green body did increase, as shown in the lower panels of Figure 5 (a) and (b). No weight percentage change was captured for the vacuum aged green body, and the HfO_2 phase is stable. The HfO_2 weight percentage increase in the air aged sample after one month. The total weight gain in the HfO_2 phase was 0.13%. Considering only ~1.25 % of HfO_2 in the initial as formed green bodies, an 0.13% increase in the oxide phase is insignificant and will not affect the microstructure of the green body.

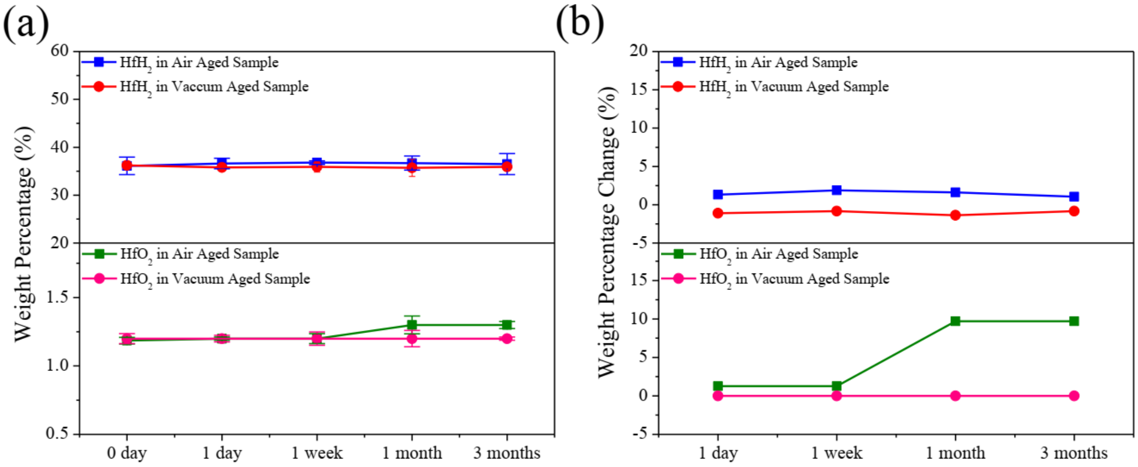

Figure 5. The XRD measured (a) weight percentage and (b) weight changes of air and vacuum aged green bodies as a function of aging time in air and vacuum.

Finally, we compared the ability to sinter the three months air and vacuum aged samples to the freshly made green body. The sintering curves are shown in Figure 6 (a). The vacuum aged and as-prepared samples' sintering curves are almost identical, with only the air aged sample showing minor higher low temperature displacement. This departure is potentially related to the removal of moisture upon heating. The final displacement and density of the three samples are similar. The XRD patterns of the three sintered compacts are shown in Figure 6 (b). The phases present in the three samples are identical with the same phase intensity. The sintering curves, density, and XRD measurement results of three MgO-HfH_2 composites with different pre-sintered aging conditions show no differences in sintering.

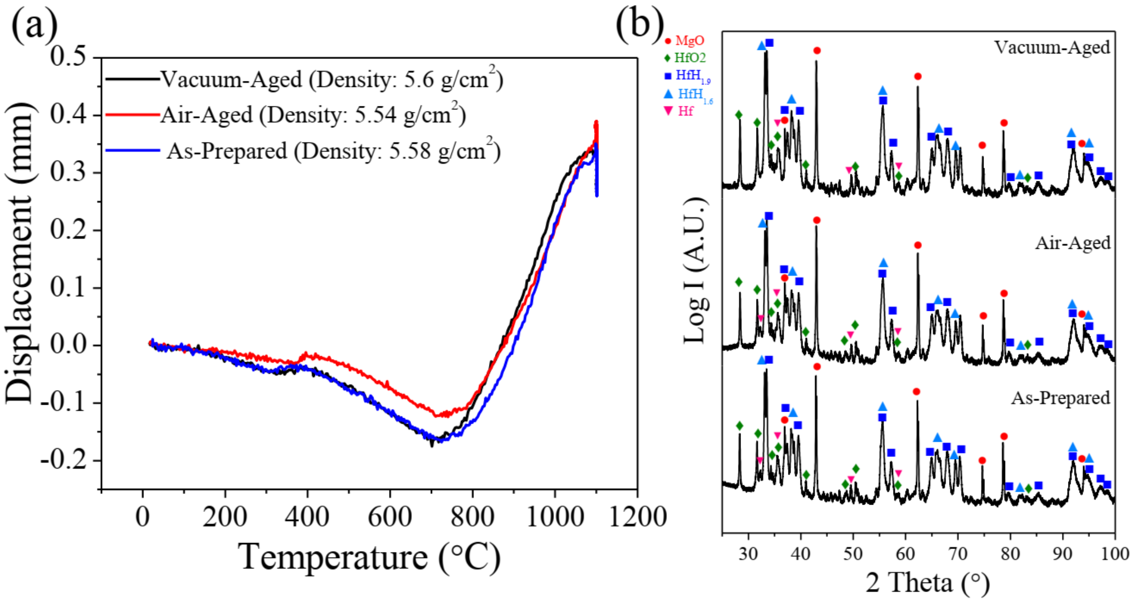

Figure 6. (a) The displacement as a function of heating temperature and (b) XRD patterns of MgO-HfH_2 composites with different pre-sintering aging conditions.

Conclusions

In this report, we performed long term aging of pre-sintered compacts to evaluate the laboratory environment's effect on moisture absorption and hydride stability. Our results show that only aging in the air after one week led to an obvious increase in weight due to moisture absorption while aging in a vacuum desiccator did not lead to any measurable moisture pick up. The XRD results indicate that only a minor amount of oxide phase increases after aging in air for one month, and the hydride phase remains stable in both air and vacuum aged compacts. Finally, both long term air and vacuum aging did not alter the sintering of cold pressed compacts. Our results met all the metrics for success: Hydrogen loss<10%, No significant changes in metal hydride microstructure, and oxygen pick up. To better preserve the original microstructure of MgO-HfH_2 pre-sintered compact, storage in a vacuum desiccator is recommended.

Acknowledgments

Ceramic Matric Composite Shields were conceptualized at Stony Brook University with all subsequent fabrication effort supported by the Advanced Research Projects Agency – Energy (ARPA-E) GAMOW Program under Contract DE-AR0001381.

3.7 QUANTIFYING THE ANISOTROPIC FORMATION OF ONE AND TWO-DIMENSIONAL DEFECTS IN SiC AND THEIR ROLE IN RADIATION-INDUCED CREEP

—D. J. Sprouster, L. L. Snead (Stony Brook University), T. Koyanagi, Y. Katoh (Oak Ridge National Laboratory), D. L. Drey (University of Tennessee, Knoxville)

PROGRESS AND STATUS

Introduction

In this work, we have utilized advanced microstructural data including quantitative atomic and microstructural defect data from X-ray Powder Diffraction (XRD) and x-ray total scattering (PDF) experiments in a series of neutron irradiated, and neutron irradiated stressed SiC test coupons. This work presented a unique way to explore the process of irradiation creep in neutron irradiated SiC by synchrotron-based 2D XRD analysis.

Experimental Procedure

The XRD and PDF measurements were performed at the National Synchrotron Light Source II (NSLS-II) at Brookhaven National Laboratory (BNL) using the X-ray Powder Diffraction (XPD) beamline 28-ID-2. All measurements were performed in transmission mode. The sample-to-detector distance and tilts of the detector relative to the beam were refined using a LaB_6 National Institute of Standards and Technology (NIST) powder standard. The wavelength of the incident X-rays was 0.1877 Å (66.05 keV), and the sample-to-detector distances were calculated to be 1567.99 mm (for XRD) and 199.16 mm (for PDF). The samples were wrapped in Kapton tape to limit radioactive contamination during shipping and handling at the beamline. Specimen details (irradiation conditions) and XRD and PDF analysis procedures utilized in extracting atomic and microstructural data can be found in [1, 2].

Results

The high-level results for the irradiated and stressed specimens are shown in Figure 1. The initial stress of >150 MPa under irradiation clearly leads to an increase in the (111) shoulder peak intensity, an indication of an increase in the stacking disordering. One of the most significant results from these investigations is the stress induced preferential nano-scale stacking disordering at low neutron damages (0.11 dpa), supporting a transient creep mechanism associated with SIPN and/or SIPA of interstitial clusters. The method employed in this study is potentially applicable to the study of irradiation creep in other materials, as SIPN and SIPA of defect clusters are the key mechanisms in irradiation induced creep in materials for fission and fusion applications followed up with a second paper detailing the atomic defect configurations from scattering in low temperature irradiated SiC specimens.

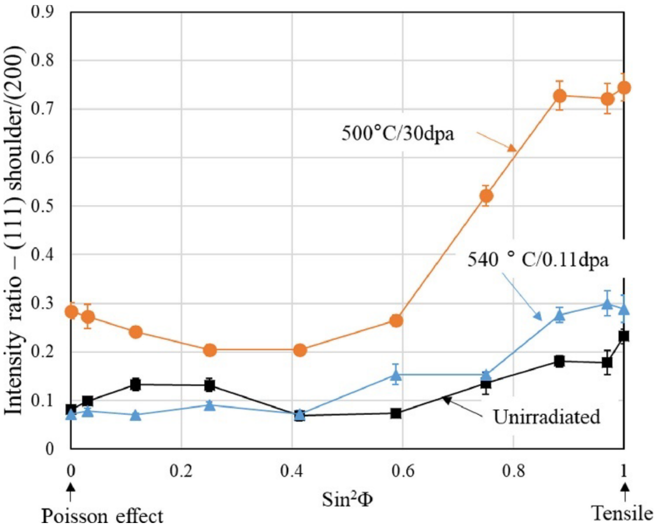

Figure 1. Intensity of (111) shoulder peaks normalized to that of (200) peak at different azimuth angles. The analysis was conducted for the integrated XRD patterns every 10 degrees. The azimuth angle (Φ) of 90° corresponds to tensile stress axis.

The detailed XRD and PDF analyses quantified the atomic and microstructural properties of as-irradiated and as-annealed specimens with irradiation doses before the onset of the amorphization. The high-level results for the low temperature neutron irradiated SiC specimens are shown in Figure 2. The XRD and PDF results show that the atomic structure in the as-irradiated samples is significantly perturbed due to a large fraction of vacancies and interstitial type defects. The large defect populations introduced by neutron irradiation include point defects which increase in concentration with increasing dose level, leading to the expanded lattice parameters and large atomic displacement parameters (ADP). These defects reduce the coherent volume by shortening the width of the unperturbed crystal regions and drive the emergence of additional diffraction/scattering components with small coherent volumes. Subsequent annealing leads to the removal of a large fraction of these point defects and the formation of some extended defects which manifest as larger micro strain values and smaller coherent grain sizes than the unirradiated state. The analysis of the PDF data, incorporating a disordered component with carbon interstitials at *24f* sites along ⟨100⟩ directions, captures the additional correlation peaks visible in the high dose specimens. The ADP quantified from the PDF analysis demonstrate that the primary defects associated with damaged SiC are carbon vacancies and interstitials and that recovery of the microstructure and different sublattices is highly correlated to the stored energy release, consistent with the initial postulation that the stored energy release in SiC is dominated by the recovery of carbon-based defects. The combination of XRD and PDF represents a strategy to determine the full spectrum of atomic and microstructural defects present in neutron irradiated materials and has the potential to validate simulations of radiation damage in other materials of interest. Finally, the impact of this paper has broad implications in generating structure property relationships in neutron irradiated materials where generating connections between the atomistic and defect structures can aid in understanding changes in macroscopic properties of interest.

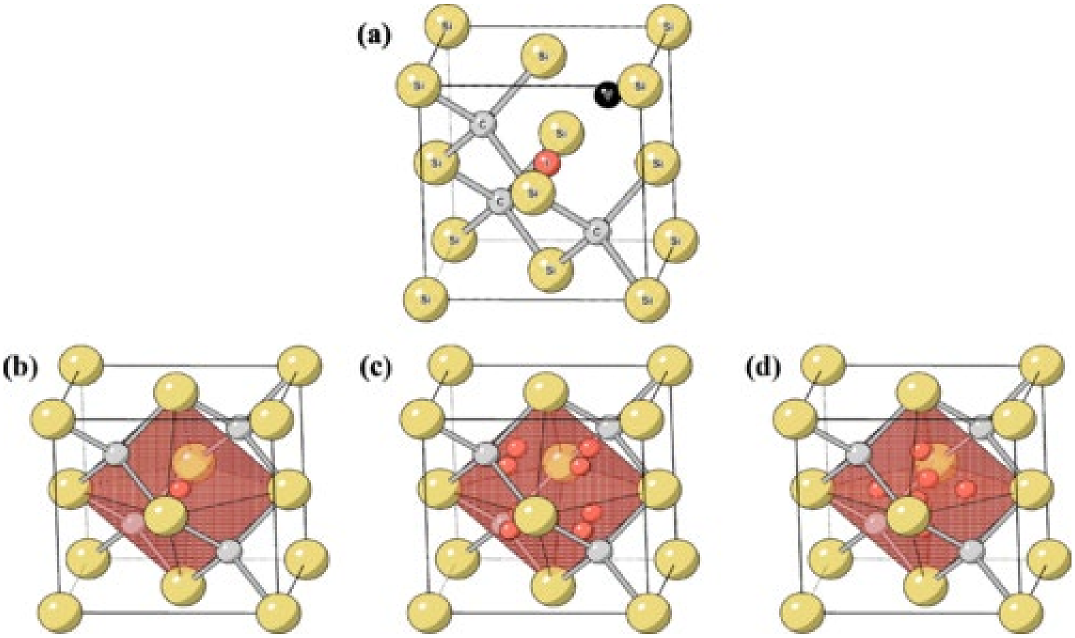

Figure 2. (a) Carbon Frenkel pair in 3C-SiC where the carbon interstitial sits on the 4b Wyckoff equipoint octahedral site. Silicon is gold spheres, carbon is gray spheres, and the interstitial and vacancy are represented by red and black spheres, respectively. Silicon octahedron with (b) carbon interstitial at the center 4b site, (c) with carbon interstitials in the octahedron faces at 16e sites along ⟨111⟩ directions, and (d) with carbon interstitials at 24f sites along ⟨100⟩ directions.

Conclusions

A mechanistic understanding of the radiation induced creep in SiC by coupling experiment and theory was successfully delivered under this task in SiC. These results, while benchmarked in SiC, will have relevance to other fusion relevant ceramic materials. We will also perform verification and validation of the defects formed and their evolution under fusion relevant irradiation conditions in SiC and other relevant ceramics. Additionally, we will couple the two-dimensional XRD results and microstructural defects quantifiable from XRD with accelerated molecular dynamics simulations to generate a realistic atomistic picture of the defect pathways that lead to radiation induced creep

Acknowledgments

These experiments and analyses were supported by the United States Department of Energy (DOE) Office of Fusion Energy Sciences under Contract No. DE-SC0018322 with the Research Foundation for the State University of New York at Stony Brook and No. DE-AC05-00OR22725 with UT Battelle, LLC. This paper was supported by the DOE, Office of Nuclear Energy under DOE Idaho Operations Office Contract No. DE-AC07-051D14517 as part of a Nuclear Science User Facilities experiment. Use of the NSLS-II, BNL, was supported by the DOE under Contract No. DE-SC0012704. The irradiation experiment was supported by DOE Office of Nuclear Energy, Advanced Fuel Campaign under Contract No. DE-AC05-00OR22725 with Oak Ridge National Laboratory (ORNL), managed by UT-Battelle, LLC. A portion of this research used resources at the High Flux Isotope Reactor (HFIR), a DOE Office of Science User Facility operated by ORNL.

References

[1] T. Koyanagi, D.J. Sprouster, L.L. Snead, Y. Katoh, X-ray characterization of anisotropic defect formation in SiC under irradiation with applied stress, Scripta Materialia 197 (2021) 113785.
[2] D.J. Sprouster, T. Koyanagi, D.L. Drey, Y. Katoh, L.L. Snead, Atomic and microstructural origins of stored energy release in neutron-irradiated silicon carbide, Physical Review Materials 5(10) (2021) 103601.

4. PLASMA-FACING AND HIGH HEAT FLUX MATERIALS AND COMPONENT TESTING

4.1 PROGRESS ON THE CHARACTERIZATION OF IRRADIATION DEFECTS IN TUNGSTEN HEAVY ALLOYS, THE ANALYSIS OF INTERPHASE BOUNDARY STRUCTURES, AND THE SYNTHESIS OF ROLLED TUNGSTEN HEAVY ALLOYS—J. V. Haag IV, M. J. Olszta, W. Jiang, W. Setyawan (Pacific Northwest National Laboratory)

OBJECTIVE

This report provides an incremental update on the status of ongoing irradiation damage characterization, interphase boundary analysis, and microstructural manipulation in tungsten heavy alloy systems.

SUMMARY

Multiple ongoing efforts are being made within Pacific Northwest National Laboratory (PNNL) to provide a broad-spectrum view of tungsten heavy alloy (WHA) materials and their proposed implementation in nuclear fusion reactors. This reporting period has seen multiple advancements in the areas of observing irradiation defect accumulation, the consideration of the underlying mechanisms behind interfacial strengthening, and the production of three additional thermo-mechanically processed WHA specimens. Major findings for this reporting period include the improvement of defect cavity visualization on WHA boundaries, the identification of structural semi-coherency at interphase boundary structures (the central focus of an upcoming manuscript nearing submission), and the production of a new batch of thermo-mechanically processed WHA specimens for future high-temperature mechanical testing and microstructural analysis.

PROGRESS AND STATUS

In the extension of characterizing radiation damage accumulation and distribution in WHA systems, an emphasis has been placed upon the visualization of cavities and precipitation on the interphase boundaries between the body-centered cubic (BCC) W and face-centered cubic (FCC) Ni-Fe-W phases. This has been done as the interphase boundaries in these materials are theorized to be responsible for the expression of the ductile phase toughening effect in WHA systems and loss of this boundary adhesion from defect segregation at these boundaries is expected to negatively affect material ductility. This segregation of cavities and precipitation at interphase boundary regions was identified in the previous reporting period [1] and further efforts have been made to characterize this boundary phenomena.

The analytical workflow for the identification and visualization of defects has improved since the previous reporting period through the implementation of through-focus rapid tilt series acquisition in a transmission electron microscope (TEM). This is a method by which the region of interest is incrementally imaged across an angular window with the collection of defocused images to allow for defect characterization through the observation of Fresnel fringes at cavity edges. This tilting process is described in Figure 1 with a schematic showing the manipulation of specimen orientation across a desired tilt range. When images are acquired sequentially across this range and then stitched together, a stereogram can be constructed which allows for a more intuitive visualization of the three-dimensional nature of cavity distribution in a TEM specimen. This method is described in greater detail in the work by Olszta in [2,3], and in this case has been purposefully applied after nanocartography mapping to avoid strong diffraction conditions in both grains of interest to minimize large swings in intensity from image to image. This is further expanded on in the acquisition of a through focus series at each orientation across the tilt range to provide sufficient contrast for the identification of defect cavities as shown in Figure 2. It should be noted that imaging in this way is more time consuming, but this sacrifice of acquisition time yields significantly improved interpretability. When taken together, tilt series acquisition utilizing image defocus allows for 3D observation of cavity distribution and deconvolution of features such as overlapping defects, leading to superior interpretability of defect morphology.

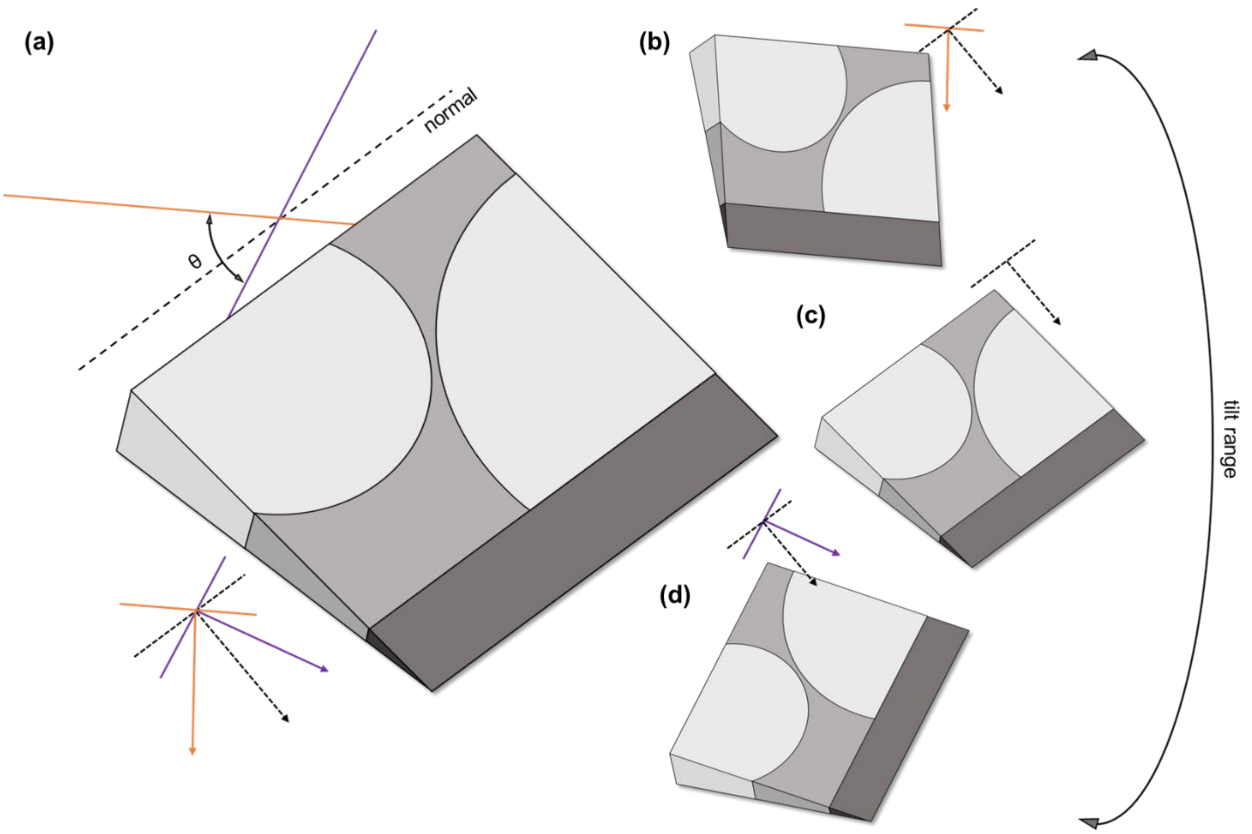

Figure 1. Schematic for the tilting of a focused ion beam (FIB) lift out specimen inside a TEM.

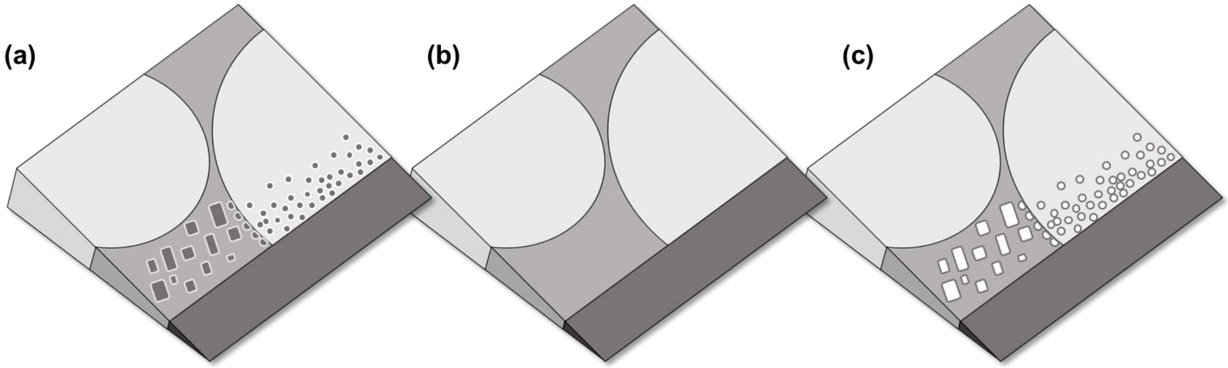

Figure 2. (a) over focus, (b) in focus, and (c) under focus schematics highlighting image contrast of defect cavities in a through focus series. Note the inversion of contrast in the cavities between (a) and (c) and the minimization of contrast for the in-focus condition (b).

While a full tilt series video cannot be adequately represented by one single image, a still frame from the under-focus tilt series of an ion irradiated WHA specimen has been provided in Figure 3. This specimen has been sequentially Ni and He ion irradiated to mimic five years of service in the Demonstration Power Plant (DEMO) fusion reactor. Details of the imposed conditions can be found in [1] but equate to approximately 27.3 dpa with 0.48 at.% He in W, and 30.6 dpa with 0.39 at.% He in the Ni-Fe-W phase. The ion irradiations were performed at 700 °C. The boundary between these phases was inclined with respect to the electron beam so that cavity distribution along the boundary can be observed. The dome like shape previously discussed in [1] is confirmed through tilt series acquisition, with a high density of intermediately sized defect cavities lying only on the Ni-Fe-W phase side of the boundary. The phenomena behind this one-sided cavity morphology are still being pursued but will be a contributing factor in the loss of adhesion at interphase boundaries over time through damage accumulation at the interphase boundary.

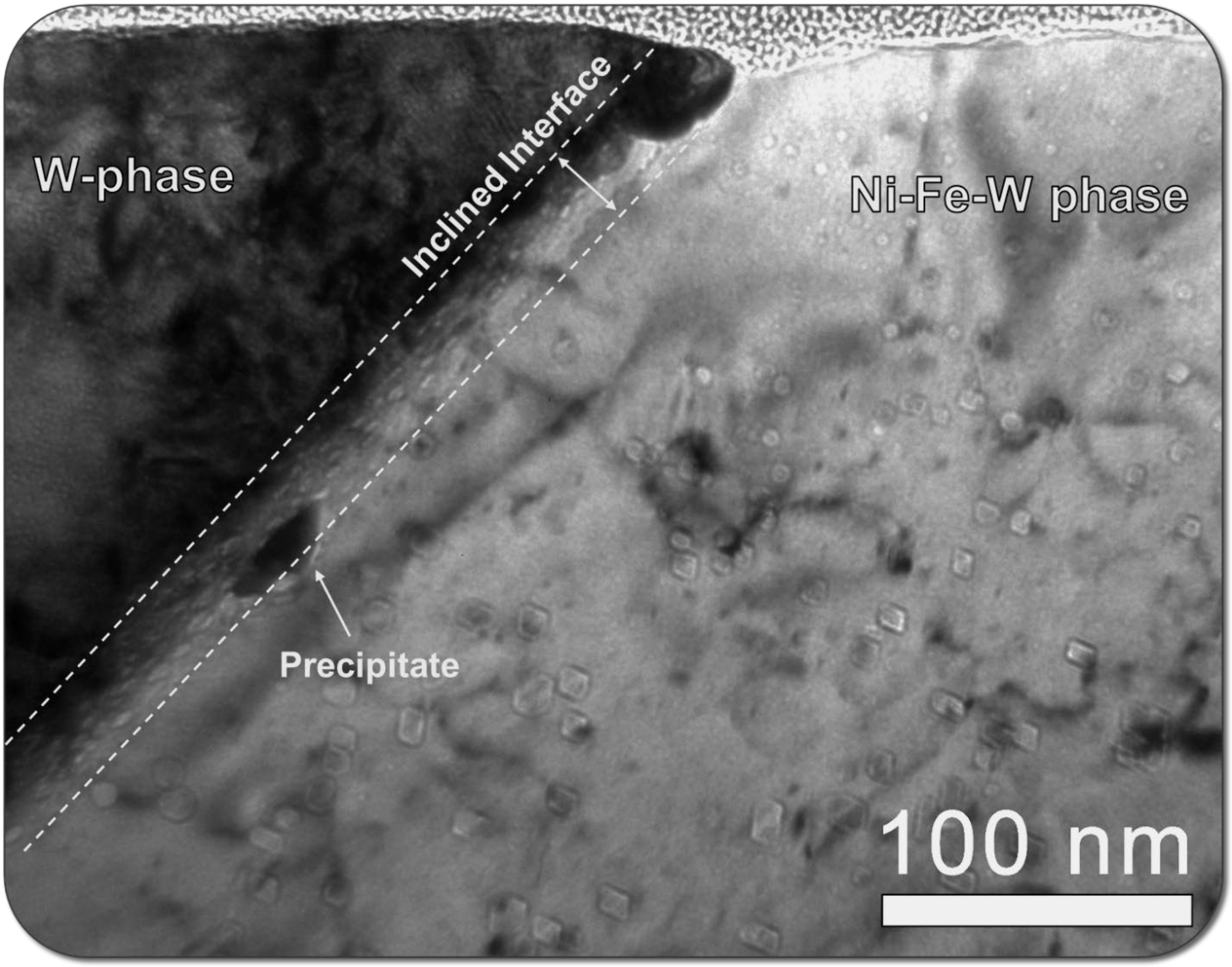

Figure 3. Under focus bright field TEM micrograph of interphase boundary of irradiated WHA acquired with a -1.5μm defocus. Interphase boundary has been inclined with respect to viewing direction to image cavities and precipitation sitting on the boundary plane.

An additional area of progress for this reporting period is in the analysis of interphase boundary structures in unirradiated WHA materials. Prior reporting periods [4] and a recent publication [5] on the role of interphase boundaries in the expression of ductile phase toughening has led to a need for atomic column analyses of the structure of these boundaries for eventual molecular dynamics (MD) and density functional theory (DFT) modelling of boundary cohesiveness. This consideration of structure is the primary focus of an upcoming manuscript which incorporates atomic column scanning transmission electron microscopy (STEM), STEM energy dispersive x-ray spectroscopy (EDS), and atom probe tomography (APT) to evaluate the atomic scale structure and chemistry of the specimen. This has been done to quantify the role of the structural and chemical nature of the boundary in its contribution to boundary energy and strength. In these analyses, boundaries such as the one shown in Figure 4 are mapped to derive the orientation relationship (OR) between the two grains. The interphase boundary in Figure 4 has been oriented edge-on to observe the structure of the boundary. At this imaging condition, the BCC W phase can be noted to be oriented to the [110] zone axis and the FCC Ni-Fe-W phase is oriented along the [001] zone axis. The boundary plane for W is approximately the $(5\,\bar{5}\,3)$ plane and the (110) plane for the Ni-Fe-W phase. These indexed planes and directions with respect to one another establish an OR of:

$$[110](5\,\bar{5}\,3)_{\mathrm{W}} \;//\; [001](110)_{\mathrm{Ni-Fe-W}}$$

This OR can then be constructed in a crystal visualization software such as VESTA to provide an experimentally based launch point for the computational modelling of WHA interphase boundaries. The hope therein being the revelation of contributing mechanisms to interphase boundary adhesion without the need for exhaustive TEM characterization and in-situ mechanical testing to observe behavior.

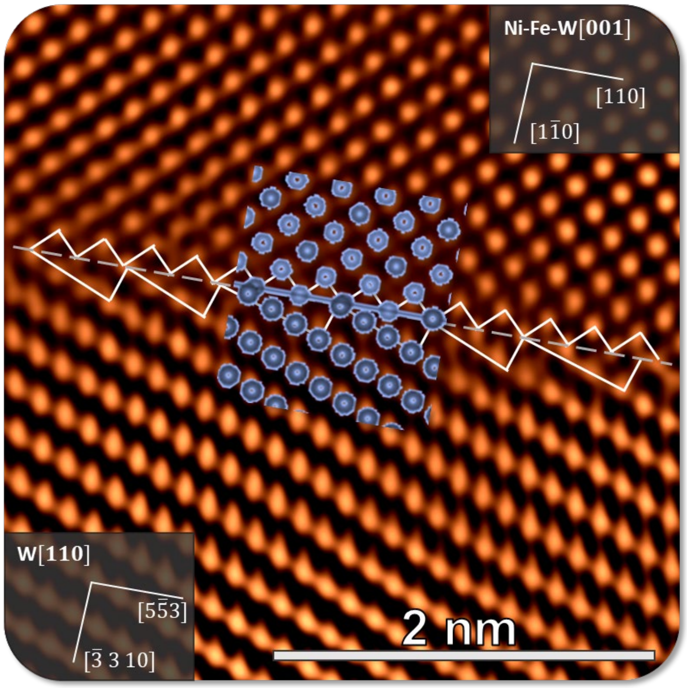

Figure 4. Atomic column STEM micrograph of an interphase boundary region between W and Ni-Fe-W phases. An inverse Fast Fourier Transform (FFT) has been applied to the micrograph to reduce noise. A VESTA model of the interphase boundary constructed from the indexed micrograph has been overlaid in blue.

In the production of new rolled WHA microstructures, a specimen of 90W, 7Ni, 3Fe (wt.%) purchased from MiTech Tungsten Metals, LLC was subjected to a series of uniaxial rolling reductions. Specimens were first equilibrated at 1150°C, rolled to approximately 10% relative reduction per pass, then reheated. After the first two rolling steps, specimens were then annealed at 1200°C for three hours in a hydrogen environment after first being purged with Ar. Each subsequent reduction was done with a 900°C preheat, 10% reduction, 1200°C Ar purge, and anneal in H_2 for three hours after each three reductions excepting the final reduction step in which four passes were made before a final anneal. Figure 5 provides an image of the instrumentation used to hot roll the specimens alongside images of the initial as-sintered specimens as well as the final hot rolled specimens. A table detailing the steps taken for the hot rolling and annealing process has been included below in Table 1.

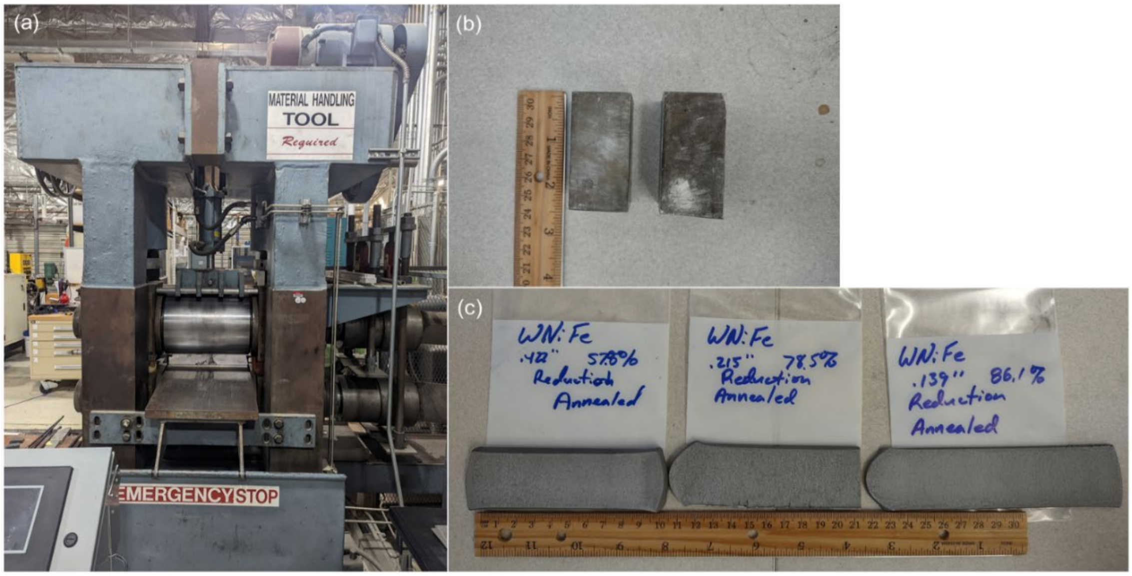

Figure 5. (a) Rolling mandrels for the hot rolling of WHA specimens. (b) two cut WHA specimens in their as-sintered state before hot rolling. (c) three different rolling reductions equating to 57.8%, 78.5%, and 86.1% total thickness reduction.

Table 1. Process to produce hot-rolled WHA specimens

Step	Reduction	Total Reduction	Temp. (C)	Time	Environment	Notes:
1	10.9%	10.9%	1150	-	Air	-
2	10.4%	20.2%	1150	-	Air	-
A1	-	20.6%	1200	3 hrs	Ar purge then H2	Descaled after annealing, measured once cooled and cleaned
3	9.6%	28.2%	900	-	Air	-
4	9.2%	34.8%	900	-	Air	-
5	9.8%	41.2%	900	-	Air	-
A2	-	41.6%	1200	3 hrs	Ar purge then H2	Descaled after annealing, measured once cooled and cleaned
6	9.6%	47.2%	900	-	Air	-
7	9.7%	52.3%	900	-	Air	-
8	10.7%	57.4%	900	-	Air	-
A3	-	57.8%	1200	3 hrs	Ar purge then H2	Saved specimen, descaled after annealing, measured once cooled and cleaned
9	10.0%	62.0%	900	-	Air	-
10	8.9%	65.4%	900	-	Air	-
11	10.1%	68.9%	900	-	Air	-
A4	-	70.0%	1200	3 hrs	Ar purge then H2	Descaled after annealing, measured once cooled and cleaned
12	9.0%	72.7%	900	-	Air	-
13	11.0%	75.7%	900	-	Air	-
14	8.6%	77.8%	900	-	Air	-
A5	-	78.5%	1200	3 hrs	Ar purge then H2	Specimen cut in half, half saved, half rolled again, descaled after annealing, measured once cooled and cleaned
15	10.7%	80.8%	900	-	Air	-
16	8.9%	82.5%	900	-	Air	-
17	11.4%	84.5%	900	-	Air	-
18	6.5%	85.5%	900	-	Air	-
A6	-	86.1%	1200	3 hrs	Ar purge then H2	Saved specimen, descaled after annealing, measured once cooled and cleaned
Degas	-	-	900	1 hr	Vacuum	Done for each of the three saved specimens (A3, A5, and A6)

For Table 1, rolling steps are numbered 1 through 18, and annealing steps have been denoted A1 through A6. Specimens were saved after steps A3, A5, and A6 equating to 57.8%, 78.5% and 86.1% reductions respectively.

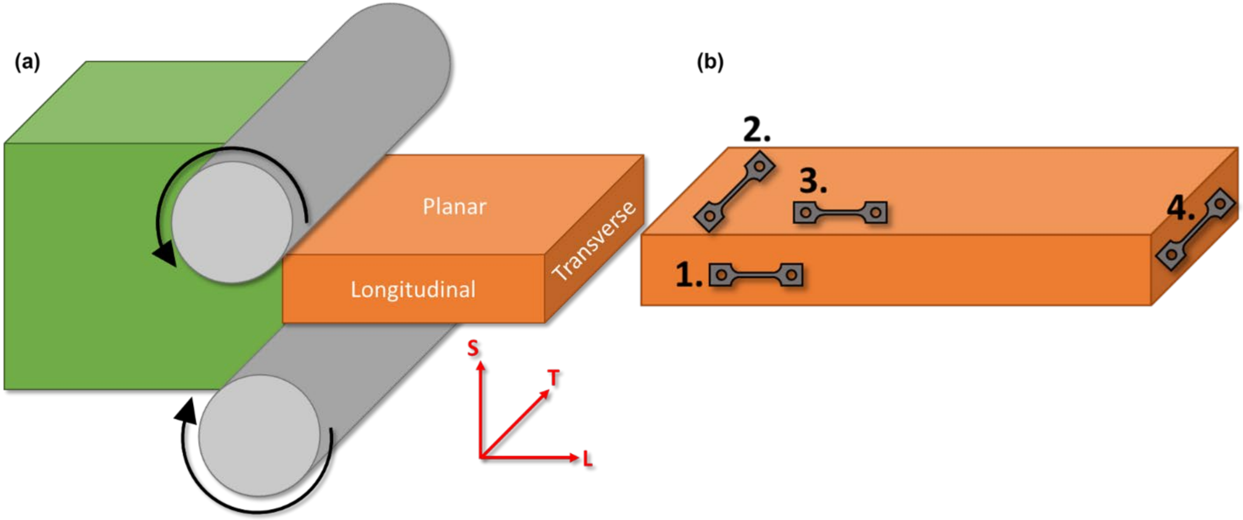

Figure 6. (a) schematic of the hot rolling process with green representing the material in its as-sintered state, and orange representing the rolled specimen. The orientations are denoted as longitudinal (L), transverse (T), and planar surface (S). (b) section of the rolled material showing the orientations for the fabrication of tensile specimens for future high temperature mechanical testing (1-4).

Once rolled, specimens were sectioned for surface analysis in a scanning electron microscope (SEM). Figure 6 has been included as a reference for the processing directions as it is imperative to retain the specimen orientation information due to the highly anisotropic nature of these bi-phase microstructures. The development of this microstructural anisotropy during the rolling process can be most easily seen in the longitudinal sections provided in Figure 7, with a clear elongation of W domains (bright phase) in the longitudinal (L) direction with a commensurate decrease in width along the surface planar (S) direction. From the initially spherical shape of these W domains in the as-sintered condition, the rolling of this material represents a gradual increase in the average aspect ratio of W domains with increasing thickness reduction.

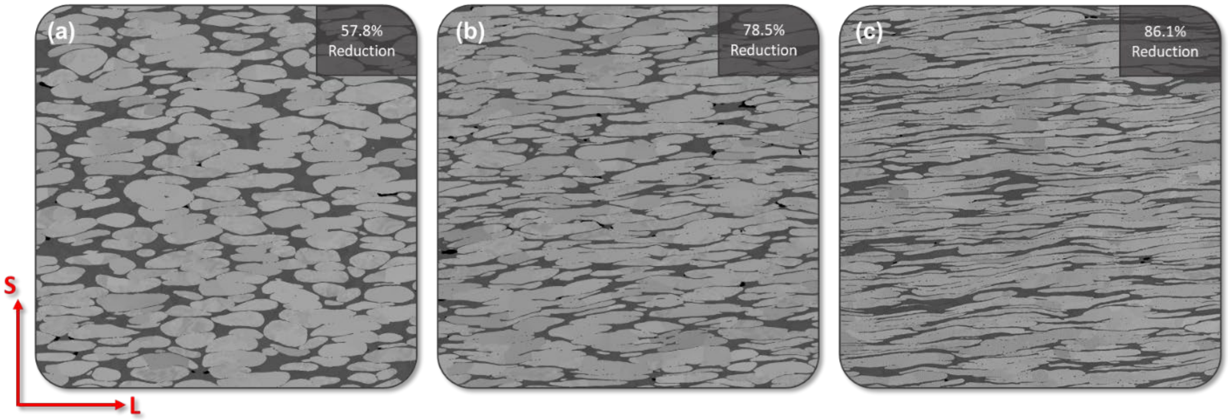

Figure 7. Backscattered SEM images of the longitudinal sections of rolled specimens from the 57.8% rolled specimen (a), the 78.5% rolled specimen (b), and the 86.1% rolled specimen (c).

In the upcoming reporting period these three rolling reduction specimens in addition to three different compositions of as-sintered specimens will be subjected to high temperature uniaxial tension testing and fracture toughness measurement. The goal therein being the analysis of the mechanical properties of these microstructures at elevated temperatures near the intended service temperature for these alloys. For each rolled specimen, four different orientations will be tested, shown in Figure 6b, as the morphological dispersion across the different orientations is expected to affect the mechanical properties of these materials. This magnitude of this effect is expected to increase with increasing temperature due to the softening of the lower melting temperature ductile phase, potentially causing a shift in the fracture behavior based on the contiguity of the W-phase. The proposed testing matrix for this work is anticipated to include six samples (90W-57.8%, 90W-78.5%, 90W-86.1% rolled samples in addition to as-sintered 90W, 95W and 97W samples) tested at three temperatures (room temperature, 590°C (representing 1/2 melting temperature of the ductile phase), and 880°C (2/3 melting temperature of the ductile phase)) and at multiple orientations across the rolled specimens. The generation of comparative data on the high temperature mechanical behavior of these alloys is essential in the prediction of their viability as plasma facing materials components, thus the upcoming experimental period will focus on the acquisition of these results.

Acknowledgements

This research was supported by the Office of Fusion Energy Sciences, United States Department of Energy and performed at PNNL under Contract DE-AC05-76RL01830. We are grateful to Zhihan Hu at Texas A&M University for ion irradiation.

References

[1] J.V. Haag IV, M. Murayama, M.J. Olszta, D.J. Edwards, W. Jiang, W. Setyawan, “Transmission electron microscopy analysis of a heavy ion irradiated tungsten heavy alloy,” DOE0313/71 (2021), pp. 98-104.

[2] M. Olszta and K. Fiedler, “Nanocartography in the Age of Automated TEM,” Microsc Microanal, vol. 26, no. S2, pp. 32–32, Aug. 2020, doi: 10/gnsfnj.

[3] M. Olszta, K. Fiedler, S. Spurgeon, S. Reehl, and D. Hopkins, “The role of Nanocartography in the Development of Automated TEM,” Microsc Microanal, vol. 27, no. S1, pp. 2986–2987, Aug. 2021, doi: 10/gnsfnk.

[4] J.V. Haag IV, M. Murayama, D.J. Edwards, J. Wang, W. Setyawan, “On the strength of interphase boundaries in a hot-rolled tungsten heavy alloy,” DOE0313/70 (2021), pp. 82-87.

[5] J.V. Haag, J. Wang, D. J. Edwards, W. Setyawan, and M. Murayama, “A boundary-based approach to the multiscale microstructural characterization of a W-Ni-Fe tungsten heavy alloy,” *Scripta Materialia*, vol. 213, p. 114587, May 2022, doi: 10.1016/j.scriptamat.2022.114587.

4.2 BEHAVIOR OF HELIUM CAVITIES IN ION-IRRADIATED W-Ni-Fe DUCTILE-PHASE TOUGHENED TUNGSTEN

W. Jiang, D. Zhang, D. Li, J. Heo, Z. Wang, L. Zhang, N. Overman, T. Varga, W. Setyawan (Pacific Northwest National Laboratory), Z. Hu, X. Wang, L. Shao (Texas A&M University)

This extended abstract presents some of the major results in a paper recently published in the Journal of Nuclear Materials 561 (2022) 153565 [1], https://doi.org/10.1016/j.jnucmat.2022.153565

This study reports on the distribution of helium (He) cavities in a hot rolled W-Ni-Fe ductile-phase-toughened tungsten (DPT W) composite irradiated to a dose and a helium concentration that are comparable to those in the material after 5-year irradiation in a conceptual fusion power plant.

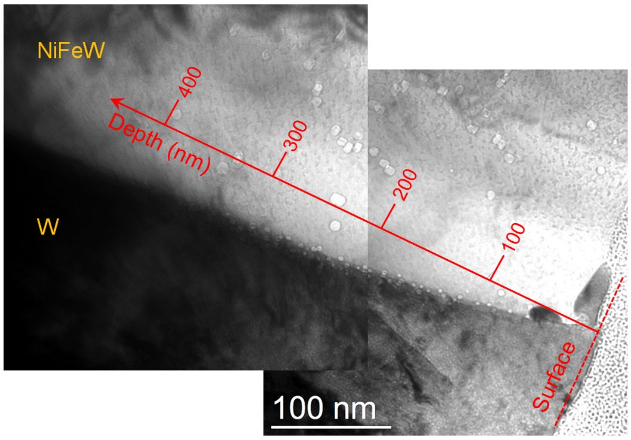

Figure 1. A general transmission electron microscope (TEM) view of the microstructure in the surface region of an 87R DPT W sample irradiated sequentially to 2.15×10^{16} Ni^+/cm^2 and 6.5×10^{15} He^+/cm^2 at 973 K.

Sequential irradiation of 87R DPT W with 1.2 MeV Ni^+ and 90 keV He^+ ions was performed to 2.15×10^{16} Ni^+/cm^2 and 6.5×10^{15} He^+/cm^2 at 973 K. A general view of the microstructure in the surface region of the sample is shown in Figure 1. Helium cavities are observed in W and NiFeW, and preferentially aggregated along their interphase boundary. The cavities in NiFeW are distributed mainly in the depth region from 200 to 300 nm. Compared to other regions, the cavities in the NiFeW region are the largest but their number density is the lowest. The different He cavity number densities and sizes in W and NiFeW phases reflect the efficiencies of nucleation and growth of He cavities in the two different materials, which may be generally associated with the production rates of mono-vacancies, He and vacancy diffusivities, and formation probabilities of stable He-vacancy clusters. The size of the He cavities along the W/NiFeW interphase boundary is between those in the two phases. The number density appears to be high, showing that the interphase boundary has a great strength of trapping vacancies and He atoms for aggregation of He cavities. In general, the cavity number density and cavity size depend on the defect mobility and trapping efficiency in the nucleation and growth processes.

Figure 2(a) shows an under-focus TEM image for W irradiated with Ni^+ and He^+ ions. The image center is located at the depth of ~100 nm with the surface direction indicated in the figure. A high density of small He cavities is observed. Each cavity in the imaged area is counted and its diameter of the first dark Fresnel ring is measured and corrected by the defocus value. The corrected cavity diameter and volume distributions are shown in Figure 2(b). The cavity number density is estimated to be 1.0×10^{18} cavities/cm^3. The measurement uncertainty for cavity diameters is ~0.2 nm in W and NiFeW and ~0.5 nm along the interphase boundaries in this study. Cavity number density is accurate to ~10% or larger. Similar data analyses were performed for the He cavities in W and along the interphase boundary. The results are summarized in Table 1. A lower number density (9.8×10^{15} cavities/cm^3) of larger He cavities (9.1 nm in diameter) in NiFeW than W (1.0×10^{18} cavities/cm^3 and 1.9 nm in diameter) is observed. There

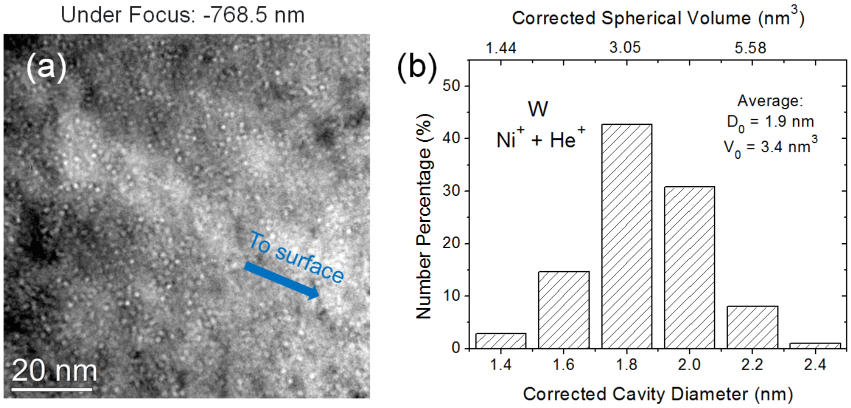

Figure 2. (a) TEM image showing a spatial distribution of He cavities at the image center depth of ~100 nm in the W phase within an 87R DPT W sample irradiated sequentially to 2.15×10^{16} Ni$^+$/cm^2 and 6.5×10^{15} He$^+$/cm^2 at 973 K. (b) Corrected He cavity diameter and volume distributions.

Table 1. Average inner diameter (D_{in}) of the first dark Fresnel ring, average corrected cavity diameter (D_0), average corrected cavity volume (V_0), and cavity number density in 87R DPT W irradiated with Ni$^+$ and He$^+$ ions at 973 K

Material	Depth (nm)	Under-focus (μm)	Cavity Number n	Ring D_{in} (nm)	Corr. Factor (D^i_{in})	Corr. D_0 (nm)	Corr. V_0 (nm^3)	Foil Thickness (nm)	Number Density (1/cm^3)
W	100	-0.7685	422	1.6	0.88	1.9	3.4	51.5	1.0×10^{18}
NiFeW	190	-0.7685	54	8.0	0.88	9.1	466	58.7	9.8×10^{15}
Boundary	160	-1.5	30	4.6	0.81	5.6	95.2	56.4	2.3×10^{17}

Both D_{in} and D_0 are subject to an uncertainty of ±0.2 nm in W or NiFeW and ±0.5 nm at boundaries. Cavity number density at the interphase boundary is estimated based on boundary thickness of $2D_0$. Cavity number density is subject to an uncertainty of up to ~10% or larger.

is a preferential distribution of medium-sized He cavities (5.6 nm in diameter) along the W/NiFeW interphase boundary. Formation of the He cavities is a result of either interaction between migrating vacancies and He atoms or trapping by existing defects in W and NiFeW during He$^+$ ion irradiation at 973 K. As significant simultaneous processes involving defect recovery and clustering in 87R DPT W during Ni$^+$ ion irradiation at 973 K are expected, dual beam irradiation with Ni$^+$ and He$^+$ ions might be able to better emulate high energy neutron irradiation in DPT W at elevated temperatures, where more mobile vacancies are available to interact with He atoms or He-vacancy defect clusters to potentially form larger He cavities and/or higher number densities. Aggregation of helium cavities formed along the interphase boundary can weaken the interfacial cohesion, which is largely responsible for the increase in the material brittleness. It remains to be investigated whether DPT W will behave differently at higher temperatures.

References

[1] W. Jiang, D.L. Zhang, D.S. Li, J. Heo, Z.Q. Wang, L.M. Zhang, N.R. Overman, T. Varga, Z.H. Hu, X.M. Wang, L. Shao, W. Setyawan, Journal of Nuclear Materials 561 (2022) 153565; https://doi.org/10.1016/j.jnucmat.2022.153565.

4.3 CONVERGENT-BEAM STEM AND STEM-EELS MAPPING OF HELIUM CAVITIES IN 87R DPT TUNGSTEN IRRADIATED WITH He$^+$ IONS AT 973 K

—W. Jiang, L. Kovarik, K. Kruska, W. Setyawan (Pacific Northwest National Laboratory)

OBJECTIVE

This work explores and applies methods to quantify helium density and pressure in He cavities and determine the size distribution of the cavities in He$^+$ ion irradiated ductile phase toughened tungsten.

SUMMARY

As a continuation of our ongoing efforts, we have further explored scanning transmission electron microscopy (STEM) and electron energy loss spectroscopy (EELS) methods to characterize the He cavities in a hot rolled, 87% thickness reduced, ductile-phase toughened tungsten (87R DPT W) composite (90W-7Ni-3Fe) irradiated with 90 keV He$^+$ ions to 1.0×10^{17} He$^+$/cm^2 at 973 K. Two separate focused ion beam (FIB) samples with very thin regions in NiFeW and W within the irradiated DPT W were prepared for this study. Convergent beam (CB) STEM has been applied successfully to image the He cavities at an atomic scale resolution. The depth profiles of the cavity size/volume and number density are measured. A quantitative analysis of the He atomic density and pressure in the cavities at sizes down to only ~1.5 nm has been achieved using STEM-EELS mapping. The He core loss peak in this study is dominated by He ionization (~24.59 eV) during high energy (300 keV) STEM-EELS rather than He 1s→2p transition.

PROGRESS AND STATUS

Introduction

As described in our previous report [1], we have been exploring CB-STEM and STEM-EELS methods to determine the characteristics and properties of He cavities in both W and NiFeW phases within He$^+$ ion irradiated 87R DPT W. In contrast to the conventional transmission electron microscopes (TEM) under a defocus condition [2,3], the CB-STEM method images the real size of cavities without needs for size correction. In addition, it can determine the cavity number density more accurately since CB-STEM imaging is performed over only an extremely thin slab of depth to minimize or avoid cavity image overlapping. The EELS method was originally proposed by Walsh, Yuan, and Brown [4] based on the scattering probability of an electron in a nanometer-sized He bubble:

$$\frac{I_{He}}{I_z} = exp\left(\frac{d}{\lambda_{He}}\right) - 1 \approx \frac{d}{\lambda_{He}} = \sigma n_{He} d \text{ or } n_{He} \approx \frac{I_{He}}{I_z \sigma d}, \text{ when } d \ll \lambda_{He}, \quad (1)$$

where n_{He} is the density of the He atoms, σ is the total cross-section for He 1s→2p transition, d is the bubble diameter, I_{He} and I_z are the integrated intensities of the He core-loss and zero loss peaks, respectively, and $\lambda_{He}(= 1/\sigma n_{He})$ is the mean free path for scattering in He gas. The pressure inside the bubble can be determined by a suitable equation of state (EOS). For an ideal gas (very low He density),

$$P = n_{He} k_B T, \quad (2)$$

where k_B is the Boltzmann constant and T is the temperature. Equation (2) and other formalisms based on the surface free energy [5] have been applied to calculate the pressure inside nanometer sized gas bubbles in various irradiated materials such as $Pd_{90}Pt_{10}$ alloy [6], martensitic steel [7], Si and Ge [8], Zr [9], and Be [10]. A more general EOS for rigid spheres has the following analytical form [11]:

$$P = n_{He} k_B T \frac{1+y+y^2-y^3}{(1-y)^3}, \; y = \frac{\pi n_{He} D^3}{6}, \quad (3)$$

where y is the volumetric fraction of gas and D is the rigid sphere diameter in the Brearley-MacInnes model [12]. More recently, the D value is determined [13] based on the Tang-Toennies potential:

$$D = 2.973[0.817 - 0.038\ln(T/10.985)], \tag{4}$$

where the units of D and T are in Å and K, respectively. Although there was an attempt to calculate the He bubble pressure in tungsten using molecular dynamic (MD) simulation [14], very few, if any, experimental reports have been published to date on the measurements of He atomic density and pressure in He bubbles in irradiated tungsten or its alloys. This experimental study uses the Walsh-Yuan-Brown [4] and Brutzel-Chartier [13] methods to determine the He density and pressure in He cavities in He⁺ ion irradiated 87R DPT W.

Experimental Procedure

SRIM Simulation, He⁺ Ion Irradiation, FIB Preparation, and Sample Characterizations

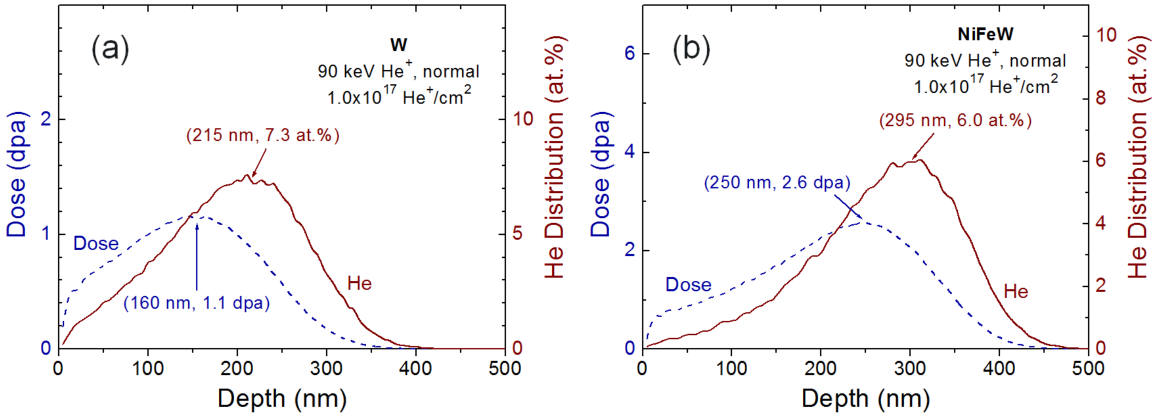

Figure 1. Depth profiles of the dose and He atomic percentage from a quick Kinchin-Pease SRIM13 simulation of 90 keV He⁺ irradiation in W and NiFeW to 1.0×10¹⁷ He⁺/cm².

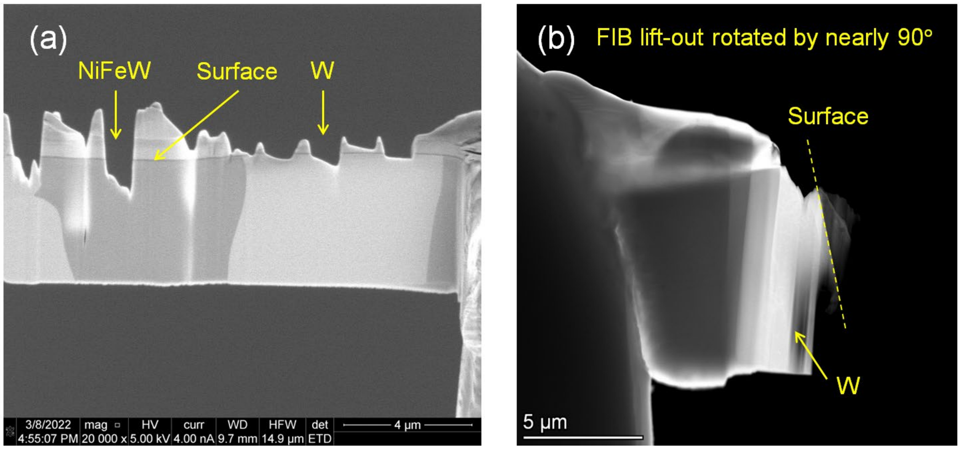

NiFeW FIB Sample W FIB Sample

Figure 2. FIB sample images for (a) NiFeW and (b) W in DPT W irradiated with 90 keV He⁺ ions to 1.0×10¹⁷ He⁺/cm² at 973 K.

A detailed description for SRIM13 (Stopping and Range of Ions in Matter, version 2013 [15]) simulation, material composition and He^+ ion irradiation in this study were reported in [1]. The simulation results for 1.0×10^{17} He^+/cm^2 in W and NiFeW are shown in Figure 1. The peak dose corresponds to 1.1 dpa at 160 nm in W and 2.6 dpa at 250 nm in NiFeW. The maximum He concentrations are 7.3 at.% at 215 nm and 6.0 at.% at 295 nm in W and NiFeW, respectively. Ion irradiation of the sample was performed with 90 keV He^+ ions at normal incidence to 1.0×10^{17} He^+/cm^2 at 973 K. The ion flux was 3.6×10^{12} $(He^{2+}/cm^2)/s$.

Two cross sectional TEM samples for W and NiFeW in the irradiated 87R DPT W were prepared using a Field Electron and Ion Company (FEI) Quanta dual beam FIB microscope. Figure 2(a) shows the microstructure of the FIB sample with a distinct contrast of W (white) and NiFeW (dark) phases. There is a very thin region in NiFeW, which is suitable for CB-STEM and STEM-EELS of He cavities. For W, an even thinner foil is required for characterization of the He cavities, which was not present in the sample [Figure 2(a)]. Additional FIB sample for W was prepared, as shown in Figure 2(b). To avoid removing surface during the thinning process, the FIB lamella was rotated nearly 90° and the thinning proceeded along a direction nearly parallel to the sample surface, as indicated in Figure 2(b).

The two FIB samples were examined using a Themis STEM from Thermo Fisher Scientific. High angle annular dark field (HAADF) CB-STEM and STEM-EELS mapping were performed at an accelerating voltage of 300 kV with a spatial resolution and a scan step of 0.1 and 0.2 nm, respectively. Compared to a lower electron energy, utilization of 300 keV electrons for STEM-EELS provides a number of advantages, including (1) minimum loss of He atoms in a cavity due to ballistic collisions [8] during repeated EELS measurements, (2) occurrence of only He ionization for the sizes of the He cavities in this study, instead of a complex combination of He excitations from 1s→2p and to higher excitation states, resulting in a convoluted He core loss peak, and (3) less stringent requirement for foil thickness.

Results

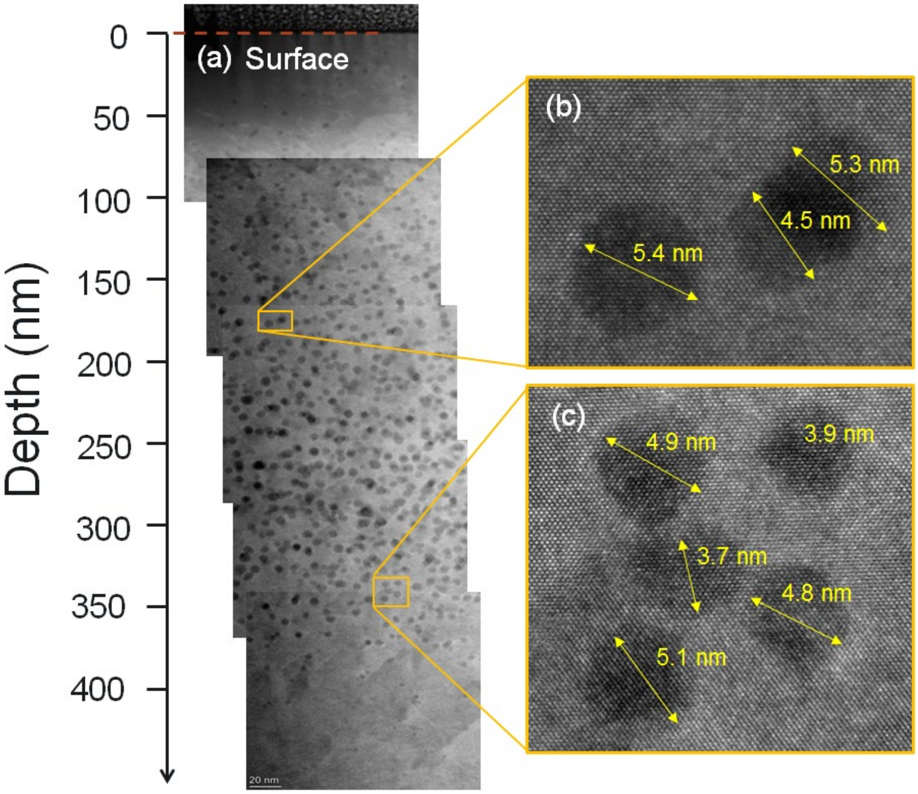

Figure 3. (a) stitched depth profile of He cavities in NiFeW within DPT W irradiated with 90 keV He^+ ions to 1.0×10^{17} He^+/cm^2 at 973 K and (b) and (c) zoomed-in HAADF STEM images showing atomic resolution for the He cavities near the He concentration peak and the profile end.

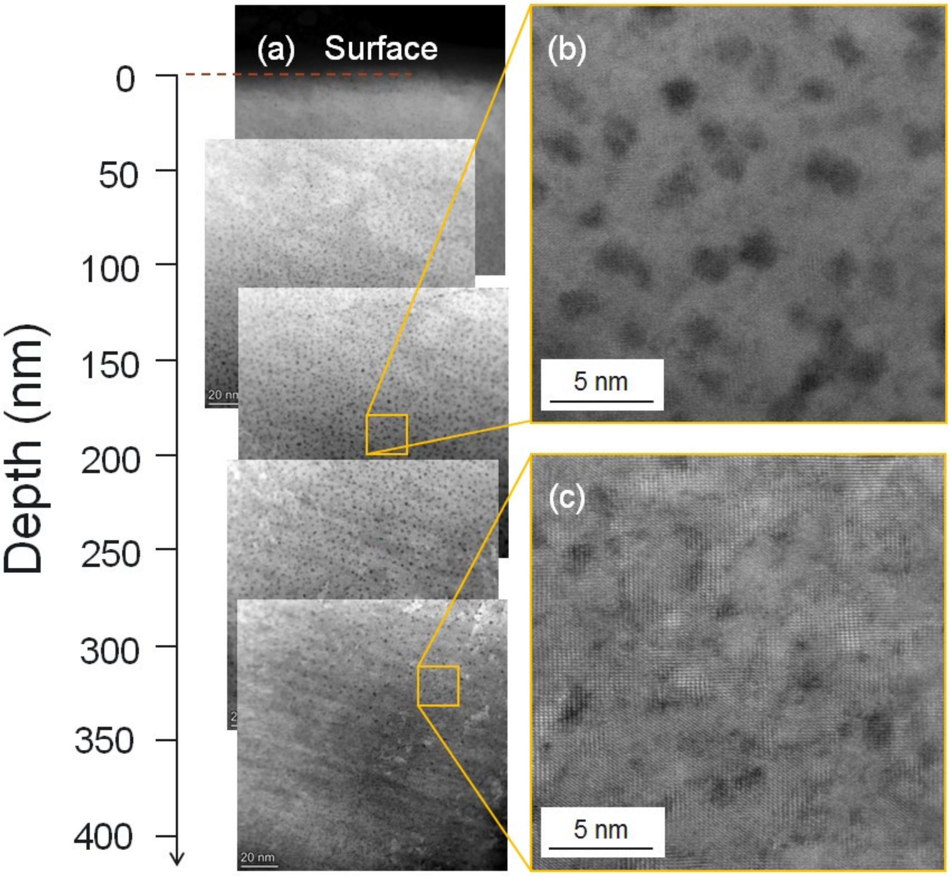

Figure 4. (a) stitched depth profile of He cavities in W within DPT W irradiated with 90 keV He^+ ions to 1.0×10^{17} He^+/cm^2 at 973 K and (b) and (c) zoomed-in HAADF STEM images showing atomic resolution for the He cavities near the He concentration peak and the profile end.

Figures 3(a) shows a stitched depth dependent high resolution HAADF CB-STEM image of He cavities in NiFeW within the irradiated DPT W. Figures 3(b) and 3(c) are the zoomed-in view of the images from the indicated areas in Figures 3(a). Under the focusing conditions, cavities are imaged in real size within the top region of TEM foil (tens of nanometers). The contrast is strongest for the cavities close to the top of the foil. Cavities are clearly visible, and the contrast is a result of the thickness difference, but not the Fresnel diffraction from a defocused beam. The He cavities show a darker contrast due to smaller thickness. Compared to imaging cavities in a thicker foil, e.g., 100 nm, using a conventional TEM under a defocus condition, the CB-STEM technique can reveal much smaller cavities in a thinner slab of depth. This can help count the cavity numbers more accurately and determine the number density with smaller errors. The cavity number density distribution as a function of depth is currently being analyzed. Clearly, the number density is lower in the surface region and near the end of the He concentration profile at the depth of ~450 nm, which is consistent with the Stopping and Range of Ions in Matter (SRIM) simulation result in Figure 1(b). The cavity size is on the order of 5.0 nm at ~200 nm and 4.5 nm at ~400 nm. The size distribution as a function of depth is being analyzed. The images in Figure 3 show a clear lattice structure at an atomic-scale resolution. Cavities imaged with CB-STEM in such an extremely high resolution have not yet been reported in the literature.

Similarly, Figure 4 shows a depth profile of the He cavities in W within the irradiated DPT W. Compared to NiFeW, the He concentration peak in W is slightly shallower, ending at the depth of ~400 nm. This result is also consistent with the SRIM prediction [Figure 1(a)]. The observed cavity size in W is generally

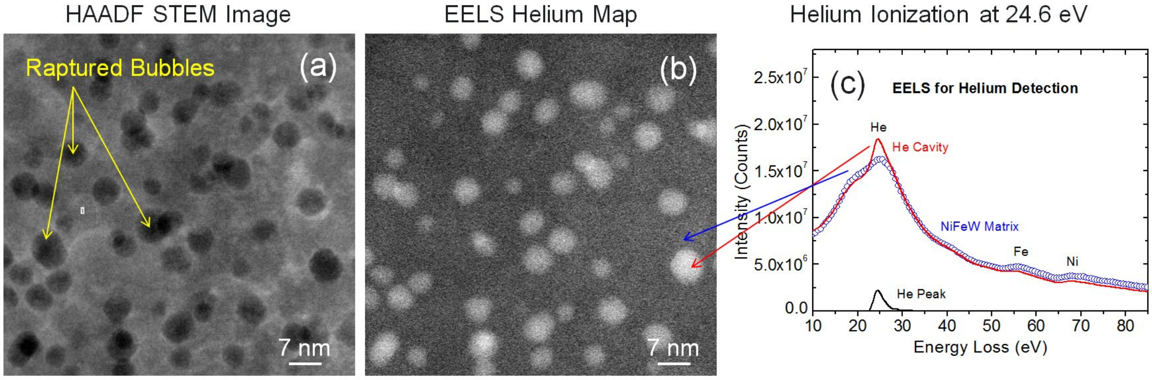

Figure 5. (a) HAADF STEM image showing He cavities and (b) STEM-EELS map showing He presence in the same region and (c) STEM-EELS spectra from two close-by areas with and without a He cavity in NiFeW within DPT W irradiated with 90 keV He^+ ions to 1.0×10^{17} He^+/cm^2 at 973 K.

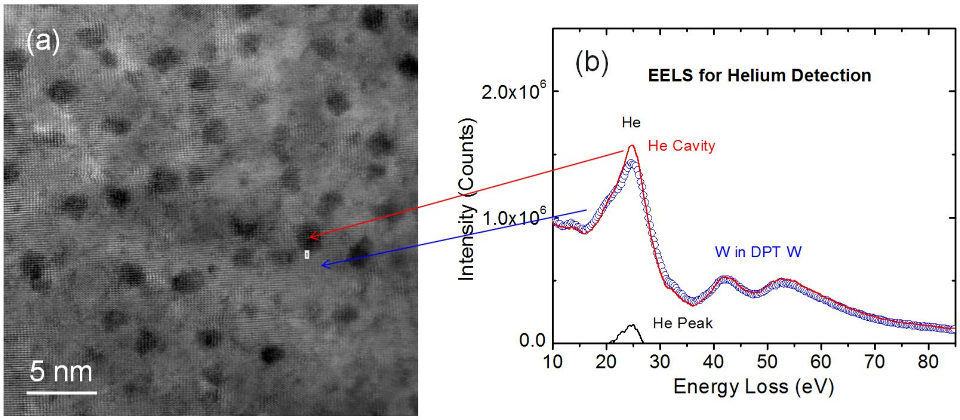

Figure 6. (a) HAADF STEM image showing He cavities and (b) STEM-EELS spectra from two close-by areas with and without a He cavity in W within DPT W irradiated with 90 keV He^+ ions to 1.0×10^{17} He^+/cm^2 at 973 K.

smaller than in NiFeW, in agreement with our previous reports [2,3]. Detailed analysis of the He cavity size distribution and number density as a function of depth is being performed.

Figure 5 shows a CB-STEM image, a STEM-EELS map and two EELS spectra from a He cavity and a neighboring area without a cavity in NiFeW. From Figures 5(a) and 5(b), some cavities in the CB-STEM image in Figure 5(a) are not visible in the STEM-EELS map in Figure 5(b), as indicated in Figure 5(a). Similar results were also reported at a lower spatial resolution [6,8]. The absence of the He cavities in the STEM-EELS map [Figure 5(b)] is a result of cavity rupture and He release from the cavities located near the cross-sectional surface during FIB preparation of the sample. Subtraction of the cavity spectrum from the matrix spectrum yields a difference spectrum, which is shown in Figure 5(c). The difference spectrum represents the He core loss spectrum that is peaked at ~24.9 eV, close to the He ionization energy (24.6 eV). The shift of a He peak from transition 1s→2p was observed and attributed entirely to the effects of He densities in a bubble [10]. While the density effect was clearly evidenced [8], the peak shifts only from 21.2 eV to 22.3 eV, but never to an energy loss of above 24 eV. Whether He excitation or ionization occurs depends on the electron velocity and the radial distance of He atoms to the electron track. The faster the electron and the closer the He atom to the electron pathway, the higher the probability of ionization of the He atom. For small He cavities with high energy electron irradiation, the whole He atoms encapsulated in it can be ionized. This is most likely the case of this study. Based on the intensities of the zero-loss peak and He core loss peak, the He density in the cavity can be estimated using the cross section of He ionization [Equation (1)]. The pressure in the bubble can be obtained from Equations (3) and (4). Estimations indicate that the He density and pressure in a 5 nm diameter He cavity in NiFeW is on the order of ~5×10^{28} at./m^3 and ~0.6 GPa at 300 K, respectively. More accurate data analysis is currently being performed as a function of cavity size and depth.

Similar results were obtained for He cavities in W, as shown in Figure 6. Figure 6(a) shows a STEM-EELS map, where He cavities as small as ~1.5 nm in size can be clearly observed. Again, a He peak is obtained from the difference in the EELS spectra from a He cavity and a neighboring area without a cavity. The He peak is also located at ~24.9 eV because He ionization. Similar data analysis is being performed. Total He retentions in NiFeW and W will be estimated, and their difference will be compared to DFT calculations.

Conclusion

Detailed analysis of the CB-STEM and STEM-EELS data is being performed. The experimental results will be presented at the TMS 2023 meeting. A manuscript based on the results will be prepared for publication. Further efforts will be focused on the study of high temperature effects on the He cavity characteristics and properties, including cavity size, He density and cavity distribution along the interphase boundary in ion irradiated DPT W.

Acknowledgements

This research was supported by the Office of Fusion Energy Sciences, United States Department of Energy and performed at Pacific Northwest National Laboratory (PNNL) under Contract DE-AC05-76RL01830. We are grateful to Charles Henager at PNNL for providing the 87R DPT W sample and to Zhihan Hu at Texas A&M University (TAMU) for ion irradiation.

References

[1] W. Jiang, L. Kovarik, K. Kruska, W. Setyawan, Fusion Materials Semiannual Progress Report for Period Ending December 31, 2021, DOE/ER-0313/71, U.S. Department of Energy, 105.

[2] W. Jiang, *et al*. J. Nucl. Mater. 550 (2021) 152905.

[3] W. Jiang, *et al*. J. Nucl. Mater. 561 (2022) 153565.

[4] C.A. Walsh, J. Yuan, L.M. Brown, Philos. Mag. A 80 (2000) 1507.

[5] H. Trinkaus, B.N. Singh, J. Nucl. Mater. 323 (2003) 229.

[6] D. Taverna, *et al*. Phys. Rev. Lett. 100 (2008) 035301.

[7] S. Fréchard, *et al*. J. Nucl. Mater. 393 (2009) 102.

[8] M.-L. David, *et al*. J. Appl. Phys. 115 (2014) 123508.

[9] M.S. Blackmur, *et al*. Scripta Mater. 152 (2018) 102.

[10] M. Klimenkov, *et al*. Micron 127 (2019) 102754.

[11] E. Thiele, J. Chem. Phys. 39 (1963) 474; M.S. Wertheim, Phys. Rev. Letters 10 (1963) E501; M.S. Wertheim, J. Math. Phys. 5 (1964) 643.

[12] I.R. Brearley, D.A. MacInnes, J. Nucl. Mater. 95 (1980) 239.

[13] L. Van Brutzel, A. Chartier, J. Nucl. Mater. 518 (2019) 431.

[14] J. Cui, M. Li, J. Wang, Q. Hou, Nucl. Instr. Meth. Phys. Res. B 352 (2015) 104.

[15] J.F. Ziegler, J.P. Biearsack, U. Littmark, *The stopping and Range of Ions in Solids* (Pergamon Press, New York, 1985); available at: http://www.SRIM.org/.

4.4 STATUS OF THE ELEVATED TEMPERATURE MECHANICAL TEST FACILITY SETUP AT PNNL

—R. Prabhakaran, C. H. Henager, W. Setyawan (Pacific Northwest National Laboratory)

OBJECTIVE

The objective of this task is to setup an elevated temperature mechanical test facility at Pacific Northwest National Laboratory (PNNL) and design appropriate fixtures so that various types of mechanical testing (tensile, bend, fracture toughness) could be performed in order to understand the mechanical behavior of ductile phase toughened tungsten heavy alloys, such as W-NiFe, for applications in fusion reactor divertor and plasma facing components.

SUMMARY

This report summarizes the progress in the elevated temperature mechanical test facility setup (furnace, utility connections and test frame) at PNNL and designing of various mechanical test fixtures to perform tensile, bend and fracture toughness testing of ductile phase toughened (DPT) W-NiFe alloys.

PROGRESS AND STATUS

Introduction

The DPT process is a fracture toughness improvement concept being utilized to develop tungsten based composites for fusion reactor divertor and plasma facing materials. Tungsten (W) is a promising candidate material for fusion reactor component applications due to its excellent high temperature strength, low sputtering rate, and high melting temperature.[1-2] However, the potential application of tungsten as a structural material is limited due to its low ductility that could further degrade after irradiation.[3] Hence, introducing a ductile phase for developing a tungsten composite could serve as an alternative route to overcome its limitations.

Previous mechanical tests have been performed at room temperature using an Instron 5582 servo-mechanical test frame equipped with an Epsilon ONE optical extensometer and the results could be found in our previous reports.[4-6] Currently, efforts are ongoing to understand the mechanical behavior of DPT W-NiFe alloys at elevated temperatures (upto 1200-1300°C) and this report is focused in documenting the current status of the elevated temperature mechanical test facility setup at PNNL.

Experimental Procedure

Elevated Temperature Mechanical Test Facility Setup

Instron 8801 servohydraulic mechanical test system

The Instron 8801 is a compact servohydraulic fatigue testing system that could be employed for performing static and dynamic mechanical testing. This frame has been utilized for testing a number of materials at ambient and elevated temperatures (600°C) using a Mellen clamshell furnace that can purged with argon gas (to minimize oxidation). This system has both Bluehill Universal and WaveMatrix software for performing axial static and dynamics tests. Additional information about this test frame can be found in the previous report.[7]

MRF Model M-4x6-M-1600-V&G Furnace

The PNNL has an Materials Research Furnaces, Inc.(MRF) Model M-4x6-M-1600-V&G front loading furnace with a usable work zone of 3.5" dia. x 4.0" high, and a maximum operating temperature of 1600°C. The hot zone is a 180° split design with tungsten mesh heating elements for operation in vacuum (50-100 milliTORR) and inert gas (Ar, N_2, or Ar/O_2 gas mixture). Additional information about this furnace can be found in the previous report.[7]

This furnace was purchased several decades ago, and it was not used for a long time. Recently, efforts were made to replace multiple components such as tungsten mesh heating elements, water cooled power cords, water lines, argon lines, water sensor and vacuum gage. The MRF furnace requires the following power: 23 kVA, 480V/1ph/60 Hz. 60 Amps (maximum). Hence, substantial modification to the existing power outlet in the lab was made to operate this furnace. Argon gas lines (2 CFM/56 LPM and 30 psig inlet pressure) were connected to the furnace through gas flowmeters.

The MRF furnace needs water at the rate of 4 GPM @ 70°F and 50-60 psig (max). A water flow meter was recently purchased and connected to the furnace. The water lines were connected to the building's chilling water supply. Earlier, the water flow rate was only about 2 GPM (due to nearby lab's test setup requirements and longer travel distance) and permission was obtained to install a small pump in the lab to get the required flow rate. By using the water pump, the furnace obtained the required flow rate of 4 GPM @ 70°F. The functioning of the water sensor (that could be set to the required gpm) that acts as a safety switch (to shut off the furnace in the event of water loss) was checked by manually reducing the flow rate and turning off the water supply.

After demonstrating the furnace's safety features, necessary approvals were obtained from various subject matter experts (SMEs), in order to turn on the furnace and check its heating elements. Initially, the furnace console power turned on but the hot zone mode could not be turned on. The electrician had to open the panel and make the necessary changes to turn on the hot zone mode. The roughing pump connected to the furnace was turned on and it was able to achieve < 50 milliTorr at the room temperature depending upon the duration of its operation. Currently, efforts are ongoing to test the furnace at different temperatures slowly and record the vacuum levels.

Figure 1 shows the photographs of the high-temperature furnace (exterior and interior) along with Instron 8801 mechanical test frame.

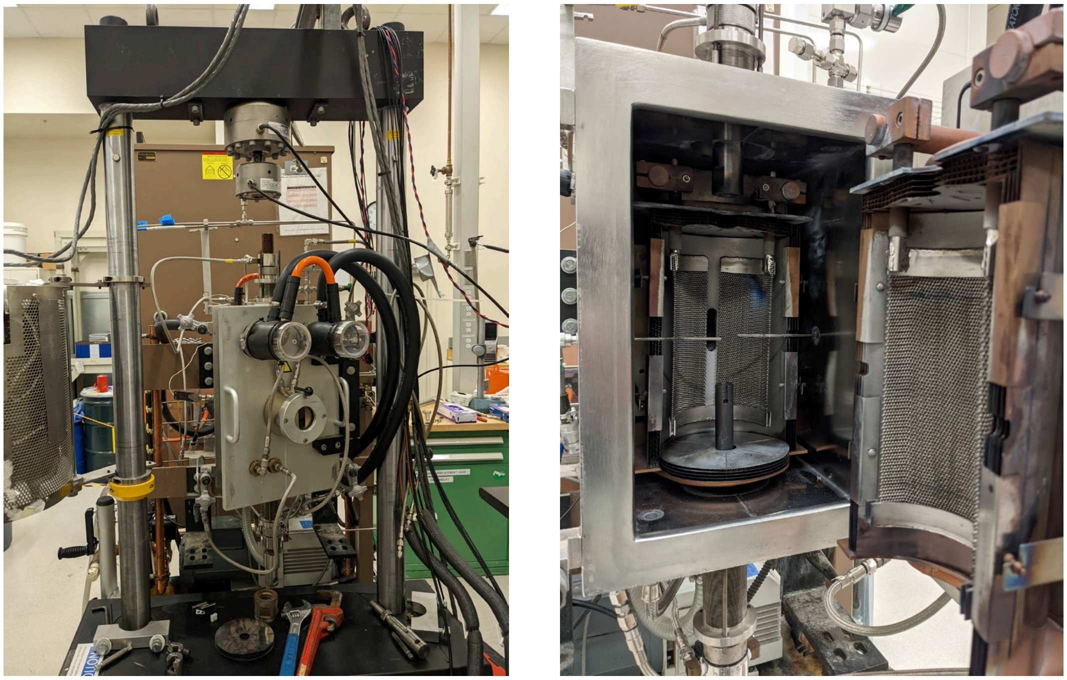

Figure 1. MRF furnace (1600°C) along with Instron 8801 mechanical test frame.

Tensile specimen and test fixture

Previous ambient temperature tensile testing was performed using age hardened Inconel 718 fixture (using the shoulder loaded design), as shown in Figure 2. The sub-size tensile specimens (see Figure 2) were shoulder loaded instead of pin loaded to avoid tear out at the pin hole as well as warping of the pins. The yield strength of DPT W-NiFe alloys at room temperature are shown in Figure 3.[8] A similar age hardened Inconel 718 fixture has been employed successfully to test irradiated samples in the PNNL hot cell using manipulators at 430°C. This fixture would be sufficient to perform intermediate temperature (590°C, which is 1/2 melting temperature of the ductile phase) tensile testing of sub-size tensile specimens.

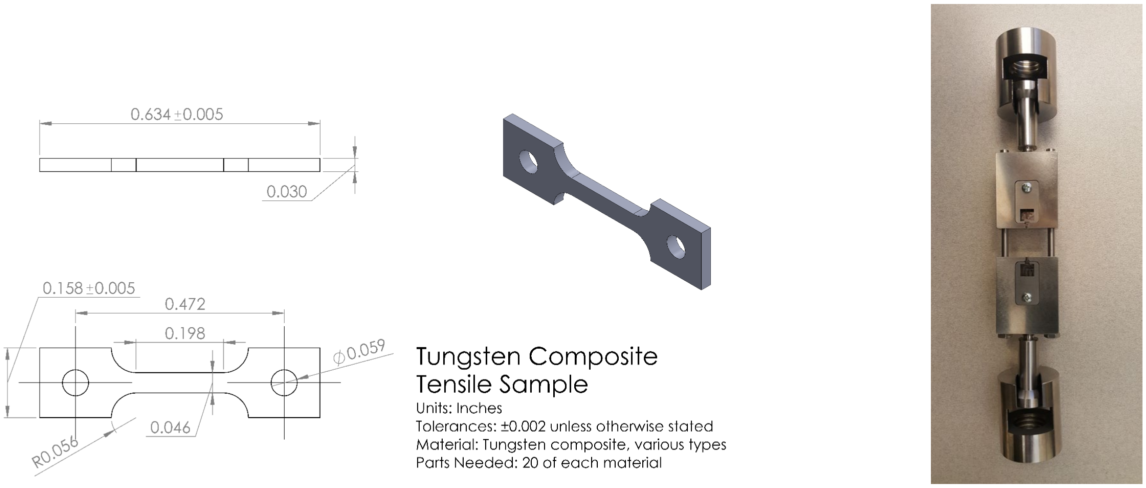

Figure 2. Tensile specimen geometry (left) and shoulder loaded tensile fixture (right).

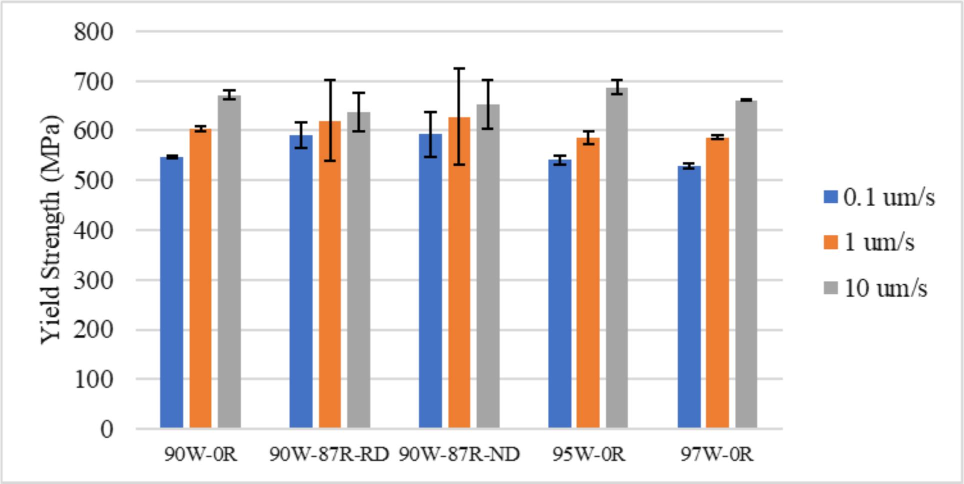

Figure 3. Ambient temperarture mechanical properties of DPT W-NiFe alloys [8].

Other researchers have studied liquid phase sintered 90W-7Ni-3Fe alloy by performing tensile testing at room temperature, and Gleeble 3800 thermal simulation test machine (with 10^{-2} Pa or 7.5 E-5 Torr vacuum) was employed to obtain mechanical properties at elevated temperatures (200-1200°C) [9]. Their results showed that the mechanical properties of the alloy were highly sensitive to temperature and decreased with increasing temperature in most cases [9]. The Gleeble system uses direct resistance heating system to heat the specimen directly (through a wire). There is a big temperature gradient as we move away from the center. The water cooled grips at the ends will not see higher temperature and typically made of stainless steel, as per the vendor.

Efforts are also ongoing to perform tensile testing of DPT W-NiFe (as-sintered and rolled) at around 880°C (2/3 melting temperature of the ductile phase) and slightly higher (1000-1200°C). In our case, the MRF furnace has a usable work zone of 3.5" dia. x 4.0" high. We have water cooled pull rods (17-4 PH stainless steel) on either side of the furnace, and we need a tensile fixture that can withstand elevated temperatures without any water cooling. The SiC fixtures can perform well at these elevated temperatures (>1000°C), however, the cost of machining is high and durability is low, especially under tensile loading. For this Fiscal Year (FY), the goal is to identify a metallic material and fixture design that would allow to utilize the furnace and perform tensile testing at the maximum possible operating temperature (based on a metallic fixture).

Extensive research was performed by looking at the literature and communicating with various mechanical test equipment vendors in order to identify a suitable metallic fixture material. The following materials were considered for this application.

Materials

UDIMET alloy 720

The UDIMET alloy 720 is a nickel base alloy, solid solution strengthened with tungsten and molybdenum and precipitation hardened with titanium and aluminum. The alloy combines high strength with metallurgical stability as demonstrated by excellent impact strength retention after long exposures at elevated temperatures. Good oxidation and corrosion resistance combined with high strength make the alloy useful in gas turbine blade and disc applications [10].

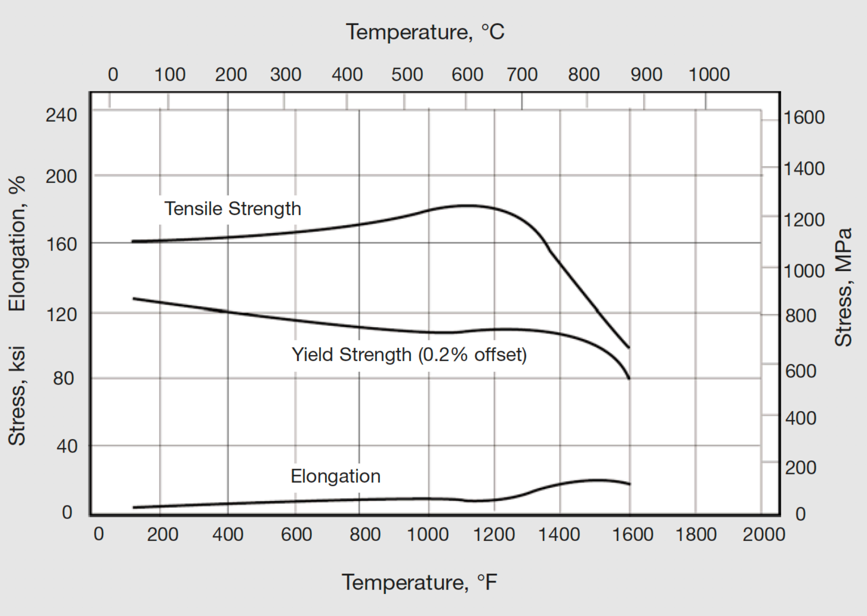

Figure 4. Typical mechanical properties of precipitation hardened UDIMET alloy 720, as per Special Metals Corporation datasheet [10].

MAR-M247

The MAR-M247 is a typical polycrystalline nickel based superalloy applied in investment casting which was developed by Danesi and Lund et al. at the Martin company in the 1970s. Its optimal alloy design and microstructural control make the MAR-M247 superalloy highly castable and very strong in high temperature.[11] The mechanical properties of Mar-M247 at room temperature (yield strength about 125 ksi/861 MPa) and elevated temperature (1037°C; yield strength about 40 ksi/275 MPa) is shown in the Table 1 [12].

Table 1. Mechanical properties of MAR-M247 at different temperatures [12].

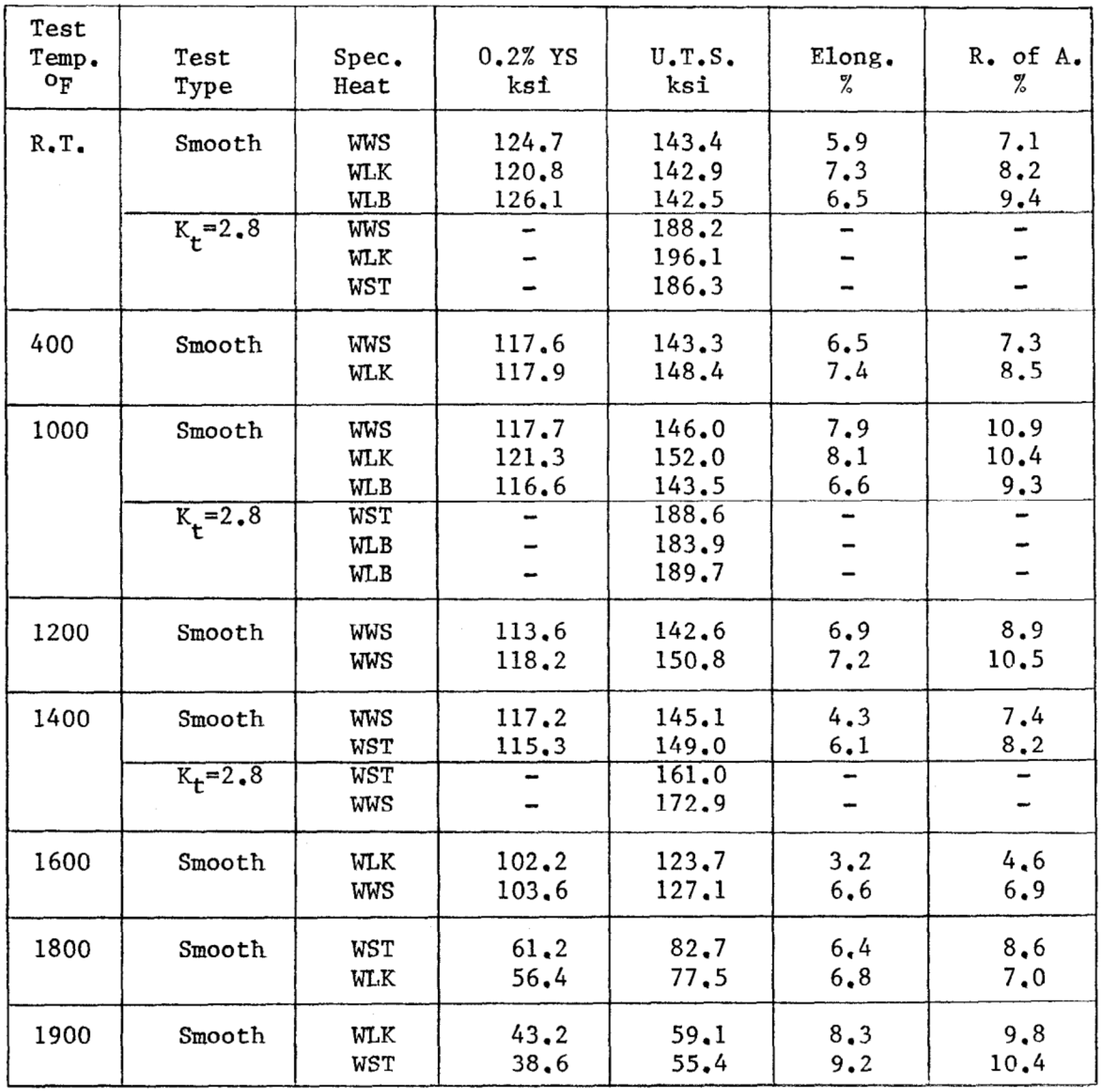

Test Temp. °F	Test Type	Spec. Heat	0.2% YS ksi	U.T.S. ksi	Elong. %	R. of A. %
R.T.	Smooth	WWS	124.7	143.4	5.9	7.1
		WLK	120.8	142.9	7.3	8.2
		WLB	126.1	142.5	6.5	9.4
	K_t=2.8	WWS	-	188.2	-	-
		WLK	-	196.1	-	-
		WST	-	186.3	-	-
400	Smooth	WWS	117.6	143.3	6.5	7.3
		WLK	117.9	148.4	7.4	8.5
1000	Smooth	WWS	117.7	146.0	7.9	10.9
		WLK	121.3	152.0	8.1	10.4
		WLB	116.6	143.5	6.6	9.3
	K_t=2.8	WST	-	188.6	-	-
		WLB	-	183.9	-	-
		WLB	-	189.7	-	-
1200	Smooth	WWS	113.6	142.6	6.9	8.9
		WWS	118.2	150.8	7.2	10.5
1400	Smooth	WWS	117.2	145.1	4.3	7.4
		WST	115.3	149.0	6.1	8.2
	K_t=2.8	WST	-	161.0	-	-
		WWS	-	172.9	-	-
1600	Smooth	WLK	102.2	123.7	3.2	4.6
		WWS	103.6	127.1	6.6	6.9
1800	Smooth	WST	61.2	82.7	6.4	8.6
		WLK	56.4	77.5	6.8	7.0
1900	Smooth	WLK	43.2	59.1	8.3	9.8
		WST	38.6	55.4	9.2	10.4

TZM

The TZM an acronym for the molybdenum alloy “titanium-zirconium-molybdenum”, is a molybdenum alloy containing 0.5% titanium, 0.08% zirconium, 0.02% carbon and the balance molybdenum. The TZM, like pure molybdenum, can be produced by powder metallurgy or arc-cast processes. Additionally, TZM has a higher recrystallization temperature than pure molybdenum, thus reduces the likelihood of embrittlement at higher temperatures; and in elevated temperature applications, TZM’s higher strength, hardness, creep resistance and ductility insures it will not weaken or soften [13].

As per the vendor (Rembar) the recommended temperatures for using TZM is between 700 and 1400°C.[13] However, like pure molybdenum, TZM begins to oxidize at 400°C and oxides rapidly in oxidizing atmospheres above 500°C. Similar in strength to pure molybdenum at room temperatures, at operating temperatures exceeding the recrystallization temperature of pure molybdenum (900 to 1100°C), TZM is much stronger. And in load bearing applications exceeding 1300°C, TZM is twice as strong as pure molybdenum, as shown in the Figure 5 [13].

Based upon material availability, machinability, cost and mechanical properties at elevated temperatures, TZM was chosen as the fixture material. Currently efforts are ongoing to fabricate tensile fixture using TZM and was expected to be complete by the middle of August 2022.

Sub-size tensile specimens for testing at various temperatures (room temperature to 1200°C) are also being machined using electrical discharge machining (EDM). Once the specimen and elevated temperature fixture fabrication is complete, we will begin the elevated temperature tensile testing.

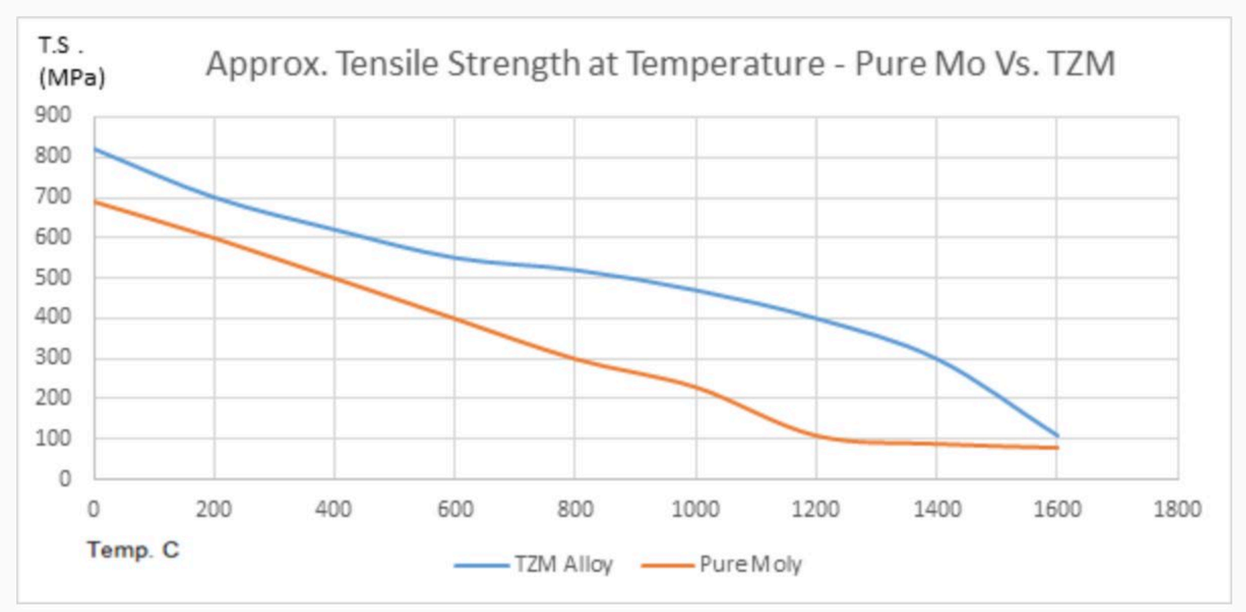

Figure 5. Tensile strength of TZM and pure Mo at various temperatures [13].

Bend test specimen and test fixture

The PNNL has several three and four point bend test fixtures. Figure 6 shows two types of four point bend test fixtures: (a) SiC fixture for testing at elevated temperatures (over 1000°C) and (b) Inconel or Hasteloy-X fixture that uses SiC pins for load transfer. Currently, efforts are ongoing to determine the type of metallic alloy by referring the old records.

In the past, different types of specimens were employed by various fusion materials researchers for a number of studies:

- The W-Cu composite was machined into 3.30-mm × 1.67-mm × 16.05-mm single-edge notched bend (SENB) specimens and as-sintered W-Ni-Fe alloy was machined into 4-mm × 3-mm × 20-mm bend bars and three-point bend tests were conducted [14].
- Four point SENB specimens measuring 25.4-mm × 1.75-mm × 4.0-mm were cut from pieces of hot rolled W-Ni-Fe materials [15].
- Room temperature fracture toughness tests were conducted on the small, fatigue pre-cracked, single edge notch bend bar specimens with a nominal length (L) x width (W) x thickness (B) dimensions of 25.4-mm × 4.0-mm × 1.75-mm [16]. Researchers at University of California, Santa Barbara(UCSB) expressed interest in sending samples to PNNL so that elevated temperature fracture toughness testing could be performed.

The PNNL researchers have also employed an Inconel 718 fixture (see Figure 7) for three point bend testing of notched stainless steel samples (13 mm x 5 mm x 3 mm). In the future, TZM will be used to fabricate a similar bend testing fixture for elevated temperature testing (upto 1200°C). Recently, efforts were made to modify the Inconel 718 fixture to accommodate four point bend testing of unnotched bars for a different project. This modified fixture design could also be employed for the fusion materials program.

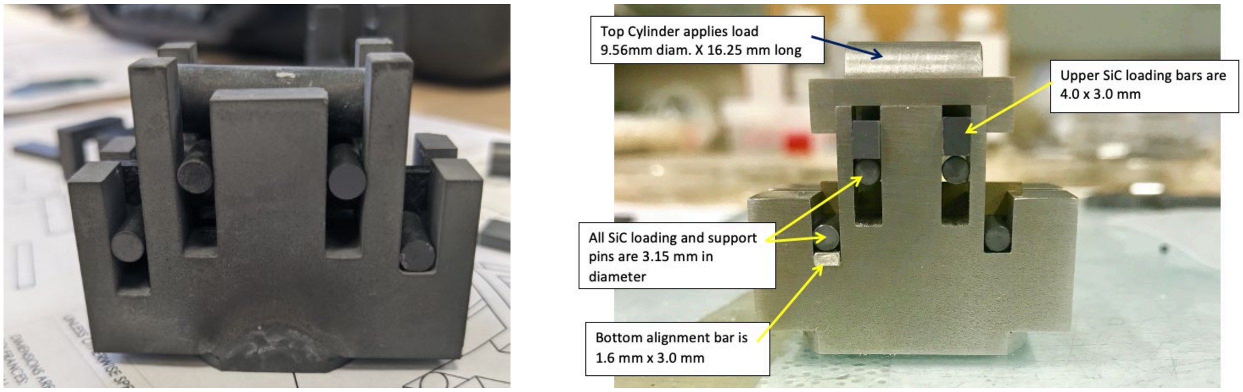

Figure 6. Four point bend fixtures: SiC fixture (left) and Inconel or Hasteloy-X fixture (right).

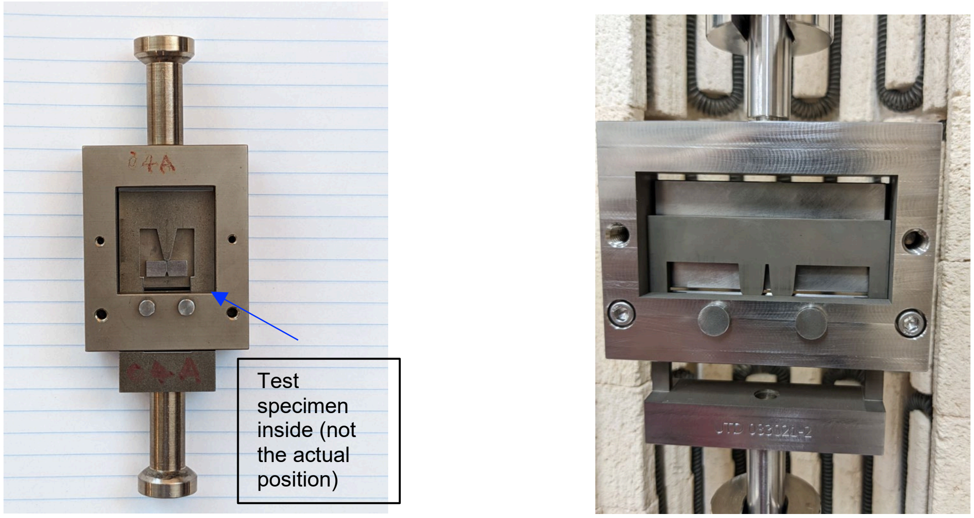

Figure 7. Three point and four-point bend fixture made of Inconel 718.

Acknowledgments

This research was supported by the United States Department of Energy (US DOE), Office of Science, Office of Fusion Energy Sciences, through Contract No. AT2030110-13784 and was performed at the PNNL, which is operated by Battelle for the US DOE under Contract No. DE-AC05-76RL0-1830.

References

[1.] S. Wurster, et al., *Recent progress in R&D on tungsten alloys for divertor structural and plasma facing materials.* Journal of Nuclear Materials, 442 (1-3): p. S181-S189, 2013.

[2.] D. Stork, et al., *Developing structural, high-heat flux and plasma facing materials for a near-term DEMO fusion power plant: the EU assessment.* Journal of nuclear materials, 455(1-3): p. 277-291, 2014.

[3.] A. Hasegawa, et al., *Neutron irradiation effects on the microstructural development of tungsten and tungsten alloys.* Journal of Nuclear Materials, 471: p. 175-183, 2016.

[4.] J. Wang, et al., *Tensile testing and microstructural characterization of ductile phase toughened W-NiFe alloys*, in *Fusion materials Semiannual Progress Report for the Period Ending June 30, 2020*. 2020.

[5.] J. Wang, et al., *Microstructural characterization and mechanical testing of ductile-phase toughened tungsten*, in *Fusion materials Semiannual Progress Report for the Period Ending December 31, 2019*. 2019.

[6.] J. Wang, et al., *Microstructure-Mechanical Property Correlation in Ductile Phase Toughened W-NiFe Heavy Alloy*, in *Fusion Materials Semiannual Progress Report for the Period Ending December 31 2020*, D. Clark, Editor. 2020.

[7.] R. Prabhakaran, et al., *Status of the elevated temperature mechanical test facility setup at PNNL*, PNNL-SA-170069, In *Fusion Materials Semiannual Progress Report for period ending December 31, 2021*, DOE/ER-0313/71, U.S. Department of Energy, 2022.

[8.] J. Wang, et al., *Tensile testing and microstructure characterization of ductile phase toughened W-NiFe alloys*, in *Fusion Materials Semiannual Progress Report for period ending June 30, 2020*. 2020.

[9.] M. Li, et al., *Elevated temperature tensile behavior and microstructure evolution of liquid phase sintered 90W-7Ni-3Fe alloy*, Journal of Alloys and Compounds 802 (2019) 528-534.

[10.] Publication Number SMC-106, Special Metals Corporation, September 2004.

[11.] H. Y. Bor, et al., *Elucidating the effects of solution and double ageing treatment on the mechanical properties and toughness of MAR-M247 superalloy at high temperature,* Materials Chemistry and Physics, Volume 109, Issues 2–3, Pages 334-341, 15 June 2008.

[12.] M. Kaufman, *Properties of cast Mar-M-247 for turbine blisk applications*, Superalloys, pp. 43-52, 1984.

[13.] Rembar website; https://www.rembar.com/when-to-use-tzm-alloy-instead-of-pure-molybdenum; updated July 30, 2020 (accessed 1 Aug 2022).

[14.] K.H. Cunningham, K. Fields, D. Gregg and T. Roosendaal, 4.1, Volume 54: *Recent Progress in the Development of Ductile-Phase Toughened Tungsten for Plasma-Facing Materials*, DOE/ER-0313/54-Volume 54, Semiannual Progress Report, June 30, 2013, edited by F.W. Wiffen, R. Godfrey and B. Waddell, US DOE, ORNL, TN, vol. 54, chapt. 4.1, pp. 95-107, 2013.

[15.] C. Henager, et al., *Ductile-phase toughened tungsten for plasma-facing materials in fusion reactors*, International Journal of Powder Metallurgy, Volume 53, No. 2, 2017.

[16.] M. Alam, et al., *The effect of hot rolling on the strength and fracture toughness of 90W-7Ni3Fe tungsten heavy metal alloys*, Materials Science & Engineering A 824, 141738, 2021.

4.5 DEFECT MICROSTRUCTURES OF IRRADIATED CCNZ/ADVANCED COPPER ALLOYS

—B Cheng, D. J. Sprouster, L. Snead (Stony Brook University), W. Zhong, Y. Yang (Oak Ridge National Laboratory), L. Yang, S. Zinkle (University of Tennessee, Knoxville)

PROGRESS AND STATUS

Introduction

The sintered CuCrNbZr (CCNZ) alloys under development at Stony Brook University (SBU) as well as the cast CCNZ under collaborative development with the University of Tennessee (UT) and Oak Ridge National Laboratory (ORNL) assume improved creep and irradiation performance from a high density of precipitates. Specifically, the high density of Cr within the copper matrix are thought to promote beneficial defect recombination. However, this point has not yet been demonstrated and will be addressed. In this work, SSJ3 specimens are part of an irradiation campaign to provide tensile performance, micromechanical data, and microstructure. The cast CCNZ specimens are to be compared with the International Thermonuclear Experimental Reactor (ITER) grade CuCrZr. Under this task SBU will carry out thermophysical and microstructural characterization of irradiated specimens in collaboration with ORNL. The multi-characterization approach proposed herein incorporate the physical property measurements located at SBU (Electrical resistivity, thermal conductivity, mechanical testing) coupled with the x-ray diffraction and small angle scattering capabilities located at the National Synchrotron Light Source-II (NSLS-II). Synchrotron-based X-ray diffraction analysis (XRD), with enhanced sensitivity to minor phases, will significantly aid in unravelling the effects of alloying elements, impurities, and processing parameters in Cu-based alloys.

Experimental Procedure

Baseline microstructural measurements for all CCNZ and CCZ specimens were performed at the NSLS-II using the high-energy X-rays available at The Pair Distribution Function (PDF) beamline. All measurements were performed in transmission mode with an amorphous Silicon-based flat panel detector (Perkin-Elmer) mounted orthogonal to and centered on the beam path. The sample to detector distances and tilts of the detector relative to the beam were refined using a LaB6 powder standard National Institute of Standards and Technology ([NIST] standard reference material 660c). The wavelength of the incident X-rays was 0.1665 Å (74.46 keV). The sample to detector distance was calculated to be 1235.20 mm. Then 600 individual patterns with detector exposures of 0.1s were collected for each specimen. All raw two-dimensional patterns were background corrected by subtracting a dark current image, and the air and Kapton scattering background within IgorPro (Wavemetrics). Noticeable artefact regions of the detector (like the beam stop, dead pixels) were masked. The corrected and masked two-dimensional detector images were then radially integrated to obtain one-dimensional powder diffraction patterns. We note that the XRD patterns collected at the synchrotron, with very high signal to noise, can be collected in under 30 seconds. Furthermore, unlike Transmission electron microscopy (TEM), no sample preparation is needed to perform these synchrotron measurements. The high throughput characterization of samples fabricated for these efforts to rapidly map out the phase space and quantify the effect of post processing heat treatments in promoting the precipitation of minor phases (to improve creep properties) is under examination for the different CCZ and CCNZ specimens.

Results

Our group have been examining, and developing, the processing structure property relationship for a series of Copper alloys prepared via DCS [1]. By controlling feedstock and sintering conditions, we will effectively control the size and fraction of these precipitates. Both cast [2], and sintered CCNZ specimens have been/are currently being irradiated at Massachusetts Institute of Technology Reactor (MITR). A matrix of the irradiated specimens is given below, with pre-irradiation characterizations that will serve as baselines and direct comparison to post-irradiation examination investigations.

Table 1. CCZ and CCNZ specimens from ORNL and SBU undergoing irradiation at MITR. Pre-IE and Post-IE characterization plans are listed for reference.

Sample ID	Composition	Number of samples	Density	Dimensions	Electrical resistivity	Synch. XRD
ORNL GenI	Cu-1.1Cr-0.04Zr	5	✓	✓	✓	✓
ORNL GenII	Cu-2Cr-1.35Nb-0.15Zr	25	✓	✓	✓	✓
SBU_CCNZ	Cu-2Cr-1.35Nb-0.15Zr	20	✓	✓	✓	✓

Representative XRD patterns collected for the unirradiated CCNZ and CCZ alloys (listed in Table 1) are shown in Figure 1. The additional minor peaks are attribute to the $CrNb_2$ and Cr precipitates previously observed with XRD and TEM [1, 2]. The strong signal from these precipitates indicate that quantification of microstructural changes post-irradiation is possible.

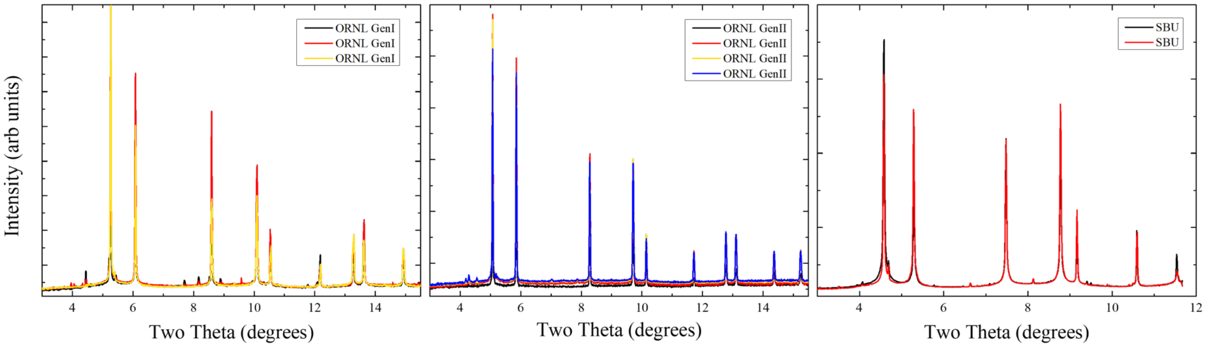

Figure 1. XRD patterns collected for CCNZ alloys from ORNL and SBU.

Conclusions

Specimens are currently undergoing cool-down following neutron irradiation in MITR. A post-irradiation examination campaign, incorporating electron microscopy, XRD (at a synchrotron light source), electrical resistivity and mechanical property evaluation is anticipated in the late part of 2022.

Acknowledgements

The work was funded under Grant DE-SC0018332 to the Research Foundation at State University of New York, SBU by the United States Department of Energy Office (US DOE) of Fusion Energy Sciences. Use of the 28-ID-1 (PDF) and 28-ID-2 (XPD) beamlines at the NSLS-II, Brookhaven National Laboratory, was supported by the US DOE under Contract No. DE-SC0012704.

References

[1] B. Cheng, L. Wang, D.J. Sprouster, J.R. Trelewicz, W. Zhong, Y. Yang, S.J. Zinkle, L.L. Snead, Tailoring microstructure in sintered Cu-Cr-Nb-Zr alloys for fusion components, Journal of Nuclear Materials 551 (2021) 152956.

[2] L. Wang, C. Zheng, B. Kombaiah, L. Tan, D.J. Sprouster, L.L. Snead, S.J. Zinkle, Y. Yang, Contrasting roles of Laves_Cr2Nb precipitates on the creep properties of novel CuCrNbZr alloys, Materials Science and Engineering: A 779 (2020) 139110.

4.6 MULTI-MODAL MICROSTRUCTURAL CHARACTERIZATION OF TUNGSTEN FOR FUSION ENERGY

—D. J. Sprouster, L.L. Snead (Stony Brook University), T. Koyanagi, Y. Katoh (Oak Ridge National Laboratory)

OJBECTIVE

Recent evidence by our team suggests that the starting material (pure W or W alloys) follow different transmutation induced embrittlement pathways. The aim of this research is to uncover the atomic and microstructural evolution in W-based materials for next generation fusion energy devices, including International Thermonuclear Experimental Reactor (ITER) and Demonstration Power Plant Reactor (DEMO). To achieve this aim, we propose a series of experiments to uncover the atomic (though X-ray absorption spectroscopy) and microstructure environments (through X-ray diffraction) of engineered W alloys exposed to neutron irradiation to induce transmutation. Recent results from our multimodal X-ray Power Diffraction (XRD) and X-ray Absorption Spectroscopy (XAS) experiments are discussed here.

PROGRESS AND STATUS

Introduction

Tungsten is presently the leading plasma facing material candidate due to its high melting point, resistance to sputtering, and chemical compatibility with tritium [1]. However, extended exposure of W to fusion plasmas and intense 14 MeV neutrons [2], resilience against plasma induced surface damage (cracking, erosion/exfoliation, and fuzz formation [3]), and degradation of bulk mechanical properties due to neutron irradiation [4] raises significant concerns about its stability. Recognizing that embrittlement due to neutron exposure is a potentially insurmountable issue for the development of first wall structures, our team have fabricated, irradiated, and are characterizing a large database of W specimens (over 100 with different irradiation conditions, and alloying contents). We have thoroughly characterized the high dose conditions with electron microscopy, and in FY21 X-ray scattering, small-angle X-ray scattering (SAXS) and XRD. These effects confirmed that the degradation in mechanical performance is directly attributable to the formation of solid nm-sized transmutation precipitates [5]. While the high dose conditions, with large Re and Os transmutation concentrations are important to embrittlement, the lower doses and evolution to precipitation are unexplored. Furthermore, electron microscopy methods have not been able to shed insight on the structure and configurations of Re and Os atoms prior to precipitation. We hypothesize that different W alloys will accommodate the transmutation alloys into different defect configurations, and subsequent high dose precipitation can be controlled by controlling the starting alloy. Through a dedicated XAS and XRD characterization campaign, we seek to identify the atomic structures of Re and Os and how they evolve into embrittling precipitates in different W alloys (W, W-Re, and K-doped W alloys). This motivates the following research questions we seek to directly answer here:

1. What are the atomic structures of Re and Os atoms at low and intermediate doses?
2. How do the atomic structures in pure W differ to those created in W alloys?

These configurations are critically important as understanding early-stage (low dose) evolution will allow strategies to effectively reduce, and/or mitigate the late-stage effects of precipitation formation through alloy design.

Experimental Procedure

Materials

The XRD and XAS experiments of unirradiated and neutron irradiated polycrystalline W, W-3%Re and K-doped W (~50ppm K) alloys, after low dose irradiation at 800°C (0.1 dpa) and after high irradiation temperature (>800°C), with Re+Os transmutation concentrations in the range of 0.01-5.0 at.%. Analysis of the XRD patterns will allow determination of the lattice strain (change in lattice parameter), change in the microstructure parameters, and formation of any secondary phases. X-ray absorption near edge structure (XANES) and extended x-ray absorption fine structure (EXAFS) will give quantitative insight into the atomic configurations of dilute Re and Os atoms as functions of both alloy type and irradiation dose. Our choice of W and W alloy compositions are also under investigation computationally (through both density functional theory and molecular dynamics) to aid in understanding the defect structures that form under irradiation. The XRD and XAS experiments will aid in validating and verifying the defect behavior predicted by modelling.

Synchrotron XRD experiments were performed at the Pair Distribution Function (PDF) beamline at the National Synchrotron Light Source II (NSLS-II). All measurements were performed in transmission mode with an amorphous silicon based flat panel detector (Perkin-Elmer) mounted orthogonal to the beam path. The sample-to-detector distance and tilts of the detector relative to the beam were refined using a LaB_6 powder National Institute of Standards and Technology (NIST) standard (SRM® 660c). The wavelength of the incident X-rays was 0.1665 Å at an energy of 74 keV. The sample-to-detector distance was calculated to be 1245.91 mm. All raw two-dimensional patterns were background corrected by subtracting a dark current image and noticeable artifact regions of the detector (like the beam stop and dead pixels) masked.

Room temperature fluorescence mode XAS with a four-element Si-drift detector at the W, Re and Os L_{III}-Edges (10207,10535;10871 eV, respectively) were performed on baselines and irradiated specimens. XANES and EXAFS were measured with the Si (111) monochromator and unfocused beam. For energy calibration, an appropriate reference foil will be simultaneously measured in transmission mode. Background subtraction, spectra alignment and normalization of the data was performed using Advanced Telescope for High-ENergy Astrophysics (ATHENA).

Results

Figure 1 (a) shows the XAS spectra at the Re and Os edges for two polycrystalline and two single crystal W specimens. The Re edges look very similar and akin to the Re atoms occupying predominately Body-centered cubic (BCC) lattice sites, with a potential Hexagonal close packed HCP) component. The subtle features in the single crystal specimen irradiated at temperatures above 800C are highlighted for reference. The Os spectra show similar features, except for the single crystal specimen irradiated at high temperate, highlighting a different atomic structure for the Os atoms in this specimen. It is probable that there are combinations of environments (BCC substitution, HCP and intermetallic). Analysis of the XANES spectra with references of theoretically simulated spectra will enable the extraction of the amount of each environment.

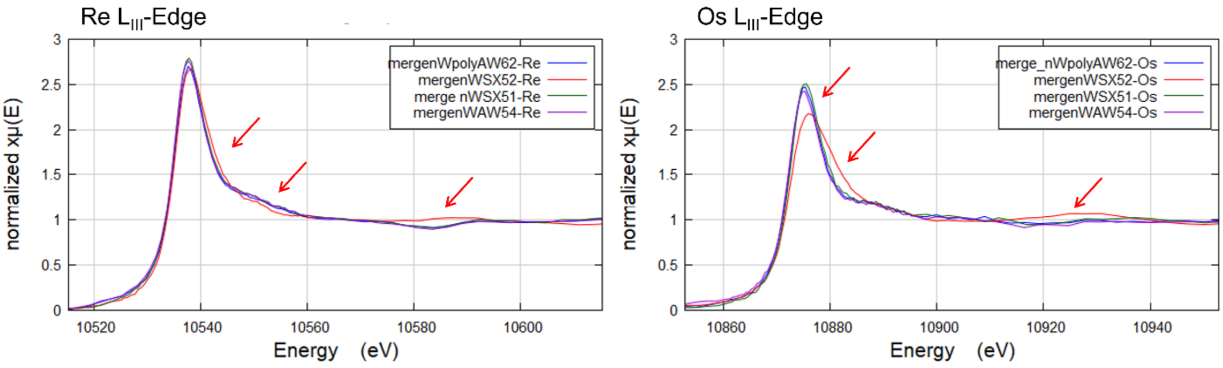

Figure 1. (a) Re L_{III}-Edge and (b) Os L_{III}-Edge XANES measurements for neutron irradiated polycrystalline and single crystal W specimens. Red arrows indicate subtle deviations indicative of multiple atomic environments.

The XRD patterns for the four samples in Figure 1 are shown in Figure 2. The XRD signal, while weak shows that minor phases are visible. The complete phase identification is planned for the next coming cycle. However, preliminary results indicate that a fraction of the Re and Os atoms are substitutional in the tungsten host ***and*** in nm-scale precipitates that contribute to the diffuse scattering background and minor XRD peaks.

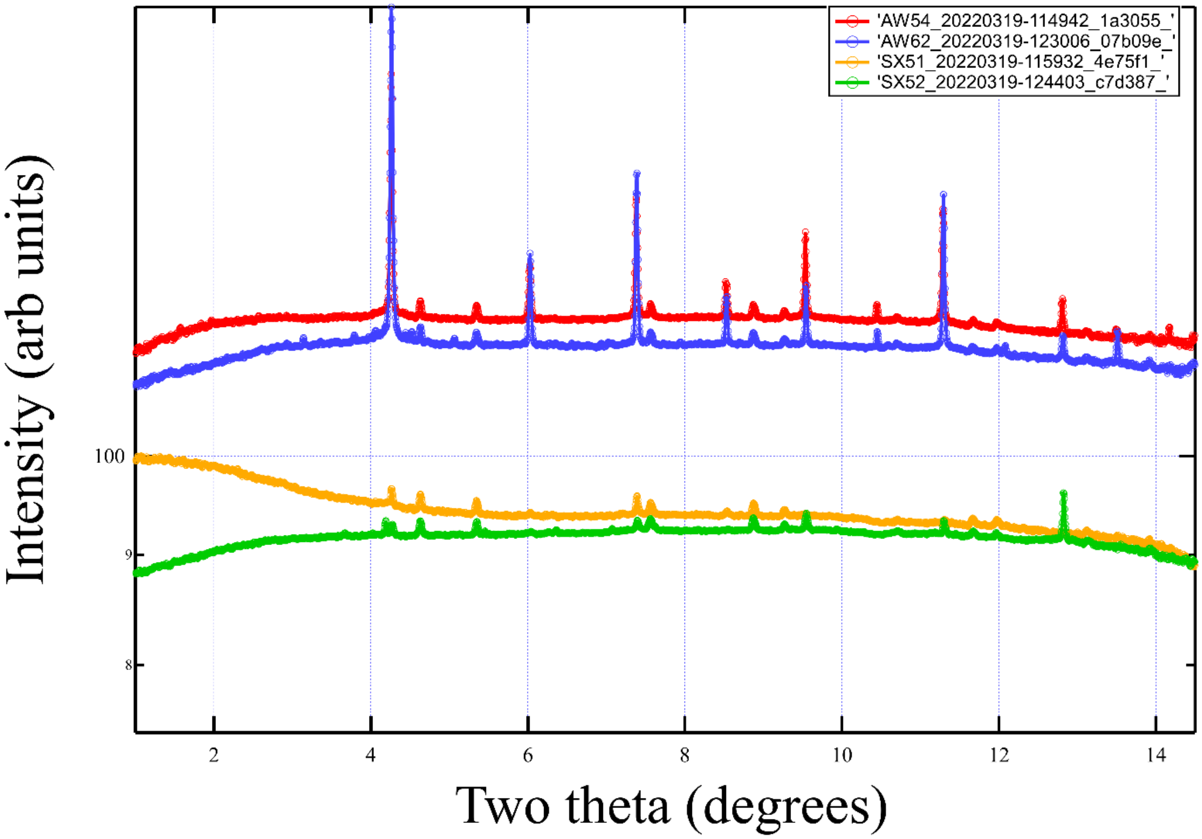

Figure 2. XRD patterns for neutron irradiated single crystal and polycrystalline W specimens. The specimens are vertically offset to show the differences in diffraction signatures.

Conclusion

The limited EXAFS range hindered by the closeness of multiple edges may make EXAFS refinements difficult. However, the XANES results were still sufficient in identifying different atomic environments of the transmutation Re and Os atoms in different W specimens. The large XRD and XAS data sets collected for this specimen series (shown in Table 1) is currently undergoing further analysis and refinements. Future work will include analyzing the XANES spectra to isolate the fraction of different atomic environments, and to analyze the XRD patterns to quantify the lattice parameters of the W host and intermetallic precipitates. Our initial hypothesize that different W alloys accommodate transmutation alloys into different defect configurations, and subsequent high-dose precipitation can be controlled by controlling the starting alloy appear reasonable based on the initial results. Future quantification will provide detailed justification and validation of this hypothesis and the atomic structures of Re and Os atoms at low and intermediate doses.

Acknowledgements

The work was funded under Grant DE-SC0018332 to the Research Foundation at State University of New York, Stony Brook University by the United States Department of Energy (US DOE) Office of Fusion Energy Sciences. Use of the 6BM Beamline for Material Measurement (BMM) and 28-ID-1 (PDF) beamlines at the NSLS-II, Brookhaven National Laboratory, was supported by the US DOE under Contract No. DE-SC0012704.

References

[1] S.J. Zinkle, L.L. Snead, Designing Radiation Resistance in Materials for Fusion Energy, 44(1) (2014) 241-267.
[2] C. Linsmeier, M. Rieth, J. Aktaa, T. Chikada, A. Hoffmann, J. Hoffmann, A. Houben, H. Kurishita, X. Jin, M. Li, A. Litnovsky, S. Matsuo, A. von Müller, V. Nikolic, T. Palacios, R. Pippan, D. Qu, J. Reiser, J. Riesch, T. Shikama, R. Stieglitz, T. Weber, S. Wurster, J.H. You, Z. Zhou, Development of advanced high heat flux and plasma-facing materials, Nuclear Fusion 57(9) (2017) 092007.
[3] M.J. Baldwin, R.P. Doerner, Helium induced nanoscopic morphology on tungsten under fusion relevant plasma conditions, Nuclear Fusion 48(3) (2008) 035001.
[4] Y. Katoh, L.L. Snead, L.M. Garrison, X. Hu, T. Koyanagi, C.M. Parish, P.D. Edmondson, M. Fukuda, T. Hwang, T. Tanaka, A. Hasegawa, Response of unalloyed tungsten to mixed spectrum neutrons, Journal of Nuclear Materials 520 (2019) 193-207.
[5] D.J. Sprouster, J.R. Trelewicz, L.L. Snead, X. Hu, D. Morrall, T. Koyanagi, C.M. Parish, L. Tan, Y. Katoh, B.D. Wirth, Advanced synchrotron characterization techniques for fusion materials science, Journal of Nuclear Materials 543 (2021) 152574.

4.7 UPDATE ON THE EFFECTS OF ANNEALING AND SPECIMEN SIZE ON THE MICROSTRUCTURE AND ROOM TEMPERATURE MECHANICAL PROPERTIES OF 90 to 97W-NiFe TUNGSTEN HEAVY ALLOYS—M.E. Alam, G.R. Odette (University of California Santa Barbara)

OBJECTIVE

This research aims to explore the effect of high-temperature annealing on the room temperature fracture toughness properties of larger specimens for 90 to 97W-NiFe tungsten heavy alloys (WHAs) for fusion divertor application.

SUMMARY

The commercially available liquid phase sintered 90, 92.5, 95, and 97 wt.% WHA show remarkable room temperature (RT) maximum load fracture toughness (K_{Jm} ≈ 38 to 107 MPa√m, depending on W content, and specimen size, 1x to 8x) compared to monolithic W (≈ 8 ± 4 MPa√m). However, these alloys are to be used as divertor in fusion reactors at a temperature ≈ 1300 ºC due to various limiting factors. Previously, we have annealed small specimens (16/3.3/1.65 mm) of all four WHAs at 1300 ºC for 24 h in a vacuum that shows improved RT ductility and toughness. Since the RT toughness shows some specimen size effect, especially for 1 and 3x specimens, therefore, we have annealed 4x larger specimens at 1300ºC/24h in this study. The 4x annealed specimens revealed improved RT roughness and lower size effect. Additionally, the 4x 97W was annealed at 1100 ºC/1h and, 1200 ºC/1h in vacuum which are failed unstably with slightly improved RT toughness.

PROGRESS AND STATUS

Introduction

The WHAs, a class of bi-phase metallic composites, are typically composed of tungsten (W) powder consolidated by liquid phase sintering (LPS) with relatively lower melting point ductile phase (DP) metals like Ni, Fe, Cu, and Co; and well known for their good room to high temperature tensile strength and ductility [1–4]. The WHAs are recently being considered as the most promising structural plasma facing materials for fusion reactor divertor applications [5–12]. The advantages and open questions about WHA related to fusion service are described elsewhere [6,8,10–14]; and WHA fabrication routes and basic properties are the subjects of extensive literature [1–4,14–16]. The selection and purpose of annealing conditions have been discussed in our previous report [17]. The RT fracture toughness on the as received 1x to 8x large 90W to 97W specimens show a significant maximum load fracture toughness (K_{Jm}) drops between 1x and 3x specimens, and a very small K_{Jm} variations between 3x and 8x large specimens for the tested WHA alloys [18]. The 1300 ºC/1h vacuum annealing on 1x 90-97W WHA specimens has shown improved RT K_{Jm} for all WHAs, especially for 97W [17]. Here, in this study, we have chosen 4x large specimens (B = 6.35 mm, equivalent to 0.25T) to represent larger specimens for the high temperature annealing performed at 1300 ºC for 24 h (later denoted as 1324). Toughness results are compared with the previously tested 1x specimens, annealed at the same conditions, and as received 3x WHA specimens. In addition, 4x 97W WHA are also annealed at 1100 ºC/1h (i.e., 111) and 1200ºC/1h (i.e., 121) to explore the annealing temperature effect.

Detail microstructural observation reveals very little change in W-particle size, contiguity, DP phase compositions, area percentage, or DP thickness for pre-and post-annealed conditions. Vickers microhardness (HV) reduces after annealing, especially for higher W content WHAs. The RT tensile results show unaffected 0.2% yield strength for all WHA's and ductility for 90 and 92.5 W WHA; however, 95 and 97W nearly double their respective ductility after annealing, while maintaining similar tensile strengths. The hardening exponent, in general, is also reduced. The RT maximum load fracture toughness, K_{Jm}, for 1x specimens increased after annealing for all the WHAs except 92.5W WHA. The K_{Jm} for the 1300ºC/24h annealed 4x specimen shows nearly similar toughness when compared to the 1300ºC/24h annealed 1x specimens, except for 97W. However, the 1300 ºC/24h annealed 4x 97W shows much higher toughness (K_{Im} ≈ 55 ± 3 MPa√m, and K_{Jm} ≈ 73 ± 29 MPa√m) compared to the as-received 3x 97W (K_{Im} ≈ 38 ± 4 MPa√m) that all break in fully elastic region. Surface damage mode profile also changes from W-microcleavage formation, arrest, and blunting for the as-received specimens to W-W and W-DP decohesion dominated mechanism for the annealed specimens.

Experimental Procedure

Details of materials acquisition, specimen fabrication, microstructural observation, pre-cracking and mechanical testing procedures can be found elsewhere [13,18,19]. Briefly, four commercially available 90, 92.5, 95, and 97 wt.% W, balanced with DP phase (Ni/Fe = 7/3 ratio), (dubbed as 90W, 92.5W, 95W and 97W, respectively) WHAs were acquired from Mi-Tech Metals, Indianapolis, Indiana in the United States of America (USA) as a liquid phase sintered plates. Basic microstructural characterization involves optical, scanning electron microscopy (SEM), energy dispersive spectroscopy (EDS) and electron backscatter diffraction (EBSD) on the pre-and post-annealed conditions. Note, at least four specimens were characterized for each conditions except for the 4x large 90, 95 and 97W WHAs where two of each were annealed at 1300 ºC for 24 h in vacuum. Additionally, one of 4x 97W specimen was also annealed at 1100 ºC/ 1h and 1200 ºC/1h to evaluate the time temperature kinematics on 97W alloy. Note, unless otherwise stated, annealing indicates here 1300ºC/24h condition. W-particles size, W-W contiguity, chemical composition of DP, DP area fraction, ligament thickness (t), thickness to W-particle (t/W), and local fracture modes are observed using mentioned characterization tools and imageJ64 software. The Vicker's HV indenter was probed on individual W and DP phases at low load (10_{gf}), and on the composites at 500_{gf} load, both for the as received and 1300 ^{0}C/24 h annealed conditions. The RT tensile tests are conducted as per ASTM International (ASTM) E8 standard [20], where as RT fracture toughness test are conducted and analyzed as per ASTM E1921 standard [21]. Reasons for using some ASTM E1921 K_{Jm} procedures are explained in [18]. Again, detailed characterization procedures are reported in [13,18].

Results

Microstructure

Figure 1 shows the SEM micrographs of the polished and etched 90-97W WHAs before (Figure 1a-d) and after (Figure 1e-h) annealing; the microstructural observation results are also summarized in Table 1. In all cases, W-particles are roughly spheroidal, surrounded by an interconnected honeycomb web structure of DP. The EDS point scan reveals W particles are nearly 100% pure, irrespective of alloy compositions or annealing conditions. The size of the W-particles also does not change before and after annealing and, are ≈ 17 ± 7 μm for 90W, increases with increasing W% content in the WHAs to ≈ 38 ± 15 μm for 97W, as shown in Table 1 and Figure 1. The DP surface area % also remains the same prior- and post-annealed conditions considering standard deviation (Table 1). The EDS's multiple point scans on the ductile phase reveal that the DP remains Ni-rich after annealing with a nominal average composition of ≈ 52% Ni, 31% W and 17% Fe from the prior-anneal 50%Ni, 32%W and 18%W condition. However, these variations are statistically insignificant as shown in Table 2 and Figure 2. The W-W contiguity increases for higher W-containing WHA's; however, that remains unchanged after annealing for the respective WHA alloys except for 97W annealed condition that reduces from 0.582 to 0.477 (≈ 18%). No DP ligament thickness (t) variations is observed irrespective of WHA alloys or annealing conditions. As expected, the t/W ratio or DP/W area fraction reduces with increasing W content in the WHA as W particle size increases. However, in both cases, this ratio does not change after annealing for the respective WHAs. The EBSD was also used on selective WHA's (90W and 97W) to observe the texture formation after annealing. The inverse pole figure (IPF) map shown in Figure 3 for annealed 90W and 97W shows that the randomly oriented W particles are embedded in very coarse-grained NiWFe DP. No high misorientation angles (>15º) were observed in W-particles at the scanned area for both annealed WHAs. However, some speckles are observed in the W or DP phases, which might be generated due to the polishing effect. The DP grains are very coarse and ≈ 165 x 165 μm area shows only ≈ two different continuous color grades with incomplete shape (Figure 3c for 90W and Figure 3f for 97W). A similar observation has been observed on as received 90W and 97W, performed at Pacific Northwest National Laboratory (PNNL) [22]. In general, 1300 ºC/24 h annealing has little to no effect on any aspect of the observed microstructures on the various as received WHA plates.

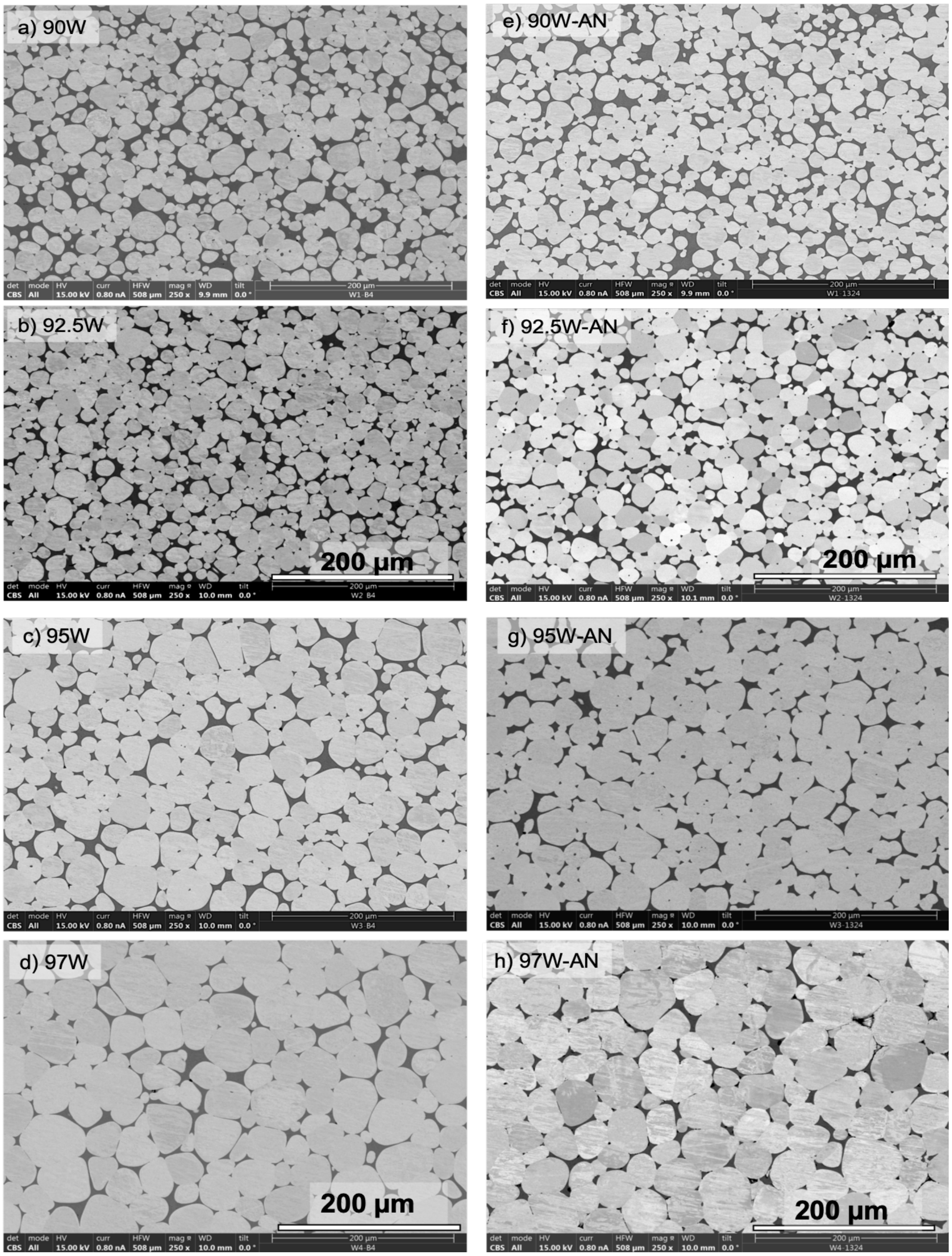

Figure 1. Low magnification SEM images of 90 to 97W WHAs before (a-d, left column), and after (e-h, right column) 1300 ºC/24 h annealing. Scale is 200 μm for all cases.

Table 1. The W-particle size, DP surface area %, W-W contiguity, DP thickness, t/W and DP/W for the as-received and 1300 ºC/24 h annealed WHA's

WHAs	Condition	W-particles, µm	DP area, %	W-W contiguity, C_w	DP thickness, t, µm	t/W µm/µm	DP/W area
90W	As-received	17 ± 7	16.1 ± 3.8	0.285	5.9 ± 5.4	0.35	0.22
	Annealed	17 ± 6	18.6 ± 0.8	0.302	5.7 ± 4.7	0.33	0.22
92.5W	As-received	18 ± 7	11.8 ± 2.2	0.402	4.0 ±. 3.7	0.22	0.12
	Annealed	19 ± 7	11.0 ± 0.8	0.408	5.7 ± 6.4	0.3	0.19
95W	As-received	26 ± 11	10.7 ± 1.3	0.426	5.1 ± 4.1	0.20	0.13
	Annealed	28 ± 11	9.3 ± 0.8	0.405	4.2 ± 3.3	0.15	0.09
97W	As-received	38 ± 15	6.4 ± 1.5	0.582	4.5 ± 5.0	0.12	0.07
	Annealed	38 ± 14	5.7 ± 0.1	0.477	5.3 ± 4.0	0.14	0.06

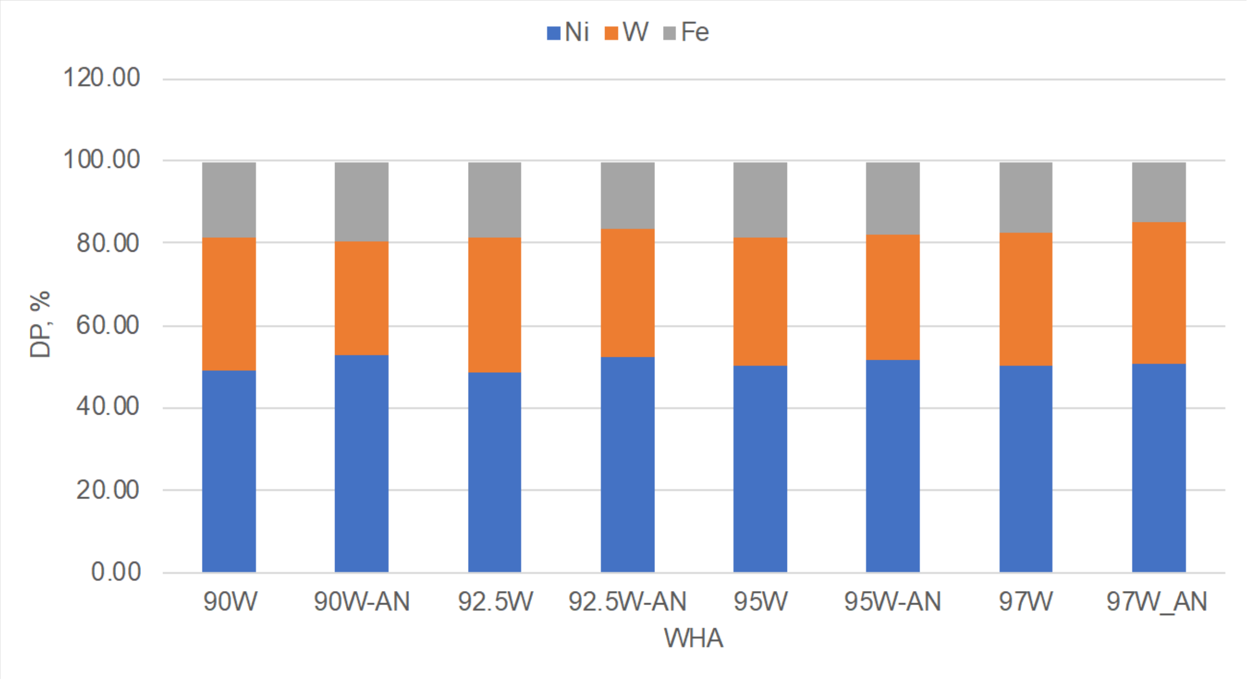

Figure 2. EDS point scan showing DP constituents (i.e., Ni, W and Fe wt.%) as a function of WHA alloy and annealing conditions.

Table 2. EDS point scan results for DP composition variations as a function of WHA alloy contents and annealing conditions.

WHAs	Condition	Ni, wt. %	W, wt. %	Fe, wt. %
90W	As-received	49.3 ± 0.4	32. 0 ± 0.4	18.7 ± 0.2
	Annealed	52.7 ± 0.9	27.6 ± 1.1	19.7 ± 0.5
92.5W	As-received	48.7 ± 0.7	32.9 ± 1.2	18.4 ± 0.6
	Annealed	52.4 ± 0.2	31.2 ± 0.3	16.4 ± 0.3
95W	As-received	50.2 ± 0.7	31.5 ± 0.9	18.3 ± 0.3
	Annealed	51.9 ± 1.2	30.2 ± 1.4	17.9 ± 0.5
97W	As-received	50.3 ± 0.6	32.3 ±0.7	17.4 ± 0.3
	Annealed	50.8 ± 0.5	34.33 ± 1.5	14.9 ± 1.5

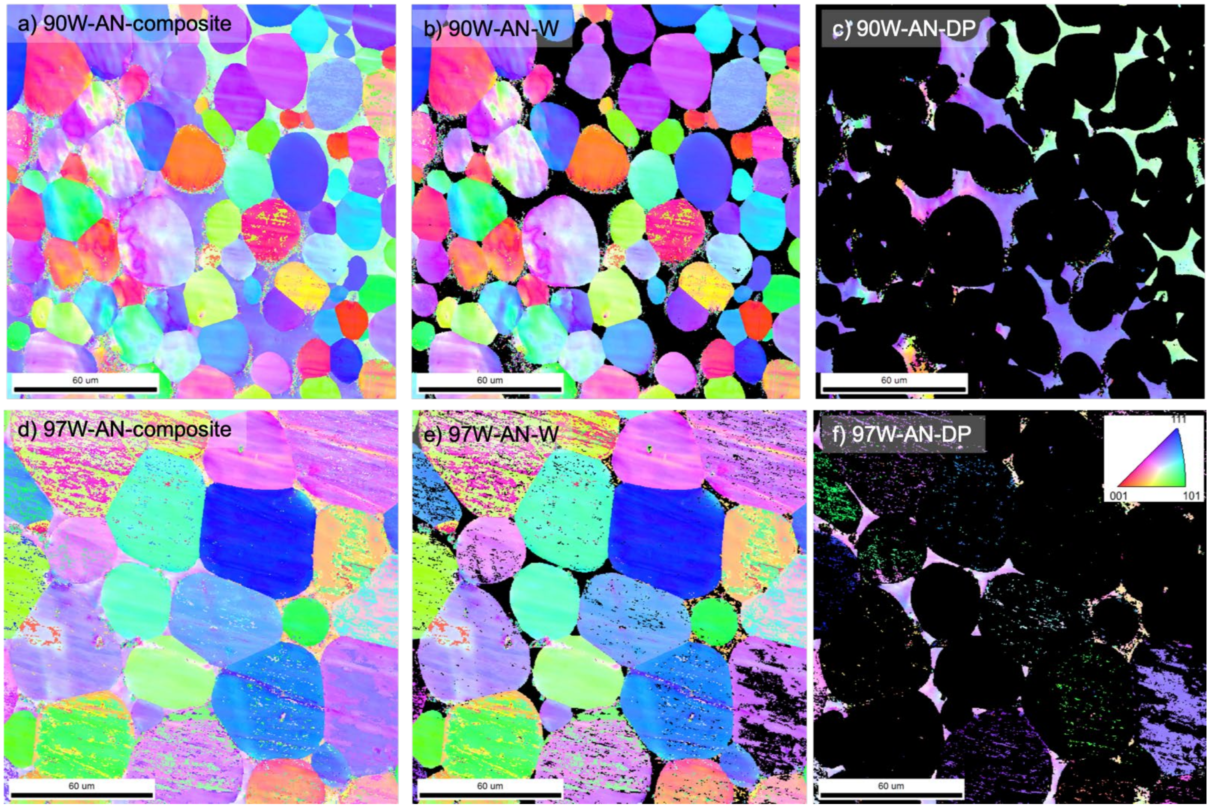

Figure 3. EBSD IPF map showing the random texture orientation for W and DP for 90W (a-c), and 97W (d-f) annealed conditions. Here, left column: composite, middle column: W, and right column: DP in both cases.

RT Microhardness and tensile tests

Room temperature Vicker's HV measurements were done on individual W and DP phases and on the composites, both at pre-and post-annealed conditions. The smaller 10_{gf} load was used in attempt to individually probe the DP and W phases. Since there is little to no variations of compositions for DP (≈ 50Ni30W20Fe, wt.%) and W (≥ 99.5% pure) phases before and after annealing, therefore the measurements were only conducted on 90W. Inset of Figure 4a shows that the as received W and DP phase hardness is ≈ 478 ± 19 kg_f/mm^2 and 348 ± 27 kg_f/mm^2, respectively, that softens after 1300ºC/24h annealing to 421 ± 20 kg_f/mm^2 (≈ 12%) and 299 ± 22 kg_f/mm^2 (≈ 14%), respectively. The 500_{gf} load was probed on the 90-97W composite structures and the results are shown in Table 3 and Figure 4a, both for the as received and annealed conditions. While the average microhardness increases with increasing W from 321 ± 8 kg_f/mm^2 for 90W to 344 ± 9 kg_f/mm^2 for 97W for as received conditions, the hardening trend is somewhat downward for annealed conditions from 319 ± 14 kg_f/mm^2 for 90W to 289 ± 18 kg_f/mm^2 for 97W 1300 ºC/24h annealed WHAs. The high temperature annealing softens the individual phases by ≈ 12-14% that reflects on overall 90-97W composite softening up to 16% for 97W, except for 90W, which remains almost unchanged. The annealed 90W composite hardness behavior is not yet fully understood.

Table 3. RT Vickers microhardness (HV), and tensile properties of WHA's

WHAs	Conditions	$HV_{0.5}$ Kg_f/mm^2	σ_y, MPa	σ_u, MPa	ε_u, %	ε_t, %
90W	As received	321 ± 8	621 ± 29	891 ± 35	18 ± 4	21 ± 7
	Annealed	319 ± 14	588 ± 12	809 ± 11	17.3 ± 1.0	22.5 ± 2.9
92.5W	As received	334 ± 8	616 ± 44	886 ± 12	13.5 ± 2.2	16 ± 4
	Annealed	302 ± 13	603 ± 4	796 ± 17	14.1 ± 2.2	17.0 ± 3.2
95W	As received	349 ± 7	600 ± 15	818 ± 10	7.3 ± 1	8 ± 1
	Annealed	279 ± 23	588 ± 9	774 ± 12	13.1 ± 1.9	15.5 ± 0.3
97W	As received	344 ± 9	594 ± 27	701 ± 67	3.4 ± 1	4 ± 1
	Annealed	289 ± 18	572 ± 14	707 ± 10	7.5 ± 0.9	8.8 ± 1.0

Figure 4b shows the representative RT engineering stress-strain ($\sigma-\varepsilon$) curves for all the 90 - 97W pre- and post-annealed WHAs. The corresponding tensile properties are shown in Figure 4c for 0.2% yield (σ_y), and ultimate tensile strengths (σ_u); and Figure 4d for total elongation (ε_t). The engineering $\sigma-\varepsilon$ curves look generally similar for the WHA's except the higher W% WHAs that systematically fail early. Further, curves are less strain hardened for the annealed condition (Figure 4b). Both Table 3 and Figure 4c show that the 1300 ºC/24 h annealing does not affect on σ_y (≈ 600 MPa with a softening of ≤ 5%), which are essentially the same for all the alloys. On the contrary, σ_u decreases for the respective WHA alloys up to 10% after annealing, except for 97W, which might be due to lower strain hardening exponent. However, annealed σ_u is nearly similar for up to 95W (≈ 793 ± 27 MPa), and then drops to ≈ 700 MPa for 97W (Table 3). Total elongation does not vary significantly for the respective WHAs for up to 92.5W after annealing but increases to ≈ 2x for the 95W and 97W. In all cases, annealed results are more consistent with lower standard deviation, which implies that annealing might help to homogenize the microstructure.

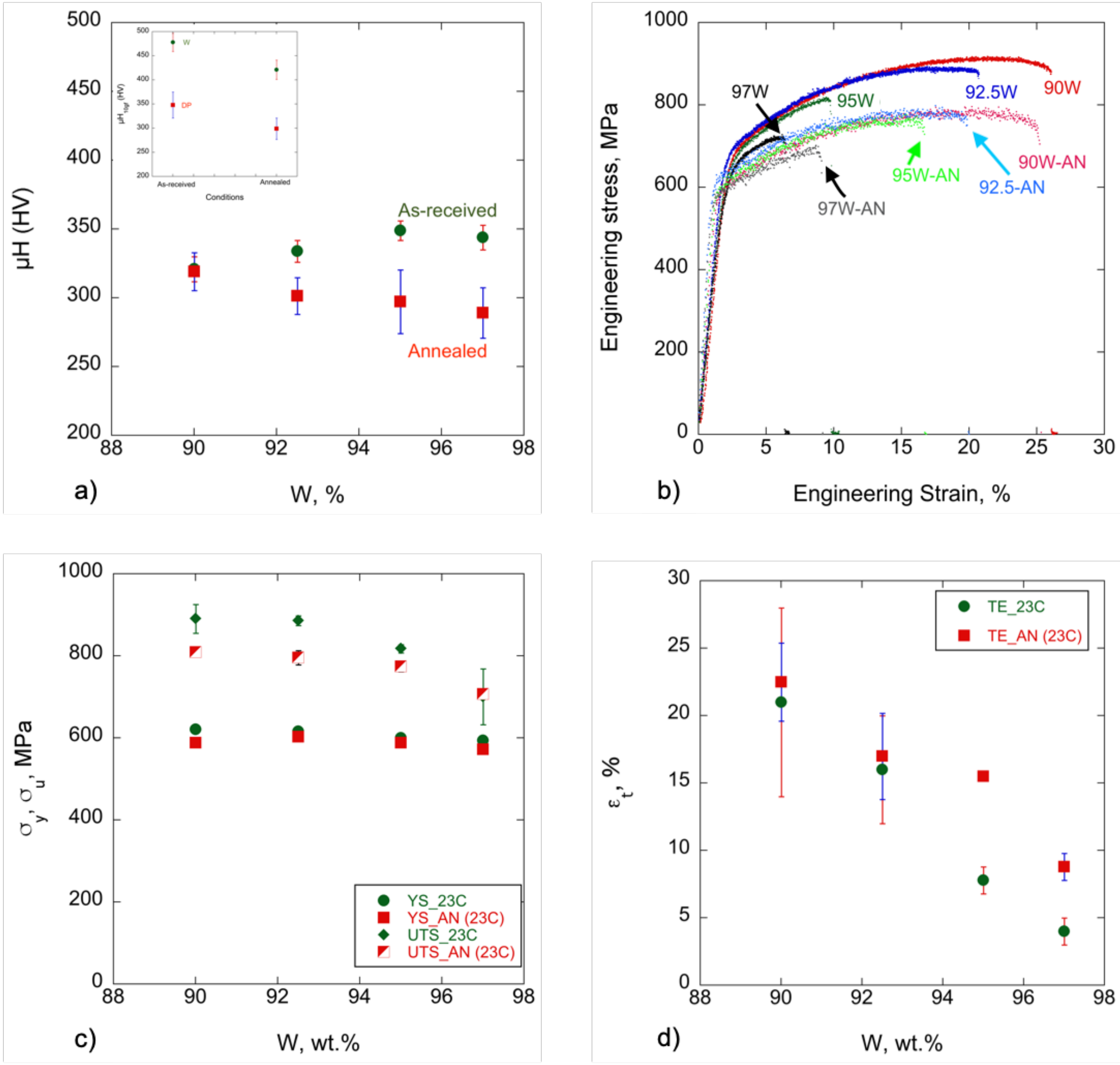

Figure 4. a) Vicker's microhardness values for as-received (green circles) and annealed (red squares) WHA's for the 500_{gf} composite load. The inset of 4a shows the HV for individual W and DP phases, probed at 10_{gf} load; b) RT engineering σ–ε curves; c) 0.2% yield (σ_y) and ultimate tensile (σ_u) strengths; and d) total elongations (ε_t) for as-received (green circles), and annealed (red squares) WHAs, respectively.

RT fracture toughness

The RT fracture toughness tests on the various WHAs are conducted on fatigue pre-cracked 3PB bars. The nominal dimensions (length/width/thickness) of these bend bars are for: smaller 1x ≈ 16/3.3/1.65 mm, larger 3x ≈ 50/10/5 mm, and 4x ≈ 60/12.7/6.35 mm. All the specimens are fatigue pre-cracked to a/W ≈ 0.4 to 0.5 at 20 Hz at a maximum $\Delta K_I \approx 15$ MPa√m and a load ratio R ≈ 0.1. The load (P) and load point displacements (d) were measured and K_{Jm} are defined at the P_m based on the ASTM E1921 standard practice method of estimating the J-integral elastic-plastic fracture toughness: $J_m = J_e + J_p$, as $K_{Jm} = \sqrt{\{J_m E/(1-\nu^2)\}}$; $J_e = K_{Im}{}^2(1-\nu^2)/E$, where K_{Im} is the elastic stress intensity factor at maximum load; and $J_p = 2A_P/Bb_o$ [21], B is specimen thickness, b_o is the initial unbroken ligament dimension, and A_p is the plastic area under the load-displacement curve [21,23,24]. It is also of interest to compare normalized P/P_o-d curves by dividing P by the plane strain limit load P_o. It is important to note that most tests that were not interrupted shortly beyond the maximum load, involved at least some ductile tearing. Details toughness characterization procedures are reported in [18].

The representative P/P$_o$ -d curves for all the tested WHAs at all conditions are plotted in Figure 5a (for 1x) and Figure 5b (for 3-4x); their corresponding K$_{Im}$ and K$_{Jm}$ values are plotted in Figure 5c and d, respectively, as well as tabulated in Table 4. As reported previously [13], all of the as received WHAs from 90 to 97W 1x specimens show very stable crack growth signalled by continuous post maximum load drops. The 1x 1300ºC/24h annealed 90-97W WHAs follow the similar P/P$_o$-d trend with stable crack growth, however, the maximum P/P$_o$ is much higher for the annealed condition. This might be due to the lower limit load (P$_o$) for annealed specimens as the flow stress (σ_o) is lower for annealed (699 MPa) vs. as received (756 MPa) conditions. The d at maximum P/P$_o$, d$_m$, also slightly increased for annealed specimens, except 92.5W (Figure 5a).

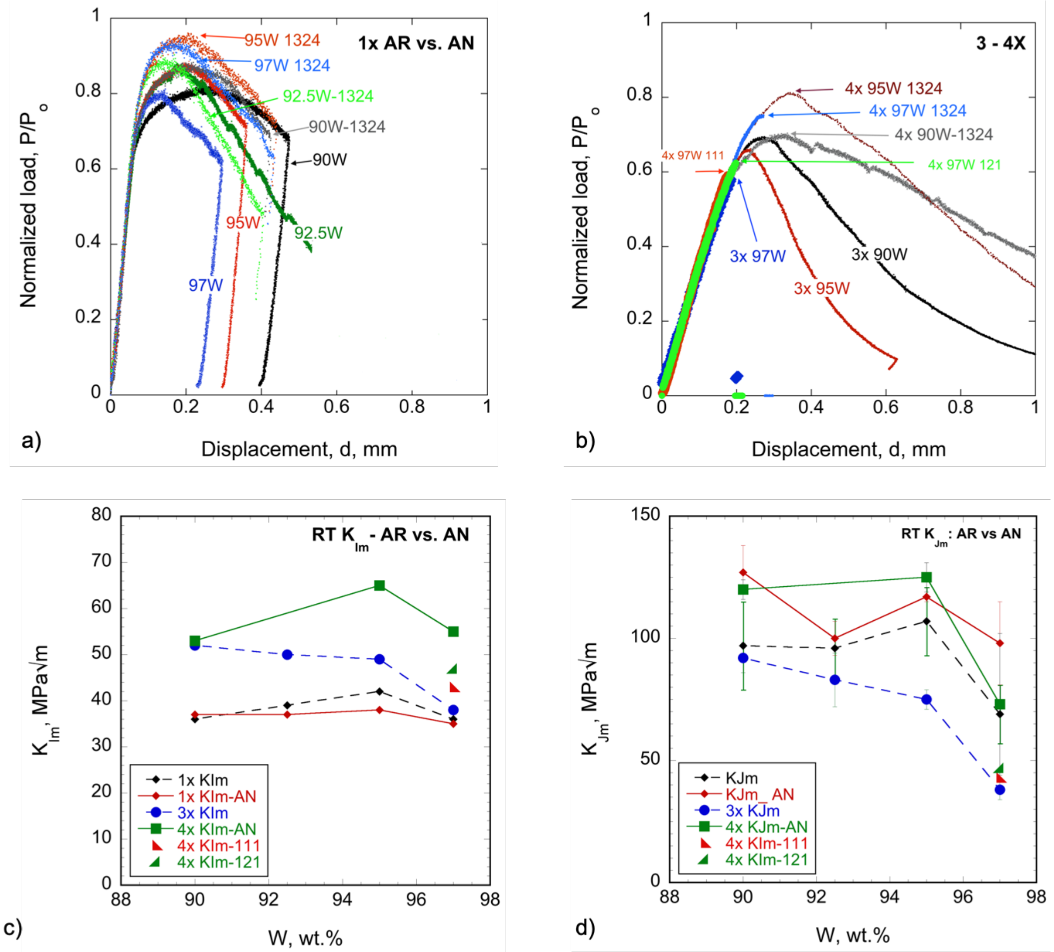

Figure 5. a,b) shows representative RT normalize load displacement (P/P$_o$ -d) curves for 1x (a), and 3-4x (b) for as-received and annealed WHAs; and c,d) shows corresponding average maximum load elastic K$_{Im}$ (c), and elastic plastic K$_{Jm}$ (d) fracture toughness. Note, all the specimens were annealed at 1300ºC/24h (i.e., 1324), except two of 4x 97W that were annealed at 1100ºC/1h (111), and 1200ºC/1h (121). AR: as-received, AN: annealed.

Figure 5b shows the corresponding RT normalized P/P$_o$ -d curves for 3x as received and 4x annealed WHAs at various annealing conditions. The 3x as received 90-95W specimens show stable crack growth while all the 3x 97W fracture unstably [18]. The 1300ºC/24h annealed 4x specimens also show stable crack growth for 90-95W WHAs, whereas one of 4x 97W annealed show some limited yielding before fast, unstable fracture whereas another one fracture at elastic loading line without signalling any yielding (Figure 5b). The 1100ºC/1h and 1200ºC/1h annealed 4x 97W specimens also fracture unstably at their elastic load line (Figure 5b). In general, the P/P_o for larger specimens are lower than the smaller 1x specimens for the respective annealing conditions due to larger crack length for larger specimen (Figure 5a and b). Note, in all annealed cases, the maximum P/P_o is higher than their as received counterparts, and the d at maximum P/P_o also increases for the stable fracture cases (Figure 5b).

The RT elastic toughness, K_{Im} and elastic plastic toughness, K_{Jm} at maximum load are shown in Figure 5c and d, respectively, and tabulated in Table 4. The average K_{Im} for 1x 90-97W specimens before and after 1300ºC/24h annealing does not change (36 ± 1 vs. 37 ± 1 MPa√m) (Table 4). As reported in Reference [18], the K_{Im} for as-received 3x specimens increases from 36 ± 1 MPa√m for 1x to 50 ± 3 MPa√m for 3x up to 95W. However, the K_{Im} for 1x and 3x 97W specimens are essentially the same (Table 4). The 1300ºC/24h annealed 4x specimens show much higher K_{Im} than all the 1x and 3x as received or 1x annealed K_{Im}, especially for 95 and 97W alloys (Table 4). For example, the 4x 95W annealed specimens show increase in K_{Im} to 65 ± 2 MPa√m from 3x as received (49 ± 1 MPa√m) and 1x as received (42 ± 6 MPa√m) condition. However, K_{Im} for 90W remains same for the larger specimens before and after annealing. In contrast, higher time and temperature annealing continuously improves K_{Im} for as received 3x large 97W from 38 ± 4 MPa√m to 43 MPa√m at 1100ºC/1h, to 47 MPa√m for 1200ºC/1h and then to 55 ± 3 MPa√m for 1300ºC/24h (Table 4, Figure 5c).

Table 4. RT maximum load fracture toughness ($K_{Jm,}$ in MPa√m) of as received [13,18] and annealed WHAs

Conditions	90W		92.5W		95W		97W	
	K_{Im} MPa√m	K_{Jm} MPa√m	K_{Im} MPa√m	K_{Jm} MPa√m	K_{Im} MPa√m	K_{Jm} MPa√m	K_{Im} MPa√m	K_{Jm} MPa√m
1x As received	36 ± 4	97 ± 18	39 ± 4	96 ± 12	42 ± 6	107± 14	36 ± 5	69 ± 12
1x annealed-1323	37 ± 0	127±11	37 ± 1	100 ± 7	38 ± 1	117 ± 2	35 ± 1	98 ± 17
3x as received	52 ± 2	92 ± 6	50 ± 3	83 ± 11	49 ± 1	75 ± 4	38 ± 4	38 ± 4
4x annealed-111							43	43
4x annealed-121							47	47
4x annealed-1324	53 ± 4	120 ± 4	-	-	65 ± 2	125 ± 6	55 ± 3	73 ± 29

The RT maximum load fracture toughness, K_{Jm} for 1x as received condition is ≈ same up to 95W (≈ 100 ± 15 MPa√m), in spite of contiguity increase (Tables 1 and 4, and in [13,18]). The as received 97W shows relatively smaller K_{Jm} with an average ≈ 69 ± 12 MPa√m. The 1300 ºC/ 24 h anneal on improves the fracture toughness for all the 1x WHAs up to 42% (for 97W), except for 92.5 WHA which shows negligible improvement (Table 4, Figure 5d). As seen from Figure 5a, such improvements for annealed 1x WHAs are the results of the combination of higher maximum P/P_o (though lower σ_o for annealed condition helps for higher P/P_o), and higher d at P_m/P_o. Note that the standard deviation for the 1x annealed specimens is reduced compared to 1x as received conditions (Table 4). Again, this suggests that annealing helps to homogenize the microstructure. Figure 5d and Table 4 also show the average K_{Jm} of the as received 3x specimen decreases between 90W and 95W from 92 to 72 MPa√m, averaging 83 ± 8 MPa√m compared to as received 1x 90-95W specimens (average ≈100 ± 15 MPa√m). The as received 3x toughness again experiences a large decrease at 97W, to an elastic K_{Im} ≈ 38 ± 4 MPa√m from it's as received 1x toughness (69 ± 12 MPa√m). In contrast, 1300ºC/24h annealed 4x WHAs improve the RT K_{Jm} from 120 ± 4 MPa√m for 90W to 125 ± 6 MPa√m for 95W. Indeed, the specimen size effect is minimal for 1300ºC/24h annealed 90-95W WHA with much improved toughness than the as received conditions. For the 4x 97W, one of two

1300 ºC/24h specimens show some yielding from elastic loading line before failed by unstable fracture that records K_{Jm} = 94 MPa√m, whereas the other one fracture unstably at elastic load line with $K_{Im} = K_{Jm} \approx 53$ MPa√m, averaging $K_{Jm} \approx 73 \pm 29$ MPa√m (Table 4). The K_{Jm} for the 1300ºC/24h annealed specimens is ≈ 9 to 16 times higher than typical monolithic W toughness ($K_{Ic} \approx 8 \pm 4$ MPa√m). The 1100ºC/1 and 1200ºC/1h annealed 4x 97W shows improvements in elastic toughness compared to 3x as received 97W, however in all these cases, the plastic contribution is zero.

Damage mechanism for tensile specimens

Figure 6 shows the side surface SEM micrographs for the RT tensile tested WHAs for as received and annealed conditions. The lower magnification SEM images for the as received 90W to 97W WHAs are shown in Figure 6a-d, whereas for annealed 90W to 97W WHAs are shown in Figure 6e-h. Relatively higher magnification SEM images for the respective alloys are shown in Figure 6i-l for as received and in Figure 6m-p for annealed conditions. It can be seen from the lower magnification SEM images for as received WHAs (Figure 6a-d) that the number of side surface cracks or damaged area reduce with increasing W% in the WHA alloys. The qualitative crack density is also reduced away from the fracture tip for the same specimen. Corresponding high magnification SEM images show that the W particles are deformed, micro cleaved, arrested, and blunted by the DP phases for the lower W% WHAs (i.e., 90W and 92.5W, Figure 6i,j). These cracks become much sharper with increasing W contents that interconnect to span several particles before failure without troubling neighbouring particles, especially for as received 95/97W WHAs (Figure 6k,l), responsible for their lower ductility. For the as received conditions, the DP effectively holds, carries, and transfers the load to W particles; hence, they deform simultaneously before failure. Details tensile test damage development for as received WHAs can be found in Reference [13].

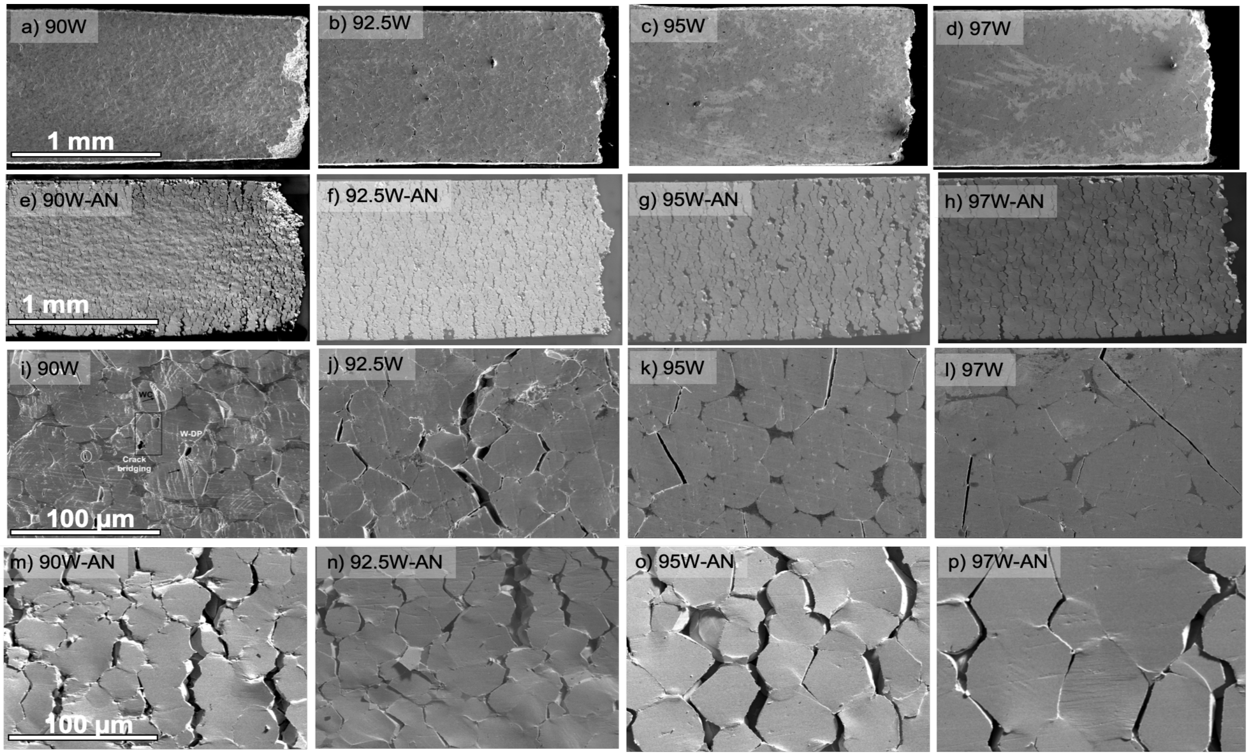

Figure 6. SEM micrographs on the side surface tensile specimens for a-d) as received, and e-h) 1300 ºC/24 h annealed WHA's for 90W, 92.5W, 95W and 97W, respectively. Higher magnification SEM images for respective WHAs are shown in (i-l) as received and (m-p) annealed conditions. Scale bars for the respective rows are shown in the first column.

In contrast to as received WHAs, all the annealed WHAs, including 97W, show well distributed damage development throughout the gage length (Figure 6e-h). High magnification side surface SEM micrographs for annealed tensile specimens also reveals that the damage mechanism had been changed from W-particle micro cleaved-arrest-blunt mechanism for as received condition to W-W, W-DP decohesion and DR dominated mechanism for annealed condition (Figure 6m-p). The 1300ºC/24 h annealing might help homogenize the composite microstructure and soften the lower melting point (MP ≈ 1500ºC) DP compared to high MP (≈ 3410ºC) W particles. Indeed, the annealed DP phase is ≈ 30% softer than the annealed W phase (299 vs. 421 $HV_{0.01}$). Therefore, mostly the DP phase all over the gage length has been deformed, whereas W particles remain relatively undeformed. Global DP deformations, especially for 95W and 97W WHAs, help to improve overall ductility for annealed WHA compared to their as received counterpart.

The SEM micrographs on the fractured face of the broken RT tensile as received and annealed WHA specimens are shown in Figure 7 that manifests all well-known four local failure modes, namely: W-W interparticle fracture (WW), W cleavage (WC), W-NiWFe interfacial debonding (WD), and NiWFe ductile phase rupture (DR). However, as evident from the side surface observations, fractured face also shows a relatively higher number of WC for the as received condition, whereas more DR is observed for the annealed condition for the respective WHA alloy.

Damage mechanism for 3PB bar fracture toughness specimens

Representative side view SEM images for as received and 1300ºC/24h annealed 1x 90W to 97W 3PB bar specimens are shown in our previous report [17], and selectively here in Figure 8a and b for 1x as received 90W and 97W, and in Figure 8e and f, for 1x annealed 90W and 97W specimens, respectively. For all the 1x as received WHA's, tests show stable crack growth, accompanied by a large numbers of particle sized WC blunted microcracks in the process zone with decreased density from lower to higher content WHAs (Figure 8a,b and References [13,17]). Some W-DP interfacial debonding (WD) and WW interface fracture events are also observed as shown in higher magnification images in Figure 9a,b. Like in the tensile tests, cleaved and unbroken W particles are also deformed along the principal stress direction. The strain in W particles normal to the loading direction, including the blunted microcracks, is again higher in the 90W WHA compared to that in 97W WHA. Nevertheless, in general, all these events develop a new toughening mechanism that involves process zone microcrack formation, arrest, blunting, and bridging by DP, as opposed to the classical macro crack bridging and deflection toughening. Detailed damage mechanism for the RT as received WHAs can be found in Reference [13].

The side surface damage profile for fracture toughness annealed 1x specimens shows similar events like the tensile damage mechanism for annealed WHAs (Figures 6 and 8e,f). Opposite to the as received damage profile, the 1300ºC/24h annealed WHAs show a well distributed plastic process zone, nearly equal in the area (or volume), irrespective of WHA alloys, though the density of damage is lower for higher W content annealed WHAs due to larger particle size as shown in Figure 8e,f and in [17]. High magnification SEM images on the side surface annealed 1x 90W and 97W WHA shown in Figures 9d and e, respectively, reveal the shifting of damage mechanism to ductile phase deformation and decohesion dominated mechanism from process-zone W particles micro cracking, arrest, and blunting mechanism for as received WHAs.

Figure 8c shows stable crack growth in the as received 3x 90W alloy test, again with extensive micro cracking, that happens up to 95W. In contrast, Figures 8d and 9c show that elastic fracture with a single, unstable macro crack occurs in the as received 3x test of a 97W alloy. Figure 8g and h show the 1300C/24h annealed 4x 90W and 97W side surface, respectively, and reveal the same toughening mechanisms of 1x annealed specimens. However, 4x 97W annealed specimen shows very minimal side surface damage compared to 4x 90W, but higher process zone damage than the as received 3x 97W, further confirms unstable crack growth with some yielding (Figures 5b, 8d,h and 9c,f).

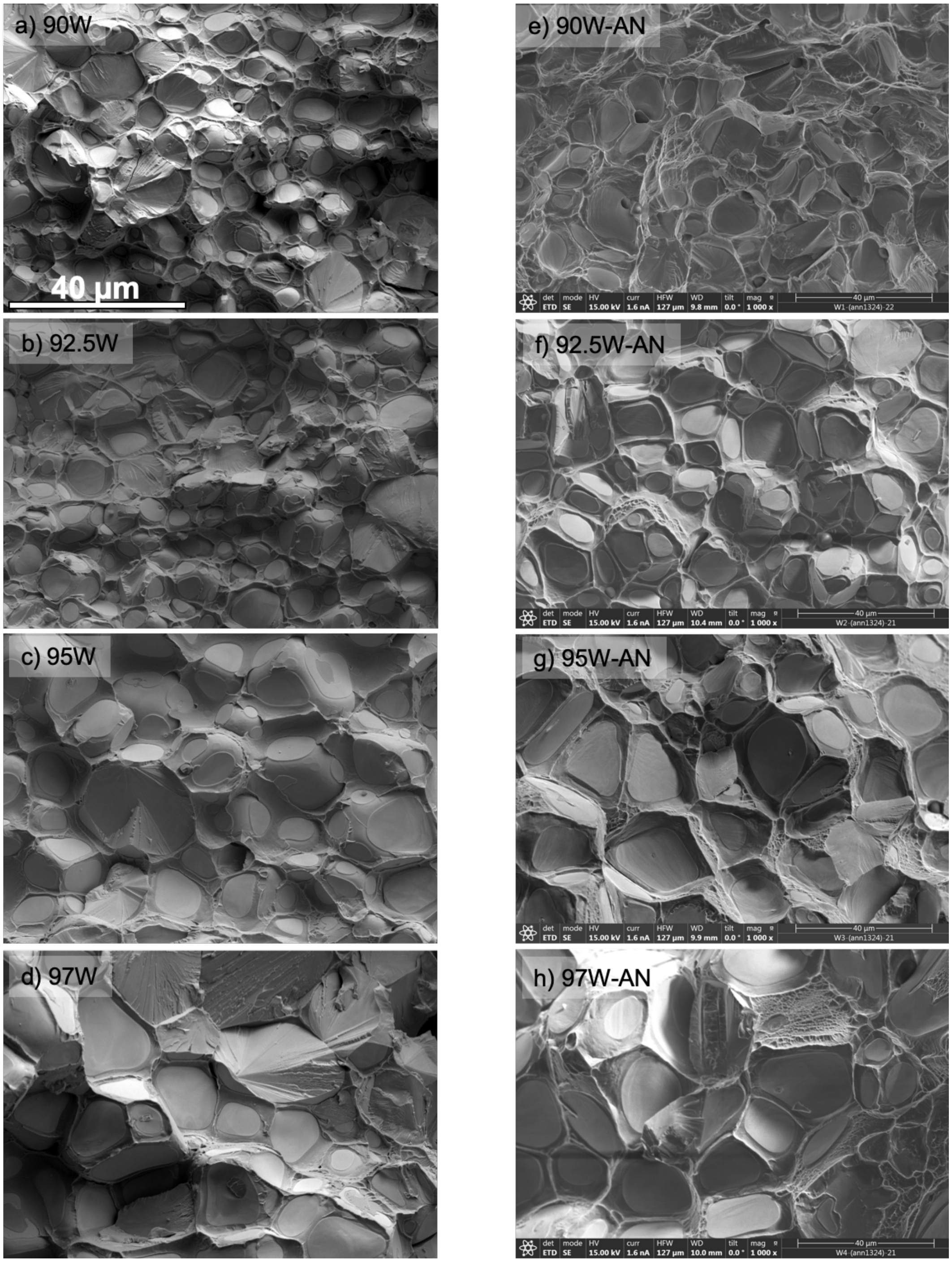

Figure 7. SEM micrographs on the fractured face for tensile specimens for: a-d) as received, and e-h) 1300 ºC/24 h annealed WHA's for 90W, 92.5W, 95W, and 97W, respectively.

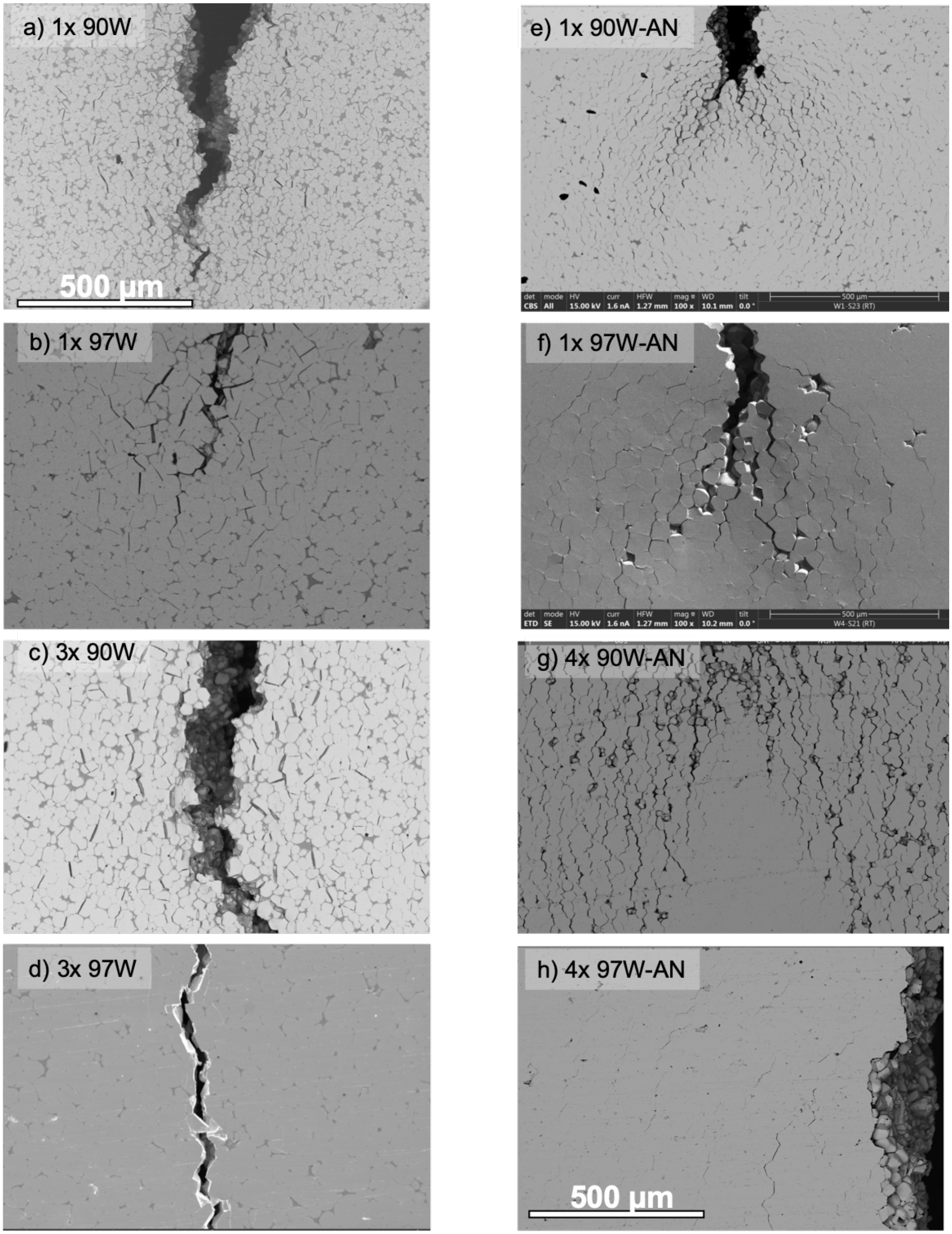

Figure 8. Low magnification, side surface SEM micrographs for the fracture toughness WHAs specimens: a-d) as received; and e-h) 1300 ºC/24 h annealed condition. Scale: 500 µm.

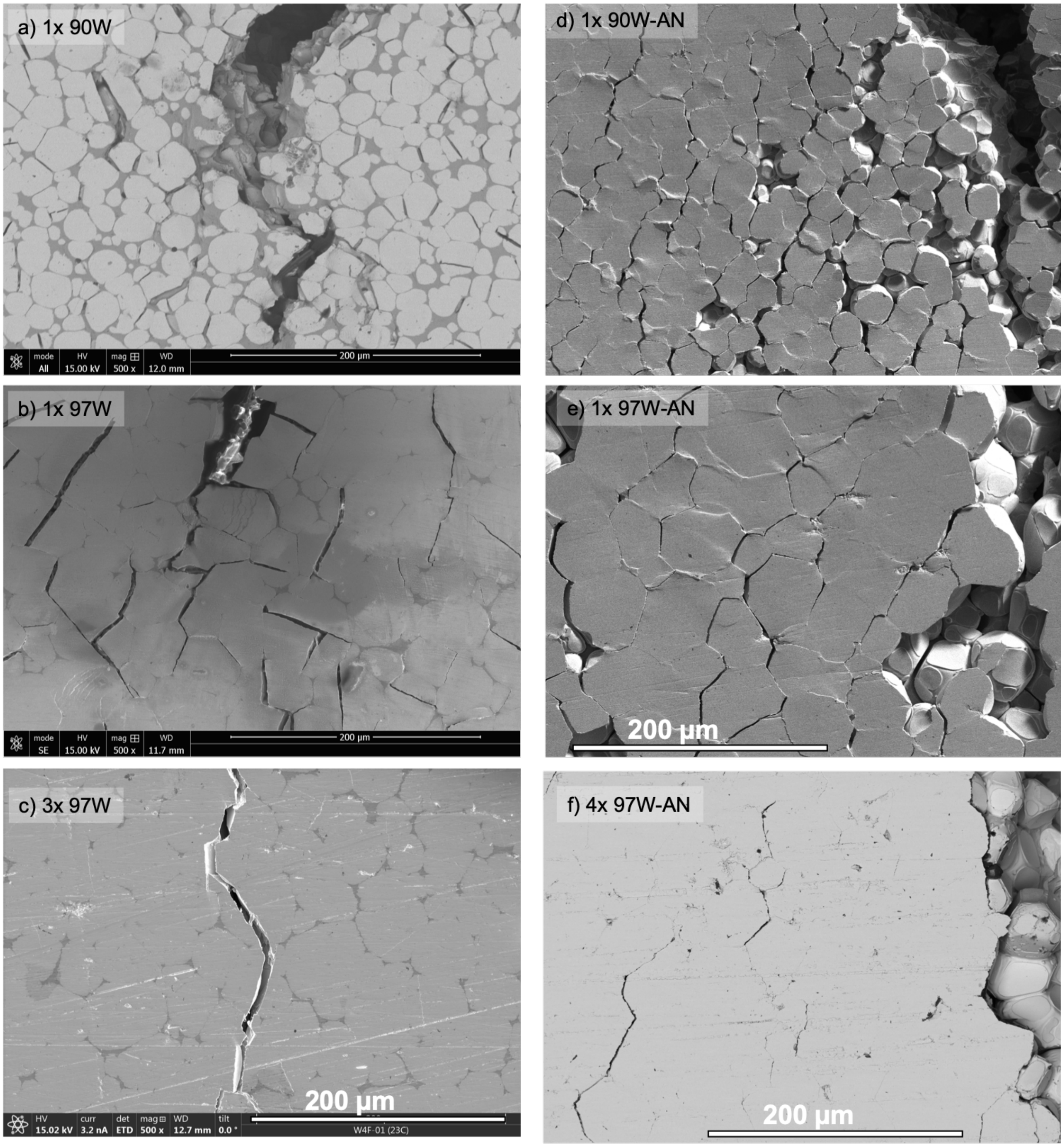

Figure 9. High magnification, side surface SEM micrographs for the fracture toughness WHAs specimens: a-c) as received 1x 90W (a), 1x 97W (b), and 3x 97W (c); and d-f) 1300 ºC/24 h annealed 1x 90W (d), 1x 97W (e), and 4x 97W, respectively. Scale: 200 µm.

Figure 10 shows the high magnification SEM images probed on the fractured face of 3PB bars, both for as-received (Figure 11a, b, and c for 1x 90W, 1x 97W, and 3x 97W, respectively), and 1300ºC/24h annealed (Figure 11d, e, f for 1x 90W, 1x 97W, and 4x 97W, respectively) conditions. All four local fracture modes (i.e., WW, WC, WR and DR) in all cases were observed, and measured by line intercept method (LIM) that are shown in Table 5 and plotted in Figure 11 for the 1x specimens. The variation of local fracture modes for the respective alloys before and after annealing seems negligible, though qualitatively, the presence of

DR seems higher for the respective annealed WHAs (indicated by red arrows in Figure 10d-f). Also note, while the as received 3x 97W show cleavage dominated fracture (Figure 10c), the 1300ºC/24h annealed 4x 97W show W-W particle decohesion domination, with some WC and DR (Figure 10f). For the 1100ºC/1h and 1200ºC/1h annealed 4x 97W, the side surface and fractured face damage profiles (not shown here) are nearly identical to the as received 3x 97W (Figures 9c and 10c).

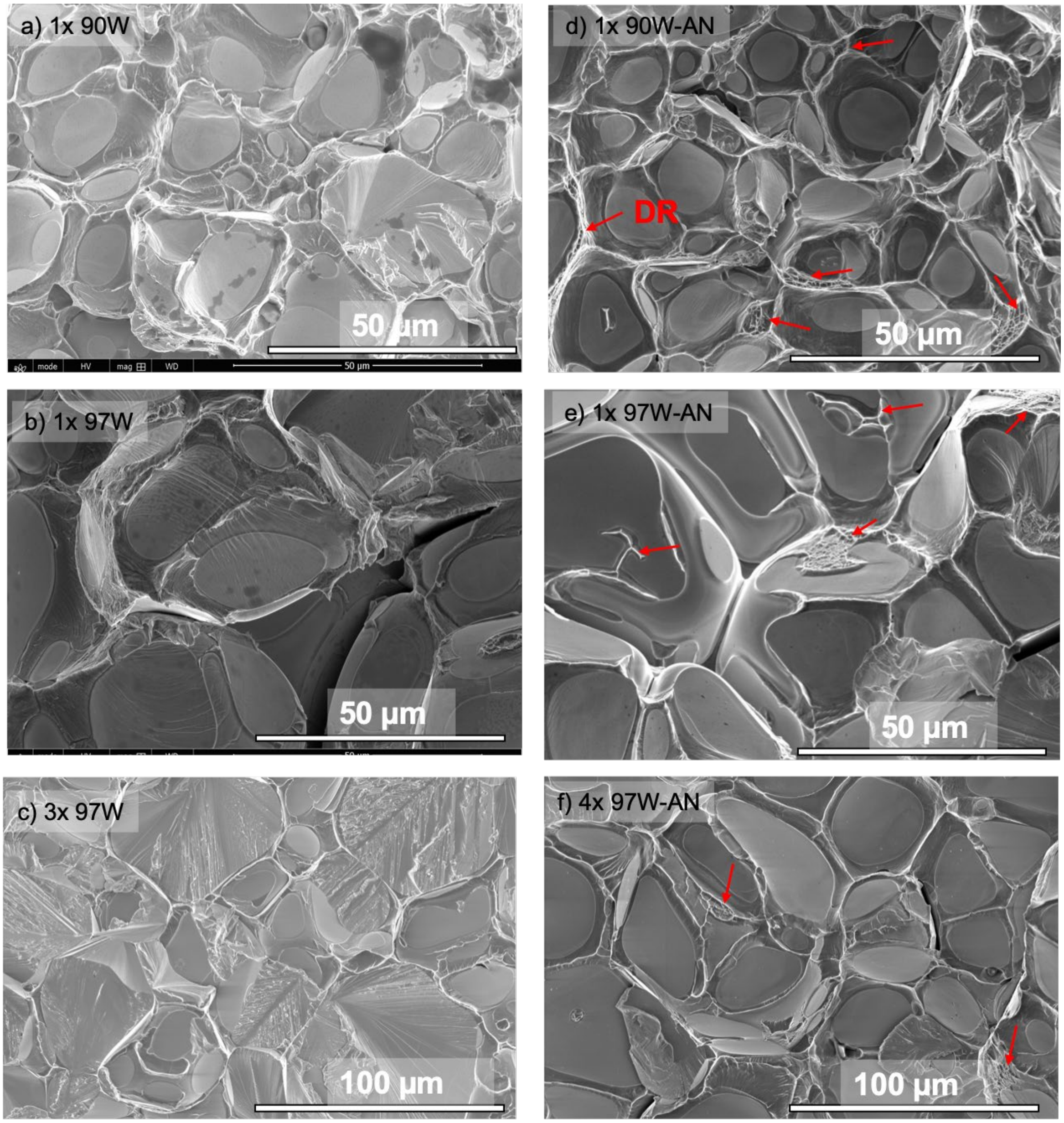

Figure 10. High magnification, SEM micrographs for the fractured face fracture toughness WHAs specimens: a-c) as received 1x 90W (a), 1x 97W (b), and 3x 97W (c); and d-f) 1300ºC/24h annealed 1x 90W (d), 1x 97W (e), and 4x 97W, respectively.

Table 5. The percentage of local fracture features from toughness fractographs of 1x WHAs

WHAs	Condition	WW	WC	WD	DR
90W	As received	31.7	12.0	44.1	12.2
	Annealed	35.4	8.8	45.7	10.1
92.5W	As received	37.1	10.9	40.5	11.5
	Annealed	47.8	7.7	37.2	7.3
95W	As received	42.6	13.5	32.8	11.1
	Annealed	45.2	13.7	33.5	7.6
97W	As received	67.2	17.6	10.8	4.4
	Annealed	56.2	22.5	16.9	4.4

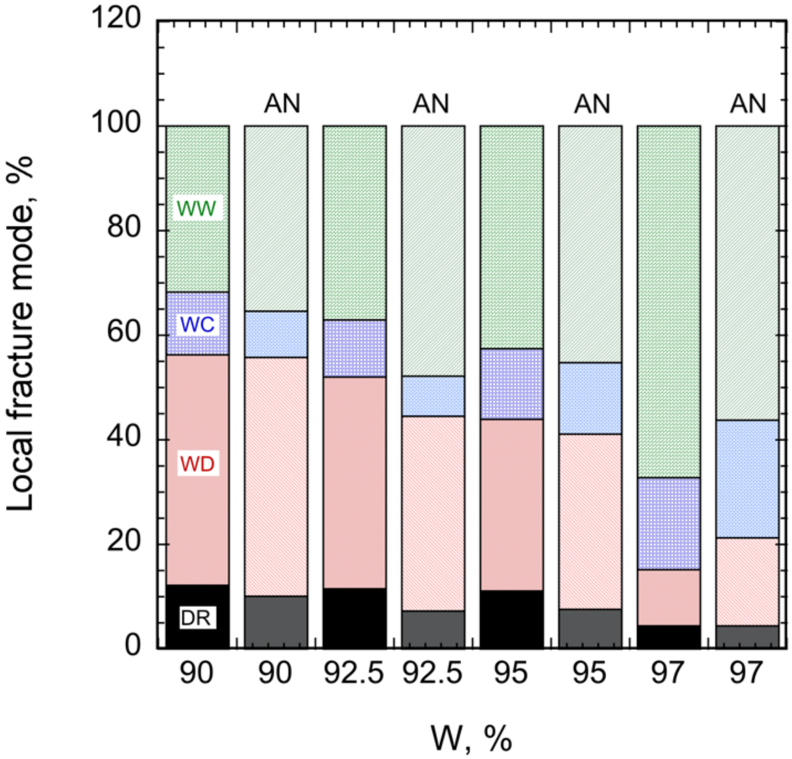

Figure 11. Local fracture modes for all the as received and annealed 1x 90 to 97 W WHAs.

Conclusion

High temperature annealing performed on four different WHAs from 90W to 97W reveals that 1300ºC/24h annealing has minimum effect on microstructure when compared with the as received condition. After annealing, the HV reduces for higher W content WHAs (16% for 97W). However, tensile strength almost remains the same for all alloys at both conditions, though the uniform and total elongation doubles for 95W and 97W. After 1300 ºC/24h annealing, RT fracture toughness for all 1x WHAs also improves up to 42% (for 97W), except 92.5W WHA, which remains almost the same. The 1300ºC/24h anneal also improves the K_{Im} and K_{Jm} for the 4x WHAs, especially for higher W content WHAs. Damage development mechanisms, both for RT tensile and fracture toughness specimens, also shift from process zone W particles micro crack formation, and dilatational toughening for the as received condition to W-W particles and W-DP decohesion-based mechanism for annealed WHAs.

Fracture toughness tests on the shallow cracked (a/W ≈ 0.2) 6x 95W (nominal dimension: 90/20/10 mm) has been performed from RT down to liquid nitrogen temperature. In all cases, the fracture propagates unstably. Next, we will perform high temperature tests on these shallow cracked 6x 95W specimens until stable crack growth occurs. High temperature tests of fracture toughness and subcritical crack growth rates will be initiated.

Acknowledgments

We like to acknowledge the support provided by United States Department of Energy (US DOE) through the Office of Fusion Energy Sciences under contract to University of California, Santa Barbara DOE-Fusion 8-442520-22419-3. The U. S. National Science Foundation supported California Nanoscience Institute provided facilities critical the success of this research.

References

[1] Y. Şahin, Recent progress in processing of tungsten heavy alloys, J. Powder Technol. 2014 (2014) 1–22.
[2] K. Hu, X. Li, X. Ai, S. Qu, Y. Li, Fabrication, characterization, and mechanical properties of 93W-4.9Ni-2.1Fe/95W-2.8Ni-1.2Fe/95W-2.8Ni-1.2Fe-1Al2O3 heavy alloy composites, Mater. Sci. Eng. A. 636 (2015) 452–458.
[3] X. Gong, J. Fan, F. Ding, Tensile mechanical properties and fracture behavior of tungsten heavy alloys at 25-1100 °C, Mater. Sci. Eng. A. 646 (2015) 315–321.
[4] U.R. Kiran, A. Panchal, M. Sankaranarayana, G.V.S.N. Rao, T.K. Nandy, Effect of alloying addition and microstructural parameters on mechanical properties of 93% tungsten heavy alloys, Mater. Sci. Eng. A. 640 (2015) 82–90.
[5] C. Henager Jr, W. Setyawan, T. Roosendaal, N. Overman, B. Borlaug, E. Stevens, K. Wagner, R. Kurtz, G.R. Odette, B. Nguyen, K. Cunningham, Ductile-phase toughened tungsten for plasma-facing materials in fusion reactors, Int. J. Powder Metall. 53 (2017) 53–69.
[6] M. Scapin, Mechanical characterization and modeling of the heavy tungsten alloy IT180, Int. J. Refract. Met. Hard Mater. 50 (2015) 258–268.
[7] R. Neu, H. Maier, M. Balden, S. Elgeti, H. Gietl, H. Greuner, A. Herrmann, A. Houben, V. Rohde, B. Sieglin, I. Zammuto, Investigations on tungsten heavy alloys for use as plasma facing material, Fusion Eng. Des. 124 (2017) 450–454.
[8] R. Neu, H. Maier, M. Balden, R. Dux, S. Elgeti, H. Gietl, H. Greuner, A. Herrmann, T. Höschen, M. Li, V. Rohde, D. Ruprecht, B. Sieglin, I. Zammuto, Results on the use of tungsten heavy alloys in the divertor of ASDEX Upgrade, J. Nucl. Mater. 511 (2018) 567–573.
[9] H. Sattar, S. Jielin, H. Ran, M. Imran, W. Ding, P. Das Gupta, H. Ding, Impact of microstructural properties on hardness of tungsten heavy alloy evaluated by stand-off LIBS after PSI plasma irradiation, J. Nucl. Mater. 540 (2020) 152389.

[10] Q. An, A. Elshafiey, L. Huang, D.A. Hammer, M. Hassani, Plasma and X-ray radiation-induced damage mechanisms in a tungsten heavy alloy, J. Nucl. Mater. 539 (2020) 152325.

[11] G.R. Odette, M.E. Alam, K. Cunningham, Ductile-Phase Toughened Tungsten for Plasma Facing Materials, DOE-UCSB-ER54275, United States, 2019.

[12] T. Laas, K. Laas, J. Paju, J. Priimets, S. Tõkke, B. Väli, V. Shirokova, M. Antonov, V.A. Gribkov, E. V. Demina, V.N. Pimenov, M. Paduch, R. Matulka, M. Akel, Behaviour of tungsten alloy with iron and nickel under repeated high temperature plasma pulses, Fusion Eng. Des. 151 (2020).

[13] M.E. Alam, G.R. Odette, On the remarkable fracture toughness of 90 to 97W-NiFe alloys revealing powerful new ductile phase toughening mechanisms, Acta Mater. 186 (2020) 324–340.

[14] M.E. Alam, J. Wang, C.H. Henager, W. Setyawan, G.R. Odette, The effect of hot rolling on the strength and fracture toughness of 90W–7Ni3Fe tungsten heavy metal alloys, Mater. Sci. Eng. A. 824 (2021) 141738.

[15] A. Upadhyaya, Processing strategy for consolidating tungsten heavy alloys for ordnance applications, Mater. Chem. Phys. 67 (2001) 101–110.

[16] W.D. Cai, Y. L, R.J. Dowding, F.A. Mohamed, E.J. Lavernia, A review of tungsten-based alloys as kinetic energy penetrator materials, Rev. Part. Mater. 3 (1995) 71–131.

[17] M.E. Alam, G.R. Odette, On the role of annealing on microstructure and mechanical properties of 90 to 97W tungsten heavy alloys, DOE Fusion React. Mater. Progr. Semiannu. Prog. Rep. DOE0313/71 (2021) 30–47.

[18] M.E. Alam, G.R. Odette, On the Influence of Specimen Size and Geometry on the Fracture Toughness of Tungsten Heavy Metal Alloys, J. Nucl. Mater. xxx (2022) xx–xx.

[19] M.E. Alam, G.R. Odette, C.H. Henager, W. Setyawan, Fracture Toughness of Rolled 90WNiFe Tungsten Heavy Metal Alloy, Fusion React. Mater. Progr. Semiannu. Prog. Rep. DOE0313/67 (2019) 52–65.

[20] ASTM E8M-15a, Standard Test Methods for Tension Testing of Metallic Materials, in: Annu. B. ASTM Stand., ASTM International, West Conshohocken, PA , United States, 2004: pp. 1–24.

[21] ASTM E1921-20, Standard Test Method for Determination of Reference Temperature , To , for Ferritic Steels in the Transition Range, in: Annu. B. ASTM Stand., ASTM International, 100 Barr Harbor Drive, PO Box C700, West Conshohocken, PA 19428-2959, United States, 2020: pp. 1–25.

[22] J. Wang, D. Collins, N.R. Overman, W. Setyawan, Tensile Testing and Microstructural characterization of Ductile Phase Toughened W-NiFe Alloys, Fusion React. Mater. Progr. Semiannu. Prog. Rep. DOE0313/68 (2020) 102–120.

[23] T.L. Anderson, Fracture Mechanics: Fundamentals and Applications, 3rd ed., Taylor & Francis Group, FL, USA, 2005.

[24] J.R. Davis, Properties and Selection: Nonferrous Alloys and Special-Purpose Materials, 10th ed., ASM Handbook, ASM, Metal Park, Ohio, 1993.

5. ADVANCED MANUFACTURING

No contributions this reporting period.

6. EFFECTS OF IRRADIATION

6.1 EFFECT OF Cr ON DISLOCATION LOOPS IN HEAVY ION IRRADIATED ULTRA-HIGH PURITY Fe-(3-8%)Cr ALLOYS

—Y. Li, Y. Zhao, S. Zinkle (University of Tennessee, Knoxville), A. Bhattacharya (Oak Ridge National Laboratory)

OBJECTIVE

The objective of this project is to study how Cr atoms affect dislocation loops by characterizing loop density, size distribution, and loop Burgers vector in high purity Fe and Fe-Cr model alloys after heavy ion irradiation at different temperatures.

SUMMARY

Scanning transmission electron microscopy (STEM) was used to characterize the size, density, and the Burgers vector of loops after 8 MeV Fe ion irradiation to 0.35 and 3.5 dpa at 350 or 450 °C in high purity Fe-(3-8%)Cr alloys. By the g·b method, we are examining the effect of Cr concentration and irradiation temperature on the formation of dislocation loops. At 350°C, irradiation induced dislocation loop decorated along preexisting dislocations. At 450°C 0.35 dpa, <001> planar petal shaped dislocation loops were observed, but at the higher dose (3.5 dpa), planar petal shaped dislocation loops decomposed into 2-D dislocation walls.

PROGRESS AND STATUS

Introduction

This report summarizes recent work on dislocation loop characterization in a series of ion irradiated high purity Fe-C alloys; prior work is summarized in previous progress reports[1-3]. Dislocation loops in 3Cr, 5Cr, and 8Cr were examined. The irradiations examined in this report were performed at 350°C or 450°C and the midrange doses were 0.35 or 3.5 dpa. This investigation is a continuation of the previous work in which the same samples were irradiated by 8 MeV Fe ions at 0.35 dpa (mid-range dose). The mid-range safe analysis region is from 750 to1250 nm, based on the method proposed by Zinkle[4].

Table 1. Alloys and irradiation conditions

450℃ 0.35 dpa 10^{-4} dpa/s	450℃ 3.5 dpa 10^{-4} dpa/s	450℃ 0.35 dpa 10^{-5} dpa/s	350℃ 0.35 dpa 10^{-4} dpa/s
Fe-3Cr	Fe-5Cr Fe-8Cr	Fe-8Cr	Fe-8Cr

All samples discussed in this report were prepared by the flash polishing method reported previously[2]. The classical g.b method was applied. Table 2 lists all the diffraction vectors g in our analysis. Loop nature analysis has been performed on Fe irradiated at 350°C and 10^{-4} dpa/s to 0.35 dpa and the loop nature has been evaluated to be predominantly interstitial type. For loops in Fe-Cr alloys, the analysis will be carried out in the future.

Table 2. Applied g vectors for loop identification in body-centered cubic (BCC) Fe-Cr system. Red cells are invisible conditions for different loops. Zero means the invisible condition and non-zero means the visible condition.

	diffraction vector (g)					
	[011] zone axis			[001] zone axis		
Burgers vector (b)	2 0 0	2 -1 1	0 -1 1	-1 1 0	-1-1 0	2 0 0
1 1 1	2	2	0	0	-2	2
1 1-1	2	0	-2	0	-2	2
1-1 1	2	4	2	-2	0	2
-11 1	-2	-2	0	2	0	-2
1 0 0	2	2	0	-1	-1	2
0 1 0	0	-1	-1	1	-1	0
0 0 1	0	1	1	0	0	0

Experimental Procedure

Fe-3Cr 450 °C 0.35 dpa 10^{-4} dpa/s

Similar to the irradiated samples at 450°C described in a previous semiannual report[2], large petal shaped planar dislocation loops located on {001} habit planes were observable in this sample. Besides the large complex shaped planar loops, small size isolated square <001> loops were also present, as shown in Figure 1. Additionally, ½ <111> loops were also present, but compared with <001> type loops, the ½ <111> loops were rare.

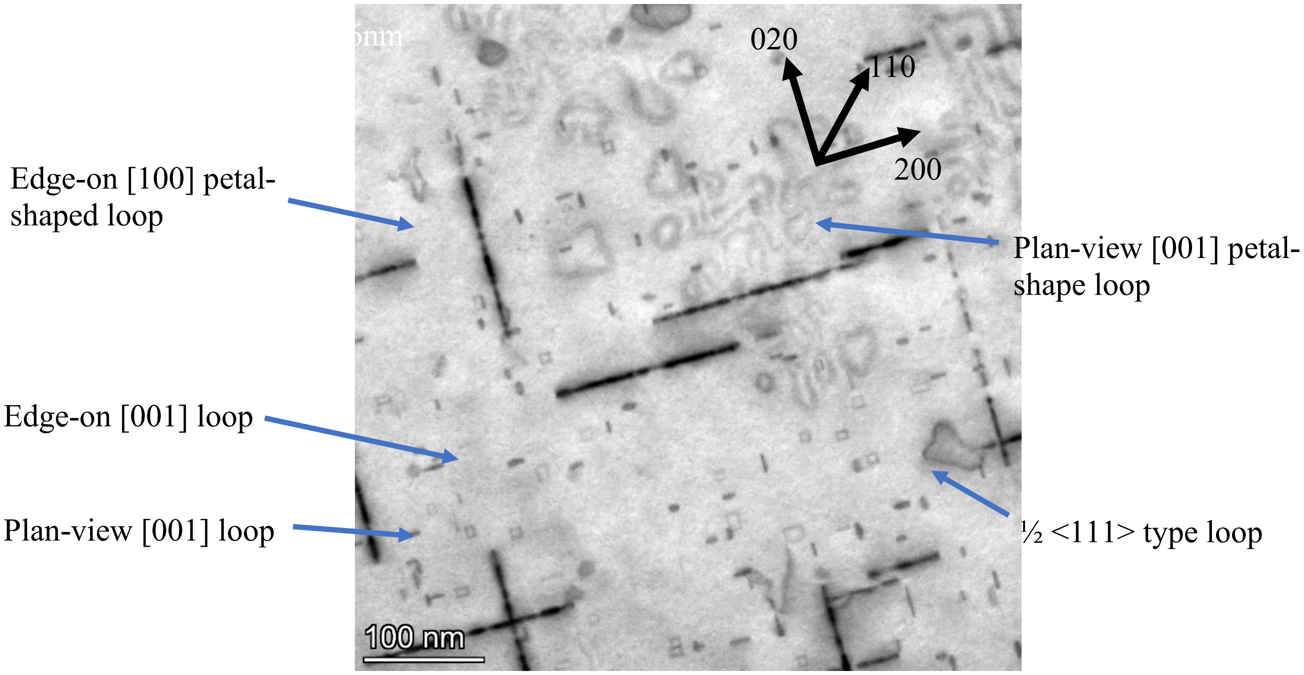

Figure 1. STEM bright field (BF) of Fe-3Cr at 450℃, 0.35dpa, 10^{-4}dpa/s safe analysis region under on-zone condition. B =001.

In the midrange safe analysis region (depth: 750-1250nm), the loop density was (1.9±0.4)×10^{21} m^{-3}, and the mean diameter of isolated loops was 13 nm. There were 261 isolated loops counted. From this, 237 were analyzed to be <001> loops, 21 loops were ½ <111> type, and 3 were not identifiable. Among the identifiable loops, 92% were <001> type. The isolated loops' size distribution was mainly concentrated near a diameter of 10 nm but the loop sizes extended up to nearly 100 nm. Lastly, ½ <111> loops mainly contributed to the large diameter tail of the size distribution, as shown in Figure 2.

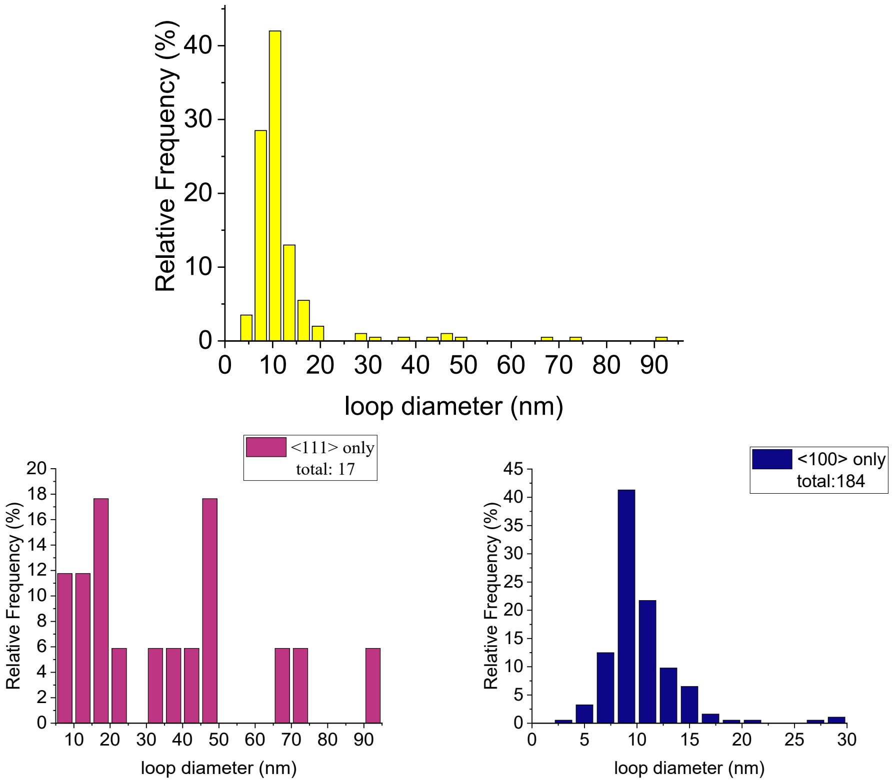

Figure 2. Isolated loop size distribution in Fe-3Cr irradiated at 450℃, 0.35dpa, 10-4dpa/s. The upper panel is the diameter distribution including all isolated loops and the lower panel is about two diameter distributions for ½ <111> and <100> loop, respectively.

Fe-8Cr 450 °C 0.35 dpa 10^{-5} dpa/s

Figure 3 shows the formation of petal shaped planar dislocation loops and numerous small "black dot" defect clusters in Fe-8Cr irradiated at 450°C to a mid-range dose of 0.35 dpa at 10^{-5} dpa/s. By the g.b analysis method and the circular loop shape revealed by the (g,4g) weak beam dark field (WBDF) method, the black dots were identified as small dislocation loops. In the midrange safe analysis region (depth: 750-1250 nm), the small black dot feature density was (1.0±0.2)×10^{21} m^{-3} and the mean diameter was 6 nm. The loop diameter distribution is shown in Figure 4. From this, 218 were identified as <001> loops, 45 were identified as ½ <111> loops and 70 were not identifiable. Among the identifiable loops, 83% were <001> loops.

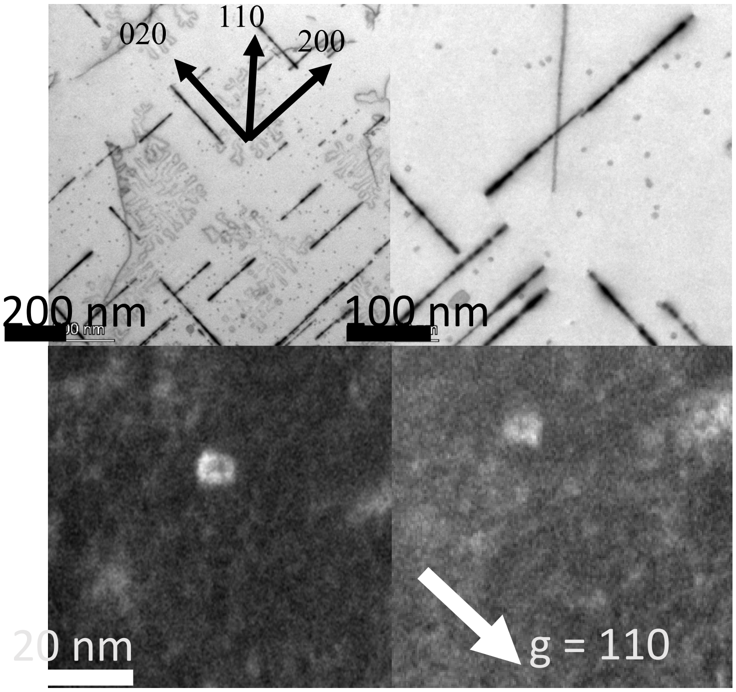

Figure 3. Loop microstructure in the safe analysis region in Fe-8Cr °C 0.35 dpa 10^{-5} dpa/s. The upper panels are STEM-BF under the on-zone condition in lower and higher magnification. The lower panel shows two examples of circular shape defects by (g,4g) WBDF. B =001.

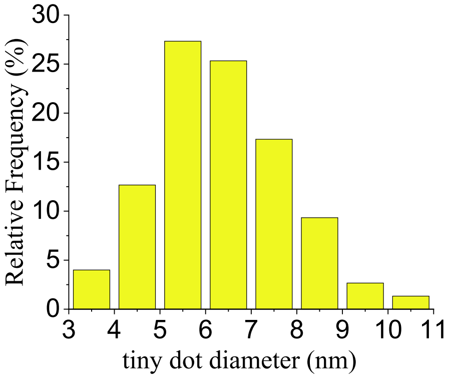

Figure 4. The diameter distribution of small loops in Fe-8Cr at 450 °C 0.35 dpa 10^{-5} dpa/s.

<u>Fe-5Cr 450 °C 3.5 dpa 10^{-4} dpa/s</u>

As shown in Figure 5, under [001] zone observation, long and thick dashed black line structures on (100) and (010) planes were observable. However, the petal shaped structures observed in other Fe-Cr alloys irradiated at 450°C to a lower dose of 0.35 dpa were absent in the 3.5 dpa Fe-5Cr sample. Instead, smaller dislocation loop features were present. Under g $=\bar{1}\bar{1}0$ two-beam viewing conditions, the sample was slightly tilted away from the on-zone position. Due to this slight specimen tilt that enabled the “thick dashed line” defects to be observed at an inclined position, finer details can be seen. We observed the dashed black lines consist of numerous <001> dislocation loops. Each black line was composed of loops with the same Burgers vector. By g.b analysis, the faint loops under the on-zone condition were [001] loops. A 1-D structure called dislocation rafts has been observed[5, 6]. It refers to dislocation loops aggregating into a line. However, the complex structures observed in our samples are not dislocation rafts. Combining these two configurations in the preceding text, these long dashed black line structures associated with defect clusters on {001} habit planes were identified to be 2-D dislocation walls.

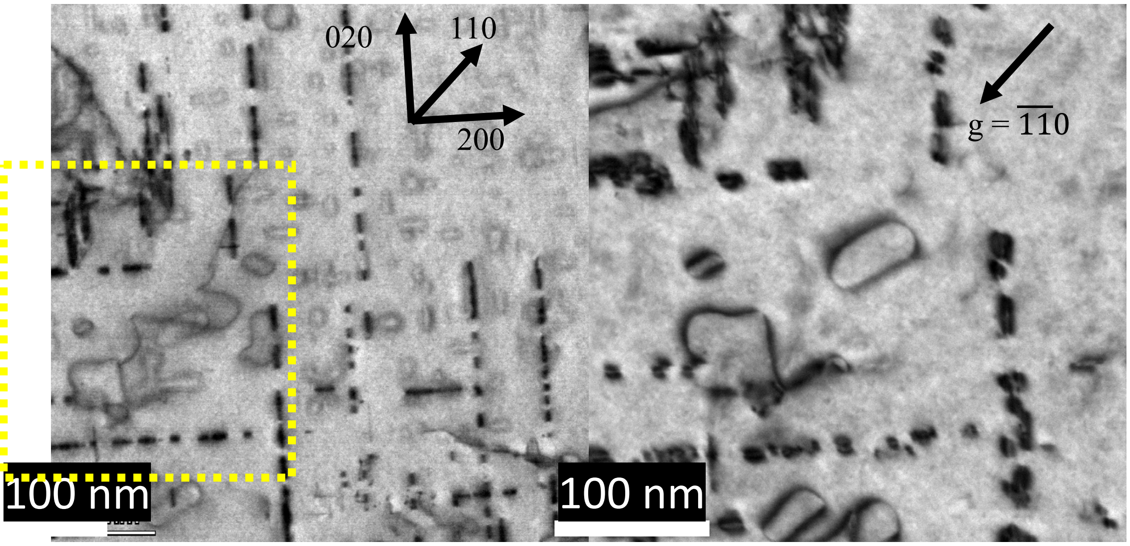

Figure 5. The safe analysis region of 5Cr 450 °C 3.5 dpa 10-4 dpa/s. (left) STEM-BF was under [001] on-zone condition. (right) STEM-BF of the same region under the two-beam approximation. The right micrograph is the region marked in the left micrograph in higher magnification.

In Figure 6, two petal shaped loops appear to be undergoing a decomposition process (dissolution of the individual irregular shaped defect clusters that make up the larger petal shaped feature). The decomposition is more pronounced in the center of the petal shaped loops. These two examples indicate the 2-D dislocation wall structure that was prevalent in the observed microstructure was due to the decomposition of petal-shaped planar dislocation loops.

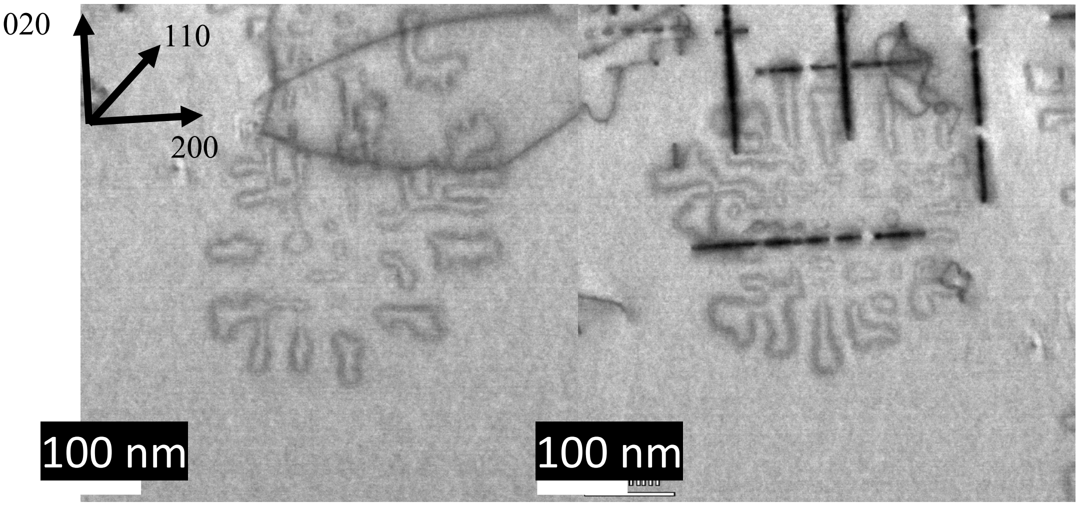

Figure 6. Two petal shaped planar dislocation loops were in the decomposition process at the depth of 2300 nm. The STEM-BF images were under on-zone condition, B = 001.

In the safe analysis region (depth: 750-1250 nm), the loop density was $(7.2\pm1.44)\times10^{21}$ m^{-3} and the mean diameter was 28 nm. The loop diameter distribution is shown in Figure 7. There were 514 loops counted. From this 457 were identified as <001> loop, 39 were identified as ½ <111> loop and 18 were not identifiable. Among the identifiable loops, 89% were <001> loops.

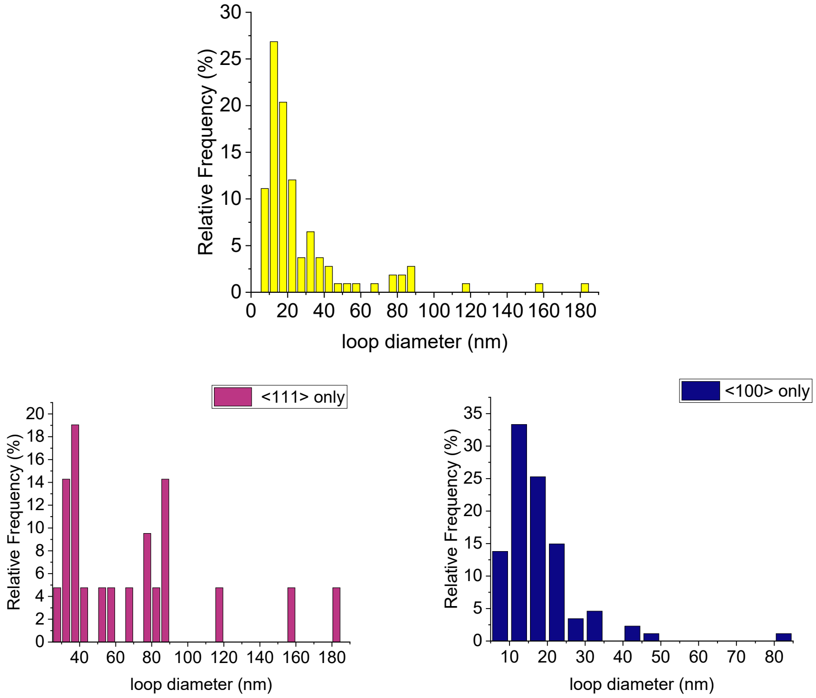

Figure 7. Loop diameter distribution in 5Cr 450 °C 3.5 dpa 10-4 dpa/s.

Fe-8Cr 450 °C 3.5 dpa 10^{-4} dpa/s

The general features were like those in 5Cr at 450°C 3.5 dpa 10^{-4} dpa/s but numerous small dots were created in 8Cr compared to the 5 Cr sample, as shown in Figure 8. The loop density was $(4.5\pm0.9)\times10^{21}$ m^{-3}. The mean diameter of loops was 13 nm. The loop size distribution is shown in Figure 9. There were 305 loops counted for Burgers vector analysis. Of this 270 loops were <001> type, 5 loops were ½ <111> type and 30 loops were not identifiable. Among the identifiable loops, the <001> fraction was 98%. Compared with 8Cr irradiated at 450°C and 10^{-5} dpa/s to 0.35 dpa, no intact petal shaped loop was observed in 8Cr irradiated to 3.5 dpa. The loop densities in both 8Cr samples were similar and <001> loops were dominant in both 8Cr samples. The mean loop diameter was larger in 8Cr irradiated to 3.5 dpa.

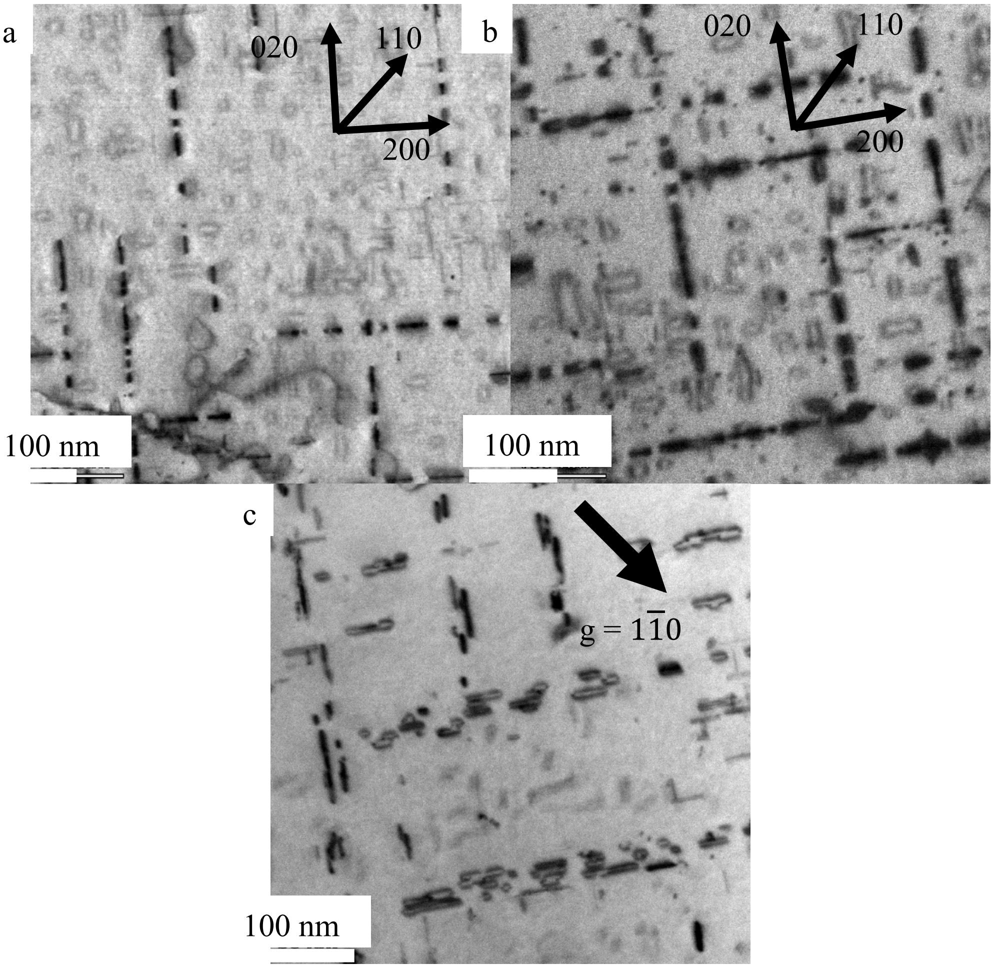

Figure 8 (a) the safe analysis region in 5Cr and (b) the safe analysis region in 8Cr. Both images were taken under on-zone condition, B = 001. (c) Finer details of 'black line' structures were observable due to the inclined 2-D loop walls.

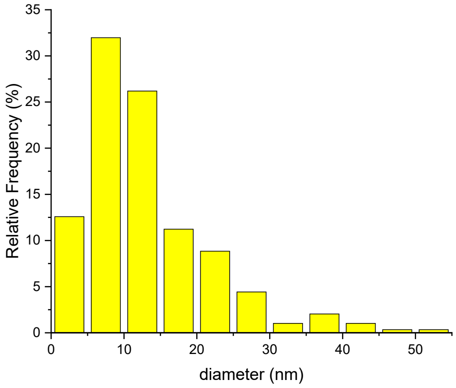

Figure 9. Diameter distribution of loops in 8Cr irradiated at 450°C 3.5 dpa 10^{-4} dpa/s.

Fe-8Cr 350 °C 0.35 dpa 10^{-4} dpa/s

The microstructure of samples irradiated at 350°C was distinct from those irradiated at 450°C in this project. Some samples irradiated at 350°C were presented in [2]. The major feature of samples irradiated at 450°C is the formation of large petal shaped planar dislocation, but the major feature of samples irradiated at 350°C was loop decoration along pre-existing dislocation lines. We will refer to the pre-existing dislocation lines as “long dislocations” in the following text. In the safe analysis region (depth: 750-1250 nm), the loop density was greatly increased in the vicinity of long dislocations; the decorating loops were preferentially distributed on one side of the long dislocations, as shown in Figure 10. Similar heterogeneous loop formation in the vicinity of network dislocations have been reported by other researchers [7-9]. The overall loop density was $(4.1\pm0.8)\times10^{21}$ m^{-3} and the loop decoration density was $(1.1\pm0.2)\times10^{22}$ m^{-3} based on the volume around long dislocations. The loop size distribution is shown in Figure 11 and the mean diameter is 7 nm. We counted 277 loops. Of these, 90 were <001> loops, 145 were <111> loops, and 42 were not identifiable. Due to the high density of loops around long dislocations, we may lose the track of loops in high angle tilting samples. Loops were only identified under [001]Z, which is enough to distinguish <001> and ½ <111> type, although the exact Burgers vector of a given loop could not be ascertained. Since all [001] loops were invisible under [001]Z, an assumption that all three types of <001> loops were created in equal probability was applied. As a result, among the identifiable loops, 48% were <001> loops.

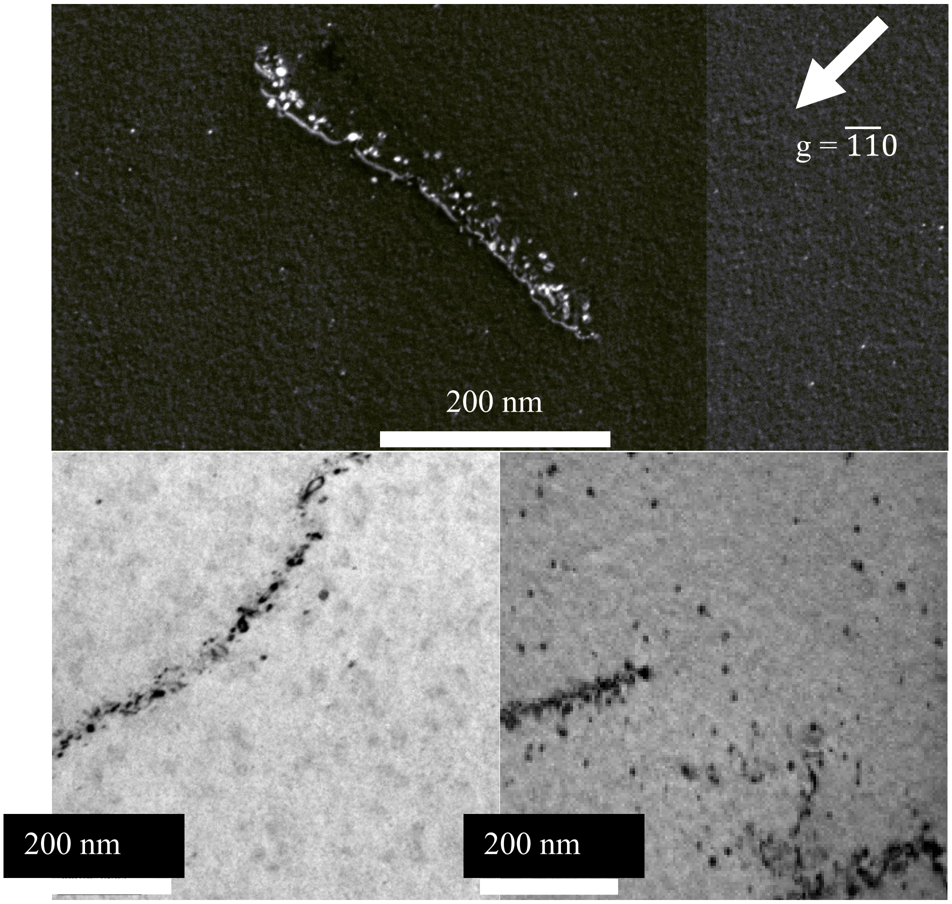

Figure 10. Safe analysis regions (a) in 8Cr at 350°C 0.35 dpa 10^{-4} dpa/s, (g,4g) WBDF, B = 001; Safe analysis regions in (b) Fe-5Cr BF, B = 001; Safe analysis regions in (c) Fe-3Cr BF, B = 001. Discussion on Fe-3Cr and Fe-5Cr was in [2].

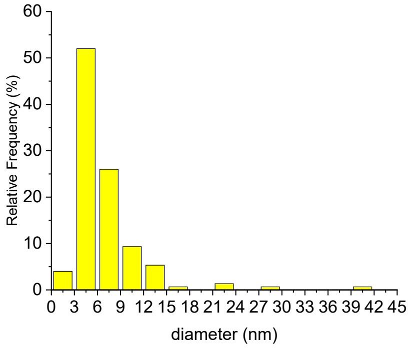

Figure 11. The size distribution of loops in 8Cr at 350°C 0.35 dpa 10-4 dpa/s.

Results

The self organization defect cluster configuration is not common in irradiated materials but this topic has been studied for decades[10-12] and the petal shaped planar dislocation loop is supposed to be a subcategory of the self organization defect. A few research groups have reported it in different materials irradiated by electrons, neutrons, and ions. Kawanishi and Ishino [13] conducted neutron experiments on FeCrNi face-centered cubic (FCC) steel. They irradiated FeCrNi and FeCrNi-X-Y (X= Ti and Nb, Y = 0C or 0.06 C). They argued the addition of extra elements into FeCrNi alloy strongly influenced the formation of petal shaped loops and all the petal shaped loops were faulted sessile loops. This is true for the addition of C into FeCrNi-X alloys (X= Ti and Nb), which only contained faulted petal shaped loops, but not true for the addition of C into FeCrNi in their experiments, which contained both perfect and faulted regular shaped loops. The results by Kawanishi indicated a correlation between sessile and/or faulted property and the formation of petal shaped loops. In BCC iron, due to its high stacking fault energy, it is generally considered to be impossible to form faulted loops [14]. Since the diffusivity of <001> loops are much smaller than that of ½ <111> loops[15], some researchers treated <001> loops in BCC Fe as sessile once the size reaches the resolution limit of diffraction contrast by transmission electron microscopy (TEM) [16]. Our result seems to support this argument, which is there is a correlation between sessile property and the formation of petal shaped loops. In Fe-3Cr irradiated at 450°C and 10^{-4} dpa/s to 0.35 dpa, the diameter of ½ <111> loops was up to ~100 nm but all petal shaped loops were <001> type structures. In Fe-8Cr irradiated at 450°C and 10^{-4} dpa/s, to 3.5 dpa, several ½ <111> loops around 200-300 nm in diameter were observed and they were not petalous, as shown in Figure 12. Years later, Kawanishi and Ishino [17] conducted another neutron experiment at the same facility on the same sample at a higher dose. No petal shaped loop was observable and part of the loops were unfaulted. Yoshida irradiated BCC Fe by 2 MeV electrons that enabled in-situ observation of the loop evolution process [18]. At 150°C and 250°C, <001> loops were formed locally at different locations but on the same or the adjacent atomic planes when the irradiation began. With increasing damage level, the <001> loops grew and more <001> loops formed. Eventually, these loops coalesced to form the complex petal shaped loops. The large petal shaped loops decomposed into smaller loops after the prolonged irradiation. Our microstructural observations are consistent with this evolution sequence: petal shaped loops formed at the lower dose (0.35 dpa) but decomposed at the higher dose (3.5 dpa). Yoshida's observation demonstrated that the formation of large petal shaped loops was via a fusion of multiple small loops. The probability of multiple <001> loops with the same Burgers vector nucleating at the same atomic plane and subsequently forming a large petal shaped loop is considered to be very low, so we hypothesize that each branch of a petal shaped planar dislocation loop is an independent <001> loop before coalescence and sits on different adjacent atomic planes having the same plane normal. To prove this idea, atomic resolution STEM micrographs will be acquired in the future.

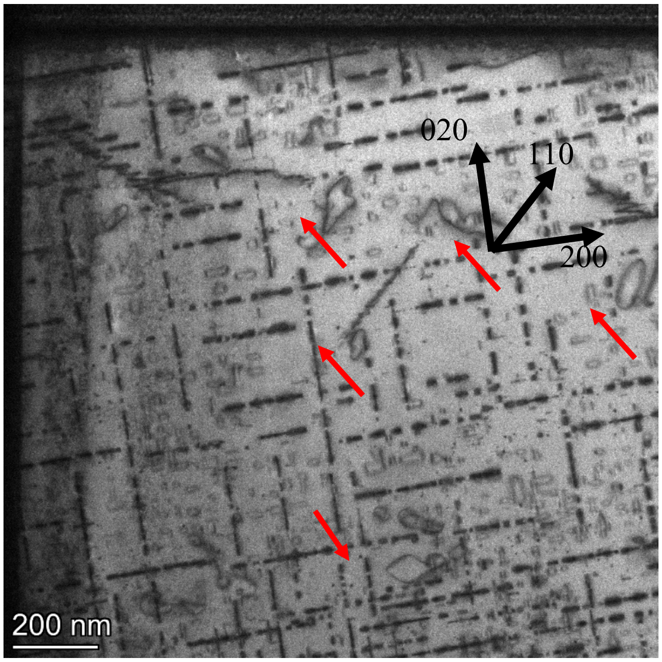

Figure 12. STEM-BF image of 8Cr at 450°C and 10^{-4} dpa/s, to 3.5 dpa under an on-zone condition, B = 001. Large ½ <111> loops are pointed by red arrows.

References

1. Li, Y., S.J. Zinkle, and A. Bhattacharya, *EFFECTS OF Cr AND C ON DISLOCATION LOOPS IN HEAVY ION IRRADIATED ULTRA-HIGH PURITY FeCr ALLOYS*, in *Fusion Materials Semiannual Progress Report For the Period Ending June 30, 2019*, F.W. Wiffen and S. Melton, Editors. DOE-ER-0313/66, Vol.66, Oak Ridge National Laboratory. p. 15-19.
2. Li, Y., et al., *EFFECT OF Cr ON DISLOCATION LOOPS IN HEAVY ION IRRADIATED ULTRA-HIGH PURITY FeCr ALLOYS*, in *Fusion Materials Semiannual Progress Report For the Period Ending June 30, 2020*, S. Melton, Editor. DOE/ER-0313/68, Vol.68, Oak Ridge National Laboratory. p. 11-21.
3. Li, Y., S.J. Zinkle, and A. Bhattacharya, *AN ELECTRON MICROSCOPE STUDY OF HEAVY ION IRRADIATED ULTRA-HIGH PURITY Fe AND Fe-Cr ALLOYS AT 350℃*, in *Fusion Materials Semiannual Progress Report For the Period Ending December 31, 2020*, S. Melton, Editor. DOE/ER-0313/69, Vol.69, Oak Ridge National Laboratory. p. 186-198.
4. Zinkle, S.J. and L.L. Snead, *Opportunities and limitations for ion beams in radiation effects studies: Bridging critical gaps between charged particle and neutron irradiations.* Scripta Materialia, 2018. **143**: p. 154-160.
5. Zinkle, S.J. and B.N. Singh, *Microstructure of neutron-irradiated iron before and after tensile deformation.* Journal of Nuclear Materials, 2006. **351**(1-3): p. 269-284.
6. Hernández-Mayoral, M., et al., *Heavy-ion irradiations of Fe and Fe–Cr model alloys Part 2: Damage evolution in thin-foils at higher doses.* Philosophical Magazine, 2008. **88**(21): p. 2881-2897.
7. Kiritani, M., *Microstructure evolution during irradiation.* Journal of Nuclear Materials, 1994. **216**: p. 220-264.
8. Hernández-Mayoral, M., C. Heintze, and E. Oñorbe, *Transmission electron microscopy investigation of the microstructure of Fe–Cr alloys induced by neutron and ion irradiation at 300 °C.* Journal of Nuclear Materials, 2016. **474**: p. 88-98.
9. Hoelzer, D.T. and F. Ebrahimi, *Effect of Copper and Nickel on the Neutron Irradiation Damage in Iron Alloys.* MRS Proceedings, 1994. **373**: p. 57.
10. Ghoniem, N.M., D. Walgraef, and S.J. Zinkle, *Theory and experiment of nanostructure self-organization in irradiated materials.* Journal of Computer-Aided Materials Design, 2001. **8**(1): p. 1-38.

11. Jäger, W., P. Ehrhart, and W. Schilling, *Microstructural evolution in metals during helium and proton irradiations.* Radiation Effects and Defects in Solids, 1990. **113**(1-3): p. 201-211.
12. Evans, J.H., *Observations of a Regular Void Array in High Purity Molybdenum irradiated with 2 MeV Nitrogen Ions.* Nature, 1971. **229**(5284): p. 403-404.
13. Kawanishi, H. and S. Ishino, *Microstructure of Fe-16Ni-15Cr alloys irradiated in JOYO.* Journal of Nuclear Materials, 1988. **155-157**: p. 806-809.
14. Osetsky, Y.N., et al., *Structure and properties of clusters of self-interstitial atoms in fcc copper and bcc iron.* Philosophical Magazine A, 2000. **80**(9): p. 2131-2157.
15. Osetsky, Y.N., et al., *One-dimensional atomic transport by clusters of self-interstitial atoms in iron and copper.* Philosophical Magazine, 2003. **83**(1): p. 61-91.
16. Yao, Z., et al., *The temperature dependence of heavy-ion damage in iron: A microstructural transition at elevated temperatures.* Philosophical Magazine, 2010. **90**(35-36): p. 4623-4634.
17. Kawanishi, H. and S. Ishino, *Characterization of microstructure at 673 K in neutron-irradiated Fe-16Ni-15Cr with the addition of C, Ti and Nb.* Journal of Nuclear Materials, 1991. **179-181**: p. 534-537.
18. Yoshida, N., M. Kiritani, and E. Fujita, *Electron radiation damge of iron in high voltage electron microscope.* Journal of the physical society of Japan, 1975. **39**(1): p. 170-179.

6.2 IRRADIATION-INDUCED DISLOCATION LOOP DECORATION AND ATOMIC STRUCTURE OF THE PETAL SHAPED DISLOCATION LOOP IN Fe-Cr ALLOYS

—Y. Li, Y. Zhao, S. J. Zinkle (University of Tennessee, Knoxville), A. Bhattacharya, Yan-Ru Lin (Oak Ridge National Laboratory)

OBJECTIVE

The objective of this project is to study the role of Cr atoms on dislocation loop evolution by characterizing loop density, size distribution, and loop Burgers vector in high purity Fe and Fe-Cr model alloys after heavy ion irradiation at different temperatures and doses.

SUMMARY

Conventional transmission electron microscopy (CTEM) was used to characterize the loop distribution and details of complex structures reported in preceding reports, called petal shaped dislocation loops and 2-D dislocation loop walls, after 8 MeV Fe ion irradiation to 0.35 and 3.5 dpa at 350°C or 450°C in high purity Fe-(3-8%)Cr alloys. By the g.b method, we are examining the effect of pre-existing dislocation lines on loop formation. At 350°C, irradiation induced dislocation loops were observed to decorate pre-existing dislocations. Screw dislocations are free from the decoration phenomenon. Loops formed on the tensile side of mixed or pure edge dislocation lines. At 450°C and 3.5 dpa, <001> 2-D dislocation loop walls were observed. By phase contrast, we identified that different dislocation loops in the same loop wall were on adjacent atomic planes which have the same plane normal.

PROGRESS AND STATUS

Introduction

This report summarizes recent work on dislocation loop characterization in a series of ion irradiated high purity Fe-Cr alloys; prior work is summarized in previous progress reports(1-3). Dislocation loops in Fe-3Cr, -5Cr, and -8Cr were examined. The irradiations examined in this report were performed at 350°C or 450°C and the midrange doses were 0.35 or 3.5 dpa. This investigation is a continuation of our previous work in which the same samples were irradiated by 8 MeV Fe ions at 0.35 dpa (mid-range dose). The mid-range safe analysis region is from 750 to 1250 nm, based on the method proposed by Zinkle(4). The TEM lamellae were lifted out from the desirable grains whose crystal directions had been determined by the electron Backscatter Diffraction (EBSD) technique. Afterward, samples discussed in this report were prepared by focus ion beam (FIB) milling followed by the flash polishing method reported previously(2).

Experimental Procedure

<u>The atomic structure of petal-shaped loops</u>

Figure 1 displays the petal shaped loops and 2-D dislocation walls created at 450°C. At low damage (0.35dpa), both [100] and [010] edge on type loops are observable when the imaging condition is close to B =001. Under the on-zone condition (B = 001), all the loops are revealed, as shown in Figure 1a. A plan view petal shaped [001] loop is observable in Figure 1a, along with multiple edge on loops. It demonstrates that each petal shaped loop consists of multiple branches. At high damage (3.5 dpa), no petal shaped loop is observed. By g.b analysis, the long ‘black lines’ in Figure 1f are edge on <100> dislocation loops. The small semicircular loops are [001] loops. Combining the edge on [100] and [010] loop clusters and the plan view [001] loop clusters, suggests that 2-D dislocation loop walls are observable. Our hypothesis for this evolution process is shown in Figure 1b – Figure 1e. One [100] loop cluster is used as an example. At the very beginning, separated small [100] loops were formed as a cluster. They sit on slightly different atomic habit planes which have the same plane normal (Figure 1b). As more self-interstitial atom (SIA) clusters are created by cascade events, the small [100] loops grow by absorbing small SIA clusters. Since [100] loops are sessile, their relative positions to each other remain unchanged (Figure 1c). With further growth, these [100] loops impinge upon the [100] loops in their neighborhood, and coalescence occurs (Figure 1a and Figure 1d), leading to the formation of the petal shaped loops. With increasing doses, the petal shaped loops coarsen, and the petal shaped loops eventually become too large to be imaged by TEM since their size is much greater than the TEM foil thickness. The inner region of a coarsened petal shaped loop is like a ‘perfect’ crystal. New small <001> loops may nucleate inside of the coarsened petal shaped loops and will form the next generation of petal shaped loops once they impinge upon the [100] loops in their neighborhood. To test our hypothesis, high resolution transmission electron microscopy (HRTEM) was carried out on Fe-5Cr irradiated to 3.5 dpa at 450°C. Figure 1g is the filtered HRTEM under B = 001 condition. Two [010] dislocation loops in the same cluster were imaged. The loop on the left side of Figure 1g is shown in higher magnification in Figure 1h. The core of this loop is visible in Figure 1h, which is pointed out. Its habit plane is determined and marked in Figure 1g. The loop on the right side of Figure 1g is shown in higher magnification in Figure 1i. Although the exact position of this loop could not be determined, a Burgers circuit containing its core is drawn in Figure 1h. The drawn line as the habit plane of the left loop in Figure 1g acts as the bottom line of the Burgers circuit. This demonstrates the habit planes of these two loops are distinct and parallel, indicating the possibility of our hypothesis.

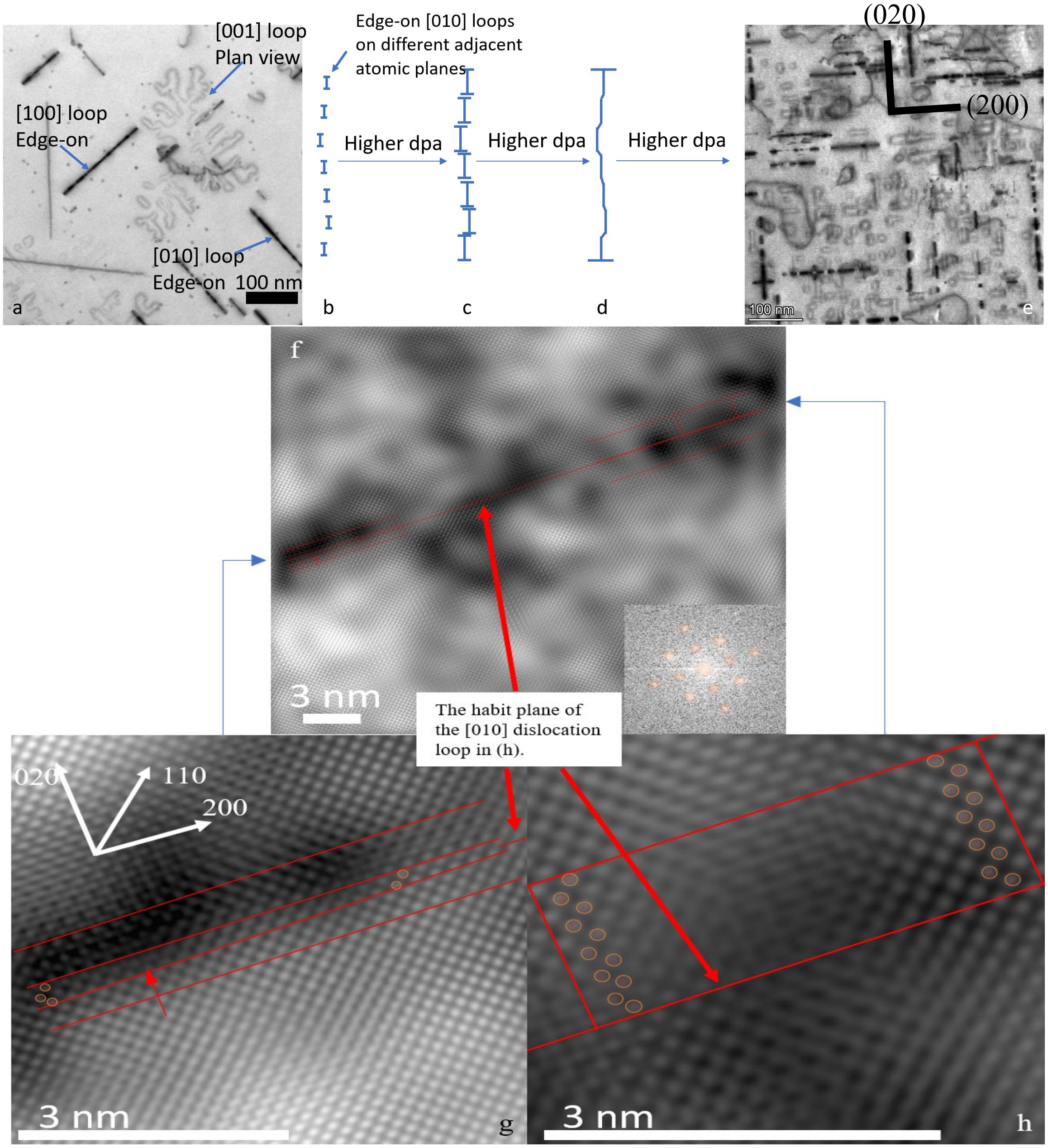

Figure 1. (a) Fe-8Cr Scanning Transmission Electron Microscopy-Bright Field (STEM-BF) imaged using on-zone, B =001 following irradiation at 450℃ to 0.35 dpa at 10^{-5} dpa/s. (b-d) a schematic illustration displays the evolution process of petal shaped dislocation loops in different phases from (b) nucleation, (c) growth, and (d) coalescence. (e) A Fe-5Cr irradiated at 450℃ to 3.5 dpa at 10^{-4} dpa/s is imaged with the STEM-BF technique. The diffraction condition was on-zone, B =001.(f) is a filtered HRTEM image of an edge on [010] loop wall in Figure 1e. Figure 1f's inset is the Fast Fourier Transform (FFT) of the original HRTEM image, B = 001. The orange discs are the mask applied in the filter. (g) is a higher magnification of the left marked region in (f) and the core of the edge type [010] dislocation loop is pointed out in (g). Three layers of [020] atomic planes are marked on the left side of the core and two layers of [020] atoms are marked on the right side of the core. (h) is a higher magnification of the right marked region in (f). Eleven layers of [020] atomic planes are marked on the left side and ten layers of [020] atomic planes are marked on the right side in (h).

Loop distribution along preexisting dislocation lines

Figure 2 displays irradiation induced defects along pre-existing dislocation lines in Fe-8Cr. The irradiation condition was 350°C at 0.35 dpa, and 10^{-4} dpa/s. For a given dislocation line, loops are clustered along the same side of the dislocation. Some dislocation lines are invisible under g = $\bar{1}\bar{1}0$ and g = $0\bar{1}1$. The g.b analysis indicated the dislocation lines are ½ [111] type. After determining the dislocation lines' Burgers vector, the dislocations were imaged with g = $\bar{1}\bar{1}0$ and g = 110. The general orientation relationship is illustrated in Figure 3. An FIB foil with [001] foil normal is imaged in TEM. The y-axis is [001] and the x-axis is [110], respectively (Figure 3a). In this configuration, a (111) plane is highlighted. For a ½ [111] edge dislocation line, it has two possible geometries. The tensile side is above or below the core of dislocations. If the tensile side is below the dislocation core, its image would be on the left side of its physical location with the g = $\bar{1}\bar{1}0$ two-beam approximation (Figure 3b). Its image would be on the right side of its physical location with the g = 110 two beam approximation (Figure 3c). If the tensile side is above its core, the relationship between the dislocation image and dislocation core would be in the opposite, as shown in Figure 3d and Figure 3e. By this method, we imaged the area shown in Figure 2 with g = $\bar{1}\bar{1}0$(Figure 2a) and g = 110 (Figure 2d). It demonstrated that the loops are all on the tensile side of pre-existing dislocation lines. Figure 2e displays a pure screw dislocation. It is free from dislocation loop decoration. From these images, it can be concluded that dislocation loop decoration occurs on the tensile side of a non-screw type dislocation line in body-centered cubic (BCC) Fe-based systems.

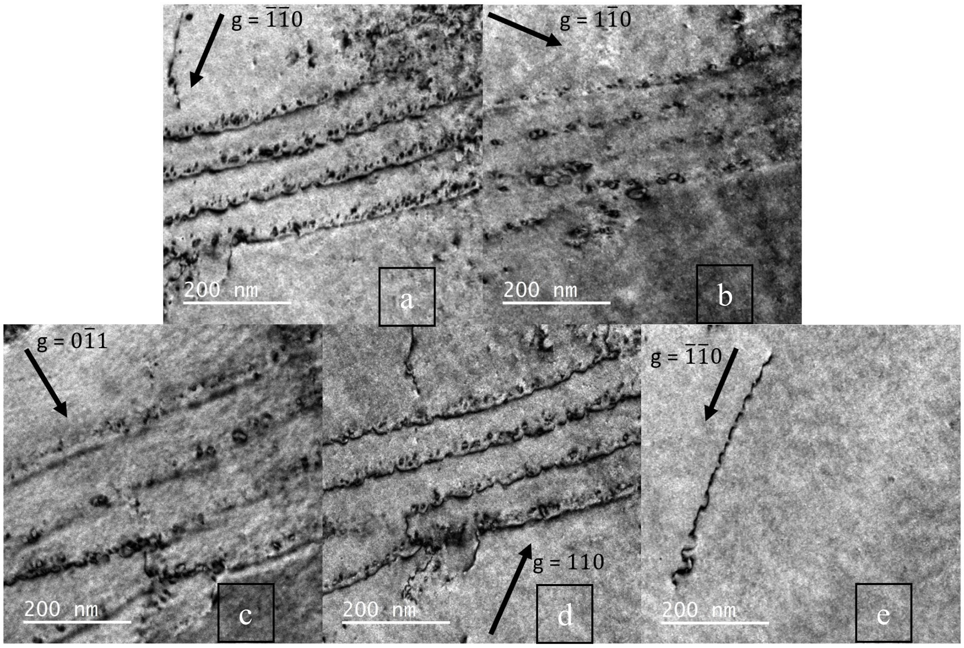

Figure 2. Dislocation loops along preexisting dislocation lines. The same area was imaged under different two-beam approximations. (a) g = $\bar{1}\bar{1}0$ and B ~ 001. (b) g = $1\bar{1}0$ and B ~001. (c) g = $0\bar{1}1$ and B ~011. (d)) g = 110 and B ~ 001. (e) A screw dislocation is free from dislocation loop decoration.

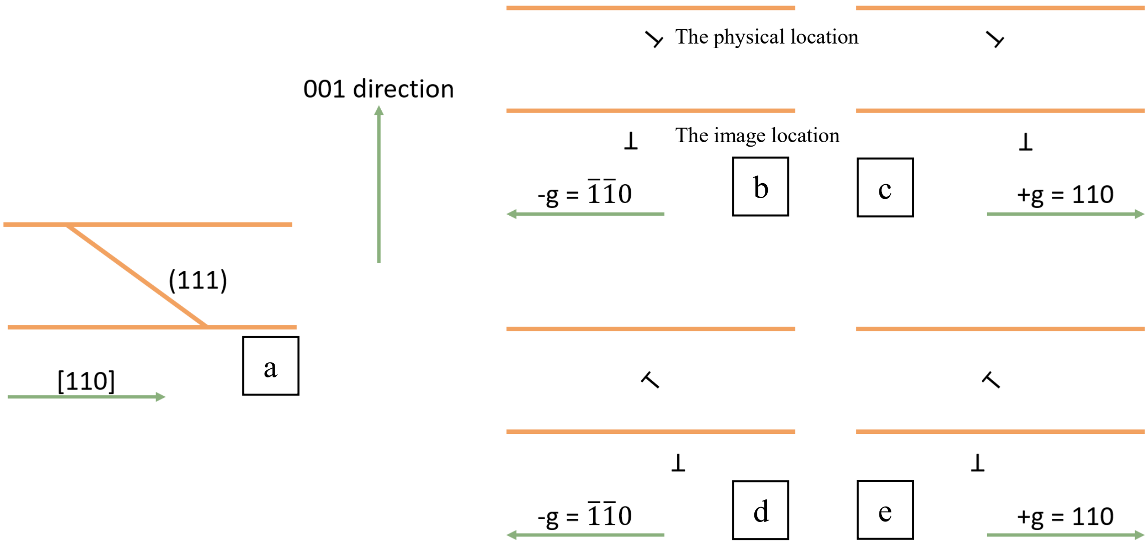

Figure 3. A schematical cartoon of dislocation line tensile side determination. (a) is the basic geometry applied in the determination. The two orange horizontal lines represent the top and bottom surfaces of the imaged TEM foil. (b-e) represent the relationship between the physical position of the dislocation line and its images. The inclined ⊥ is the physical position. (b) and (c) are about a ½ [111] dislocation line whose tensile side is below its core. (d) and (e) are about a ½ [111] dislocation line whose tensile side is above its core.

Results

The phenomenon of irradiation induced dislocation loop decoration along pre-existing dislocation lines has been observed in BCC and face-centered cubic (FCC) systems by many researchers(5-9). According to the point defect rate theory, it is widely accepted that dislocation lines with edge components are sinks for interstitials and vacancies and are biased to interstitials due to the tensile strain field(10). However, around 50% of surviving SIAs by cascade events are in clusters(11). The single SIAs diffuse as 3-D walkers whereas the SIA clusters whose size is greater than four diffuse as 1-D walkers(12). The different diffusion processes have a great impact on the subsequent microstructural evolution. Since our sample was irradiated by 8MeV ions, the point defect rate theory may not be accurate to describe the phenomena observed. Trinkaus examined the probability of the loop decoration along pre-existing dislocation lines because of the capture of 1-D SIA clusters and the single SIAs enhanced agglomeration in the form of loops If the enhanced agglomeration of single SIAs occurs, it would result in the reduced agglomeration of SIAs on the tensile side and depletion of SIA on the compressive side. This depletion may enhance the agglomeration of vacancies on the compressive side. In contrast, the agglomeration of SIA clusters on the tensile side can be rationalized in terms of the capture of 1-D SIA clusters(13). The dislocation decoration along pre-existing dislocation lines depends on the irradiation temperature. Trinkaus predicts that at high temperatures, the Burgers vector of a trapped loop by dislocation line has a higher probability to be absorbed by the dislocation line (14). Our observation support Trinkaus simulation. In our samples irradiated at 450°C, the decoration is not observable. The long dislocation lines' shape indicates irradiation induced dislocation loops were absorbed by the long dislocation lines. One example is arrowed in Figure 4.

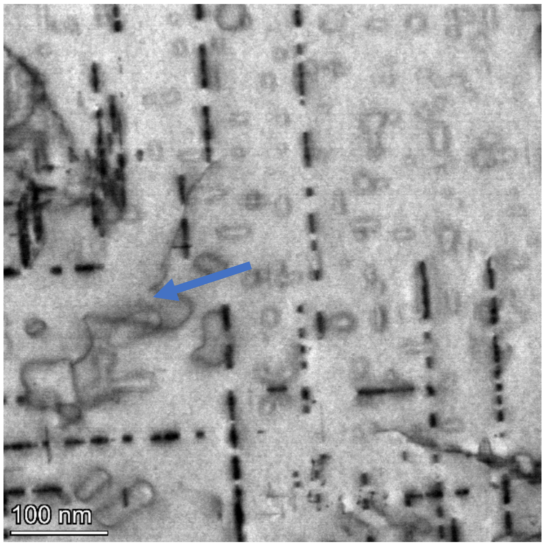

Figure 4. An on-zone STEM-BF micrograph of the safe analysis region of 5Cr irradiated at 450°C to 3.5 dpa.

References

1. Li Y, Zinkle SJ, Bhattacharya A. EFFECTS OF Cr AND C ON DISLOCATION LOOPS IN HEAVY ION IRRADIATED ULTRA-HIGH PURITY FeCr ALLOYS. Oak Ridge National Laboratory; 2019 June 30. Report No.: DOE-ER-0313/66.
2. Li Y, Zinkle SJ, Wang L, Bhattacharya A. EFFECT OF Cr ON DISLOCATION LOOPS IN HEAVY ION IRRADIATED ULTRA-HIGH PURITY FeCr ALLOYS. Oak Ridge National Laboratory; 2020 June 30. Report No.: DOE/ER-0313/68.
3. Li Y, Zinkle SJ, Bhattacharya A. AN ELECTRON MICROSCOPE STUDY OF HEAVY ION IRRADIATED ULTRA-HIGH PURITY Fe AND Fe-Cr ALLOYS AT 350℃. Oak Ridge National Laboratory; 2020 December 31. Report No.: DOE/ER-0313/69.
4. Zinkle SJ, Snead LL. Opportunities and limitations for ion beams in radiation effects studies: Bridging critical gaps between charged particle and neutron irradiations. Scripta Materialia. 2018;143:154-60.
5. Kiritani M, Yoshida N, Ishino S. The Japanese experimental program on RTNS-II of DT-neutron irradiation of materials. Journal of Nuclear Materials. 1984;122(1):602-7.
6. Hernández-Mayoral M, Heintze C, Oñorbe E. Transmission electron microscopy investigation of the microstructure of Fe–Cr alloys induced by neutron and ion irradiation at 300 °C. Journal of Nuclear Materials. 2016;474:88-98.
7. Kojima S, Yoshiie T, Kiritani M. Defect structure evolution from cascade damage in 14 Mev neutron irradiated nickel and nickel alloys. Journal of Nuclear Materials. 1988;155-157:1249-53.
8. Satoh Y, Ishida I, Yoshiie T, Kiritani M. Defect structure development in 14 mev neutron irradiated copper and copper dilute alloys. Journal of Nuclear Materials. 1988;155-157:443-8.
9. Horton LL, Bentley J, Farrell J. A TEM study of neutron-irradiated iron. Journal of Nuclear Materials. 1982;108&109:222-33.
10. Was GS. Fundamentals of Radiation Materials Science: Metals and Alloys. New York: Springer Science+Business Media; 2017.
11. Bacon D, Gao F, Osetsky YN. The primary damage state in fcc, bcc and hcp metals as seen in molecular dynamics simulations. Journal of Nuclear Materials. 2000;276:1-12.
12. Anento N, Serra A, Osetsky YN. Atomistic study of multimechanism diffusion by self-interstitial defects in α-Fe. Modelling and Simulation in Materials Science and Engineering. 2010;18(2).
13. Trinkaus H, Singh BN, Foreman AJE. Mechanisms for decoration of dislocations by small dislocation loops under cascade damage conditions. Journal of Nuclear Materials. 1997;249:91-102.

14. Trinkaus H, Singh BN, Foreman AJE. Segregation of cascade induced interstitial loops at dislocations: possible effect on initiation of plastic deformation. Journal of Nuclear Materials. 1997;251:172-87.

6.3 DETERMINING THE PHASE BOUNDARY BETWEEN α AND α+α’ IN Fe-Cr ALLOYS WITH PROTON IRRADIATIONS AND THERMAL AGING

—Y. Zhao, P. Zhu, S.J. Zinkle (University of Tennessee, Knoxville), A. Bhattacharya (Oak Ridge National Laboratory)

SUMMARY

The FeCr based steels are promising structural materials for various industrial applications, but they can become hard and brittle due to Cr-enriched α’ precipitation. However, the phase boundary between α and α+α’ at temperatures of technical interest (~250-400°C) is not well determined. In this study, proton irradiations at 250-450°C to 2 dpa and longtime thermal aging at 450-500°C were performed on Fe(5-18%)Cr binary alloys, followed by characterizing the Cr atom distributions using atom probe tomography (APT). The α’ was not observed in Fe12Cr at 450°C and Fe8Cr at 350°C. In all other investigated conditions, α’ was distributed either homogeneously or agglomerated together. At temperatures of 350-500°C, the phase boundary can be determined rather accurately, in which the lower bounds were determined from alloys without α’ formation, and upper bounds were measured from matrix Cr concentrations after various treatments. At 250°C, agglomerated α’ precipitates formed in Fe(5-8)Cr alloys, while homogenously nucleated precipitates are major features in more concentrated alloys. Currently, it is difficult to determine whether they are induced or enhanced by irradiations, and thus the precise location of the thermal equilibrium phase boundary at 250°C is still unclear.

PROGRESS AND STATUS

Introduction

The FeCr binary alloys may undergo the phase separation process to form Cr-enriched α’ precipitates after thermal aging for a long time or neutron irradiation at temperatures ≤500°C; these α’ precipitates are known to cause severe hardening and embrittlement problems [1, 2]. One of the largest barriers that hinder the design of alloys to prevent these problems is the lack of an accurate phase boundary between the α/α+α’ at low to intermediate temperatures. Due to the very slow diffusivity of Cr atoms at temperatures below 450°C, the thermal equilibrium state is not achievable by thermal annealing alone even for annealing times exceeding one year. For example, Fe-20Cr steels were aged at 350°C for 200,000 hours (~23 years), and the equilibrium Cr concentration of α’ was not reached [3]. On the other hand, well developed α’ precipitates were observed after aging at 500°C for a much shorter time of ~1000 hours in both Fe-18Cr and Fe-20Cr alloys [4, 5]. The most frequently cited phase boundaries were calculated from the Calphad database, fitted from the available neutron irradiation results, or obtained from ab-initio calculations, which show large discrepancies at temperatures below 500°C [6-8]. Although the version from Bonny et al agrees better with currently available electron irradiation or thermal aging results, a moderate difference exists at 500°C, and the temperature independence of solubility limit at <450°C is scientifically difficult to understand [4, 5, 7].

Due to the potential applications of FeCr based Ferritic Martensitic steels in fusion and fission nuclear reactors, the stability of α’ precipitates under irradiation conditions has been extensively studied in recent decades [9-17]. During particle irradiations, the diffusion process can be accelerated by orders of magnitude resulting from supersaturated point defect concentrations. However, most irradiation works performed on FeCr based specimens used neutrons or heavy ions, which could potentially modify the phase boundary by dissolving the thermodynamically favorable α’ precipitates with displacement damage cascades [9-11]. Proton irradiations, on the opposite, introduce only low energy (~ several hundred eV) primary knock-on atoms (PKA) and create a high concentration of point defects without forming displacement cascades. In principle, proton irradiations can accelerate the phase separation process without changing the phase boundary, and thus provide a convenient way to determine the phase boundary at low temperatures.

The objective of this work is to accurately measure the phase boundary between the α-Fe and α+α’ two-phase region at temperatures of 250-500°C. The distribution of α’ precipitates and related chemical compositions were measured through APT technique. The solubility limits at the lower temperature regime of 250-450°C were obtained from proton irradiations, while the locations of phase boundary at 450-500°C were determined from thermal aging. To account for any potential artifacts that may be caused by proton irradiations, a comparison of the results after proton irradiation and thermal aging at 450°C was conducted.

Experimental Procedure

High purity FeCr specimens from CEA were used in this study. Their chemical compositions, which were measured by glow discharge mass spectrometry, are listed in Table 1 and have been reported earlier [18]. The as received cylindrical specimens were cut into either disk or rectangular shapes using electrical discharge machining (EDM) method. The disk-shaped specimens had dimensions of 3 mm in diameter and 1mm in thickness, and they were used for thermal aging. The rectangular shaped samples, which are 2 mm or 5 mm long, 2 mm wide and 1 mm thick, together with the available disk-shaped samples were used for proton irradiations.

Table 1. The chemical compositions of high purity FeCr alloys

specimen	element concentration						
	Cr (wt. %)	Cr (at. %)	C (ppm)	S (ppm)	O (ppm)	N (ppm)	P (ppm)
Fe5Cr	5.40	5.79	4	3	6	2	5
Fe8Cr	7.88	8.41	5	2	7	2	
Fe10Cr	10.1	10.77	4	4	4	3	<5
Fe12Cr	11.63	12.38	5	2	4		
Fe14Cr	14.25	15.18	5	7	4	5	<10
Fe18Cr	17.97	19.05	7	2	6	5	

Thermal aging was performed at 450°C, 475°C and 500°C for various time lengths for the purpose of achieving thermal equilibrium states, thus the aging time was longer at the lower temperatures. Thermal aging at 500°C was performed only on Fe18Cr specimens, and the thermally aged Fe18Cr specimens were used for a series of ion irradiation experiments [19]. FeCr alloys with 10-18% Cr were included in the thermal aging experiments at 450°C and 475°C, after which hardness tests were conducted. The temperatures in furnaces during aging were monitored by both thermocouples inherent to the furnace and 1 or 2 external thermocouples inserted into the vicinity of specimens. Temperature variations between measured and target values were less than 5°C.

Proton irradiations at 250°C, 350°C, and 450 °C were performed in the Michigan Ion Beam Laboratory (MIBL). Since the major problem associated with proton irradiations is beam induced heating and temperature rising at specimen surfaces, relatively low ion energy and low dose rate (ion flux) are preferred. However, to achieve steady states within a reasonable amount of time, a high dose rate and dose (ion fluences) are desired. As a compromise, irradiations using 800 keV protons at mid-range dose rates of 2×10^{-5} dpa/s (1.8×10^{14} ions/cm^2×s) and final doses of 2 dpa (1.8×10^{19} ions/cm^2) were performed at all the three temperatures. The irradiation time for a single experiment was ~28 hours. The irradiation damage and injected ion concentration profile was calculated with Stopping and Range of Ions in Matter (SRIM)-2013, using full cascade damage energy method, with the displacement energy of Fe set as 40 eV [20]. The result is plotted in Figure 1(a), in which the analysis region was taken from ~3 μm below the sample surface. All the specimens were mechanically polished to mirror surface, finishing with 0.05 μm colloidal silica before irradiation. The specimens were mounted on Cu plates using silver paste as demonstrated in Figure 1(b). Four thermocouples were welded on two guide bars for calibrating a thermal imager, so that the temperatures on sample surfaces could be continuously monitored, which showed variances from target temperatures of less than 5°C. The average target chamber pressure was maintained as < 1×10^{-7} Torr during irradiations.

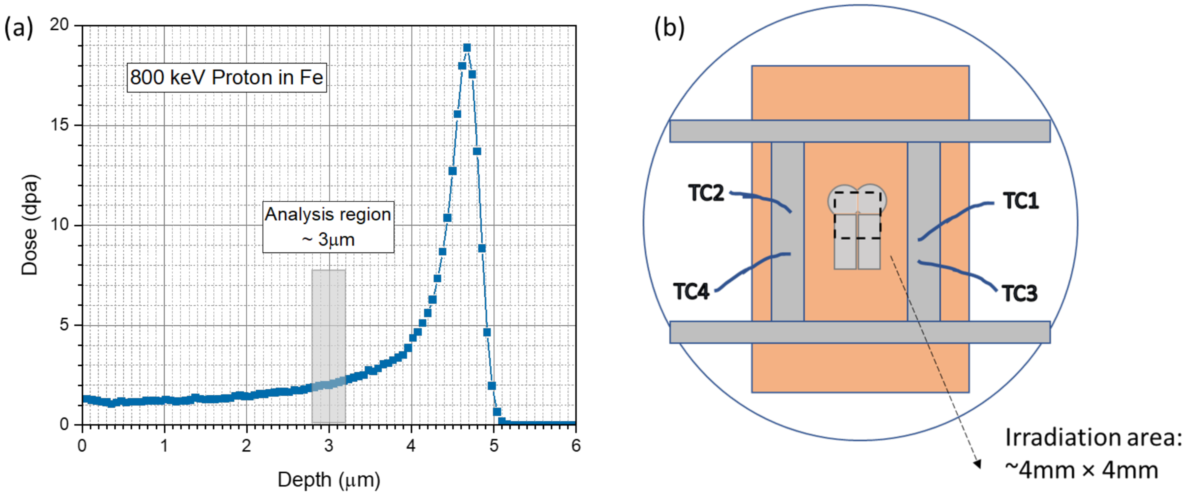

Figure 1. (a) SRIM prediction of the irradiation damage dose profile. (b) schematic of sample arrangement on the Cu plate. "TC" is short for thermocouples.

The needle shaped APT specimens were prepared through the focused ion beam (FIB) lift out method. To achieve the desired depth more easily during field evaporations, both the Pt cap and the corresponding length of sampled materials below it were removed during sharpening. During the reconstruction of APT datasets, tip radii were adjusted to give the correct interplanar spacings along <110> or <200> directions. The evaporation field of Fe 33 V/nm was used as an approximation, and the image compression factor was kept as a constant of 1.65. The field factors were calculated to be ~5 in datasets collected in voltage mode and ~3 in laser-pulsed datasets. The Cr concentrations in matrix and precipitate phases were measured through the proximity histogram (proxigram) method.

Results

α' formation after proton irradiations

Proton irradiations at lower temperatures were conducted to accelerate the kinetics of phase separation. Through APT characterization, α' precipitates were identified in a wide range of specimens as presented in Figure 2. They were observed in all specimens after irradiation at 250°C, in both Fe10Cr and Fe18Cr specimens at 350°C, and only in Fe18Cr at 450°C. The number density of precipitates is much higher in Fe18Cr alloys at 250-350°C than in all other conditions.

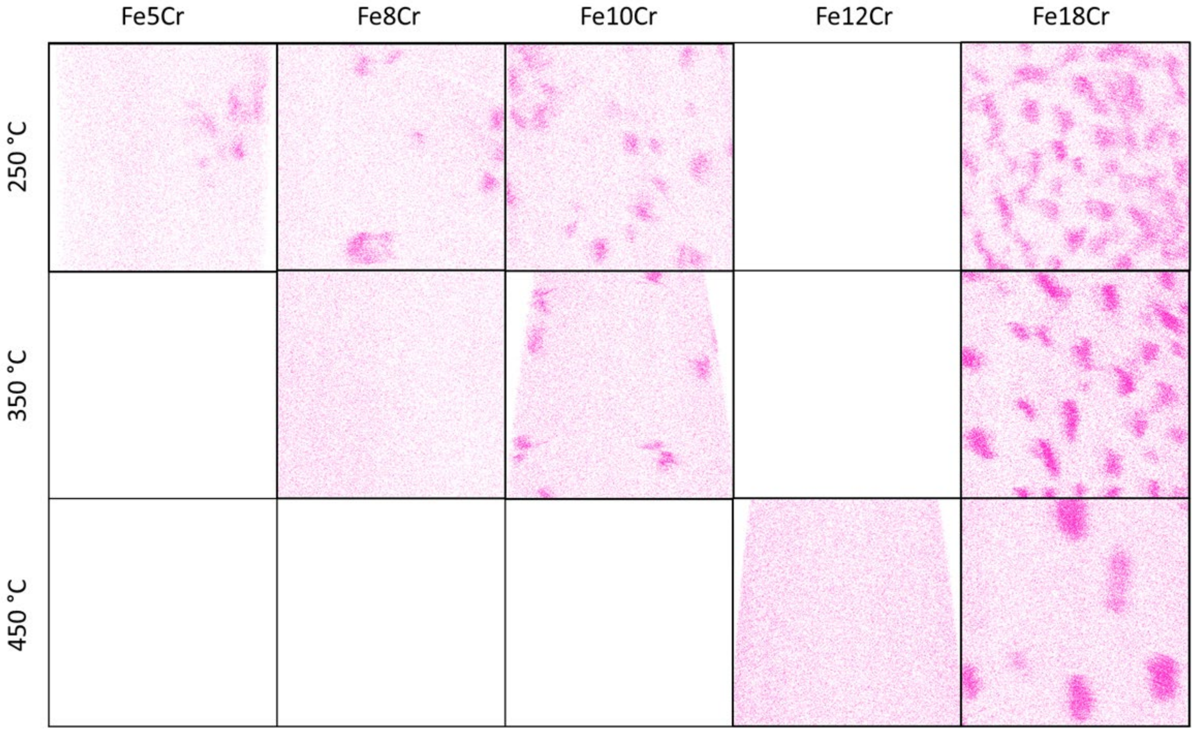

Figure 2. Cr atom maps of FeCr alloys irradiation by protons at 250°C, 350°C and 450°C. The imaged volume for each condition is 40×40×10 nm^3.

Using the APT technique, not only the presence or absence of α' can be detected, but also the matrix Cr concentrations can be measured. The matrix Cr will equal the solubility limit if the thermal equilibrium state is reached and higher than the solubility limit if thermal equilibrium state is not reached. Bachhav et al pointed out that the measured matrix compositions would change as a function of the threshold solute values used to create interfaces [13]. Therefore, to minimize the artifact associated with selecting inappropriate threshold values and to obtain more objective results, multiple values in 20-50% were used. As shown in Figure 3(a) and 3(b), increasing the threshold values not only shifts proxigrams to the left side, but also leads to the change in the shape and height of the curve at the matrix side. As the distance from interface increases or the distance value becomes more negative, the Cr concentration in each bin decreases and then increases due to intersecting neighboring precipitates, so matrix solute concentrations were taken as the lowest points on the proxigram, and five bins were averaged to give the result.

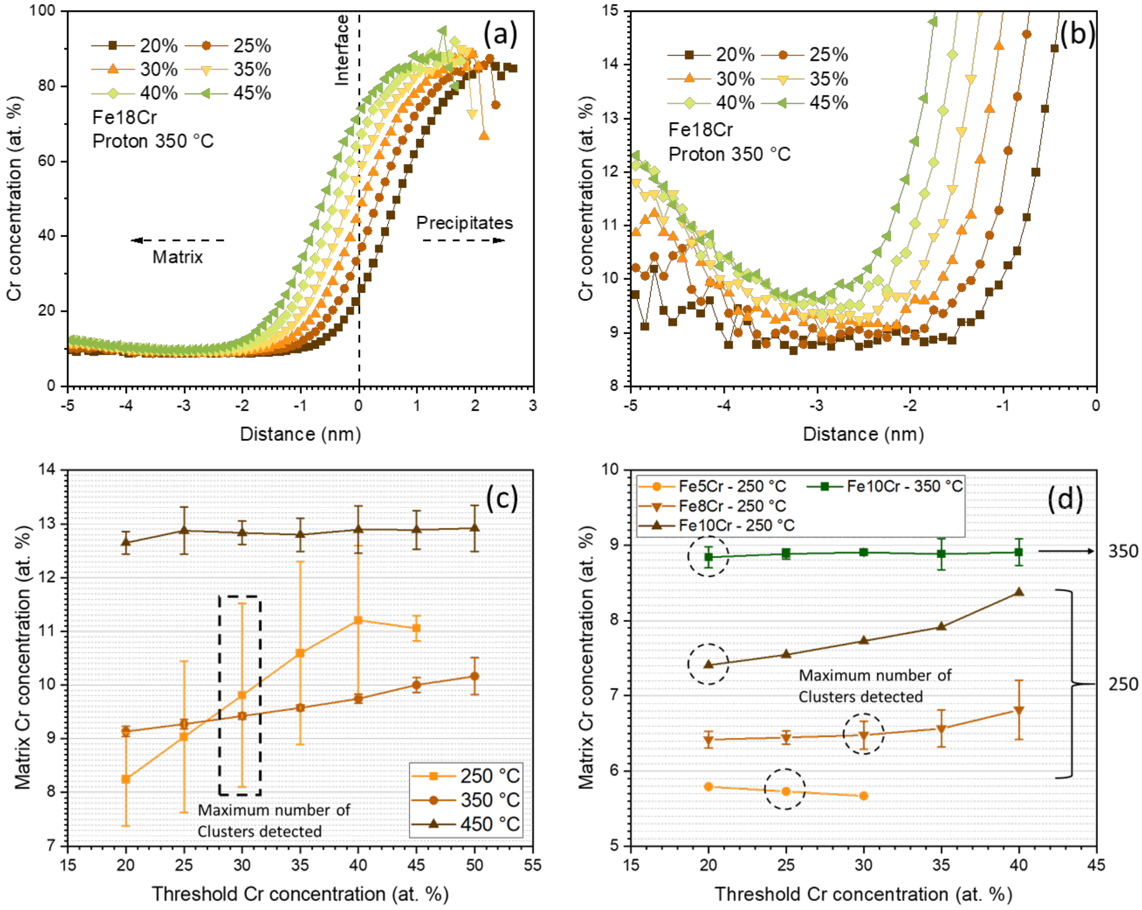

Figure 3. (a) proxigrams of Fe18Cr alloy irradiation by protons at 350°C to 2 dpa demonstrate the shift and change resulting from changes in threshold Cr concentration values. (b) Zoom in view of the matrix side in (a). The dependence of matrix Cr concentration on threshold values in (c) Fe18Cr and (d) Fe(5-10)Cr specimens. The dashed box in (c) and dashed circles in (d) point out the threshold Cr concentration values at which maximum numbers of clusters were detected.

The dependence of matrix solute concentrations on threshold values varies widely among specimens. For example, in Fe18Cr given in Figure 3(c), the matrix values are almost independent of threshold values at 450°C, while the dependence becomes stronger at lower temperatures where the number density of precipitates gets larger as shown in the atom maps. The reason for this dependence can be attributed to the merging or splitting of precipitates that is controlled by changing concentration values at interfaces, which is more likely to happen when the precipitate number density is very high. Results from alloys with much lower bulk solute concentrations are plotted in Figure 3(d); the negligible dependence at 350°C and decreasing dependence in more dilute alloys at 250°C agree with this logic. Although the matrix Cr content can be accurately measured in cases where the dependence is weak, under other conditions the stronger dependences place difficulties in the determination of chemical compositions. The method proposed by Bachhav et al was used here, who suggested using the threshold values gives the maximum number of iso-concentration interfaces.

The resulting matrix solute concentrations are compared to the available phase diagrams in Figure 4. The bulk compositions of alloys (listed in Table 1) in which α’ was not observed were also overlaid (black filled symbols), which represent the lower limits of the phase boundary. The measured matrix concentrations are relatively widely distributed, especially at the lowest temperature of 250°C. This can be attributed to a higher dose being required to achieve steady state at lower temperatures, and this dose also increases with bulk solute concentrations due to the involvement of a larger amount of solute migrations. This observation is consistent with that of Bachhav et al, who found the matrix Cr contents in Fe(15-18)Cr were higher than that in Fe(9-12)Cr specimens after neutron irradiation to the same dose. Therefore, at each temperature, the lowest matrix solute concentrations, which were usually obtained from the most dilute alloys, would be closer to the thermal equilibrium solubility limit. Three versions of possible phase boundaries are included in Figure 4 for comparison, in which the one from Bonny et al was fitted from neutron irradiation results [7], the one from Andersson et al was calculated from Calphad simulation [6], while the one from Xiong et al was the smooth connection of 475°C annealing results and solubility limits of Cr at 0 K that was obtained from ab initio calculations [8]. Among these three versions, our data points agree most closely with the prediction of Xiong et al, especially at temperatures >350°C. At temperatures ≤350°C, matrix concentrations lower than their predictions were measured.

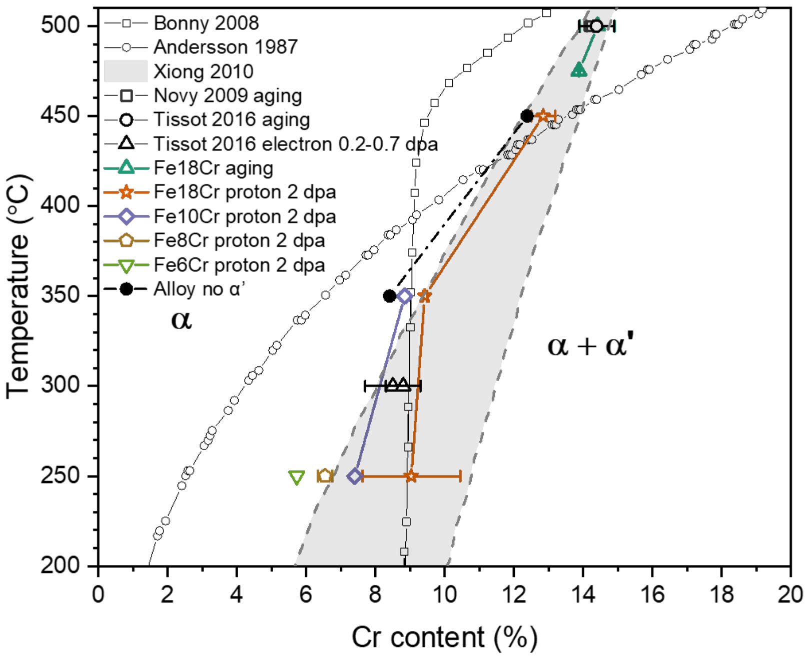

Figure 4. A comparison of measured matrix Cr concentrations in FeCr alloys after thermal aging [4, 5], electron [17] or proton irradiations with available phase boundaries [6-8] in literature. The bulk compositions of alloys without α' are also included.

Generally, the precipitation process under irradiation conditions is more complicated than thermal annealing alone. The precipitate formation can be enhanced, induced or modified by particle irradiations. Historically, α' formation under irradiation was claimed to be a radiation enhanced precipitation phenomenon, because it was observed in supersaturated alloys, and the precipitates were homogeneously distributed in sampled volumes [9, 13, 17]. This mechanism suggests that the measured matrix solute concentrations should be higher than or equal to the solubility limits because supersaturation is necessary for phase separation. In our previous work, we found the α' evolution agreed more with a radiation modified precipitation mechanism [19]. However, the modification from thermal equilibrium states is expected to be large only under high dose rate heavy ion irradiations, which introduce displacement damage cascades to dissolve precipitates. In the case of 800 keV proton irradiations, the average energy of PKA is 289 eV, which is only a few times the displacement energy of 40 eV, so mainly point defects are created. Therefore, the variation of steady states from thermal equilibrium states should not be significant, and the precipitation behavior will be more like an enhanced precipitation process. Radiation induced α' formation in Fe(9-50)Cr alloys has been reported by Wakai et al under-electron irradiations [21]. They observed the decoration of dislocation loops by precipitates, which were revealed to be α' according to the measured interplanar spacings of 2.035 angstroms. These α' precipitates were distributed along the edge of loops and were proposed to form from radiation induced segregation of Cr atoms and interstitials to loops, which then form complexes of Cr-impurity interstitials and stabilize Cr-enriched clusters. If α' formed through this path, their features would be non-homogeneous distribution and co-clustering with impurity atoms.

In fact, from atom maps in Figure 2 and the Cr-enriched clusters visualized by 25% Cr iso-concentration interfaces in Figure 5, both homogeneous distributed and inhomogeneous agglomerated precipitates can be found. α' in Fe18Cr alloys are predominantly homogeneously distributed at 350°C and 450°C, and thus were enhanced by irradiations. At 250°C, Figure 2 shows a small portion of elongated precipitates, which might be related to spinodal decomposition occurring at the beginning of irradiation due to a high solute supersaturation. However, the distribution and morphology of precipitates in the more dilute alloys are very different. In Fe10Cr, all the Cr clusters were homogenously distributed with near spherical shapes after irradiation at 350°C, while both spherical and agglomerated non-spherical clusters were present at 250°C. On the other hand, mainly agglomerated clusters with a few isolated ones can be seen in Fe8Cr, and only agglomerated ones were present in Fe5Cr at the same temperature. Proxigrams showing the Cr concentration gradients across the interfaces are plotted in Figure 5(e). Fe10Cr irradiated at 350°C gave the highest cluster core concentration of ~90%. Similar compositions of ~80% were measured at all other conditions, and there was no clear distinction between the agglomerated non-spherical and homogenous spherical precipitates that were both detected in Fe10Cr at 250°C. Therefore, it is currently unclear whether the agglomerated precipitates are radiation enhanced or induced products. On one side, their inhomogeneous distribution would imply a radiation induced behavior. However, the lack of association between the agglomerated precipitates with carbon atoms (Figure 5(a)), which were observed to segregate to dislocations in our previous ion irradiation studies [19], their similar chemical compositions with the spherical ones, and the fact that there was no correlation among the orientations of single precipitates or clusters of precipitate tend to favor a radiation enhanced precipitation mechanism. Further characterization using scanning transmission electron microscopy (STEM) - Energy Dispersive Spectroscopy (EDS) would be beneficial to clarify their positional relationship. However, even if there is an association between agglomerated α' and loops, it can't be attributed to radiation induced segregation or precipitation. It is also possible that the loops only act as preferential nucleation sites of α' due to the lower nucleation energy barrier, which is very high for homogeneous nucleation due to both low temperature and low solute supersaturation, and the preferential coupling of Cr atoms and point defects plays a less important role. More work is needed to differentiate these two mechanisms.

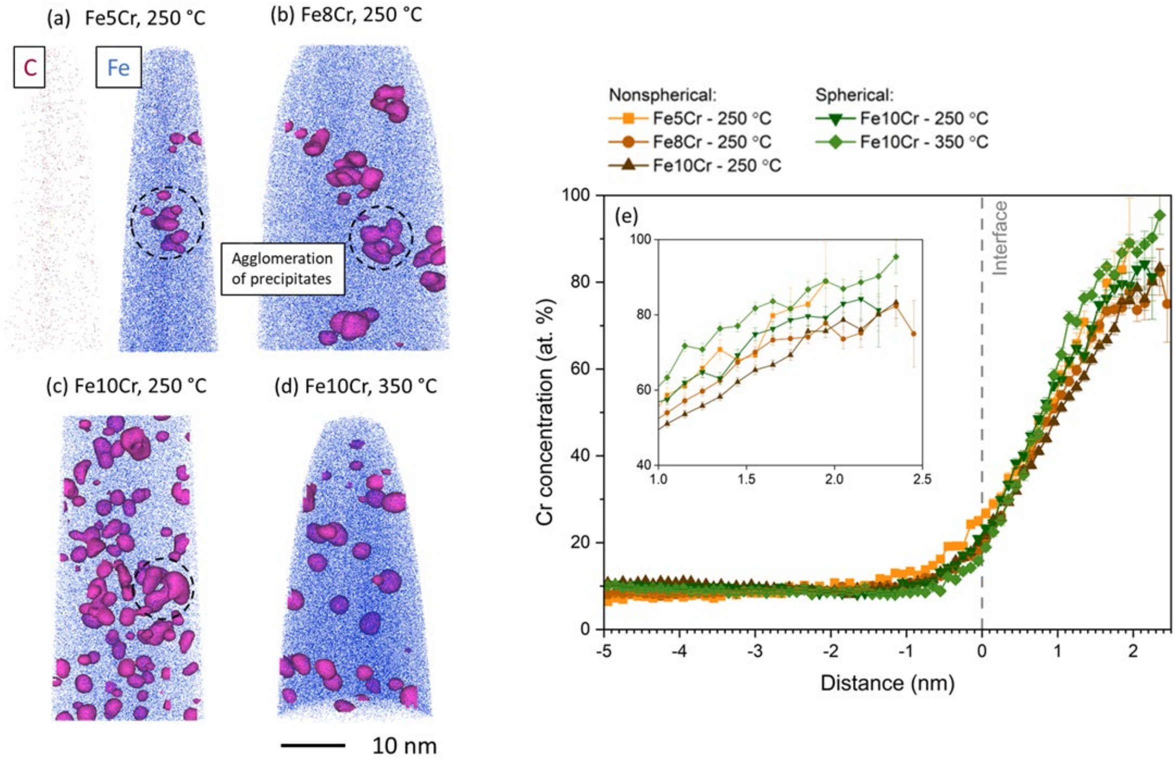

Figure 5. Reconstructions showing the distribution of C, Fe atoms and the α' precipitates highlighted by 25% Cr iso-concentration interface in (a) Fe5Cr, (b) Fe8Cr, (c) Fe10Cr irradiation at 250°C and (d) Fe10Cr irradiation at 350°C. The agglomerated precipitates are marked by dashed circles. (e) Proxigrams calculated from part of precipitates shown in (a)-(d).

Hardness change after thermal aging

The distribution of α' in Fe-18Cr after aging at 475°C and 500°C to 900 hours have been reported in our previous works [18, 19]. In the current study, FeCr alloys with Cr concentrations of ~10-18% were aged in furnaces for a longer time of more than 3000 hours. Since α' precipitates can result in the hardening of specimens, any trace of α' formation can be tracked through Vickers hardness tests, the results of which are plotted in Figure 6. At both 450°C and 475°C, an obvious hardness increase was observed in alloys with Cr concentrations >15 at. %, which implies these two alloys are in the two-phase region of the phase diagram. On the other hand, Fe10Cr and Fe12Cr alloys showed no difference in hardness after thermal aging compared to their as-received (solution annealed) states, and thus their compositions appear to be below the solubility limit, in which there is no thermodynamic driving force for phase separation. These results indicate the phase boundary at 450-475°C should be between 12.4 and 15.2 at.% and is consistent with the proton irradiation APT results. Therefore, pronounced radiation induced α' precipitation didn't occur in the specimens irradiated at 450°C, and instead the precipitation can be attributed to radiation enhanced diffusion that caused pronounced alpha prime precipitation during proton irradiation at 2×10^{-5} dpa/s within ~28 hours. However, thermal aging tests at 450°C for ~28 h will be useful to confirm the effect of thermal annealing alone on α' formation.

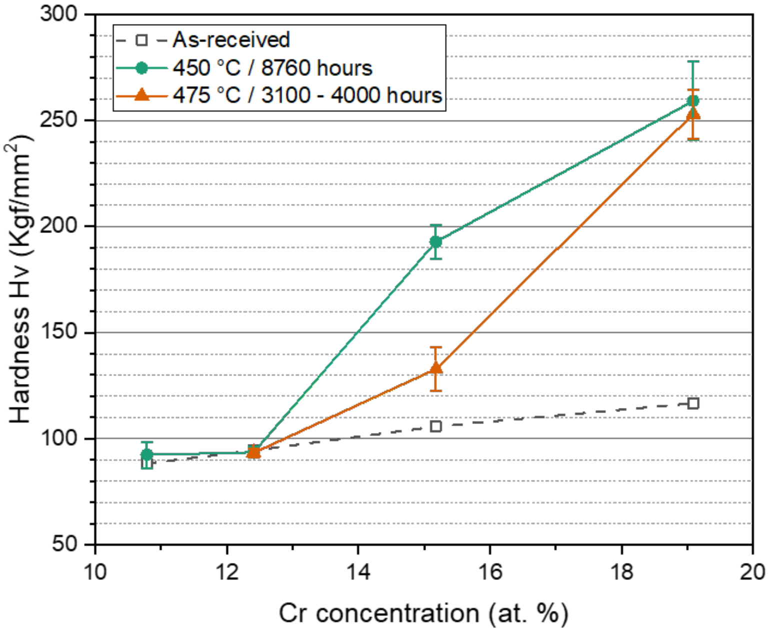

Figure 6. Vickers hardness of FeCr alloys in as-received and aged states.

Discussion

Proton irradiations at 250-450°C to 2 dpa and thermal aging at 450-500°C up to one year were performed to form Cr-enriched α’ precipitates in high purity FeCr alloys. The APT was used to detect the presence of α’, and to measure the matrix solute concentrations after proton irradiations. α’ precipitates were not observed in Fe12Cr at 450°C and Fe8Cr at 350°C, which suggests the bulk compositions of these specimens are on the left-hand side of the solvus line (i.e., single phase alpha region). On the contrary, α’ formed in more concentrated alloys at these two temperatures and all studied specimens at 250°C. The measured matrix concentrations and the bulk compositions of alloys without α’ formation suggested an α - α’ phase boundary that agreed more with the prediction of Xiong et al [8]. However, the deviation of our experimental results from their predictions exists at lower temperatures. From APT reconstructions, most precipitates formed in Fe18Cr alloys at all temperatures or more dilute alloys at 350-450°C were homogeneously distributed and were likely to be enhanced by irradiations, while the precipitates observed in Fe(5-8)Cr at 250°C were agglomerated, and a mixture of spherical and agglomerated precipitates were present in Fe10Cr at 250°C. Currently, the positional associations of agglomerated precipitates with dislocation loops and potential effects on the phase boundary determination are still unclear, and STEM-EDS will be needed for verification. After thermal annealing, hardness tests were conducted to measure any hardening resulting from phase separation. At both 450°C and 475°C, hardness increase occurs in Fe(15-18)Cr alloys, but not in Fe(10-12)Cr alloys, which indicates a solubility limit of 12.4-15.2 at.% at this temperature range. This is consistent with proton irradiation results at 450°C and implies radiation enhanced rather than radiation induced α’ formation at this temperature.

References

[1] D. Chen, A. Kimura, W. Han, Correlation of Fe/Cr phase decomposition process and age-hardening in Fe–15Cr ferritic alloys, J. Nucl. Mater. 455(1-3) (2014) 436-439.

[2] P. Grobner, The 885 F (475 C) embrittlement of ferritic stainless steels, Metallurgical Transactions 4(1) (1973) 251-260.

[3] C. Pareige, S. Novy, S. Saillet, P. Pareige, Study of phase transformation and mechanical properties evolution of duplex stainless steels after long term thermal ageing (>20years), J. Nucl. Mater. 411(1-3) (2011) 90-96.

[4] S. Novy, P. Pareige, C. Pareige, Atomic scale analysis and phase separation understanding in a thermally aged Fe–20at.%Cr alloy, J. Nucl. Mater. 384(2) (2009) 96-102.

[5] O. Tissot, C. Pareige, M.H. Mathon, M. Roussel, E. Meslin, B. Décamps, J. Henry, Comparison between SANS and APT measurements in a thermally aged Fe-19 at.%Cr alloy, Mater. Charact. 151 (2019) 332-341.

[6] J.-O. Andersson, B. Sundman, Thermodynamic properties of the Cr-Fe system, Calphad 11(1) (1987) 83-92.

[7] G. Bonny, D. Terentyev, L. Malerba, On the α–α′ miscibility gap of Fe–Cr alloys, Scr. Mater. 59(11) (2008) 1193-1196.

[8] W. Xiong, M. Selleby, Q. Chen, J. Odqvist, Y. Du, Phase Equilibria and Thermodynamic Properties in the Fe-Cr System, Crit. Rev. Solid State Mater. Sci. 35(2) (2010) 125-152.

[9] O. Tissot, C. Pareige, E. Meslin, B. Décamps, J. Henry, Influence of injected interstitials on α′ precipitation in Fe–Cr alloys under self-ion irradiation, Mater. Res. Lett. 5(2) (2016) 117-123.

[10] E.R. Reese, N. Almirall, T. Yamamoto, S. Tumey, G. Robert Odette, E.A. Marquis, Dose rate dependence of Cr precipitation in an ion-irradiated Fe 18Cr alloy, Scr. Mater. 146 (2018) 213-217.

[11] R.W. Harrison, A.W. Carruthers, J.A. Hinks, M.G. Burke, S.E. Donnelly, Cascade size and dose rate effects on α′ precipitation in ion-irradiated Fe14Cr alloy, Scr. Mater. 172 (2019) 33-37.

[12] V. Kuksenko, C. Pareige, P. Pareige, Cr precipitation in neutron irradiated industrial purity Fe–Cr model alloys, J. Nucl. Mater. 432(1-3) (2013) 160-165.

[13] M. Bachhav, G. Robert Odette, E.A. Marquis, α′ precipitation in neutron-irradiated Fe–Cr alloys, Scr. Mater. 74 (2014) 48-51.

[14] W.-Y. Chen, Y. Miao, Y. Wu, C.A. Tomchik, K. Mo, J. Gan, M.A. Okuniewski, S.A. Maloy, J.F. Stubbins, Atom probe study of irradiation-enhanced α′ precipitation in neutron-irradiated Fe–Cr model alloys, J. Nucl. Mater. 462 (2015) 242-249.

[15] C. Pareige, V. Kuksenko, P. Pareige, Behaviour of P, Si, Ni impurities and Cr in self ion irradiated Fe–Cr alloys – Comparison to neutron irradiation, J. Nucl. Mater. 456 (2015) 471-476.

[16] E.R. Reese, M. Bachhav, P. Wells, T. Yamamoto, G. Robert Odette, E.A. Marquis, On α′ precipitate composition in thermally annealed and neutron-irradiated Fe- 9-18Cr alloys, J. Nucl. Mater. 500 (2018) 192-198.

[17] O. Tissot, C. Pareige, E. Meslin, B. Decamps, J. Henry, Kinetics of α′ precipitation in an electron-irradiated Fe15Cr alloy, Scr. Mater. 122 (2016) 31-35.

[18] P. Zhu, Y. Zhao, S. Agarwal, J. Henry, S.J. Zinkle, Toward accurate evaluation of bulk hardness from nanoindentation testing at low indent depths, Mater. Design 213 (2022) 110317.

[19] Y. Zhao, A. Bhattacharya, C. Pareige, C. Massey, P. Zhu, J.D. Poplawsky, J. Henry, S.J. Zinkle, Effect of heavy ion irradiation dose rate and temperature on α′ precipitation in high purity Fe-18% Cr alloy, Acta Mater. 231 (2022) 117888.

[20] S. Agarwal, Y. Lin, C. Li, R. Stoller, S. Zinkle, On the use of SRIM for calculating vacancy production: Quick calculation and full-cascade options, Nuclear Instruments and Methods in Physics Research Section B: Beam Interactions with Materials and Atoms 503 (2021) 11-29.

[21] E. Wakai, A. Hishinuma, Y. Kato, H. Yano, S. Takaki, K. Abiko, Radiation-Induced α' Phase Formation on Dislocation Loops in Fe-Cr Alloys During Electron Irradiation, Le Journal de Physique IV 05(C7) (1995) C7-277-C7-286.

6.4 IN-SITU IRRADIATION ON EXTRACTION REPLICAS REVEAL RADIATION INDUCED AMORPHIZATION OF CARBIDES IN ADDITIVELY MANUFACTURED & CONVENTIONAL FM STEELS

—A. Bhattacharya, C.M. Parish, P.D. Edmondson (Oak Ridge National Laboratory), S.M. Levine, S.J. Zinkle (University of Tennessee, Knoxville), W. Y. Chen, P. Baldo (Argonne National Laboratory)

OBJECTIVE

In-situ irradiations were performed using energetic ions at Intermediate Voltage Electron Microscopy (IVEM) facility on extraction replica samples from a Eurofer97 steel and an additively manufactured Grade91. The experiments were aimed at validating the use of replica samples for irradiation experiments and understand amorphization behavior of different carbide phases in conventional Ferritic/Martensitic (FM) and Reduced Activation Ferritic/Martensitic (RAFM) steels in absence of a surrounding matrix. Here, experimental results regarding amorphization behavior of $M_{23}C_6$ and strong resistance to amorphization of Macromolecular Crystallography (MX) phases is presented.

SUMMARY

In-situ irradiations using 1 MeV Kr^{2+} ions in a transmission electron microscope (TEM) were performed on carbon-based extraction replica samples containing $M_{23}C_6$ carbides and MX carbonitrides from two FM steels: (i) 9%Cr-1%W-TaV based Eurofer97 in non-standard metallurgical condition (henceforth called as CEA-Eurofer97) and (ii) 9%Cr-1%Mo-VNb (all in wt.%) based additively manufactured (AM) Grade91 steel. The irradiations were performed between 100 – 773 K up to a maximum dose of ~2.4 displacements per atom (dpa). The $M_{23}C_6$ carbides are highly susceptible to radiation induced amorphization (RIA), while the MX type nanoprecipitates are highly amorphization resistant across the entire irradiation temperature range. Between 100 – 423 K, RIA of $M_{23}C_6$ carbides occurs very rapidly with critical amorphization doses ranging between ~0.35 – 0.9 dpa, increasing to higher doses at 573 K. With the present irradiation conditions (ion species, dose rate), results show that complete amorphization of the $M_{23}C_6$ carbides up to doses of ~2.4 dpa is not possible at 773 K. The critical temperature for the crystalline-to-amorphous phase transformation ($T_{c\rightarrow a}$) of $M_{23}C_6$ carbides irradiated as replica samples, i.e., without the surrounding metal matrix, was estimated to be ~812 K. The critical amorphization dose of $M_{23}C_6$ carbides increases nearly exponentially with irradiation temperature. Comparing the present results with neutron irradiation data on bulk samples reveals a decrease in the critical amorphization dose for $M_{23}C_6$ and an increase of $T_{c\rightarrow a}$, highlighting the effect of dose rate on the amorphization behavior that is qualitatively consistent with literature on other non-metals. Changes in the minor chemistry of $M_{23}C_6$, such as presence or absence of W, V, Nb, Mo, seems to have negligible effect on the amorphization behavior. In-situ irradiations on extraction replica samples provide a novel pathway to explore radiation tolerance of nano precipitates in nuclear structural materials without interference from the matrix.

PROGRESS AND STATUS

Introduction

Figure 1 presents a dose temperature map of $M_{23}C_6$ carbide evolution in CEA-Eurofer97. The RIA of $M_{23}C_6$ occurred at all T_{irr} between 100 K and 773 K for doses up to 2.4 dpa (evaluated using nano beam diffraction, [NBD]). Between 100 – 573 K, complete amorphization of $M_{23}C_6$ occurred, but diffraction spots were visible up to the highest irradiation dose at 773 K, indicating partially crystalline $M_{23}C_6$. At cryogenic temperatures (100 K), amorphous rings in the diffraction patterns, representing the early stages of crystalline to amorphous transformation, were detected at doses as low as ~0.1 – 0.12 dpa, with complete amorphization occurring by 0.24 dpa. The doses at which $M_{23}C_6$ completely amorphized increased with T_{irr}. At 773 K. Figure 1 suggests that doses higher than 2.4 dpa will be needed to completely amorphize $M_{23}C_6$ (or 773 K is closer to the boundary at which amorphization can occur). Figure 2 presents a similar dose-T_{irr} mapping of $M_{23}C_6$ in AM-Grade91 steel for T_{irr} = 100, 293 and 423 K. At each T_{irr}, the doses at which these carbides amorphized was nearly identical to $M_{23}C_6$ in CEA-Eurofer97. This implies that the amorphization behavior of $M_{23}C_6$ in a RAFM steel such as Eurofer97 and conventional FM steels (AM-Grade91 in this study) follows very similar patterns with respect to dose and temperature. The chemistry difference between $M_{23}C_6$ phase (M = Fe, Cr, W, V rich) in Eurofer97 and $M_{23}C_6$ (M = Fe, Cr, Nb, Mo) rich in AM Grade91 seems to have negligible effect on RIA.

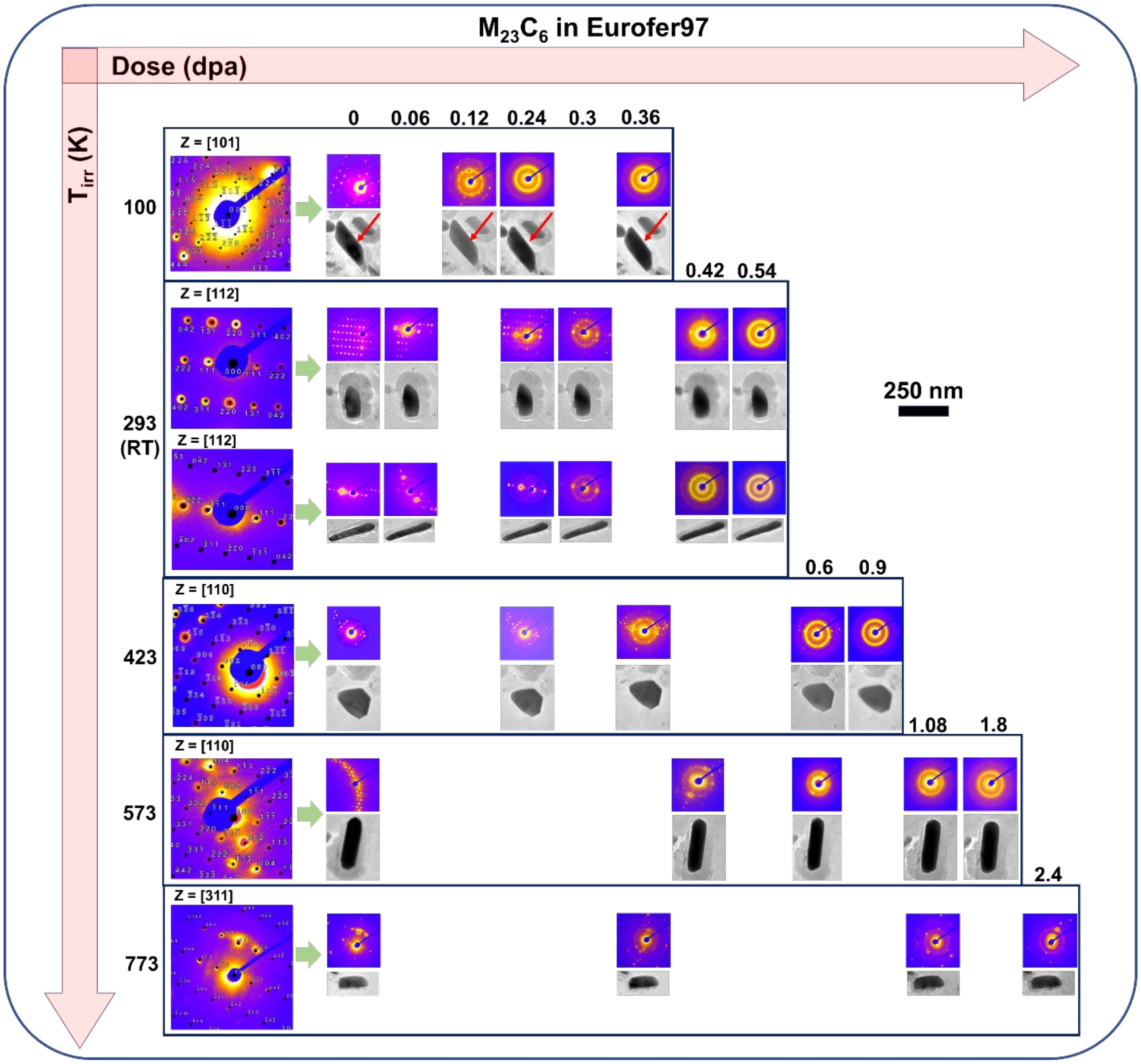

Figure 1. Dose temperature mapping of RIA in $M_{23}C_6$ nanoprecipitates extracted from CEA- Eurofer97 steel and irradiated using 1 MeV Kr ions. The figure presents evolution of $M_{23}C_6$ particles using bright field (BF) TEM imaging and the associated NBD patterns.

The experimentally measured critical amorphization dose and amorphization onset doses are plotted in Figure 3 and fitted using the equation below that describes the relationship between irradiation temperature and critical amorphization dose:

$$D_c = \frac{D_0}{1 - exp\left[\left(\frac{E_a}{k_b}\right)\left(\frac{1}{T_{c \to a}} - \frac{1}{T_{irr}}\right)\right]} \quad (1)$$

where D_0 is the dose to achieve amorphization at 0 K, k_b is Boltzmann constant, E_a is activation energy (in eV) associated with defect migration/recombination, defect and ion diffusion in the amorphous material, or epitaxial recrystallization at the crystalline amorphous interface [1]. Equation 1 provided an excellent fit for the experimental data in Figure 3. By fitting our experimental data with Equation 1 and using a least squares refinement for each temperature, we obtained $T_{c \rightarrow a}$ of ~812 K for irradiations on extraction replicas.

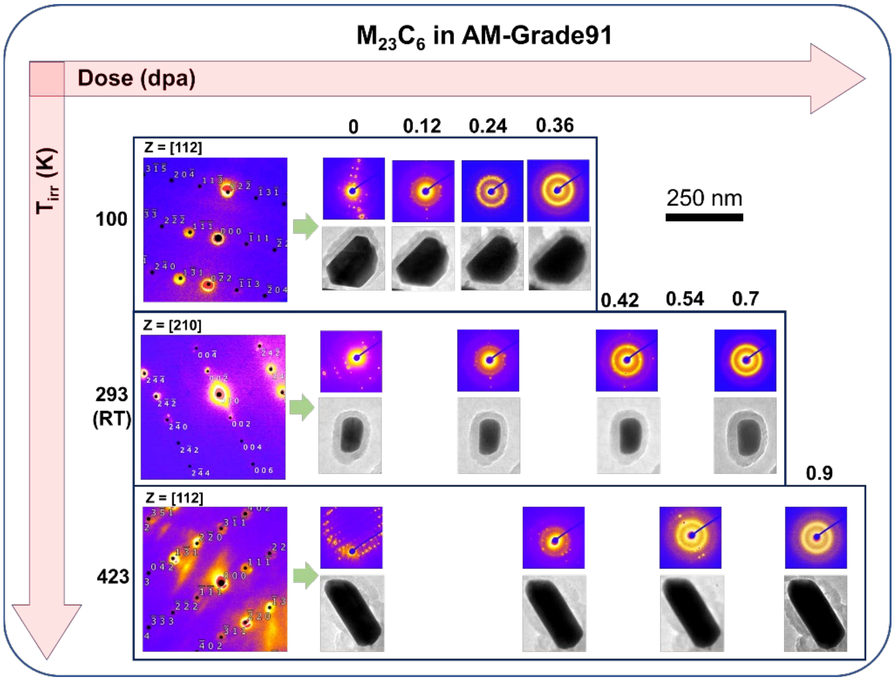

Figure 2. Dose temperature mapping of RIA in $M_{23}C_6$ nanoprecipitates extracted from AM-Grade91 steel.

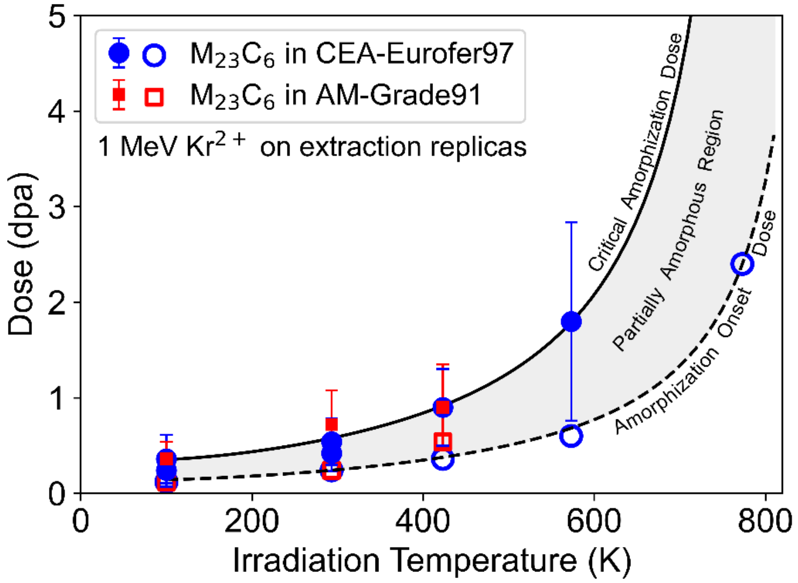

Figure 3. Evolution of critical amorphization dose and onset amorphization doses of $M_{23}C_6$ carbides in CEA-Eurofer97 and AM-Grade91 steel for irradiations using 1 MeV Kr^{2+} ions on extraction replica samples. Curves fitted using equation (1).

The RIA was also studied for MX nanoprecipitates in AM-Grade91 steel at the two lowest temperatures of 100 and 293 K. In this material, the MX particles were primarily V-rich carbonitrides. Up to ~ 2 dpa, the MX phase remained crystalline – as proven by the presence of diffraction contrast in the BF TEM images and NBD patterns in Figure 4, where fully amorphous rings were detected for $M_{23}C_6$ carbides while strong diffraction spots are indexed for the MX particles. Many MX particles in this steel were large and almost equivalent in size to $M_{23}C_6$. This shows that the difference in the amorphization behavior is likely not due to any size difference but reflects the inherent radiation tolerance of MX type particles.

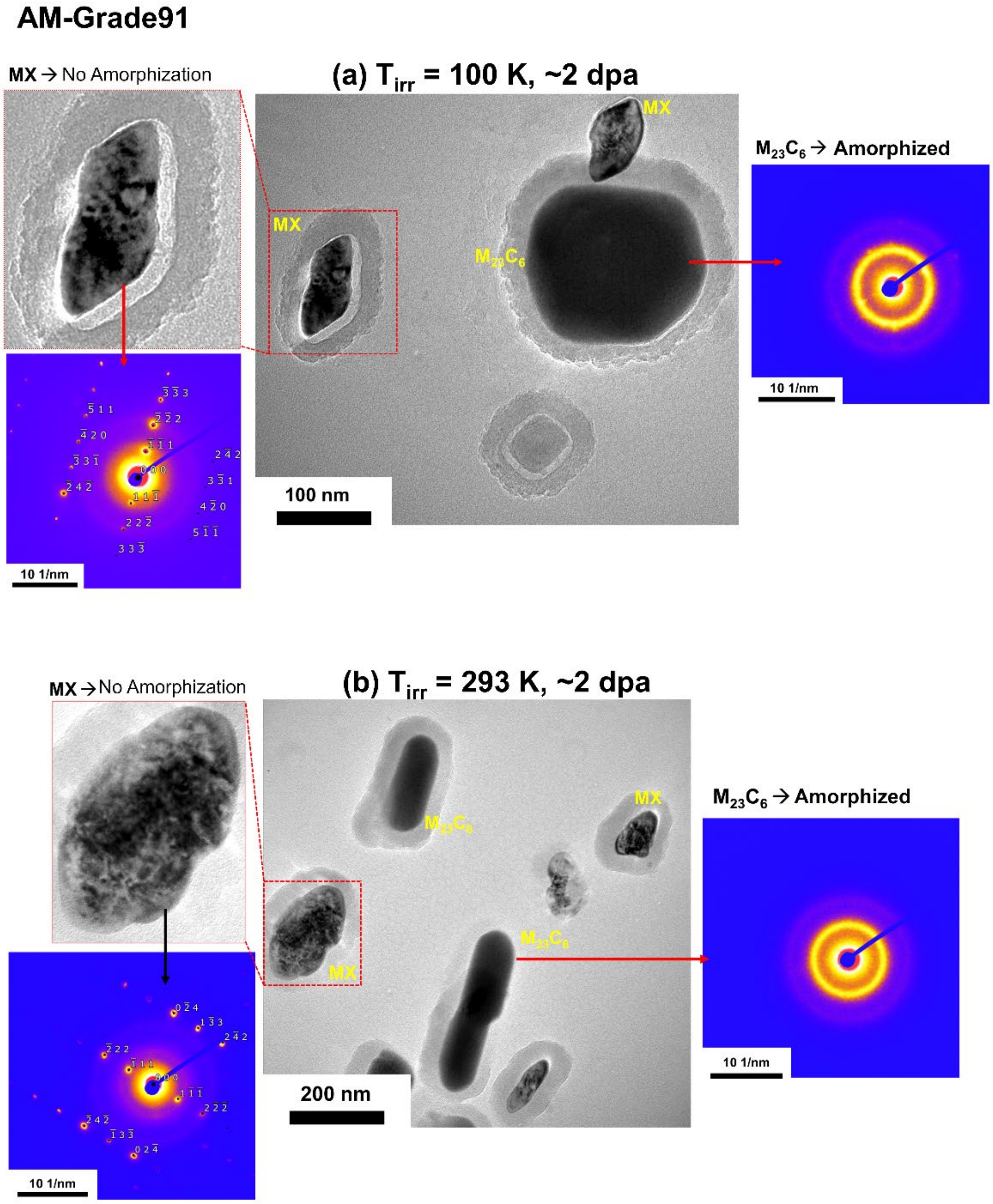

Figure 4. BF TEM images and diffraction patterns comparing MX and $M_{23}C_6$ particles after ~ 2 dpa irradiations on extraction replicas at (a) 100 K and (b) 293 K.

Results

This study is complete with a publication (Bhattacharya et al. J. Nucl. Mater. 563 (2022) 153646). The results from this study will be used to develop a procedure to extract $M_{23}C_6$ and MX particles from High Flux Isotope Reactor (HFIR) irradiated (radioactive) RAFM steels followed with advanced electron microscopy characterization.

References

[1] W.J. Weber, R.C. Ewing, C.R.A. Catlow, T. Diaz De La Rubia, L.W. Hobbs, C. Ki- noshita, H. Matzke, A.T. Motta, M. Nastasi, E.K.H. Salje, E.R. Vance, S.J. Zinkle, Radiation effects in crystalline ceramics for the immobilization of high-level nuclear waste and plutonium, J. Mater. Res. 13 (1998) 1434–1484.

7. PLASMA-MATERIAL INTERACTIONS

No contributions this reporting period.

8. CORROSION AND COMPATIBILITY IN FUSION SYSTEMS

8.1 ADDITIONAL CHARACTERIZATIONS OF ODS FeCrAl AND SiC SPECIMENS AFTER EXPOSURE TO FLOWING PbLi—M. Romedenne, B. A. Pint (Oak Ridge National Laboratory)

OBJECTIVE

The goal is to characterize the corrosion layer formed on the surface of the SiC specimens after exposure in a PbLi thermal convection loop (TCL) with a peak temperature of 650°C. Initial results and characterizations were reported in the previous semi-annual report DOE/ER-0313/71. Additional characterizations using transmission electron microscopy (TEM) including energy-dispersive X-Ray (EDX) line scans, mapping of different elements and electron diffraction patterns are reported.

SUMMARY

Chemical vapor deposited (CVD) SiC and aluminized F82H corrosion and tensile specimens were exposed in a TCL made of pre-oxidized Kanthal APMT (Fe-21Cr-5Al-3Mo) tubing filled with PbLi for 1000 h with a peak temperature of 650°C. The aluminized specimens were pre-oxidized for 2 h at 800°C in air to further minimize the interaction between the steel and liquid. The dissolved Fe and Cr from the pre-oxidized APMT coupons reacted with the CVD SiC specimens to form consecutive layers rich in Ni-, Fe-, Cr-, Si- and O-rich layers of various grain sizes from the SiC interface towards the surface. The EDX and selected area electron diffraction (SAED) revealed the presentation of M_3Si (M= Fe and Ni) and amorphous SiO_2.

PROGRESS AND STATUS

Introduction

Intensive research has been accumulated on the compatibility of austenitic and ferritic steels for use in Pb-17 at%Li (PbLi) metal blankets of fusion reactors. Studies from the 1980s [1-4] and 1990s [5-7] observed dissolution, intergranular penetration, interstitial element transfer, and mass transfer caused by thermal and concentration gradients in TCLs and Forced Convection Loops (FCLs). The corrosion behaviors and dissolution rates of austenitic steels (316 type), ferritic steels (HT9, 9Cr1Mo types), and, more recently, Reduced Activation Ferritic-Martensitic steels (RAFM) (Manet and F82H types) were evaluated. Although lower dissolution rates were measured for the ferritic and RAFM steels (HT9, 9Cr1Mo types) than austenitic steels in PbLi, high corrosion rates [1-10] and metallurgical considerations [1] limit their use as blanket material below 475°C [1,8].

Different strategies have been investigated to improve liquid metal compatibility above 500°C such as alloying to form FeCrAl alloys [11-13] and the use of Al-rich coatings on RAFM-type steels [14-16]. Either alloying or coating when pre-oxidized enables the formation of an adherent surface oxide such a-Al_2O_3 [11-16] that prevents the direct contact between steel and liquid. These strategies have shown very promising results in static and flowing PbLi [11-16]. For SiC, most studies have shown good PbLi compatibility for both monolithic SiC (e.g., high purity CVD material) and SiC-SiC composites [17-20]. However, only a few studies have exposed SiC to PbLi in the presence of Fe or Cr, which both form more stable carbides than SiC. Previous capsule testing showed some changes when SiC was exposed in Fe capsules [18]. To further explore a possible dissimilar material interaction between low-Cr ODS FeCrAl [21,22] and CVD SiC, a TCL experiment was conducted with flowing PbLi at a peak temperature of 700°C [23]. Like results with only APMT in the TCL, significant metal dissolution occurred at >650°C [23]. With SiC specimens present in the TCL, Fe and Cr dissolved from the FeCrAl specimens reacted with the SiC coupons forming thick carbide and silicide layers [23]. In the next experiment, the peak temperature was lowered to 650°C and the ODS FeCrAl specimens were replaced with pack aluminized F82H (Fe-8Cr-2W) specimens [24]. The current results after 1,000 h operation are presented.

Experimental Procedure

Thermal convection loop and materials

Details about the TCL experimental procedure were given in a previous report [25]. However, for better clarity, a succinct experimental protocol is reported here. The TCL operated at a peak temperature of 650°C (top of the hot leg) and at a minimum temperature of 550°C (bottom of the cold leg) and was made of pre-oxidized (8 h in air at 1050°C) APMT. The TCL contained pre-oxidized (2h at 800°C in air) APMT coupons and bare, high purity CVD SiC-SiC specimens. The alloy compositions (loop and specimens) are reported in Table 1. The specimens were exposed for 1000 h in the TCL filled with 10 kg of flowing liquid eutectic PbLi (0.77 cm/s) provided by GMH Stachow-Metall GmbH (analyzed composition in Table 2). A total of 12 CVD SiC coupons and 4 APMT coupons were exposed in the TCL. Aluminized F82H coupons (10) and tensile specimens (14) were also exposed, and results were reported previously [25].

Table 1. Alloy compositions measured using inductively coupled plasma and combustion analyses in wt.%

Alloy	Fe	Cr	Al	Ni	Si	C	Others
APMT	69.0	21.6	4.9	0.12	0.53	0.03	2.8Mo, 0.1Mn, 0.2Hf, 0.1Y, 0.1Zr
APMT tube*	70.0	21.4	4.9	-	0.34	0.04	3.1Mo, 0.2Mn, 0.02Cu
CVD SiC	-	-	-	0.01	69.8	30.2	0.003O

*reported by manufacturer [11]

Table 2. As-received PbLi composition measured using inductively coupled plasma and combustion analyses in at.%

Pb	Li	C	H	O	N
15.05	80.62	0.42	2.02	1.90	<0.01

Characterizations

After exposure, the PbLi was drained into a stainless-steel tank and the TCL was cleaned using acetic acid, ethanol, and hydrogen peroxide [11-13]. Specimens were cleaned and weighed before and after exposure using a Mettler Toledo X205 balance with an accuracy of ±0.04 mg. Focused ion beam (FIB) based lift out process was used to extract specimens for transmission electron microscopy characterizations. An extreme field emission gun (XFEG) Scanning Transmission Electron Microscopy (STEM) (Talos F200X) equipped with four detectors was used for elemental mapping using EDX spectroscopy (Super-X EDS) and another TEM (Japan Electron Optics Laboratory Co., Ltd [JEOL] JEM-2100F) equipped with three STEM detectors, Oxford X-Max detector, Gatan Orius charged-coupled device (CCD) camera and Gatan Image Filter (GIF Quantum 963 SE) was used for SAED.

Results

Dark Field images and Elemental maps

After exposure mass gains were observed for the SiC coupons (up to 1.2 mg.cm^{-2}) while mass losses were measured for the APMT specimens (average mass losses of -0.09 +0.05 mg.cm^{-2}). In agreement with previous observations [23], Fe and Cr from the APMT specimens dissolved into the liquid PbLi during exposure and further reacted with the SiC coupons. The mass transfer between the alloys is clearly visible in Figure 1 where the thickness of the surface corrosion layer was measured to increase with decreasing temperature.

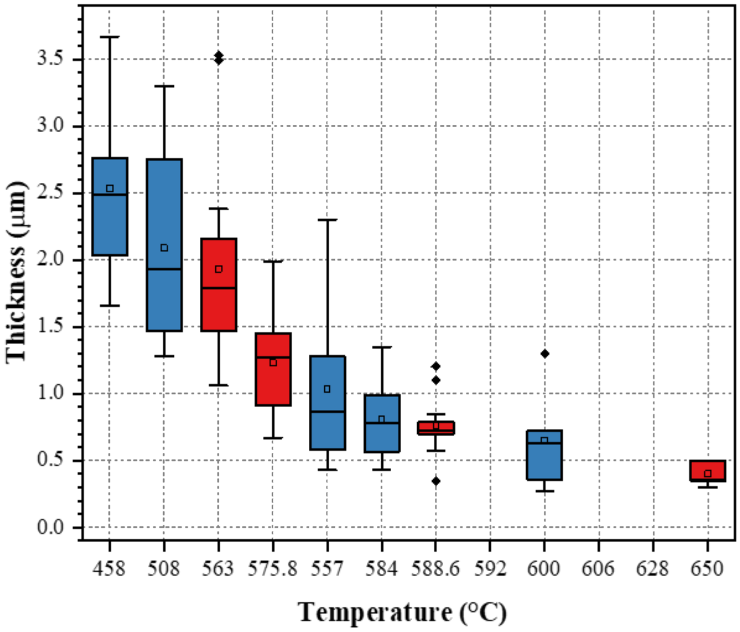

Figure 1. Thickness of the corrosion layer formed on the surface of the CVD SiC coupons as a function of temperature (location in the TCL).

Previous surface X-ray diffraction (XRD) analyses suggested the formation of Cr_3C_2, Cr_3Si and Fe_8SiC [25]. A dark field TEM image of the FIB specimens extracted from the surface of the SiC coupon exposed at the lowest temperature in the cold leg (458°C) is reported in Figure 2. A complex microstructure constituted of large grains near the CVD-SiC interface and fine grains towards the surface below an O-rich layer (Figure 3).

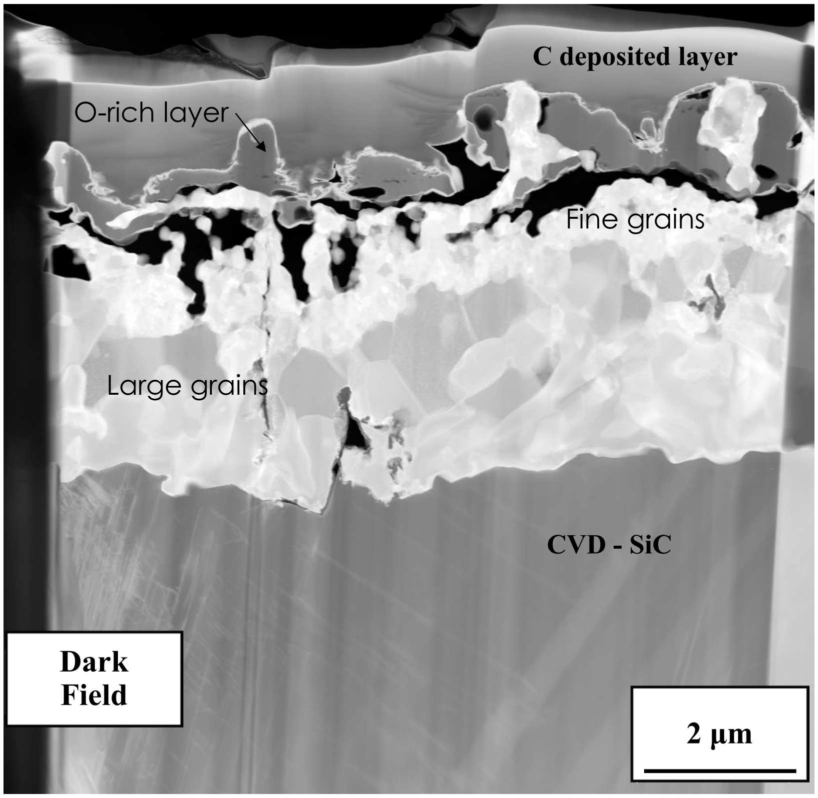

Figure 2. TEM Dark Field image of the corrosion layer formed on the surface of the CVD SiC coupon located at the bottom of the cold leg (estimated temperature of 458°C) after 1,000 h exposure in flowing PbLi.

The EDX quantified elemental maps revealed the presence Ni-, Fe-, Cr- and Si- and O-rich consecutive layers. The presence of Ni in the corrosion layer (Figure 3) was quite surprising since none of the exposed materials in the PbLi TCL contained Ni. However, the stainless-steel pot used to melt the PbLi in a glovebox before being attached to the top of the hot leg contained Ni that could have been dissolved and later reacted with the SiC coupons during exposure.

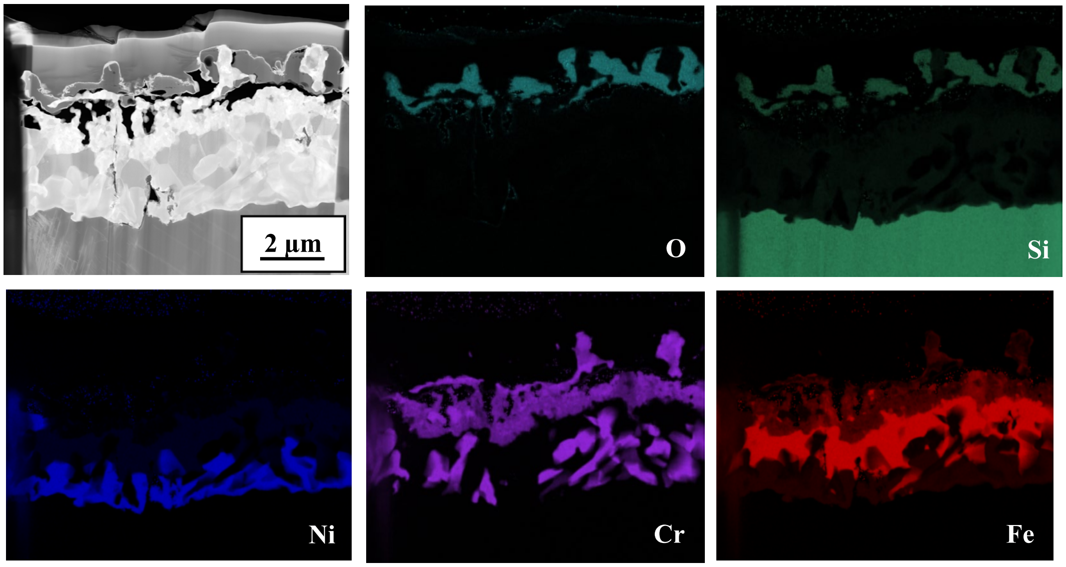

Figure 3. Dark field TEM image and quantified elemental EDX maps of the CVD SiC specimen located at the bottom of the cold leg (458°C) after 1000 h in the TCL filled with liquid eutectic PbLi.

The larger grains were identified as M_3Si (M= 69 ± 3 at.% Fe and 10 ± 1 at.% Ni) using SAED and EDX point analyses (Figure 4a) in agreement with surface XRD results. The SAED and EDX results revealed the formation of amorphous SiO_2 on the surface of the corroded layer (Figure 3 and Figure 4b).

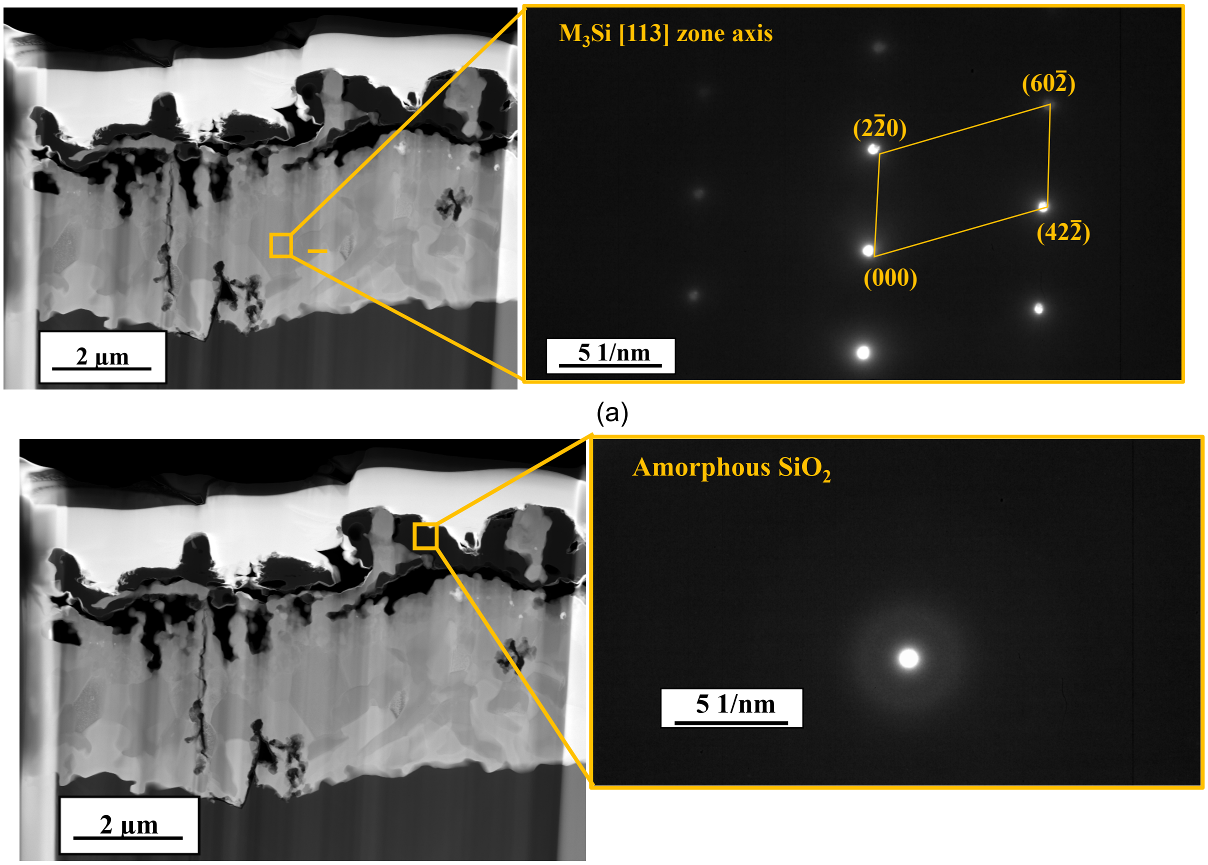

(a)

(b)

Figure 4. High angle annular dark field (HAADF) images with identified SAED patterns for (a) M$_3$Si and (b) SiO$_2$ layers on the surface of the CVD SiC specimen located at the bottom of the cold leg (458°C) after 1000 h in the TCL filled with liquid eutectic PbLi.

References

[1] O. K. Chopra, P. F. Tortorelli, J. Nucl. Mater. **123** (1984) 1201.
[2] P.F. Tortorelli and J.H. De Van, J. Nucl. Mater. 141-143 (1986) 592.
[3] G.M. Gryaznov, V.A. Evtikhin, L.P. Zayval'skii, N.V. Samsonov and A.A. Gusakov, Atomnaya Energiya. 355-358 (1985) 59.
[4] H.U. Borgstedt, G. Drechsler, G. Frees and Z. Peric, J. Nucl. Mater. 155-157 (1988) 728-731.
[5] J. Sannier, M. Broc, T. Flament and A. Terlain, Fus. Eng. Design 299-307 (1991) 14.
[6] J. Sannier, T. Dufrenoy, T. Flament and A. Terlain, J. Nucl. Mater. 191-194 (1991) 975-978.
[7] P. F. Tortorelli, J. Nucl. Mater. 191-194 (1992) 965-969.
[8] J. Konys, W. Krauss, H. Steiner, J. Novotny and A. Skrypnik, J. Nucl. Mater. 1191-1194 (2011) 417.
[9] J. Konys and W. Krauss, J. Nucl. Mater. S576-S579 (2013) 442.
[10] P. Chakraborty, V. Kain, P. K. Pradham, R.K. Fotedar and N. Krishnamurthy, J. Fus. Eng. 371-378 (2015) 34.
[11] S. J. Pawel and K. A. Unocic, J. Nucl. Mater. 492 (2017) 41.
[12] K. A. Unocic and B. A. Pint, J. Nucl. Mater. 455 (2014) 330.
[13] J. Jun, K. A. Unocic, M. J. Lance, H. M. Meyer and B. A. Pint, J. Nucl. Mater. 528 (2020) 151847.
[14] H. Glasbrenner, Z. Peric and H. U. Borgstedt, J. Nucl. Mater. 233-237 (1996) 1378.
[15] W. Krauss, J. Konys, S.-E. Wulf, J. Nucl. Mater. 455 (2014) 522.

[16] B. A. Pint, J. Jun, E. Cakmak, D. J. Sprouster, N. Olynik and L. L. Snead, Fus. Sci. Tech. 77 (2021) 761.
[17] T. Yoneoka, S. Tnaka and T. Terai, Mater. Trans. 1019-1023 (2001) 42.
[18] B.A. Pint and K.A. Unocic, J. Nucl. Mater. 442 (2013) S572.
[19] P. Chakraborty, S. Kumar, R. K. Fotedar and N. Krishnamurthy (2013, June) *Interaction of α-silicon carbide with lead-lithium eutectic.* AIP Conference Proceedings 538, 34, Carbon Materials, Granada, Spain.
[20] S. Tosti, A. Moriani and A. Santucci, Fus. Eng. Design 2479-2483 (2013) 88.
[21] B. A. Pint, S. Dryepondt, K. A. Unocic and D. T. Hoelzer, JOM 66 (2014) 2458.
[22] S. Dryepondt, K. A. Unocic, D. Hoelzer, C. P. Massey, B. A. Pint, J. Nucl. Mater. 501 (2018) 59.
[23] B. A. Pint, J. Jun and M. Romedenne, Fus. Eng. Design 166 (2021) 112389.
[24] B. L. Bates, Y. Q. Wang, Y. Zhang and B.A. Pint, Surf. Coat. Technol. 204 (2009) 766.
[25] M. Romedenne, B.A. Pint, "Liquid metal compatibility of SiC and aluminized F82H in flowing PbLi", Fusion Materials Semiannual Progress Report for period ending Dec. 31, 2021, DOE/ER-0313/71 (2021), p. 153-161.

9. MODELING AND COMPUTATIONAL STUDIES

9.1 COMPUTATIONALLY INVESTIGATING THE EFFECTS OF TEMPERATURE AND HELIUM ON TUNGSTEN HEAVY ALLOYS

—R. Beall, J. V. Haag IV, K. C. Pitike, W. Setyawan (Pacific Northwest National Laboratory)

OBJECTIVE

To generate an atomistic database of irradiation effects on the structure and mechanical property of interphase boundaries in W-Ni-Fe heavy alloys (a bi-phase composite consisting of body-centered cubic (BCC) W particles embedded in face centered cubic (FCC) Ni-Fe-W ductile solid solution matrix) as a structural material in a divertor.

SUMMARY

Informed by high-angle annular dark field scanning transmission electron microscopy (HAADF-STEM) images, a new stairstep BCC/FCC interphase boundary model is constructed, namely BCC{332}<110>//FCC{100}<100>. The model is used to study the temperature effect and W concentration in the FCC ductile phase on the tensile properties of the boundary. The study is performed using molecular dynamics method. Tensile strength decreases by 24.74% and 48.55% at 1/2 and 2/3 of the melting temperature of Ni, respectively compared to room temperature. Ductile phase comprising of Ni-W solid solutions exhibit a higher ultimate tensile strength compared to a pure Ni ductile phase, namely by over 20% for all models with 15 at% W or more.

PROGRESS AND STATUS

Previously, molecular dynamics (MD) calculations of fracture energy of W/Ni-W interphase boundary were performed using BCC{110}<100>//FCC{111}<110> IB model to investigate the effect of W concentration in the Ni-W ductile phase on the fracture energy at 1000°C [1,2]. In this reporting period, we explore a different IB model based on a recent HAADF-STEM image that we acquired. The STEM image showed an orientation relationship of BCC[110] parallel to FCC[100] and it was found that for every 4 BCC{220} planes there are 5 FCC{200} planes (taken as the x dimension of the simulation cell). Using experimental lattice parameters of W (3.1652 A) and Ni (3.5295 A), a good lattice matching is found between W[1-13] and Ni[010], thus taken as the y dimension. The cross product of the x and y crystal directions give the z dimension oriented as W[3-3-2] and Ni[001], which is the boundary normal direction. The STEM revealed the boundary forms stair steps. However, the height of the steps could not be resolved. Therefore, three models of a W and Ni interphase were constructed with different ratios of W to Ni layers based the lattice spacing indicating a ratio of 1 Ni per every 2.62 W would match perfectly. From this ratio, Model 1 with 1 Ni per every 2 W, Model 2 with 1 Ni per every 3 W, and Model 3 with 2 Ni per every 5 W were chosen to determine which boundary structure was the most stable and thereby the most probable to form. To create each model, the *axis* code was used to make a W332 slab and a Ni100 slab. These were then exported into VESTA, a visualization software, to delete the specific atoms needed to make these models. Then, using Large-scale Atomic/Molecular Massively Parallel Simulator (LAMMPS), these slabs were put together and relaxed, as shown in Figure 1.

To find which model was the most stable, and thereby most likely to form, interphase boundary energy (E_{IB}) was calculated. In addition, the ideal fracture energy (E_{fr}) of the IB was calculated. To compute these values for each model, the total energy and number of atoms from the relaxed model had to be calculated for the models, bulk Ni, bulk W, the top slab, and bottom slab. The x and y dimensions were also allowed to relax. Additionally, the surface energy (γ) of a Ni100 slab and a W332 slab had to be calculated. The total energy of Model 1, Model 2, Model 3, Ni100 slab, W332 slab, each possible type of top slab (Ni10x1z and Ni10x2z), each possibly type of bottom slab (W8x2z, W8x3z, and W8x5z), the dimensions of each interphase, and the energy per atom based on the W and Ni bulk were used to calculate the interfacial boundary and fracture energies. Model 1 with 1 Ni layer per 2 W layers was found to have the smallest interfacial boundary energy as shown in Table 1, making it the most stable model. Albeit Model 2 has a similar interfacial boundary energy, only 66 mJ/m^2 higher than Model 1's energy of -1055 mJ/m^2. Further studies could be conducted on this model, as it could form as well, but is less likely.

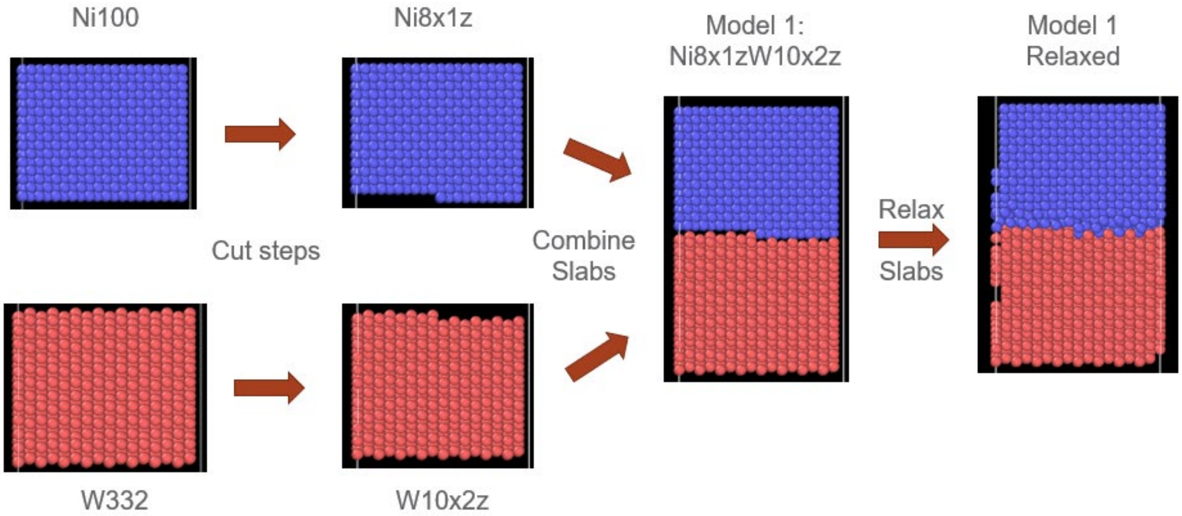

Figure 1. Process of creating an interphase boundary model of a Tungsten Heavy Alloy (WHA).

Table 1. IB Energy and Fracture Energy for the three different step interphase models

Model	Interfacial Boundary Energy (mJ/m^2)	Fracture Energy (mJ/m^2)
1	-1055	5136
2	-989	5138
3	-658	5459

Then the most stable model underwent tensile test simulations at room temperature (27°C), 1/2 the melting temperature of Ni (590°C), and 2/3 the melting temperature of Ni (880°C) to analyze the fracture behavior and determine the tensile strength from the stress strain curves. Each tensile simulation had a strain rate of 0.5 ns^{-1} and the x and y dimensions are allowed to relax. As shown in Figure 2, the WHA seemed to fracture in the elastic region at 27°C. The tensile test simulation at 590°C shows fracture in the elastic region as well; however, as the stress decreases following fracture, there are small plateaus which could be attributed to the speed of the tensile test and relatively large interatomic forces trying to reconnect the atoms being separated in the tensile test simulations. However, this behavior cannot be confirmed, as experimental tensile tests are impossible to conduct on a sample on this scale. Lastly, the 880°C sample appears to have entered the plastic deformation region and breaks at a far larger strain than the other two samples.

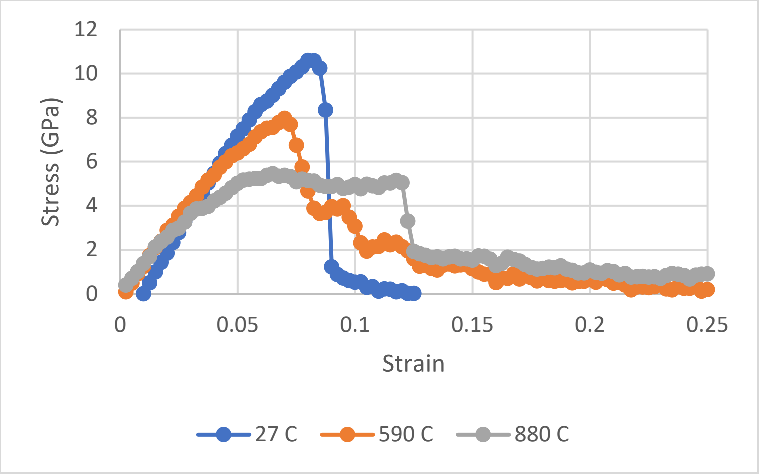

Figure 2. Engineering stress-strain curve for Model 1 at 27°C, 590°C, and 880°C.

Another piece of information that can be determined from the stress strain curves in Figure 2 is the ultimate tensile strength for each sample. The ultimate tensile strength is the highest point of stress on the curve before fracture. As shown in Table 2, the 27°C sample has an ultimate tensile strength of 10.6 GPa, while the 590°C and 880°C samples have ultimate tensile strengths of 8.0 GPa and 5.5 GPa. Respectively. The 590°C shows a decrease of 24.74% from the 27°C sample, while the 880°C shows a decrease of 48.55% from the 27°C sample and a decrease of 31.63% from the 590°C sample.

Table 2. Ultimate Tensile Strength of Model 1

Temperature (°C)	Ultimate Tensile Strength (GPa)	Change from 27°C
27	10.6	-
590	8.0	-24.74%
880	5.5	-48.55%

Interphases between dissimilar elements often form a chemically diffused region to minimize the interfacial energy. Atomic probe tomography (APT) showed that the Ni phase in the WHAs contain substitutional W. Therefore, more complex models of Model 1 were created with solid solutions of the top Ni100 slab with 3, 6, 9, 12, 15, 20, 30, 40, 50, and 60 at% of W. Ten samples of each concentration were constructed and averaged to then calculate the interphase boundary energy to then determine the most stable composition using Equation 1. Ten samples of bulk Ni, top slab, bottom slab, and Ni100 slab were also constructed for each of the concentrations in to obtain their energies to calculate the surface energy of Ni100 and each of the interphase boundary value. Tensile test simulations were also performed on each new solid solution model at room temperature (27°C) at a strain rate of 0.5 ns^{-1}. From these simulations, the energy difference before and after fracture from the tensile simulations, were used to calculate fracture energy for each concentration.

Concentration of substitutional W within the ductile phase also plays a part on the ultimate tensile strength, interfacial boundary energy, and fracture energy. As shown in Figure 3, at 27°C, generally as the atomic percent of W in the top slab is increased, the ultimate tensile strength increases as well. Additionally, each sample maintains the behavior of the sample with the pure Ni ductile phase at 27°C where fracture occurs in the elastic region.

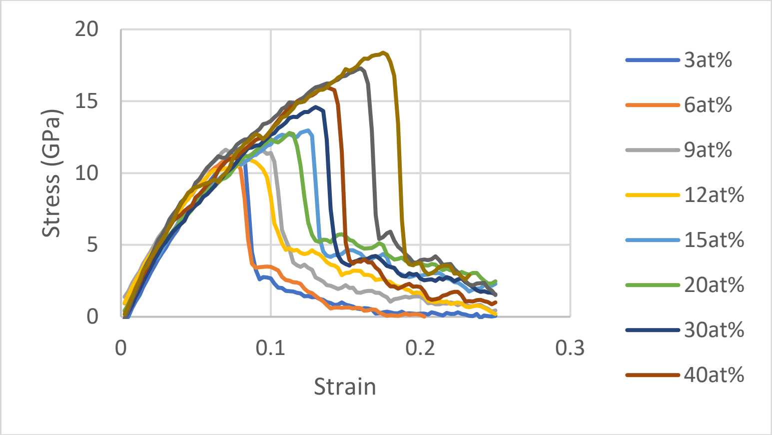

Figure 3. Engineering stress strain curve at 27°C for each composition of the WHA model where the ductile-phase slab has been simulated as a random solid solution. The atomic percentage shown corresponds to the concentration of W in the Ni-W solid solution.

The percent increase for each concentration compared to a pure Ni ductile phase is shown in Table 3. The WHA sample with only Ni as the ductile phase has the lowest ultimate tensile strength, with other concentrations varying from a 3.58% increase to a 73.40% increase. Though the exact concentration of substitutional W atoms is unknown, it is important to characterize the ultimate tensile strength that is to be expected at each concentration. Nevertheless, it is unlikely that some of the higher percentages of W are structurally feasible, as they may add too much stress to the FCC lattice structure of the top slab.

Table 3. Ultimate tensile strength of models with a ductile phase of Ni and various atomic percentages of W at 27°C

At% W	Ultimate Tensile Strength (GPa)	Change from pure Ni
0	10.6	-
3	11.8	10.90%
6	11.2	5.66%
9	11.6	9.69%
12	11.0	3.58%
15	13.0	22.33%
20	12.8	20.70%
30	14.6	37.70%
40	16.0	50.64%
50	17.3	63.14%
60	18.4	73.40%

The stability of the model can be somewhat be examined through interphase boundary energy calculations. As shown in Figure 4, 60 at% of W in the ductile phase has an interphase boundary energy of 1134.11 mJ/m^2, which is the only positive value, and approximately 2000 mJ/m^2 higher than any other interfacial boundary energy values. This extremely large value, relative to the other samples, indicates it may be too unstable of a concentration to be structurally feasible, experimentally. Aside from a pure Ni ductile phase, the next lowest energy value was 40 at% W, which had an interfacial boundary energy of -598.356; however, this could be explained by larger standard in energy and slab dimensions with larger concentrations of W, causing a larger potential error.

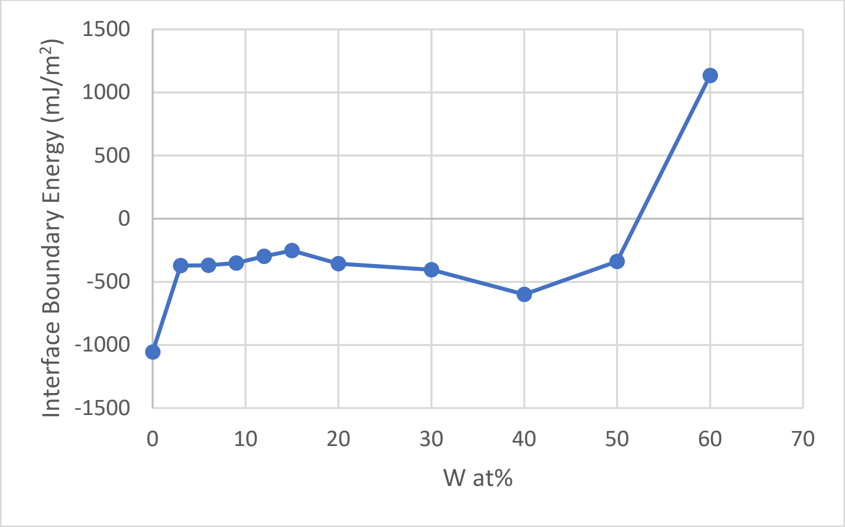

Figure 4. Interphase boundary energy for each composition of the ductile phase slab.

If fracture occurs at the interphase boundary, a smaller interfacial boundary energy would correspond to a larger fracture energy because a larger energy is required to fracture a stronger (more stable) boundary. If fracture occurs at the ductile phase near the boundary, the above correlation may still hold. Therefore, the somewhat inverse relationship between Figure 4 and Figure 5 is logical. The ductile phase being pure Ni, Ni with 40at% W, and Ni with a 50at% W are the highest fracture energy values, just as they were the three of the lowest interfacial boundary energies. However, 60 at% W shows far less deviance from the other compositions, while still showing a sharp downward trend which mirrors the sharp upward trend in Figure 4 for interfacial boundary energy.

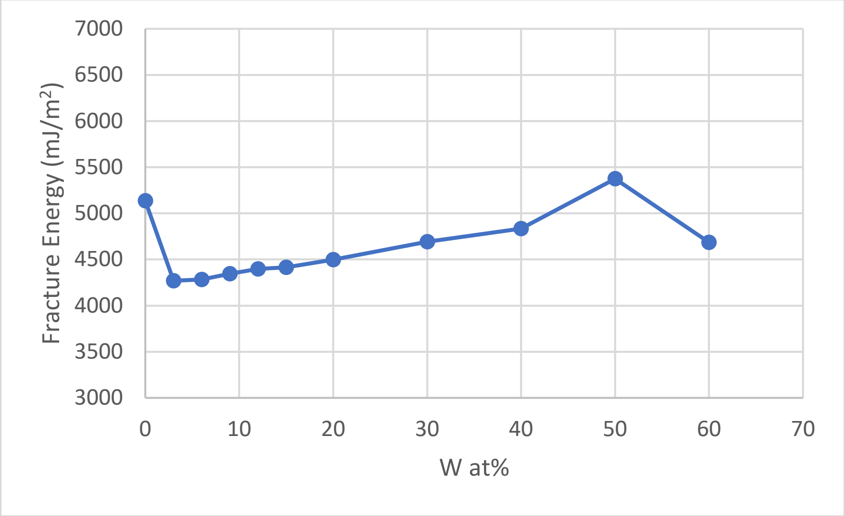

Figure 5. Fracture energy for each composition of the ductile phase slab.

Future work includes exploring segregation and clustering behavior of He atoms near the boundary and their effects on the tensile and fracture properties of the boundary. In addition, as more HAADF-STEM images are obtained and boundary structures are determined, studies will be extended using these structures.

Acknowledgements

This research has been supported by the U.S. Department of Energy (US DOE), Office of Science, Office of Fusion Energy Sciences and performed at the Pacific Northwest National Laboratory (PNNL) under contract number DE-AC05-76RL01830 and by the US DOE, Science Undergraduate Laboratory Internship (SULI) program (PNNL project #45260).

References

[1.] W. Setyawan, Density functional theory calculation of helium segregation and decohesion effect in W110/Ni111 interphase boundary, Journal of Applied Physics, 128, 145101 (2020).
[2.] S. P. Edwards, N. Chen, W. Setyawan, Molecular dynamics study of interphase boundaries in W-Ni-Fe Tungsten Heavy Alloys, Fusion Semiannual Progress Report for Period Ending June 30th 2021, DOE/ER-0313/70, p. 194.

9.2 EXTENTION OF KSOME TO HANDLE LONG-RANGE INTERACTION BETWEEN POINT DEFECTS AND ITS EFFECTS ON DIFFUSION-REACTION PROCESSES

—G. Nandipati, K. J. Roche, R. J. Kurtz, W. Setyawan (Pacific Northwest National Laboratory), B. D. Wirth (University of Tennessee, Knoxville)

OBJECTIVES

This task aims to incorporate long range interaction between point defects in kinetic simulations of microstructural evolution (KSOME) [1-3], allowing KSOME to simulate the diffusion of mobile point defects under the influence of elastic interaction from all its neighboring defects within the range of interaction.

SUMMARY

The report details how the long-range interaction energies between point defects are calculated for a defect that changed during the most recent KMC step, and correspondingly, the energies of its neighboring point defects are corrected due to the change. As well as how the migration barriers for mobile point defects are adjusted according to the change in the interaction energies.

PROGRESS AND STATUS

Introduction

The pairwise elastic interaction energy between a point defect *i* and its neighboring point defect *j* is given as [4]

$$E_{ij} = \frac{A_{ij}}{r_{ij}^{\alpha_{ij}}} \qquad (1)$$

where A_{ij}, α_{ij} and r_{ij} are the strength of the interaction, the exponent, and the center-to-center distance between *i* and *j* , respectively. The subscript ij, for A and α in eq. (1) is used to indicate that their numerical values depend on the properties and/or type of the interacting defects. The A has a negative or a positive value depending on whether the interaction is attractive or repulsive. A defect that moved or reacted during the most recent KMC step is called a primary defect (PD). Its total energy, due to its interaction with all its neighbors E_{PD} is given as

$$E_{PD} = \sum_j \frac{A_j}{r_j^{\alpha_j}} \quad \text{where } j = \{\text{all neighbors}\} \qquad (2)$$

After each KMC step, the computation of the total interaction energy ($\mathrm{E_{PD}}$) of the primary defect is repeated. At the same time, those of its neighbors are corrected by the amount of change in the pairwise interaction energy between the PD and its neighbor. Neighbor defects can be categorized into three groups, depending on whether they interact with PD after its diffusion or reaction event.

- Continuing in-range defects (CID): Defects that continue to interact with PD.
- New in-range defects (NID): Defects that begin to interact with PD after its diffusion or reaction event.
- Out-of-range defects (ORD): Defects that no longer interact with PD after its diffusion or a reaction event.

Note that a recalculation of PD's energy and an adjustment of neighbors' energies are required if any or all the values of A, and r change after a KMC event.

Experimental Procedure

Updating Energies of Neighboring Defects

The total interaction energy of a CID before the KMC step is E_o^{nb}, and assuming that the PD is the *jth* neighbor of CID, then the new total interaction energy of the CID, taking both the interaction strength, exponent and the distance between the PD and CID change, after each KMC step is given as

$$E_n^{nb} = E_o^{nb} + \left(\frac{A_{j(n)}}{r_{i(n)}^{\alpha_{i(n)}}} - \frac{A_{j(o)}}{r_{i(o)}^{\alpha_{i(o)}}}\right) \qquad (3)$$

where notation (o) and (n) correspond to values before and after the KMC step, and the superscript nb stands for *neighbor*. Note that when the PD is removed from a simulation after the KMC step, then the term $\frac{\mathrm{A}_{\mathrm{j(n)}}}{\mathrm{r}_{\mathrm{i(n)}}^{\alpha_{\mathrm{i(n)}}}} = 0$. Moreover, the removal of PD from the simulation corresponds to the case where PD becomes out of range or no longer interacts with the neighboring defect. Then the interaction energy of the neighboring defect (ORD) is given as

$$E_n^{nb} = E_o^{nb} - \frac{A_{j(o)}}{r_{i(o)}^{\alpha_{i(o)}}} \qquad (4)$$

On the other hand, if a PD was added to the simulation during the KMC step, then the term $\frac{\mathrm{A}_{\mathrm{j(o)}}}{\mathrm{r}_{\mathrm{i(o)}}^{\alpha_{\mathrm{i(o)}}}} = 0$ and corresponds to the case where the PD becomes in-range or starts interacting with the neighboring defect. The interaction energy of the neighboring defect (NID) is given as

$$E_n^{nb} = E_o^{nb} + \frac{A_{j(n)}}{r_{i(n)}^{\alpha_{i(n)}}} \qquad (5)$$

The energies of the PD and its neighbors are updated in steps, as shown in Figure 1 after each KMC step. Note that the KMC step can be either a reaction event or a diffusion hop of a mobile defect. Note that the number of times the required energy correction for affected neighboring defects is calculated is equal to the number of defects involved in the reaction event that occurred during the last/or most recent KMC step.

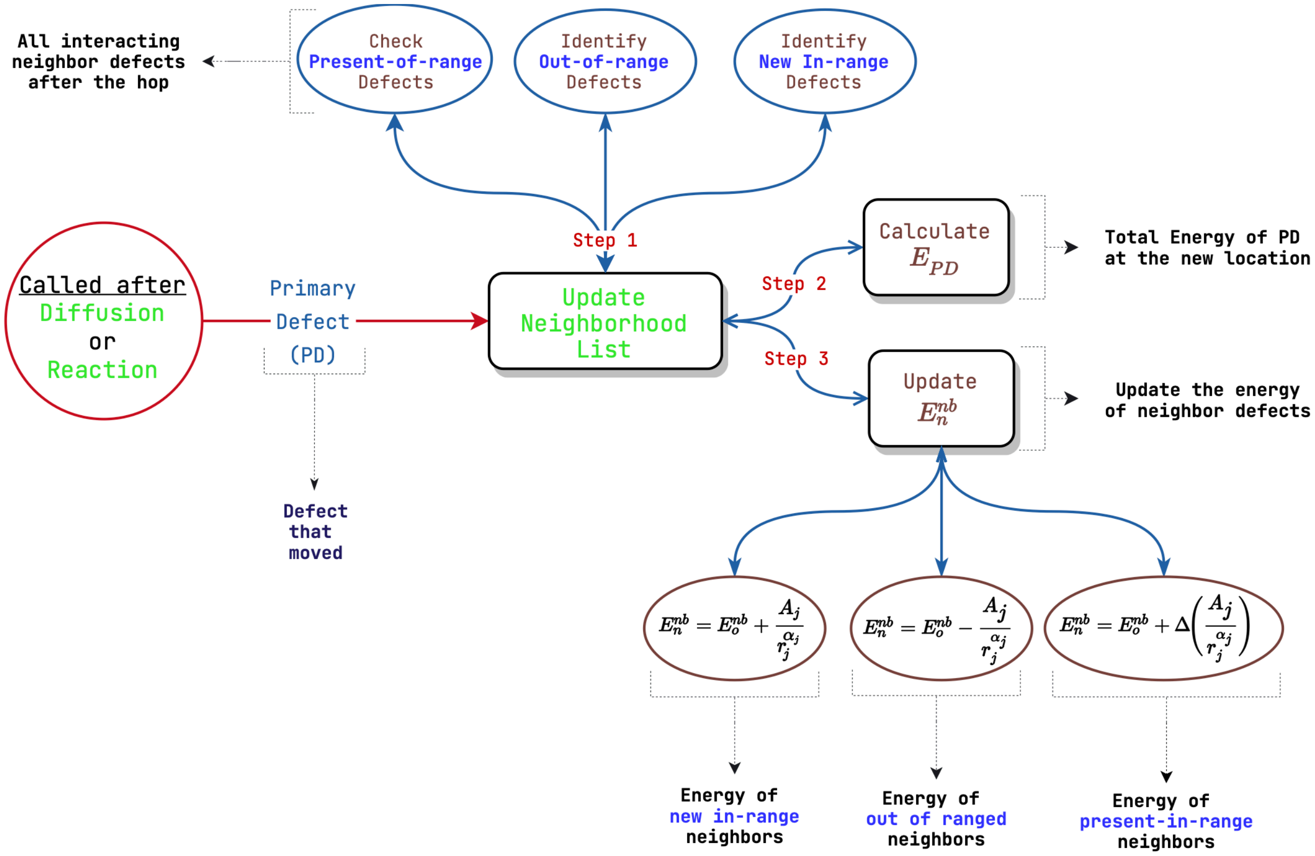

Figure 1. Flow diagram showing how the interactions would be updated after a KMC step.

Update of Migration Barriers

With kinetic Monte Carlo simulations, all the processes and its rate must be known a priori. Accordingly, if the PD is mobile, its activation energy barriers to jump in various directions must be modified according to how its total interaction changes along the jump directions. Suppose that the energy of the mobile PD at its current (present) location and the final location of the hop in the direction i are E_{PD}^{p} *and* E_{PD}^{i}, respectively. Then the activation energy barrier $E_a^i\{PD\}$ along the direction *i* is given as

$$E_a^i\{PD\} = E_a\{PD\} + \Delta E_{PD}^{i-p} = E_a\{PD\} + \left(E_{PD}^i - E_{PD}^p\right) \qquad (6)$$

where $E_a\{PD\}$ is the activation energy barrier along direction *i* without the long-range interaction. Note that in equation (6), for simplicity, ΔE_{PD} is taken to be energy difference between the initial and final location. Rigorously, ΔE_{PD} is the energy difference between the initial and saddle point locations. If the neighbors of the PD are also mobile, their activation energy barrier $E_a^i\{NB\}$ is modified accordingly as

$$E_a^i\{NB\} = E_a\{PD\} + \Delta E_{NB}^{i-p} = E_a\{NB\} + \left(\Delta E_{NB}^i - \Delta E_{NB}^p\right) \qquad (7)$$

where $E_a\{NB\}$ is the activation energy barrier for the neighboring mobile defect along direction *i*, without the long-range interaction. ΔE_{NB}^i and ΔE_{NB}^p are the pairwise interaction energies changes when placed at the location after the hop and its present location. If a defect can hop in *n* different directions, then *n+1* energy calculations are required for the PD and *n+1* corrections for neighboring mobile defects.

Acknowledgements

The work described in this article was performed at Pacific Northwest National Laboratory, which is operated by Battelle for the United States Department of Energy (US DOE) under the contract DE-AC05-76RL01830. The US DOE, the Office of Fusion Energy Sciences (FES), and the Office of Advanced Scientific Computing Research (ASCR) have supported this study through the SciDAC-4 program on Plasma-Surface Interactions [5].

References

[1.] G. Nandipati, W. Setyawan, H. L. Heinisch, K. J. Roche, R. J. Kurtz, B. D. Wirth, *J. Nucl. Mater.* **462** (2015) 338.
[2.] G. Nandipati, W. Setyawan, H. L. Heinisch, K. J. Roche, R. J. Kurtz, B. D. Wirth, *Semiannual Progress Report* DOE/ER-0313/54 (2013) 179.
[3.] G. Nandipati, Kinetic Simulations of Microstructural Evolution, [Scientific Software, Ver.: 1.0] (Aug 26, 2020).
[4.] A. Weerasinghe, L. Hu, K. D. Hammond, B. D. Wirth, D. Maroudas, *J. Appl. Phys.* **12**, (2020) 165109.
[5.] Plasma Surface Interactions: Predicting the Performance and Impact of Dynamic PFC Surfaces (https://tinyurl.com/ru8mwqt).

9.3 PREDICTIVE MODELS FOR MECHANICAL PROPERTIES OF OXIDE DISPERSION STRENGTHENED ALLOYS: CONSTITUTIVE MODELING AND DAMAGE PREDICTION

B. N. Nguyen, W. Setyawan (Pacific Northwest National Laboratory)

OBJECTIVE

This research aims at developing mechanical property models to predict the constitutive behavior of oxide dispersion strengthened (ODS) alloys and composites as a function of their constituent mechanical properties, interfaces, particle volume fraction and temperature. The objective also includes the combination of the developed constitutive model with an elastic plastic damage model to investigate the particle strengthening effects on the mechanical performance of the tungsten (W) brick-and-mortar (BAM) composite structures that contain an ODS alloy as the matrix material.

SUMMARY

A computational homogenization model using an incremental Eshelby-Mori-Tanaka Approach (EMTA) combined with an inverse method was developed to predict the constitutive behavior of ODS alloys as a function of their constituent mechanical properties, volume fractions and the interfaces between the oxide particles and baseline matrix. The model was applied to predict the elastic plastic response of 9%Cr steels strengthened by yttria (Y_2O_3) nanoparticles at selected concentrations at 400°C and 600°C. Next, the predicted elastic plastic response of the ODS steel was introduced in ABAQUS and was used with an elastic plastic damage model from this code to predict the alloy response up to total fracture. Finally, ODS steels with selected concentration of Y_2O_3 were employed as the matrix in W-BAM microstructures to investigate the ductile phase toughening effects of these materials on the mechanical performance of the W-BAM composites through finite element analyses (FEA) using the developed model.

PROGRESS AND STATUS

Introduction

Strengthening an alloy or a matrix material in a composite with the oxide particles that form coherent or semi-coherent interfaces with the baseline material can produce a composite with significantly higher strength and toughness than the unstrengthened material. Our research focuses on oxide particles as strengthening materials for the ductile matrix in alloys and composites relevant to fusion energy applications. At this stage, Y_2O_3 particles have been considered for our model development and validation due to their potentials for fusion energy materials and the available literature data for ODS steels containing these particles [1-6]. Figure 1 gives a schematic picture of a representative volume element (RVE) or unit cell of an ODS alloy that contains a nanoscale oxide particle embedded in a ductile alloy matrix. During forming, the particles may have aligned with the matrix lattice tending to full coherency. However, due to the difference in the lattice constant and in addition to the fast cooling of the alloy, only semi-coherency may practically remain at the interfaces between the matrix and the oxide particles. This semi-coherency indicates that the shearing of oxide particles by dislocations will be difficult leading to increased hardening observed for the ODS alloys [2]. The particle/matrix interface is responsible for the remarkable increase in strength observed in ODS alloys compared to the baseline unstrengthened materials.

In this work, the interface between the oxide particle and matrix is modeled as a distinct material (Figure 1). The constitutive behavior of this interface is identified by a homogenization procedure for a three-phase composite (i.e., matrix, particle, and interface) based on the incremental EMTA [7-9] associated with an inverse method. The incremental EMTA was subsequently used to compute the elastic plastic behavior of the ODS alloy as a function of the oxide particle volume fraction up to failure initiation corresponding to the alloy ultimate tensile strength (UTS). The data for the 9wt% Cr steel strengthened by 0.25wt% Y_2O_3 at 400°C and 600°C from Reference [4] were used for the model development. This alloy and its associated

ODS steels are like the Eurofer97 and ODS Eurofer alloys investigated by various authors [1,3,5-6,10-11]. Therefore, mechanical property data (e.g., elastic modulus, yield strength (YS), and UTS) for Eurofer97 and an ODS Eurofer from these references were used for the model validation. Next, the yield stress versus plastic strain results predicted for the 9%Cr Y_2O_3-strengthened steel at 400°C and 600°C as a function of the Y_2O_3 concentration were used with an elastic plastic damage model in ABAQUS to simulate the ODS alloy stress strain response up to total fracture. Finally, the combined constitutive model has been used in FEA to describe the elastic plastic behavior of an ODS Eurofer alloy considered as the matrix of the W/ODS-Eurofer BAM composites subjected to tensile loading. The BAM composites are of interest for potential plasma facing material applications since they possess hierarchical microstructures exhibiting high mechanical performance needed for such applications [12]. Our parametric FEA using the developed models provide insights on the role of constituent materials as well as the damage and deformation mechanisms that govern the mechanical performance and integrity of these composites.

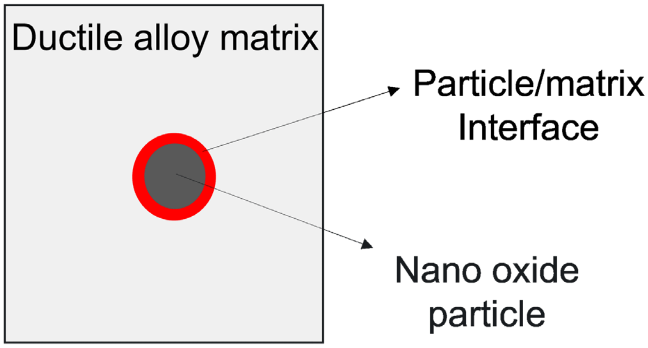

Figure 1. Schematic of a RVE for an alloy strengthened by oxide particles.

Experimental Procedure

Constitutive Modeling

A computational method using an incremental EMTA combined with an inverse method was developed to predict the elastic plastic behavior of an ODS alloy up to failure initiation as a function of the particle volume fraction. The incremental EMTA that is derived from the Nguyen et al.'s model [9] for a two-phase elastic plastic composite has been extended to model a three-phase composite representative of the ODS alloy in which the matrix and particle/matrix interface behave elastic plastically while the oxide particle remains elastic. The elastic plastic stress strain response of the ODS composite is computed incrementally:

$$\Delta\sigma_{ij} = C_{ijkl}(\varepsilon_{ij}, T)\Delta\varepsilon_{kl} \qquad (1)$$

where $\Delta\sigma_{ij}$ and $\Delta\varepsilon_{ij}$ denote the composite stress and strain increments and $C_{ijkl}(\varepsilon_{ij}, T)$ is the composite tangent stiffness tensor that depends on the current deformation state and temperature, T. If the constituent temperature dependent mechanical properties (e.g., tangent moduli) are known for a given deformation state, $C_{ijkl}(\varepsilon_{ij}, T)$ can be computed by an EMTA model and $\Delta\sigma_{ij}$ can be determined in terms of $\Delta\varepsilon_{ij}$ using Equation (1). If the stress increment is given, the strain increment is computed as

$$\Delta\varepsilon_{ij} = C^{-1}_{ijkl}(\varepsilon_{ij}, T)\Delta\sigma_{kl} \qquad (2)$$

where C^{-1}_{ijkl} is the composite compliance tensor (the inverse of $C_{ijkl}(\varepsilon_{ij}, T)$). The current tangent modulus of the interface of the ODS alloy is not known and thus must be determined to compute $C_{ijkl}(\varepsilon_{ij}, T)$. In this work, the experimental tensile stress strain response for an alloy strengthened by the same particles at a given volume fraction was used to identify the behavior of the interface by means of an inverse method. An initial guess for the interface plastic modulus is needed to start this inverse method that considers the interface volume fraction in the [0, f_p] range (with f_p being the particle volume fraction). The 0-value of the interface volume fraction represents the EMTA solution for a two-phase composite that cannot capture the interface effect on the composite hardening behavior. Therefore, the interface volume fraction must be greater than 0 and is taken to be equal to f_p in this work. Lower or higher interface volume fractions than f_p represent the particle size effect that is not currently investigated. The interface tangent modulus calculated from the plastic modulus initial guess is then used to compute the current stiffness tensor $C_{ijkl}(\varepsilon_{ij}, T)$ from which the composite tangent modulus at the current iteration is computed. If the computed tangent modulus agrees with the actual value determined from the stress strain data within a given margin error (e.g., 5%), the inverse procedure converges, and the interface tangent modulus is determined for the current increment. If the convergence criterion is not met, the initial guess for the interface tangent modulus is adjusted, and the inverse procedure continues until the criterion is satisfied. At convergence, the composite stress and strain tensors are updated to continue the computation for the next stress increment. The whole computation procedure stops when the matrix equivalent stress attains the matrix uniform elongation introduced as an input data.

The interface stress strain behavior numerically identified by the above method can be subsequently used in the direct EMTA computation to predict stress strain responses for the same type of ODS alloys as a function of the particle volume fraction. This has been conducted using the data for 9wt% Cr steel strengthened by 0.25wt% of Y_2O_3 at 400°C and 600°C [4] to determine the particle/matrix interface behavior in the Y_2O_3 strengthened steels. The average Y_2O_3 particle radius from Reference [4] is 6.8 ± 1.4 nm. The baseline 9wt% Cr steel from Reference [4] has a similar composition to Eurofer97 investigated by various authors [1,3,5-6,10]. Figure 1(a-b) report the predicted true stress strain responses of these alloys at 400°C and 600°C as a function of Y_2O_3 concentration. The model predicts increase in strength for the alloy with the increase in particle concentration from 0 to 5wt%, and such strength improvement is more significant at 400°C than at 600°C. However, strength improvement with increase in particle concentration has led to reduction in ductility as observed in Figure 2. Physically, higher well dispersed particle concentration creates more obstacles for the dislocation movements leading to increase in hardening and strength but reduction in ductility for the ODS alloy. Our predictions are consistent with the experimental observations in References [13-14] for other ODS alloy systems. Figure 3(a-b) compares the predicted YS and UTS of 9wt% Cr - 0.3wt% Y_2O_3 steel at 400°C and 600°C to the experimental results from References [1,3,5-6] for similar ODS-Eurofer alloys strengthened by dispersed Y_2O_3 particles at the same concentration as a function of temperature. Good agreements in trends and values between the predictions and data were found.

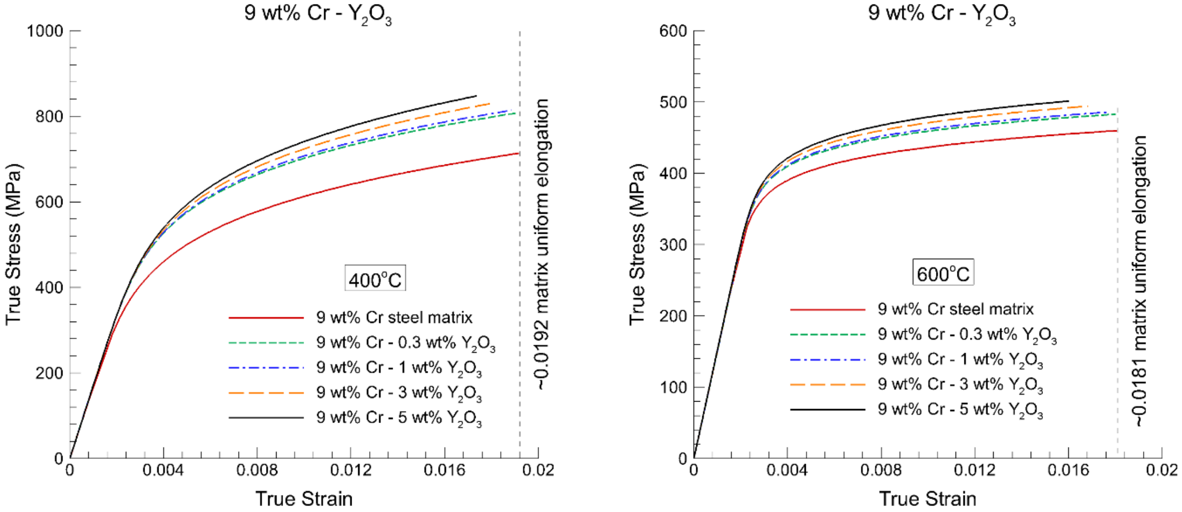

(a) (b)

Figure 2. Predicted stress strain responses of 9wt% Cr - Y_2O_3 steel as a function of Y_2O_3 concentration at (a) 400°C and (b) 600°C.

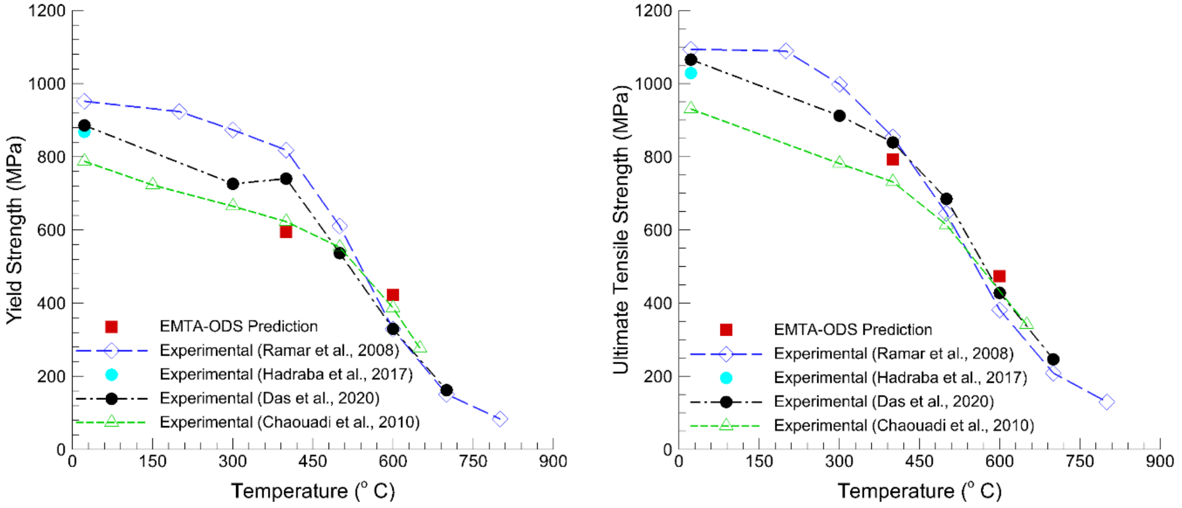

(a) (b)

Figure 3. Predicted (a) YS and (b) UTS for a 9wt% Cr – 0.3wt% Y_2O_3 steel compared to the experimental results from References [1,3,5-6].

The YS versus plastic strain determined by this incremental EMTA method for the ODS alloy with a given concentration of particle was introduced in ABAQUS to be used with an elastic plastic damage model with isotropic hardening from this code to compute the composite response up to total fracture. Total elongation data for Eurofer97 from References [1,10] have guided the fracture energy estimate used in the ABAQUS model. Figure 4(a-b) reports the FEA results for the uniaxial tension of the 9wt% Cr-Y_2O_3 steel at 400°C and 600°C as a function of Y_2O_3's concentration. On these figures, the ODS steel stress strain responses up to UTS where failure initiation occurred reproduce the incremental EMTA predictions while the failure behaviors up to total fracture were predicted by the elastic plastic damage model.

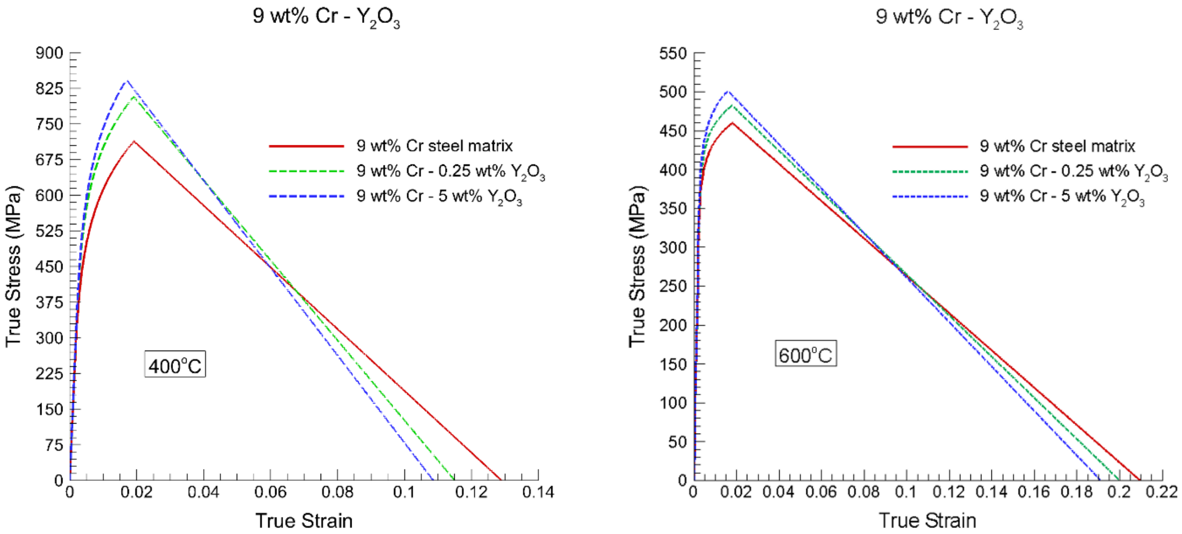

(a) (b)

Figure 4. Predicted stress strain responses of 9wt% Cr - Y_2O_3 steel as a function of Y_2O_3 concentration at (a) 400°C and (b) 600°C.

Analysis of W-BAM Composites

A typical BAM composite made of W bricks embedded in a 9wt% Cr - Y_2O_3 steel (W-Eurofer97 or W-ODS Eurofer) was designed to investigate the effects of Y_2O_3 particle strengthening of the 9wt% Cr steel matrix on the BAM composite stress strain behavior. Figure 5a shows the (10 mm x 10 mm) BAM meshed domain contains W bricks with the length-to-height ratio of 8. The domain thickness is 1 mm. Symmetric boundary conditions (BCs) were applied to this domain to simulate the tensile loading of a specimen designed with this BAM composite. The constitutive behavior of 9wt% Cr - Y_2O_3 steels at 600°C given in Figure 4b was used to describe the mortar matrix while a high mechanical performance W (~642-MPa YS and ~679-MPa UTS) at 600°C studied in Reference [15] was considered for this W-BAM composite. The elastic plastic behavior of W obeys the same constitutive law accounting for damage as the ODS steel matrix with W's constitutive parameters identified using the data from Reference [15]. Figure 5(b-d) gives the damage and fracture patterns in the BAM composites designed with the steel matrix without Y_2O_3 strengthening (Figure 5b), or with 0.25wt% (Figure 5c) or 5wt% (Figure 5d) Y_2O_3 particles. Figure 5b shows that the BAM without Y_2O_3 has already failed at 0.008 applied strain since several transverse cracks formed by the linkup of vertical microcracks breaking the W bricks occurred whereas the BAMs with Y_2O_3 strengthening (Figure 5c and 5d) could still sustain the loading. Figure 5c and 5d show that most of W bricks were not broken in these BAMs at 0.008 applied strain. These findings are confirmed on Figure 6a that gives the engineering stress versus applied strain for all the cases. Figure 6a shows stress reduction before and after 0.008 applied strain for the BAM without Y_2O_3 strengthening. The BAMs with Y_2O_3 strengthening failed at higher applied strains (≥ 0.01) when the microcracks initiated in the ODS steel matrix could break the W bricks to linkup (Figure 6c and 6d compared to Figure 6b). Finally, to quantify the increases in strength and ductility, Figure 7 reports the true stress versus true strain for all the cases. The BAM without Y_2O_3 strengthened matrix exhibits 604-MPa true strength at 0.007 true strain while those with 0.25wt% and 5wt% Y_2O_3 show 620-MPa and 627-MPa true strengths at 0.0086 and 0.0092 true strains, respectively.

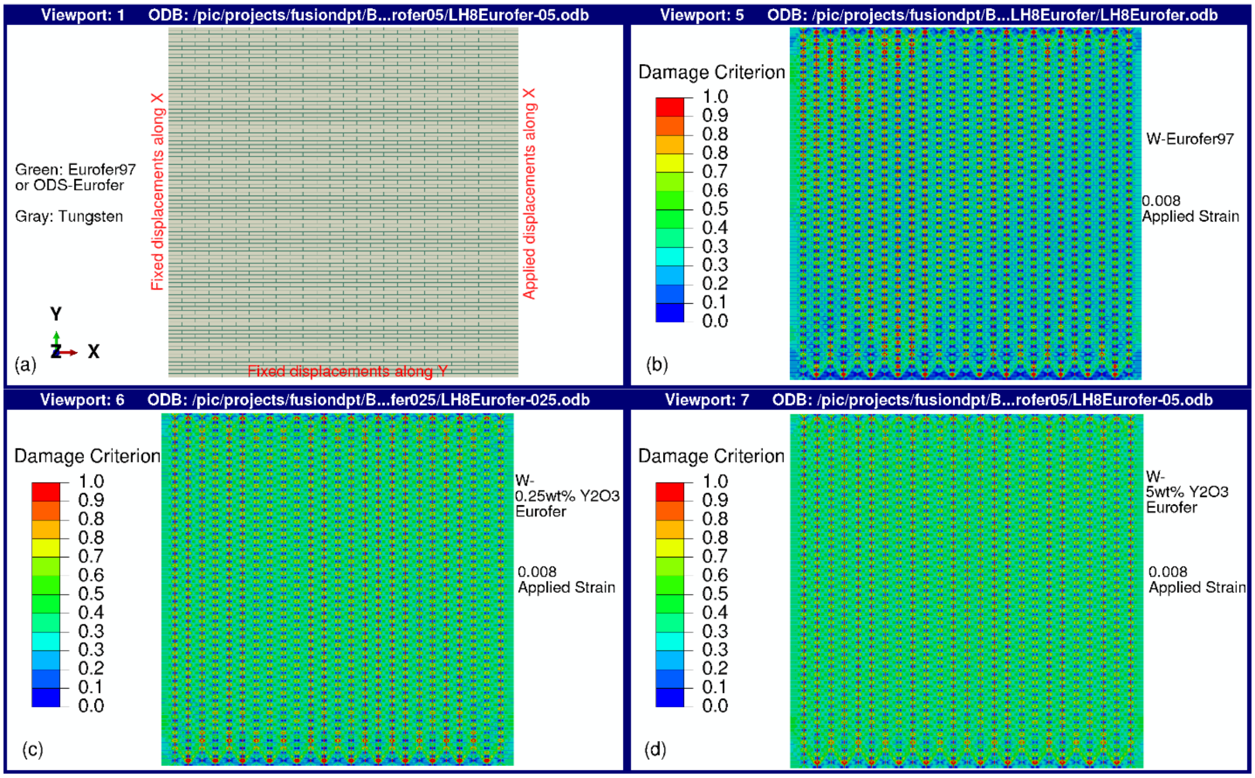

Figure 5. (a) FEA plane stress model for a W-BAM domain with prescribed BCs; Damage and fracture patterns at 0.008 applied strain predicted for (b) W-BAM without Y_2O_3 strengthening (W-Eurofer97), (c) W-0.25wt% Y_2O_3 Eurofer, and (d) W- 5wt% Y_2O_3 Eurofer.

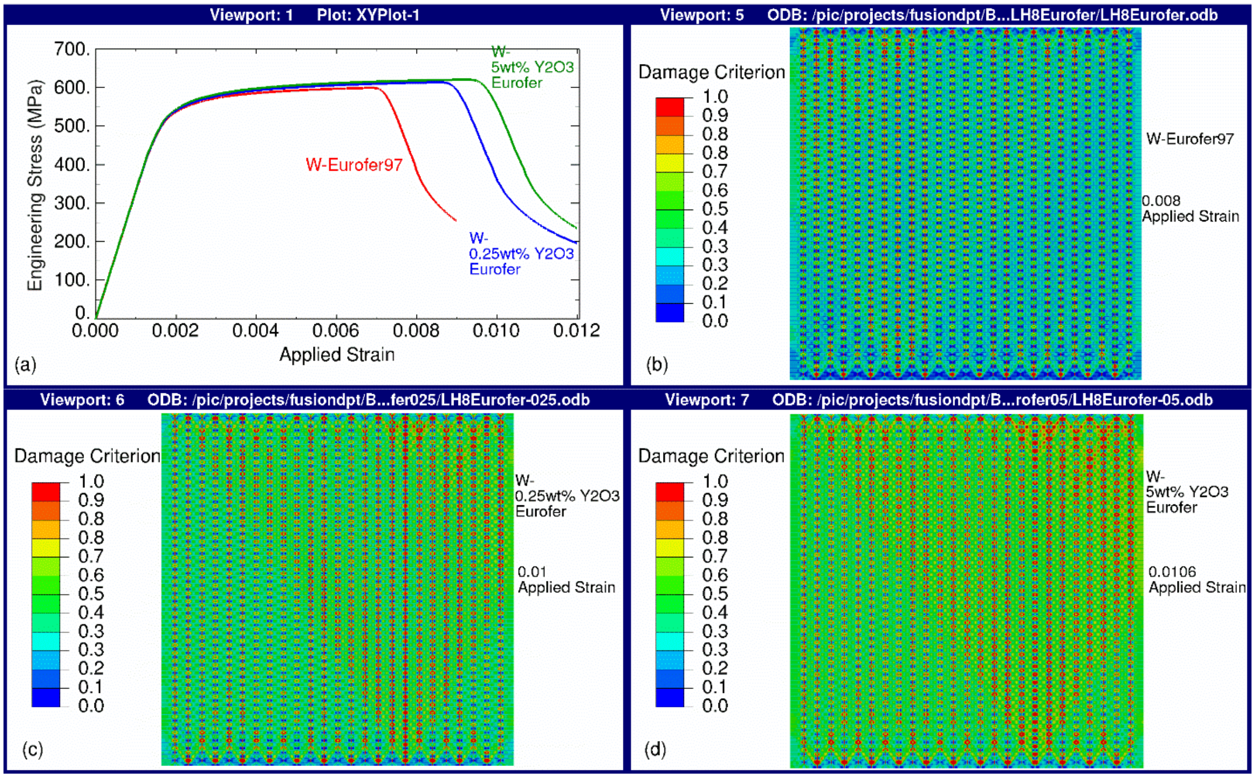

Figure 6. (a) Engineering stress versus applied strain predicted W-Eurofer97, W-0.25wt% Y_2O_3 Eurofer, and W- 5wt% Y_2O_3 Eurofer BAMs; Damage and fracture patterns predicted for (b) W-Eurofer97 BAM at 0.008 applied strain; (c) W- 0.25wt% Y_2O_3 Eurofer BAM at 0.01 applied strain; (d) W- 5wt% Y_2O_3 Eurofer BAM at 0.0106 applied strain.

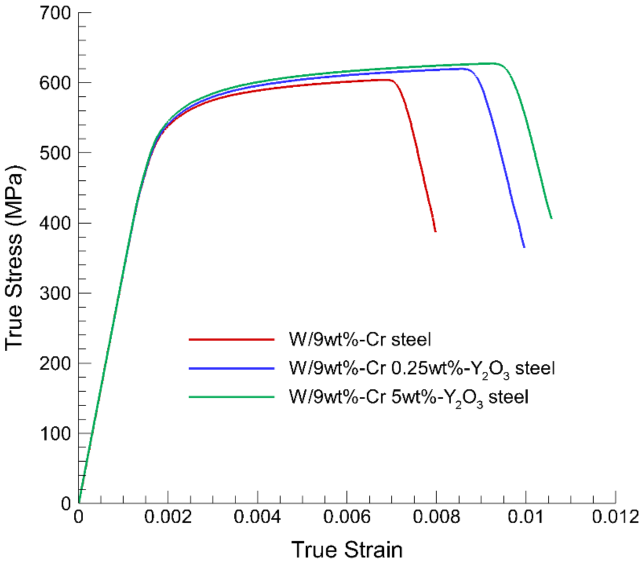

Figure 7. True stress versus true strain predicted for the three analyzed W-BAM composites.

Results

Significant progress has been made during this reporting period. We have developed and implemented an incremental EMTA to predict the stress strain response of an ODS alloy up to its failure initiation as a function of particle volume fraction and temperature. The YS's versus plastic strains obtained from the EMTA model were then used in conjunction with the elastic plastic ductile damage model with isotropic hardening from ABAQUS to predict the stress strain response of the ODS alloy up to total fracture. The combined model has been successfully applied to 9wt% Cr steels strengthened by Y_2O_3 particles at various concentrations. Finally, the constitutive model was used in FEA to describe the elastic plastic behavior of the ODS Eurofer steel used as the matrix of the W/ODS-Eurofer BAM composites subjected to tensile loading at 600°C. Our preliminary parametric analyses using the developed models have provided insights on the role of constituent materials as well as the deformation and cracking mechanisms that govern the mechanical performance and integrity of these composites in terms of strength and ductility. The next steps include sensitivity analyses of W-BAM composites to investigate other grades of W and the effects of W brick geometrical features.

Acknowledgements

This research was supported by the Office of Fusion Energy Sciences, United States Department of Energy and performed at Pacific Northwest National Laboratory under Contract DE-AC05-76RL01830.

References

[1] A Ramar, P Spätig, R Schäublin. *Journal of Nuclear Materials* 382 (2008) 210–216.
[2] A Ramar, N Baluc, R Schäublin. *Journal of Nuclear Materials* 386-388 (2009) 515–519.
[3] H Hadraba, R Husak, L Stratil, F Siska, Z Chlup,V Puchy, J Michalicka. *Fusion Engineering and Design* 124 (2017) 1028–1032.
[4] F Siska, L Stratil et al. *Materials Science & Engineering A* 732 (2018) 112-119.
[5] A Das, P Chekhonin, E Altstadt, D McClintock, F Bergner, C Heintze, R Lindau. *Journal of Nuclear Materials* 542 (2020) 152464.
[6] R Chaouadi, G Coen, E Lucon, V Massaut. *Journal of Nuclear Materials* 403 (2010) 15–18.
[7] JD Eshelby. *Proceedings of the Royal Society of London A: Mathematical, Physical and Engineering Sciences* 252 (1959) 561-569.
[8] T Mori T, K Tanaka. *Acta Metallurgica* 21 (173) 571–574.
[9] BN Nguyen, SK Bapanapalli, V Kunc, JH Phelps, and CL Tucker, III. *Journal of Composite Materials* 43 (2009) 217-246.
[10] E Lucon, W Vandermeulen. Overview and Critical Assessment of the Tensile Properties of Unirradiated and Irradiated EUROFER97. Report Nr. SCK•CEN-BLG-1042 REV.(1), SCK-CEN, Mol, Belgium.
[11] JH Kim, TS Byun, DT Hoelzer. *Journal of Nuclear Materials* 425 (2012) 147–155.
[12] BN Nguyen, CH Henager Jr., J Wang, W Setyawan. *Journal of Nuclear Materials* 540 (2020) 152382.
[13] Y Wu, H Zhao, J Li, Y Zhang, T Liu. *Materials Science & Engineering* A 804 (2021) 140734.
[14] H Jia, R Zhang, D Long, Y Sun, Z Zhou. Materials Science & Engineering A 839 (2022) 142824.
[15] C Yin, D Terentyev et al. *International Journal of Refractory Metals & Hard Materials* 75 (2018) 153-162.

9.4 PREDICTIVE MODELING OF HE BUBBLE ACCUMULATION IN NANOSTRUCTURED FERRITIC ALLOYS—K. C. Pitike, W. Setyawan (Pacific Northwest National Laboratory)

OBJECTIVE

The overall objective of this work is to develop a predictive model of helium (He) bubble accumulation and distribution in irradiated nanostructured ferritic alloys under relevant fusion environments. As a first step, we have developed an accurate Fe-He neural network potential to study defect binding in small He clusters and bubbles in pure BCC-Fe.

SUMMARY

This report is an extended abstract for a manuscript to be submitted in Acta Materialia, titled: “Accurate Fe–He machine learning potential for studying He effects in ferritic steels”.

A machine learning potential (MLP) based on neural networks is developed to describe the Fe-He interactions from density functional theory (DFT) calculations. The developed MLP performs with near-DFT accuracy and several orders of magnitude faster than DFT. The MLP can accurately predict the bulk properties of Fe, formation energies of point defects, and binding energies of He with He clusters and Bubbles. In addition, we have investigated the effects of supercell size on defect binding energies and relaxation volumes. Furthermore, we have employed the MLP to evaluate the trap mutation effects of He clusters and bubbles as a function of temperature.

PROGRESS AND STATUS

Introduction

Nanostructured ferritic alloys (NFAs) containing dispersed nanosized oxide particles are being actively investigated for their potential application as structural materials in advanced fusion reactors. Due to the lack of fusion irradiation facilities with a sufficiently high flux, many neutron irradiation studies of NFAs have been done in fission reactors. Hence, a predictive mesoscale model is critical to understand radiation damage of NFAs in fusion environments, including the effect of He bubble accumulation. The mesoscale model should accurately represent the atomistic data of defect clusters of various types, sizes, and configurations at nanoscale, where the DFT calculations are prohibitively expensive. Interatomic potentials are routinely used to generate such atomistic data to develop the mesoscale model. To provide input to the mesoscale model, accurate interatomic potentials are needed to calculate atomistic data of defect clusters of various types, sizes, and configurations. The accuracy of the mesoscale simulations depends on the choice of interatomic potential. Furthermore, a coherent interatomic potential is not yet available to study the full interactions of He/H and Y-Ti-O in Fe.

Recently, MLPs have shown promising results due to their high adaptability to a wide range of complex chemical environments, and performance with a near-DFT accuracy for a fraction of computational cost. Hence, MLPs are an appropriate choice to study the He bubble accumulation in chemically complex NFAs. As a preliminary step, we develop a Fe-He potential, based on ~10,000 atomic configurations sampled using DFT. The developed MLP not only predicts the bulk properties of Fe, such as lattice constant (a_0), elastic constants (c_{11}, c_{12}, c_{44}), and phonon frequencies (ω), but also the formation energies (E_f) of point defects such as vacancy (V), interstitial ($\mathrm{He_{tet}}$, $\mathrm{He_{oct}}$) and substitutional Helium ($\mathrm{He_{sub}}$). Comparison of above-mentioned property values estimated using MLP in reference to DFT are given in Table 1. Evidently, the accuracy of the MLP is excellent.

Table 1. Comparison of bulk and defect properties estimated from DFT and MLP

Property	Units	DFT	MLP	MLP-DFT	$\frac{\text{MLP}-\text{DFT}}{\text{DFT}}$ [%]
a_0	Å	2.832	2.832	0.000	-0.008
c_{11}	GPa	253.564	270.909	17.345	6.841
c_{12}	GPa	156.951	140.971	-15.979	-10.181
c_{44}	GPa	106.886	93.022	-13.865	-12.971
ω_Γ	cm^{-1}	0.000	0.000	0.000	0.000
ω_P	cm^{-1}	305.019	295.284	-9.734	-3.191
ω_H	cm^{-1}	245.850	246.276	0.426	0.173
ω_N1	cm^{-1}	183.257	179.427	-3.830	-2.090
ω_N2	cm^{-1}	215.767	206.422	-9.346	-4.331
ω_N3	cm^{-1}	317.833	314.601	-3.232	-1.017
$E_f[V]$	eV	2.150	2.226	0.075	3.508
$E_f[\mathrm{He_{tet}}]$	eV	4.552	4.580	0.028	0.607
$E_f[\mathrm{He_{oct}}]$	eV	4.680	4.715	0.035	0.742
$E_f[\mathrm{He_{sub}}]$	eV	2.222	2.142	-0.080	-3.597

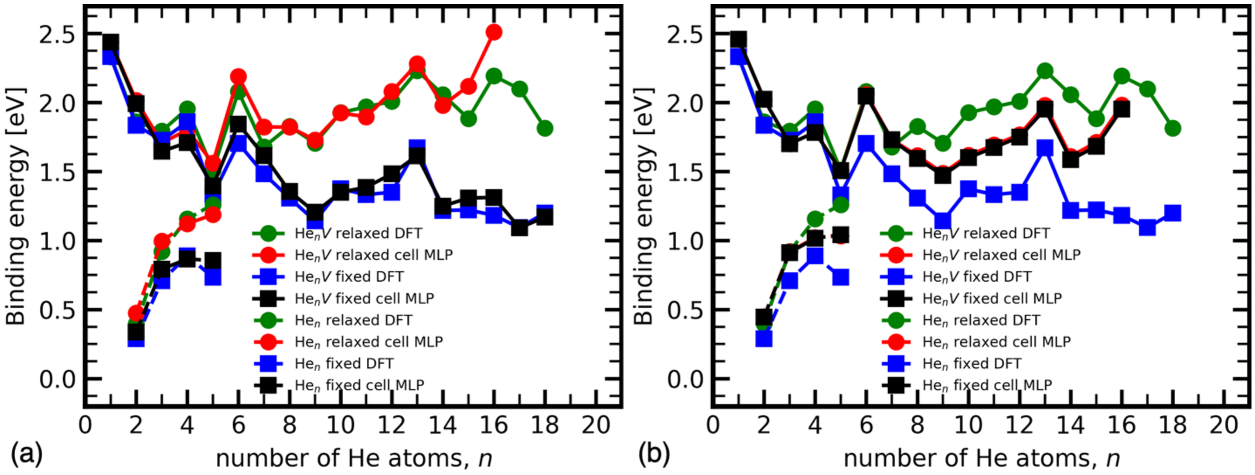

Figure 1. Comparison of binding energies of He with He_nV bubbles and He_n clusters as the final products, estimated using DFT and MLP. The binding energies are estimated using (a) 4×4×4 and (b) 12×12×12 supercells.

Figure 1(a) presents the comparison of binding energies of He with He_nV bubbles (solid lines) and He_n clusters (dashed lines) using DFT (green and blue lines) and MLP (red and black lines). Both DFT and MLP binding energies in Figure 1(a) were estimated using 4×4×4 supercells. Data calculated using fixed cell method (green and red lines) and relaxed cell method (blue and black lines) are both presented to show the effect of cell relaxation. First, we find that the binding energies predicted by MLP agrees well with DFT.

The mean absolute error (MAE) in predicting binding energies by MLP is ~80 meV. Whereas the value of MAE of classical potentials in predicting binding energies is ~280 meV. Second, we find that the relaxed cell binding energies (RCBEs) are greater than fixed cell binding energies (FCBEs) for all values of n, both for clusters and bubbles. The fixed cell calculations suffer from lattice stresses, even though the cell remains cubic. On the other hand, in the relaxed cell calculations, the cell shape may deviate significantly enough from the ideal body centered cubic (BCC) Fe structure. Hence, RCBEs and FCBEs estimated using small supercells (such as 4×4×4) does not accurately represent the 'true' nature of the He binding with bubbles and clusters in a real crystal.

The accurate binding energies, representative of a real crystal, can be calculated using a large supercell. The MLP developed in this project allows us to determine the minimum supercell size to get accurate binding energies. Since the MLP predicts the bulk elastic constants, as well as RCBEs and FCBEs in 4x4x4 supercells with near-DFT accuracy, we expect that the MLP to perform with the same accuracy even in larger supercells. We find that the values of RCBEs and FCBEs converge when the size of the supercell is increased from 4×4×4 to 12×12×12. Figure 1(b) presents RCBEs and FCBEs computed in a 12×12×12 supercell. Here, we have also investigated the size effects on defect relaxation volumes (difference between volume of the supercell with and without the defect) induced by bubbles and clusters. First, we find that the relaxation volumes predicted by MLP in a 4×4×4 supercell agrees well with DFT values. Second, the relaxation volumes estimated using a 12×12×12 supercells are smaller than the relaxation volumes estimated using a 4×4×4 supercell – indicating that the relaxation volumes are overestimated if small supercells are employed.

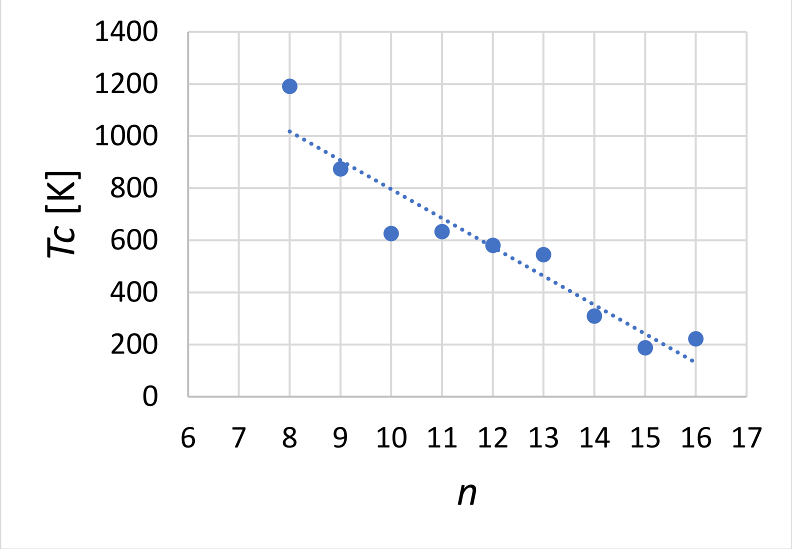

Figure 2. The temperature, T_c, at which trap-mutation reactions occur for He_nV bubbles.

Finally, we have also investigated the temperature effects on the self-trapping (ST), He_n → He_nV + SIA; and trap mutation (TM) He_nV → He_nV_2 + SIA reactions of the He_n cluster and He_nV bubbles. From the DFT calculations in this project, the ST and TM reactions of He clusters, and bubbles spontaneously occurs at temperature $T = 0$ K for $n = 6$ and $n = 17$, respectively. These observations agree with the values in literature: $n = 6$ and $n = 19$ for clusters and bubbles, respectively [1]. However, the influence of temperature on these ST and TP reactions is largely unknown. Figure 2 plots the temperature, T_c, at which the TM reactions occur for the $\mathrm{He_nV}$ bubble. We find that T_c decreases with the bubble size. While at $T = 0$ K, TM reaction can only occur for bubbles with $n > 17$, higher temperatures are required for smaller bubbles. For example, $T \approx$ 300, 700, 900, and 1200 K are required for bubbles with $13 < n \leq 16$, $9 < n \leq 13$, $n = 9$, and $n = 8$, respectively. Temperatures above 1200 K were not included in this study as BCC structured ferrite could phase transform to face centered cubic (FCC) structured austenite beyond this temperature; and the MLP is trained reveal this phase transition. Furthermore, in the case of He_n clusters, the ST reaction occurs at $T_c \approx$ 100, 350 and 1100 K for $n =$ 5, 4, and 3, respectively.

For the next steps, we are planning to employ the developed Fe-He potential to study the lifetimes of bubbles (clusters) before the trap mutation (self-trapping) reaction occurs. Furthermore, there are several logical extensions to this work: (i) Develop the Fe-H MLP to investigate the binding of Hydrogen with clusters and bubbles in BCC-Fe. (ii) Develop Fe-He-H MLP to predict the synergistic effects of He and H in BCC-Fe with near-DFT accuracy. (iii) Finally, develop the Fe-He-H-(Y-Ti-O) MLP to study the effects of oxide particle on the He+H bubble growth and segregation.

Acknowledgements

This research was supported by the United States Department of Energy (US DOE), Office of Science, Office of Fusion Energy Sciences, through Contract No. AT2030110-13784 and was performed at the Pacific Northwest National Laboratory (PNNL), which is operated by Battelle for the US DOE under Contract No. DE-AC05-76RL0-1830. The research was performed using resources available through Research Computing at PNNL.

References

[1] P. Zhang, C. Zhang, R. Li, J. Zhao, “He-induced vacancy formation in bcc Fe solid from first-principles simulation”, J. Nucl. Mater. 444 (2014) 813 147–152.

9.5 COMPUTATIONAL STUDY OF THE EFFECT OF HYDROGEN ON GRAIN BOUNDARY PROPERTIES IN TUNGSTEN—T. Frolov, R. E. Rudd (Lawrence Livermore National Laboratory)

OBJECTIVE

The objective of this study is to assess whether hydrogen isotopes in tungsten can segregate to grain boundaries at some level and affect the grain boundary (GB) structure and properties. Even without hydrogen, grain boundaries can exhibit phase transformations depending on temperature and other conditions. The changes in GB structure alter the GB such as mobility and impurity diffusivity along the GB. It is unknown whether the phase affects the level of hydrogen segregation and hydrogen storage. It is also unknown whether hydrogen induces significant structural changes in the tungsten at the boundary. Using advanced genetic search algorithms to identify tungsten GB phases with hydrogen as well as using molecular dynamics to determine the kinetics of hydrogen diffusion into, out of, and along the boundary, we aim to determine this behavior and provide guidance to continuum level thermomechanical modeling of first wall material performance in a tokamak.

PROGRESS AND STATUS

Introduction

Here we describe preliminary results showing that hydrogen segregation occurs at a level that depends on the GB phase, and the hydrogen at the boundary can become ordered in a way that also depends on the GB phase, i.e., that depends on the structure of the tungsten atoms within the GB. We have previously undertaken research to determine whether GB phase transformations in tungsten exist and, if so, how they affect the metal's behavior at tokamak operating conditions [1-6]. Plasma facing materials are required to operate at elevated temperatures while exposed to impurities, such as helium (He) and deuterium (D). These conditions, as well as radiation damage defects, are likely to modify GBs in a way that is not well understood. The goal of this activity is to investigate GB structures in tungsten in the context of possible structural transformations induced by temperature and chemical composition (e.g., impurity levels) to understand the impact on structure and properties.

The research on hydrogen in tungsten builds on our prior work which addressed the role of GBs in tungsten plasticity, including GB mobility, which affects recrystallization, and the interaction of dislocations with the grain microstructure, which is an important part of the embrittlement problem. The GBs also play a key role in intergranular fracture. The GB mobility for tungsten is important input for thermo mechanical models of recrystallization. The GB research has leveraged a new capability developed with laboratory directed research and development (LDRD) funding at Lawrence Livermore National Laboratory (LLNL) to determine GB structure [6]. This capability uses evolutionary algorithms to generate a large ensemble of candidate structures, and it uses machine learning (ML) to establish relationships between different boundary structures and classify them into phases. This work represents an important advancement in the capability to model GBs. Recent high resolution transmission electron microscopy experiments have confirmed the occurrence of GB transformations at high temperature as well as finding the structures predicted by our atomistic methods [5]. Traditional GB theory would have said that tungsten GB structure is determined uniquely by the five degrees of freedom describing the misorientation of the two grains coming together at the boundary and the orientation of the boundary as it slices through the metal, but the recent modeling and experiments show that the structure may undergo discontinuous structural transformations as conditions such as temperature change.

Tungsten is a material of interest to meet the requirements for tokamak first wall materials due to its high thermal conductivity, acceptable activation levels, high melting temperature, mechanical strength at elevated temperatures, and resistance to surface sputtering. However, conventionally processed tungsten is not mechanically robust at desired operating conditions, and the path forward to improve its performance is work in progress. Recrystallization and embrittlement are important remaining challenges. Plasma facing components need to operate below their recrystallization temperature to prevent grain growth and embrittlement. Grain growth involves the motion of grain boundaries, and their motion can be affected by structural changes due to grain boundary phase transformations. The presence of hydrogen may further alter GB structure and affect the properties of the boundary. While there has been previous computational work studying hydrogen and He in tungsten grain boundaries for fusion energy [7-13], the interplay of hydrogen with GB phases is an open question both in terms of structure and properties. Molecular dynamics can provide predictions of the motion of grain boundaries, both through explicit simulations and through the identification of mechanisms used to construct analytic models.

The first question we have addressed in the study of hydrogen in tungsten is whether the hydrogen segregates to the GBs. We have considered several GBs. Here we will focus on two GBs with 20° and 109° misorientations that have been studied previously for pure tungsten [3]. Two GB phases are considered for each boundary. We introduced hydrogen into the simulation at a range of concentrations. Here will focus on W-1atm%H at a temperature of 500K. The system was then equilibrated with molecular dynamics (MD) as described in Reference [3] for 10-20 ns. The first figure shows the resulting distribution of hydrogen. There is significant segregation of hydrogen to the GB. There are two boundaries: both run horizontally through the image: at the center and top. Not only is the hydrogen concentration greater at the boundary, but it is ordered in a way that is complementary to the tungsten structure.

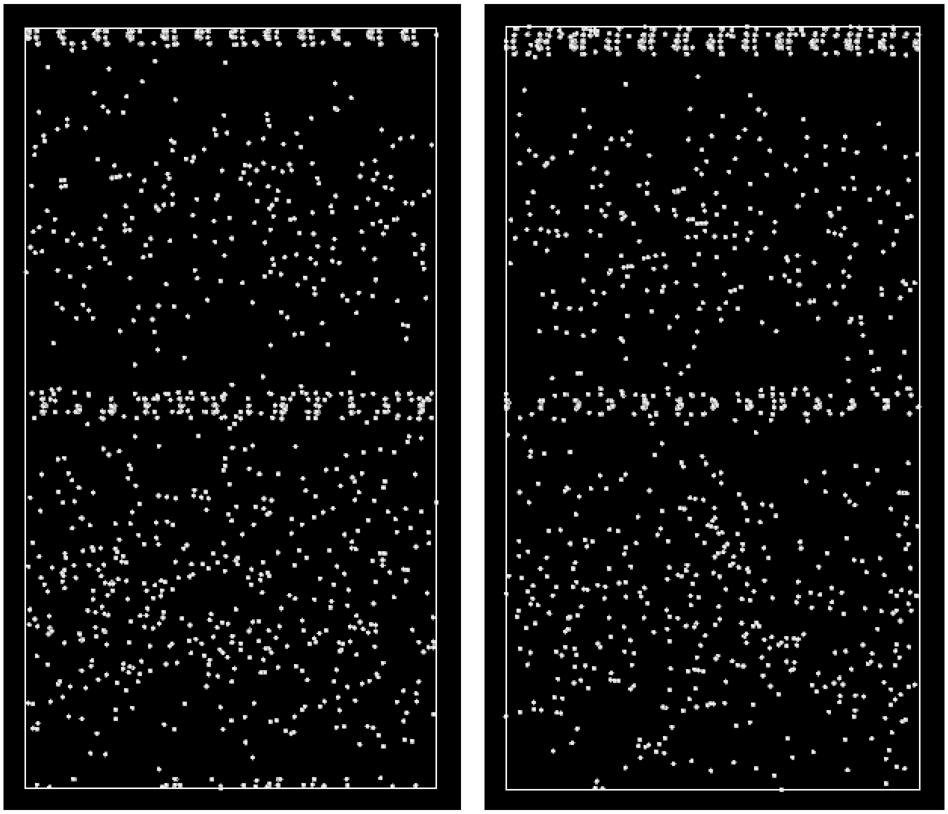

Figure 1. Distribution of hydrogen in tungsten as simulated in a system with two of the same 20° grain boundaries, both running horizontally through the image (at the center and top). The two panel show the distribution for two systems with the same grain misorientations and GB orientations but different GB phases. In both cases, the hydrogen concentration is enhanced at the GB and depleted in the region around the GB. The hydrogen in the boundary takes on a structure that is complementary to the tungsten GB atoms, resulting in the differences that are apparent in the images.

While the amount of hydrogen segregation is similar for the two GBs with 20° and 109° misorientations, we have found one case of a twist boundary in which the hydrogen does not segregate to the GB. The moderately long 10-20 ns simulations were needed in the tilt boundary cases to observe the hydrogen to diffuse from the initially uniform distribution to the segregated distribution with a relaxed GB structure.

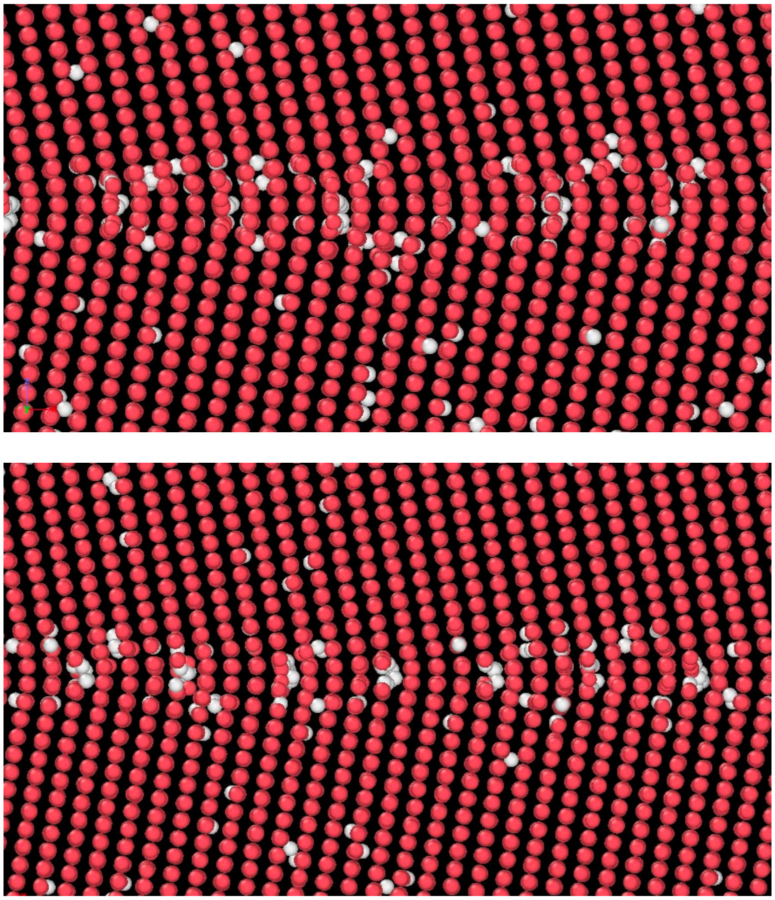

Figure 2. Edge on view of tungsten GBs with hydrogen present, as simulated with MD. These are the same boundaries and phases as shown in the first figure (the upper panel corresponds to the left-hand panel in the first figure). The atoms are colored according to the element: tungsten is red; hydrogen, gray. The pattern in the hydrogen distribution is seen to be commensurate with the atomic structure of the W GB.

Results

We will continue to develop a broader understanding of the effect of hydrogen on tungsten GB structure. This continuing investigation will consider additional grain boundaries to get a better understanding of the response of the range of grain boundaries that are present in tungsten. We will then use these GB structures to calculate the mobility of tungsten GBs under applied shear stress, with the aim of establishing whether the significant differences seen for some pure tungsten GBs are typical and persist, or are exacerbated, when hydrogen is present. The mobilities are important input for thermo mechanical models, including the recrystallization model being developed by the Marian group at the University of California, Los Angeles (UCLA). The question of whether GB transformations can lead to a marked change in recrystallization is critical and remains unanswered.

Acknowledgments

This work was performed under the auspices of the United States Department of Energy (US DOE) by LLNL under Contract DE-AC52-07NA27344. This material is based upon work supported by the US DOE, Office of Science, Office of Fusion Energy Sciences. Computing resources for this work came from the LLNL Institutional Computing Grand Challenge program.

References

[1] I. S. Winter, T. Oppelstrup, T. Frolov, and R. E. Rudd, Acta Mater. 237, 118067 (2022).
[2] I. S. Winter, T. Oppelstrup, T. Frolov, and R. E. Rudd, Phys. Rev. Lett. 128, 035701 (2022).
[3] T. Frolov, Q. Zhu, T. Oppelstrup, J. Marian, and R. E. Rudd, Acta Mater. 159, 123 (2018).
[4] T. Frolov et al., Nanoscale 10, 8253 (2018).
[5] T. Meiners, T. Frolov, R. E. Rudd, G. Dehm, and C. H. Liebscher, Nature 579, 375-378 (2020).
[6] Q. Zhu, A. Samanta, B. Li, R. E. Rudd, T. Frolov, Nature Comm. 9, 467 (2018).
[7] K. Ohsawa et al., Phys. Rev. B 82, 184117 (2010).
[8] W. Xiao and W. T. Geng, J. Nucl. Mater. 430, 132 (2012).
[9] K. D. Hammond, L. Hu, D. Maroudas and B. D. Wirth, EPL 110, 52002 (2015).
[10] N. Fernandez, Y. Ferro and D. Kato, Acta Mater. 94, 307 (2015).
[11] J. Marian et al., Nucl. Fusion 57, 092008 (2017).
[12] A. De Backer et al., Phys. Scr. T170, 014073 (2017).
[13] B. Fu, M. Qiu, J. Cui, J. Wang, and Q. Hou, J. Nucl. Mater. 543, 152599 (2021).

10. IRRADIATION & TESTING ANALYSIS, METHODS, EXPERIMENTS, AND SCHEDULES

10.1 HFIR IRRADIATION EXPERIMENTS—C. On (Oak Ridge National Laboratory)

OBJECTIVE

The goal of this report is to describe the progress of the neutron irradiation experiments that were performed in the High Flux Isotope Reactor (HFIR) and the operating status.

SUMMARY

During the six-month period starting from January 1st to June 30th, 2022, a total of thirty-four rabbit capsules continued their irradiation. There were twenty-six new capsules inserted into HFIR, while eleven capsules were removed. The cycles 496 through 498 were completed during this period, but cycle 496 was split into three (496A, 496B, and 496C), and 498 was split into two (498A and 498B) due to an electrical outage and reactor scrams.

PROGRESS AND STATUS

introduction

Neutron irradiation experiments were performed in support of the research and development of fusion reactor materials using various materials irradiation facilities in the HFIR. The reactor operating history for the period from January 1-June 30, 2022 is detailed in Table 1.

Table 1. HFIR operating record for the semi-annual FY2022

Cycle Number	Cycle End Date	Power (MWD)
496*	February 4	2210.62
497	March 20	2183.34
498**	May 7	2152.69

*Cycle was in three parts, due to reactor scram and electrical outage. Cycle 496A received 6.147 MWD, 496B received 890.653 MWD, while cycle 496C received 1313.82 MWD.

**Cycle was in two parts, due to reactor scram. Cycle 498A received 895.91 MWD, while cycle 496B received 1256.78 MWD.

All the Fusion Materials Program irradiation experiments performed during this period (FY2022) used the nominally two-inch rabbit capsules, with no full-length target rod nor instrumented reflector position capsules within that period. Thirty-four target zone rabbit capsules remain in the reactor to complete the scheduled irradiations. Table 2 lists the new capsules that were loaded into HFIR in cycles 496, 497, and 498. On the other hand, Table 3 lists the capsules that were removed from HFIR during cycles 496, 497, or 498. The capsules listed in Table 4 were inserted either during or before FY2022 and will continue in FY2022 and beyond. Tables 2 through 4 give condensed information on the material, specimen type, temperature, fluence, and period of irradiation.

Table 2. New capsules starting irradiation in cycles 496, 497, and 498

Experiment Designation	Primary Materials	Specimen Types	Irradiation Temperature (°C)	Max Exposure (dpa)	Number of Reactor Cycles	HFIR Cycles Start – End
FH11	F82H-IEA / F82H-mod3	Tensile	300	80	46	496 - 541
FH12	F82H-IEA / F82H-mod3	Tensile	400	80	46	496 - 541
FH13	F82H-IEA / F82H-mod3	Tensile	500	80	46	496 - 541
FH21	F82H-IEA / F82H-mod3	Bend Bar	300	80	55	496 - 550
FH22	F82H-IEA / F82H-mod3	Bend Bar	300	80	55	496 - 550
FH23	F82H-IEA / F82H-mod3	Bend Bar	400	80	55	496 - 550
FH24	F82H-IEA / F82H-mod3	Bend Bar	400	80	55	496 - 550
FH25	F82H-IEA / F82H-mod3	Bend Bar	500	80	48	496 - 543
FH26	F82H-IEA / F82H-mod3	Bend Bar	500	80	48	496 - 543
FR15	Joint Tungsten Alloy	Disc (D6)	800	0.6	3	496 - 498
FR21	Joint Tungsten Alloy	Fracture Toughness Bar	300	0.2	1	496 - 496
FR22	Joint Tungsten Alloy	Fracture Toughness Bar	500	0.2	1	496 - 496
FR23	Joint Tungsten Alloy	Fracture Toughness Bar	800	0.2	1	496 - 496
FR32	Joint Tungsten Alloy	Disc (D3)	500	0.2	1	496 - 496
FR12	Joint Tungsten Alloy	Disc (D6)	300	1.2	6	497 - 502
FR14	Joint Tungsten Alloy	Disc (D6)	500	0.6	3	497 - 499
FR41	Joint Tungsten Alloy	Fracture Toughness Bar	300	0.6	3	497 - 499
FR42	Joint Tungsten Alloy	Fracture Toughness Bar	500	0.6	3	497 - 499
FR43	Joint Tungsten Alloy	Fracture Toughness Bar	800	0.6	3	497 - 499
FR01	Joint Tungsten Alloy	Disc (D6)	300	0.4	2	495, 498 - 495, 498

FR02	Joint Tungsten Alloy	Disc (D6)	300	0.4	2	498 - 499
FR05	Joint Tungsten Alloy	Disc (D6)	500	0.2	1	498 - 498
FR06	Joint Tungsten Alloy	Disc (D6)	500	0.2	1	498 - 498
FR08	Joint Tungsten Alloy	Disc (D6)	800	0.2	1	498 - 498
FR34	Joint Tungsten Alloy	Disc (D3)	800	0.2	1	498 - 498
FR53	Joint Tungsten Alloy	Disc (D3)	800	0.6	3	498 - 500

Table 3. The rabbit capsules removed from HFIR during cycles 496, 497, or 498

Experiment Designation	Primary Materials	Specimen Types	Irradiation Temperature (°C)	Max Exposure (dpa)	Number of Reactor Cycles	HFIR Cycles Start – End
FR21	Joint Tungsten Alloy	Fracture Toughness Bar	300	0.2	1	496 - 496
FR22	Joint Tungsten Alloy	Fracture Toughness Bar	500	0.2	1	496 - 496
FR23	Joint Tungsten Alloy	Fracture Toughness Bar	800	0.2	1	496 - 496
FR32	Joint Tungsten Alloy	Disc (D3)	500	0.2	1	496 - 496
FR13	Joint Tungsten Alloy	Disc (D6)	500	0.6	3	495 - 497
F13B4	FeCrAlY Steel	Tensile	300	50	29	451 - 497
FR05	Joint Tungsten Alloy	Disc (D6)	500	0.2	1	498 - 498
FR06	Joint Tungsten Alloy	Disc (D6)	500	0.2	1	498 - 498
FR08	Joint Tungsten Alloy	Disc (D6)	800	0.2	1	498 - 498
FR15	Joint Tungsten Alloy	Disc (D6)	800	0.6	3	496 - 498
FR34	Joint Tungsten Alloy	Disc (D3)	800	0.2	1	498 - 498

Table 4. The HFIR fusion materials program rabbit capsules to continue irradiation in FY2022

Experiment Designation	Primary Materials	Specimen Types	Irradiation Temperature (°C)	Max Exposure (dpa)	Number of Reactor Cycles	HFIR Cycles Start – End
FH11	F82H-IEA / F82H-mod3	Tensile	300	80	46	496 - 541
FH12	F82H-IEA / F82H-mod3	Tensile	400	80	46	496 - 541
FH13	F82H-IEA / F82H-mod3	Tensile	500	80	46	496 - 541
FH21	F82H-IEA / F82H-mod3	Bend Bar	300	80	55	496 - 550
FH22	F82H-IEA / F82H-mod3	Bend Bar	300	80	55	496 - 550
FH23	F82H-IEA / F82H-mod3	Bend Bar	400	80	55	496 - 550
FH24	F82H-IEA / F82H-mod3	Bend Bar	400	80	55	496 - 550
FH25	F82H-IEA / F82H-mod3	Bend Bar	500	80	48	496 - 543
FH26	F82H-IEA / F82H-mod3	Bend Bar	500	80	48	496 - 543
FMP07	F82H	Tensile	300	20	21	487 - 507
FMP08	F82H	Tensile	300	80	45	487 - 531
FMP11	F82H	Tensile	385	20	21	488 - 508
FMP12	F82H	Tensile	385	80	45	488 - 532
FMP14	F82H	Tensile	525	20	21	484 - 504
FMP17	F82H	Tensile/MPC*	650	80	45	484 - 528
FMP22	F82H	Bend Bar	300	20	21	488 - 508
FMP23	F82H	Bend Bars	300	80	45	488 - 532
FR02	Joint Tungsten Alloy	Disc (D6)	300	0.4	2	498 - 499
FR11	Joint Tungsten Alloy	Disc (D6)	300	1.2	6	495 - 500
FR12	Joint Tungsten Alloy	Disc (D6)	300	1.2	6	497 - 502
FR14	Joint Tungsten Alloy	Disc (D6)	500	0.6	3	497 - 499
FR41	Joint Tungsten Alloy	Fracture Toughness Bar	300	0.6	3	497 - 499
FR42	Joint Tungsten Alloy	Fracture Toughness Bar	500	0.6	3	497 - 499
FR43	Joint Tungsten Alloy	Fracture Toughness Bar	800	0.6	3	497 - 499
FR53	Joint Tungsten Alloy	Disc (D3)	800	0.6	3	498 - 500
JCR11-03	SiC/SiC	Mini Bend Bar	950	200	100	487 - 586
JCR11-05	SiC/SiC	Mini Bend Bar	950	200	115	444 - 568
JCR11-08	SiC/SiC	Mini Bend Bar	950	200	115	444 - 560
JCR11-11	SiC/SiC	Mini Bend Bar	950	100	55	448 - 524
SCF4	SiC/SiC	Miniature Flexure Bar	250	100	90	457 - 547

SCF5	SiC/SiC	Miniature Flexure Bar	250	200	45	457 - 511
SCF8	SiC/SiC	Miniature Flexure Bar	600	100	45	457 - 502
SCF9	SiC/SiC	Miniature Flexure Bar	600	200	90	457 - 548
SCF11	SiC/SiC	Miniature Flexure Bar	950	100	57	458 - 517

*MPC= Multi-Purpose Coupon

10.2 HFIR IRRADIATION PROGRAM - FUSION 2021 FRONTIER TASK 3 IRRADIATION CAPSULE DESIGN—N. Russell (Oak Ridge National Laboratory)

OBJECTIVE

The Fusion 2022 Frontier Task 3 irradiation program plans to irradiate five capsules with a design temperature of 400°C. Loading will include FeCrAl tensile specimens and Sn shot designed to melt and interact with the specimens to test corrosion performance.

SUMMARY

The Fusion 2022 Frontier Task 3 irradiation program plans to irradiate FeCrAl tensile specimens submerged in molten Sn to determine corrosion effects during irradiation. The design has a target average specimen temperature of 400°C for one High Flux Isotope Reactor (HFIR) cycle. Images of the thermal analysis for the molten Sn corrosion design are shown in Figure 1.

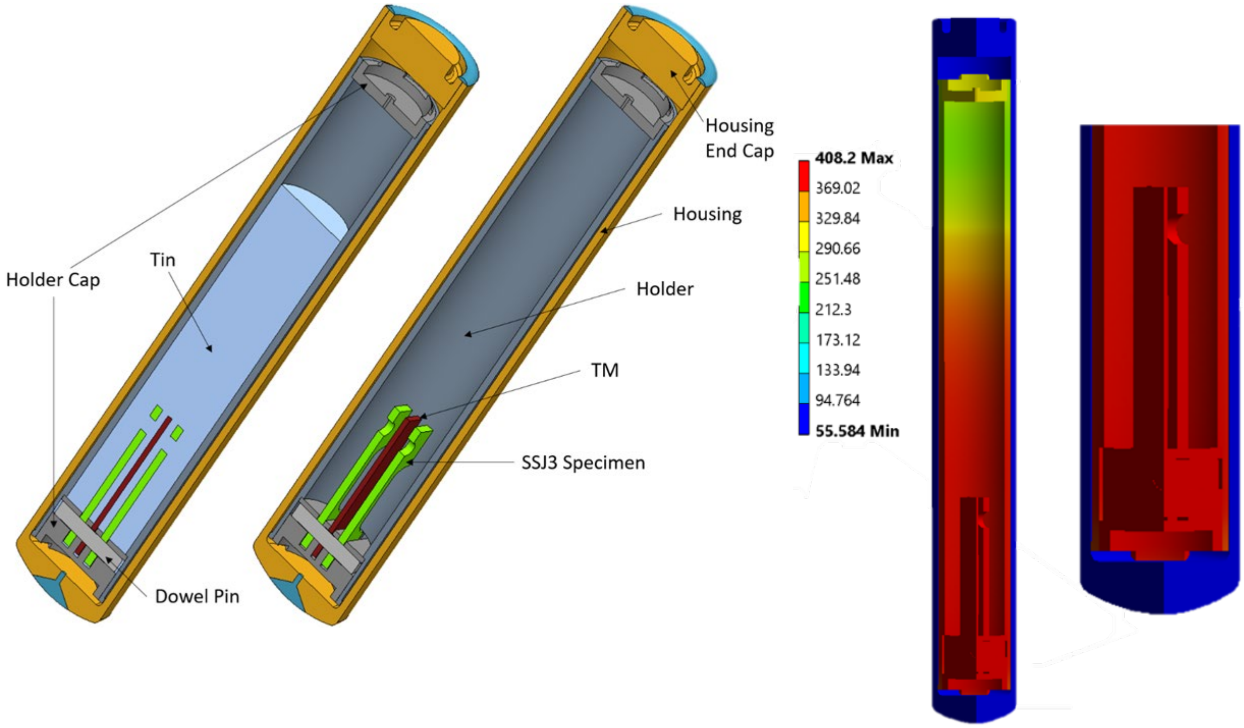

Figure 1. Computer-aided design (CAD) representation (left) with Sn hidden for ease of viewing and representative thermal analysis (right) of Frontier Task 3 molten Sn corrosion irradiation capsules.

The design uses a sealed molybdenum holder to provide a secondary containment within the aluminum housing. The holder has small tabs on the sides to center the holder within the housing. The bottom end cap of the holder assembly has slots for the specimens and thermometry. The specimens are intended to be pinned to the bottom end cap so that during post-irradiation disassembly in the hot cell, the targets can be heated to remove the tin from the specimens.

PROGRESS AND STATUS

Introduction

These five rabbit capsules are intended for irradiation in HFIR cycle 500. Parts and specimens for these capsules have been assembled and the internal welding has begun. After the welding on the internal holder assembly is finished the assembly will undergo non-destructive examination to check for leaks. An example set of capsule assembly photos is shown in Figure 2.

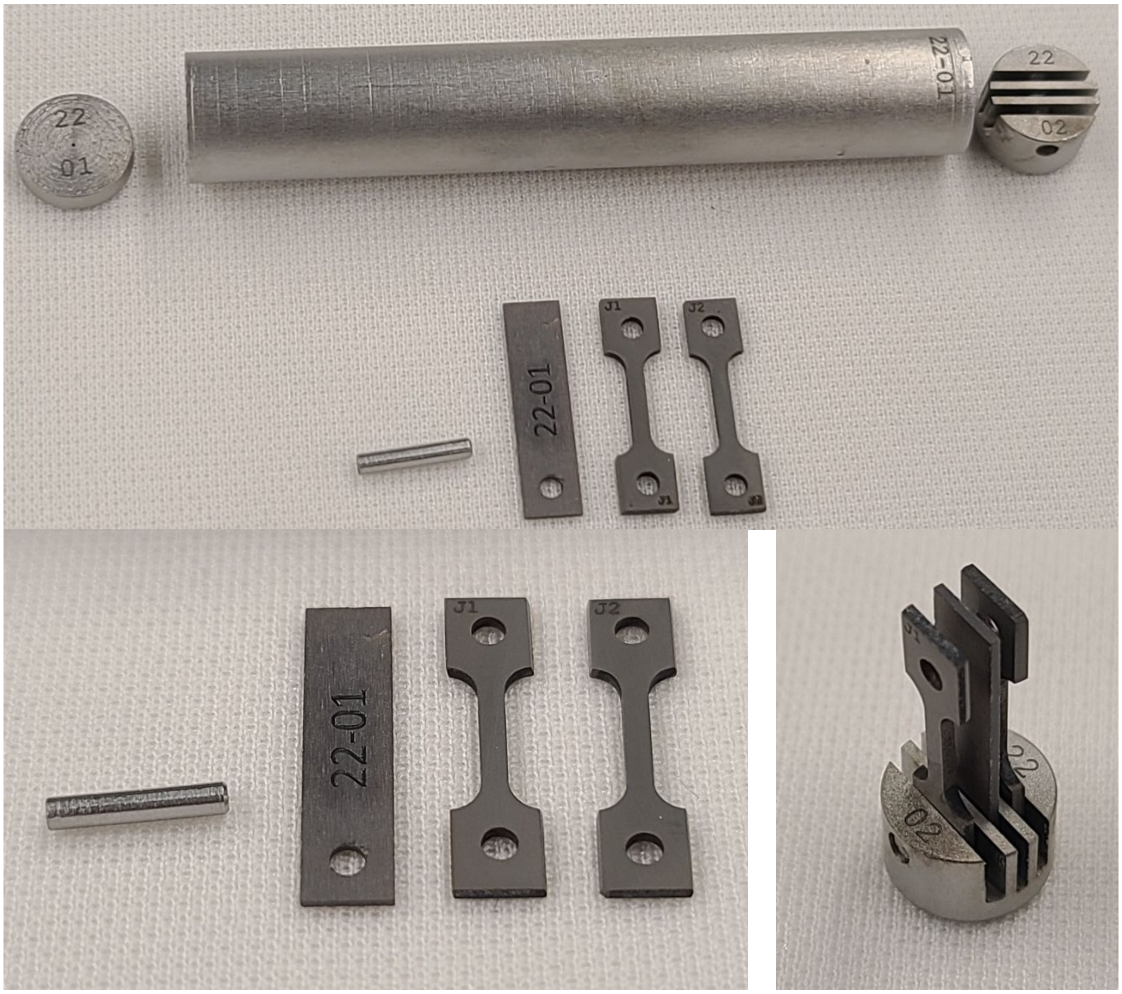

Figure 2. SNF01 internal parts.

The thermal safety calculation has been prepared and reviewed internally and submitted to Research Reactors Division (RRD) for final review. As part of the safety review, a single molybdenum secondary containment was filled with tin, welded, and tested for leaks per standard building procedures. This secondary containment underwent a set of tests to prove that a breach in the holder was not likely due to thermal cycling or HFIR safety limiting condition scenario (LCS). The thermal cycling represents the event that HFIR has an unplanned scram, allowing the experiment to cool, and then reheat when the reactor continues operation. The holder assembly was welded into a stainless-steel capsule to represent the inert atmosphere of the experiment and was heated in a furnace to 400°C and allowed to cool. This was repeated for a total of five cycles. Then, the target was heated in the furnace to 750°C to represent the experiment during an LCS in HFIR. No evidence of a failure in the holder assembly was witnessed. The holder assembly used for the heated testing was also used to perform a demonstration disassembly with the hot cell staff to give confidence the disassembly procedure. A summary of the five rabbit capsule builds is shown in Table 1 with the predicted temperatures in Table 2.

Table 1. Rabbit capsule build summary

Capsule ID	Holder OD (mm)	Housing ID (mm)	Gas gap (μm)	Fill Gas	Specimen Type (Specimen IDs)
SNF01	9.350	9.521	85.5	Helium	Japan ODS (J1, J2)
SNF02	9.355	9.523	84.0	Helium	Japan ODS (J3, J4)
SNF03	9.360	9.527	83.5	Helium	ORNL ODS (O1, O2)
SNF04	9.350	9.522	86.0	Helium	ORNL ODS (O3, O4)
SNF05	9.360	9.525	82.5	Helium	APMT (1, 2)

Table 2. Predicted rabbit capsule temperatures

Capsule ID	Part	Temperature (°C)		
		Avg	Max	Min
SNF01	Specimen	410.1	417.5	387.7
	Specimen Gauge	404.0	410.8	398.1
	TM	411.4	420.9	393.6
SNF02	Specimen	406.3	414.3	383.9
	Specimen Gauge	400.2	407.1	394.3
	TM	407.6	417.1	389.8
SNF03	Specimen	405.2	413.2	382.8
	Specimen Gauge	399.1	405.9	393.2
	TM	406.5	416.0	388.6
SNF04	Specimen	411.5	418.8	389.1
	Specimen Gauge	405.4	412.2	399.5
	TM	412.7	422.2	394.9
SNF05	Specimen	402.5	410.5	380.1
	Specimen Gauge	396.4	403.2	390.5
	TM	403.7	413.3	385.9

10.3 IRRADIATION OF QST F82H TENSILE AND BEND BAR SPECIMENS IN HFIR—N. Russell, C. On, X. Chen, J. Geringer (Oak Ridge National Laboratory)

OBJECTIVE

The objective of this task is the implementation of the general tensile (GENTEN) and general bend bar (GENBEN) designs for irradiation of National Institutes for Quantum Science and Technology (QST) F82H specimens in the High Flux Isotope Reactor (HFIR). There is a total of 21 irradiation capsules within this campaign consisting of three low dose capsules (5 dpa) and 18 high dose capsules (50 and 80 dpa, 9 of each). There are three different average specimen irradiation temperatures of 300°C, 400°C, and 500°C for these capsules.

SUMMARY

The temperature performance within an irradiation capsule is controlled by optimizing the specimen holder outer diameter (OD), holder material, and fill gas to create an insulating gas gap between the hot inner holder assembly and the cold capsule housing in direct contact with HFIR coolant. Much care and consideration was taken to apply the existing GENTEN and GENBEN designs. These designs developed a surface response model that allows the user to quickly and accurately determine a combination of holder OD, holder material, and fill gas to achieve an average specimen goal temperature. These two capsule designs can be seen below in Figure 1 and Figure 2.

The QST requested hold points be introduced to our standard irradiation capsule build procedure. These hold points give the Principal Investigators (PIs) an opportunity for input into the design and build. The first hold point was for holder design approval. This allowed the Oak Ridge National Laboratory (ORNL) PI and QST PI to be involved in choosing appropriate holder ODs considering the neutron induced swelling. All the first hold point forms for the QST irradiation capsules have been reviewed and signed by the capsule designer, ORNL PI, and QST PI. The second hold point was introduced between assembly of the capsule parts and before welding. This hold point form for the capsules show pictures of every step in the assembly process so that QST could review the process and confirm specimen orientation. This hold form is approved for all capsules.

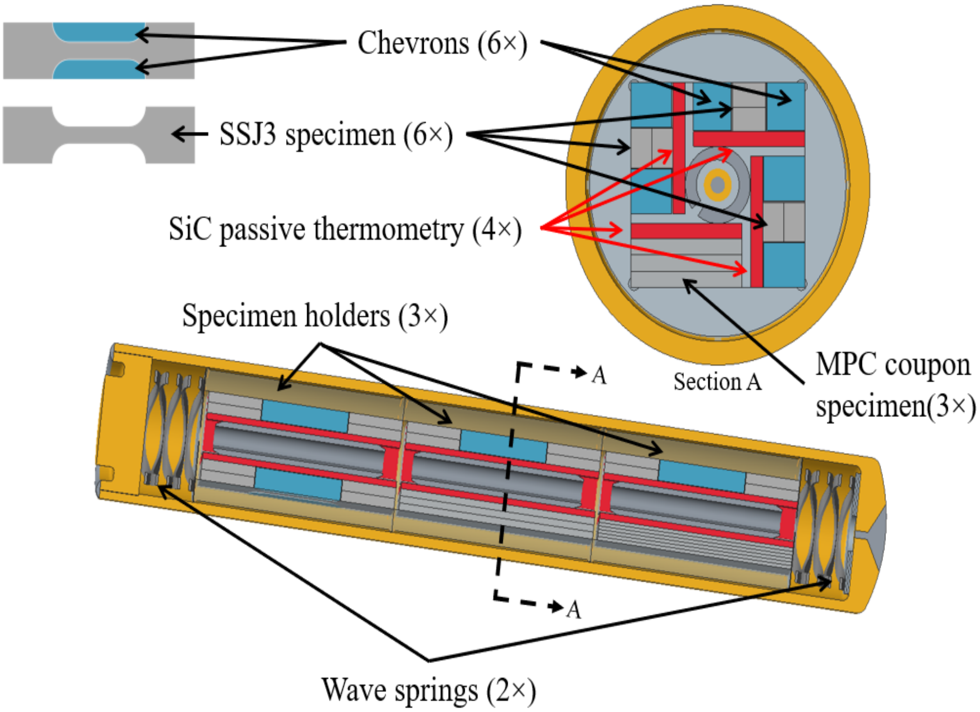

Figure 1. GENTEN irradiation capsule design.

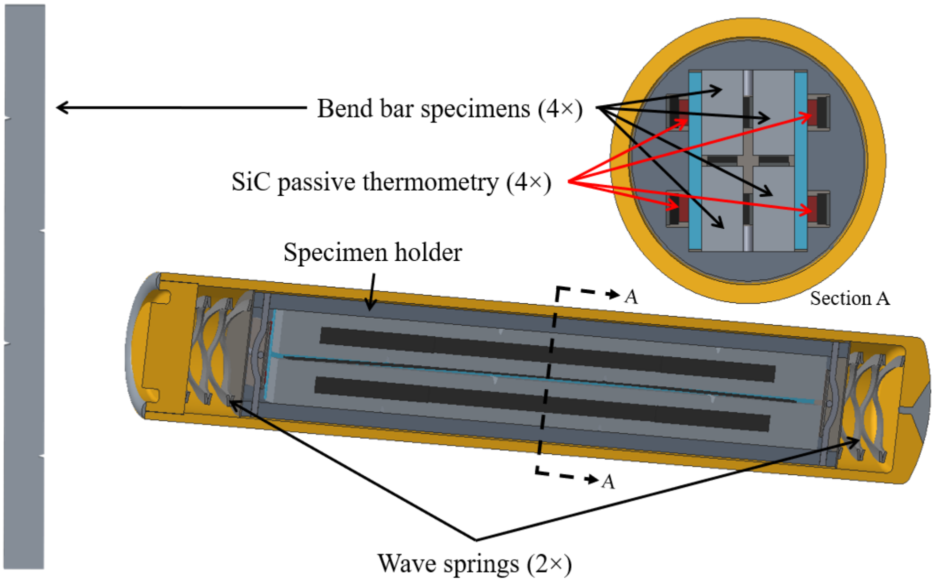

Figure 2. GENBEN irradiation capsule design.

Figure 3. 50 dpa capsule GENTEN example (FH33).

Figure 4. 50 dpa GENBEN example (FH44).

PROGRESS AND STATUS

Introduction

Moving forward, all the low dose capsules have completed irradiation in HFIR (cycles 490-493). The 80 dpa irradiation capsules began irradiation in HFIR cycle 496. All the hold point forms for the capsules have been approved and are included with the fabrication packages. The 50 dpa capsules have been assembled per the sponsor supplied specimen load list. The 50 dpa high dose capsule assemblies have been approved by the ORNL PI and QST PI. Some example photos of the 50 dpa GENTEN assembly are shown in Figure 3, with a GENBEN example in Figure 4. The rabbits are currently undergoing welding and non-destructive testing. The 50 dpa capsules are expected to start irradiation in FY2022.